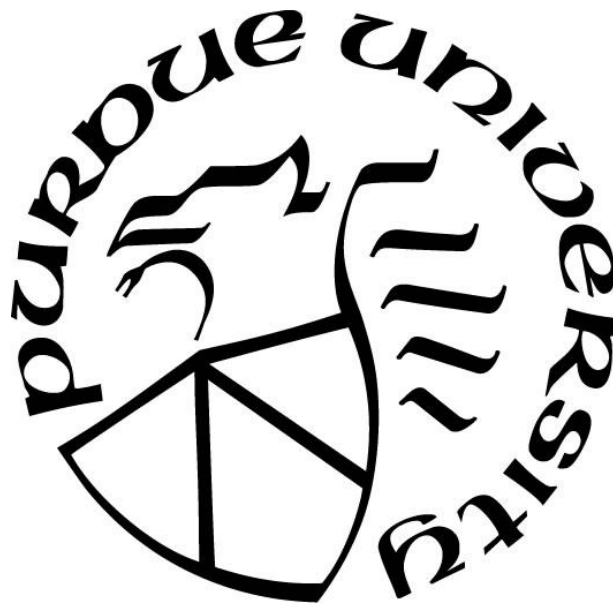# LASER-INDUCED SPARK IGNITION IN FLOWING GASES

by

Seunghyun Jo

A Dissertation

Submitted to the Faculty of Purdue University

In Partial Fulfillment of the Requirements for the degree of

Doctor of Philosophy

School of Mechanical Engineering

West Lafayette, Indiana

August 2021

THE PURDUE UNIVERSITY GRADUATE SCHOOL
STATEMENT OF COMMITTEE APPROVAL

Dr. Jay P. Gore, Chair

School of Mechanical Engineering

Dr. Robert P. Lucht

School of Mechanical Engineering

Dr. Steven F. Son

School of Mechanical Engineering

Dr. Terrence R. Meyer

School of Mechanical Engineering

Dr. Li Qiao

School of Aeronautics and Astronautics

Approved by:

Dr. Nicole Key

ACKNOWLEDGMENTS

TABLE OF CONTENTS

LIST OF TABLES

LIST OF FIGURES

ABBREVIATIONS

LSD   Laser Supported Detonation

LSR   Laser Supported Radiation

MIE   Minimum Ignition Energy

MIP   Minimum Ignition Power

PIV   Particle Imaging Velocimetry

B.R.   Blockage ratio

NOMENCLATURE

A Surface area of a flame kernel

A_g Surface area of heated gas

A_{laser} Aear of laser beam

A_T Constant for temperature of plasma

A_0 Avogadro's number

B_v Constant for wave speed in plasma

c_p Specific heat at a constant pressure

c_v Specific heat at a constant volume

c_0 Speed of light

D Nozzle diameter

dL Change of flame kernel length

dt Time interval between Schlieren images

d_q Quenching distance

E_{ig} Ignition energy

E_{in} Incident energy

E_{loss} Energy loss

E_{pulse} Energy of laser pulse

E_{PR} Plasma radiation

E_{tr} Transmitted energy

h	Energy loss coefficeint
h_{cond}	Heat transfer coefficient by conduction
h_{conv}	Heat transfer coefficient by convection
h_{rad}	Heat transfer coefficient by radiation
$\bar{h}$	Planck's constant
I_0	Energy of laser source
I_{air}	Rayleigh scattering signal intensity of air
I_{back}	Background signal intensity
I_{flame}	Rayleigh scattering signal intensity of flame
I_{irr}	Laser irradiance
I_r	Total Rayleigh scattering intensity
I_{spark}	Intensity of a laser-induced spark
I_{tur}	Turbulence intensity
$I_{b\lambda}$	Blackbody spectral intensity
I_λ	Radiation intensity
$I_{\lambda_{total}}$	Spectral intensity
$I_{\Delta\lambda}$	Radiation intensity
k	Thermal conductivity
k_b	Bolzmann's constant
l_0	Integral length scale
l	A length of a laser beam segment imaged onto a detector

l_g Length of heated gas

m Mass of a flame kernel

m_{crit} Mass of a critical sphere

$\bar{\bar{m}}_f$ Volumetric mass production rate

N Molecular number density

Nu Nusselt number ni Refractive index for each species

P_{laser} Laser power

Pr Prandtl number

$\dot{Q}_{cond}$ Heat lost to cold gas by conduction

$\dot{Q}'''$ Volumetric energy generation rate

q Heat transfer rate

R_{crit} Minimum (critical) radius

R_{ii} Autocorrelation function

R_u Universal gas constant

Re Reynolds number

Re_t Turbulent Reynolds number

r Radius

S_F Flame kernel propagation speed

S_f Flame speed

S_L Laminar flame speed

S_T Turbulent flame speed

x Path length

T_{air} Temperature of air

T_b Temperature of burnt gas

T_f Temperature of flame

T_{flame} Temperature of Flame

T_g Temperature of heated gas

T_k Temperature of a flame kernel

T_p Temperature of plasma

$T_{p,cal}$ Calculated temperature of plasma

T_s surrounding temperature

T_{TC} Thermocouple temperature

T_u Temperature of unburnt gas

T_∞ Plasma temperature

U Mean velocity

u_g Internal energy at heated gas temperature

u_p Internal energy at plasma temperature

u_0 Internal energy at initial temperature

u_{rms} Root-mean-square velocity in the x direction

u' Root-mean-square velocity

V Volume

V_D Detonation wave speed

V_{bulk} Bulk velocity

V_w Wave speed

$V_{w,exp}$ Experimental wave speed

$V_{w,LSP}$ Calculated wave speed using the laser-supported radiation model

v_{rms} Root-mean-square velocity in the y direction

w Beam radius

X_i Mole fraction

z Axial distance from a focal point

Greek Symbols

α Thermal diffusivity

α_T Constant for plasma temperature

α_λ Spectral absorption coefficient

β_v Constant for wave speed in plasma

γ Consant for forced heat convection transfer

γ_k Specific heat ratio

Δh_c Heat of combustion

Δt Time

ε Emissivity

ε_p Plamsa emissivity

$\varepsilon_{p,cal}$ Calculated plasma emissivity

θ Angle between the incident laser and the scattered light

κ_λ	Linear absorption coefficient
λ	Wavelength
ν	Kinematic viscosity
υ_0	Frequency
ϕ	Equivalence ratio
ρ	Density
ρ_b	Density of burnt gas
ρ_u	Density of unburnt gas
ρ_v	Depolarization ratio
ρ_0	Density at initial temperature
σ	Stefan-Boltzmann constant
σ_i	Rayleigh scattering cross section
$\sigma_i{'}$	Differential Rayleigh scattering cross section
τ_λ	Optical thickness
χ	Loss factor in plasma
Ω	Solid angle between a laser sheet and a collection optic

ABSTRACT

This research has been studied a laser-induced spark in flowing gases. The relationship between the minimum ignition energy (MIE), the turbulence intensity, and the flame kernel propagation speed is considered. Plasma emission, produced by the laser-induced spark, and flame kernel generation by the plasma are investigated. The energy balance equation between an ignition energy and energy losses by heat transfer is studied at laminar flows and turbulent flows. Hydrogen and air mixtures were used in a premixed jet burner for ignition experiments. Particle image velocimetry (PIV) examined the velocity and the turbulence intensity under the turbulent flows. The flame kernel development was visualized using Schlieren imaging and infrared images (IR camera). Flame kernel temperatures were measured through Rayleigh scattering and infrared images (IR camera). Plasma evaluations were captured through an intensified CCD camera (ICCD camera). Minimum ignition energies were measured at the laminar flows and the turbulent flows. The MIE decreases with an increase in the turbulence intensity which varied by ignition locations and perforated plates at the constant bulk velocity. Improved mixing rates due to the ignition locations or the geometry of the perforated plates decrease the MIE at the constant bulk velocity. The turbulence intensity increases wrinkles in the flame kernel surface, thus the contact between the flame kernel and reactants increases due to the wrinkles. Therefore, the flame kernel propagation speed increases as the turbulence intensity is higher since the increased reaction by the wrinkles and the contact. Thus, the MIE decreases as the turbulence intensity increases at the constant ignition condition, including bulk velocities and ignition heights, since the high turbulence intensity increases the flame kernel propagation speed. Laser energy differences affect the plasma expansions by the laser absorption. Laser-supported radiation (LSR) wave speeds were measured and calculated using energy balance equations. Velocity does not affect the flame kernel temperature distribution during the early reaction steps because the plasma generates a flame kernel and determines the flame kernel temperature distribution. The MIE increases with increasing the bulk velocity. The energy losses considering convection, conduction, and radiation were calculated using the flame kernel radius, the flame kernel temperature, mixture properties, and the flame speed. The energy balance equation in the ignition of flowing gases is newly written at the laminar flows and the turbulent flows.

1. INTRODUCTION

1.1 Motivation

Ignition in combustion devices is always a essential factor for stable combustion. An ignition device should generate proper ignition energy to initiate combustion devices. From the energy balance equation, the ignition energy must be equal to or higher than the energy loss by a surrounding gas for a successful ignition. The energy loss in stagnation flow is heat conduction. Flowing fluid provides different conditions with stagnation flow. Therefore, appling minimum ignition energy (MIE) [3], obtained from stagnation flow conditions, to flowing fluid environments may lead to failure of ignition or unexpected explosions. Studying the energy balance in the ignition flowing gases is important not only for ignition of combustion devices but also for prevention of unexpected explosions. Many experimental groups have studied ignition energy in flowing gases [1-10]. They observed that the MIE increased with increasing flow velocity, and estimated that the velocity increases heat convection [1,3-6]. However, a clear relationship between energy advection and MIE has not been established [1,3-6]. The reason is they did not prove an accurate relationship between the MIE and the forced convection heat transfer [1,3-6]. Therefore, the study for the energy balance in the ignition of flowing gases is needed to understand dominant energy loss and estimate the MIE.

The MIE increases with increasing velocity from previous studies [1,3-6]. As velocity is faster, MIE should be increased to ignite reactants [1,3-6]. Gas turbine engines that produce high power need a large ignition device, using high ignition energy, to ignite propellants of high velocity. If we can reduce MIE at a constant flow velocity, gas turbine engines will have a lot of profit in terms of efficiency, weight, and space. Because a small igniter, having low weight and volume, can produce low ignition energy; thus, gas turbines using a small igniter can decrease the weight of a vehicle and can increase an efficiency regarding power to weight ratio. In general, it is challenging to reduce MIE at a constant ignition condition without changing a design of an engine. Turbulence intensity may become a solution that can decrease MIE at a consistent ignition condition since the turbulence intensity affects the turbulence flame speed and the flame kernel growth [11–16]. Different locations in a flow field or various structures in perforated plates change the turbulence intensity [17–21]. In other words, different ignition locations or perforated plates

may be able to change MIE by turbulence intensity. Few studies have experimentally studied the effect of the turbulence intensity on the MIE in flwoing gases [2,8-10]. The MIE increased with increasing the turbulence intensity in the papers [2,8-10]. However, the experiments did not use consistent experimental conditions to examine the influence of the turbulence intensity on the MIE [2,8-10]. Therefore, performing ignition experiments under constant experiment conditions is required to define the effect of turbulence intensity on MIE.

A lot of research has investigated plasma produced by a laser for 30 years through visualized approach methods [22-32]. However, almost all plasma studies have independently evaluated the plasma without research regarding a flame kernel growth with reactants [22-68]. Many industrial fields, like gas turbines, burners, and rockets, using the plasma to ignite reactants. Applying the plasma analysis, studied independently without considering reactants, to real work is not a good method because an exact situation immediately after ignition by the plasma is not clear. Therefore, studying the plasma generated by a laser and the ignition of reactants by the plasma is required to analyze the laser ignition and to apply the plasma analysis to real industries. Especially, an effect of velocity on a flame kernel should be also investigated since many devices use fluid and the velocity of reactants may affect plasma expansion and flame kernel growth.

(a)   (b)
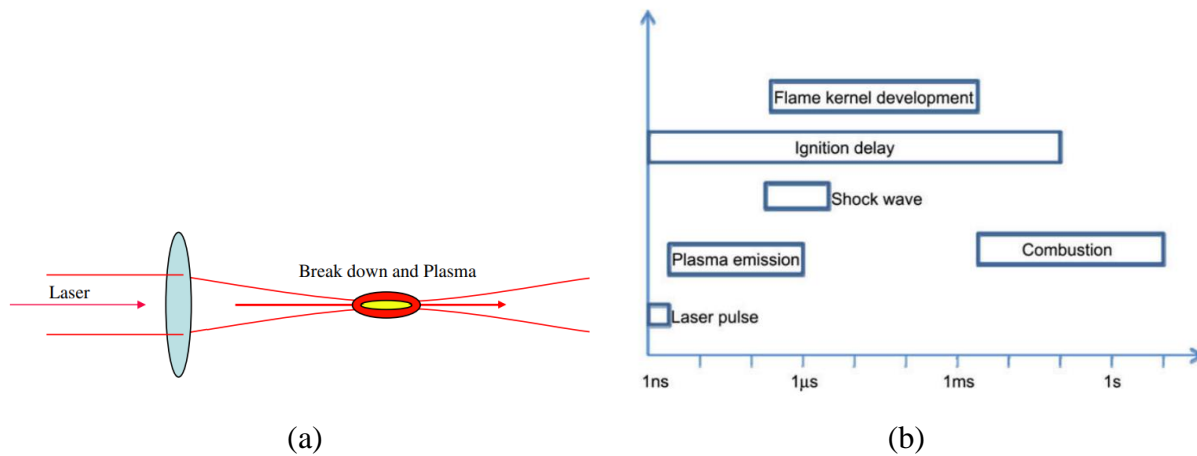
Fig.1-1. (a) Laser-Induced Spark (b) Range of Timescales for Various Processes Involved in Laser-Induced Spark Ignition: the Lengths of the Box Indicate the Durations of the Indicated Processes [72].

1.2 Ignition in Premixed Flame

1.2.1 Laser-Induced Spark Ignition

Laser ignition has advantages than conventional electric-spark ignition [3, 31,69-71]. Laser ignition can precisely control ignition energy. An ignition location can be positioned in a desired location by a laser. Quenching effects and heat conduction by spark electrodes do not occur in laser ignition. Precisely ignition timing can be controlled with laser ignition. Laser ignition uses a laser to ignite mixture and can be classified into four categories [31,69]. Laser thermal ignition excites the kinetic energy of molecules to a translational, rotational, or vibrational mode using a laser beam. As a result, the laser beam breaks the molecular bonds and occur chemical reactions. Laser-induced photochemical ignition dissociates target molecules into highly reactive radical species by laser photons. The radical species initiate chemical chain-branching reactions and, after that, ignites mixture. Resonant breakdown ignition generates seed electrons through the non-resonant multiphoton photodissociation and the resonant photoionization. The formation of the seed electrons leads to the generation of plasma and ignition. Laser-induced spark ignition initiates with released electrons by multi-photon ionization of gas molecules. The liberated electrons collide with other molecules and ionize the other molecules. The ionization leads to a rapid increase in electrons and breakdowns the gas, after that, generates a plasma and ignites mixtures. Laser-induced spark ignition has been widely studied since every wavelength can be used it. Laser-induced spark ignition is also referred to as non-resonant breakdown.

Many studies have investigated laser-induced spark ignition in terms of plasma, flame kernel growth, ignition energy, ignition probability, wavelength, pulse duration, and focal length [3,4,8,10,22-81].

1.2.2 Spark Ignition

Spark ignition system consists of electrodes and an electrical circuit. If a voltage between the electrodes continuously increases, electrons are released from the anode [82,83]. After that, the voltage reaches sufficient energy that can breakdown gases. The electric field at the breakdown voltage accelerates the electrons that can ionize other molecules in the space between the electrodes by collisions. The ionization leads to an electron avalanche. After the breakdown, a plasma is generated between the electrodes and ignites reactants.

1.3   Minimum Ignition Energy

Minimum ignition energy (MIE) is defined as an energy needed to form a flame kernel that has sufficient size and temperature to propagate a stable flame. MIE has various values according to ignition conditions. If ignition energy is lower than a heat loss at a specific condition, a flame kernel will be extinguished by the heat loss. In contrast, if ignition energy is sufficiently high enough to overcome a heat loss at an ignition condition, a flame kernel can develop into a flame. In other words, MIE must be higher than a heat loss or must be equal to a heat loss to propagate a sustainable flame.

$$E_{ig} = E_{loss}. \tag{1.1}$$

1.3.1   Minimum Ignition Energy in Flowing Gases

Swett studied the MIE of propane/air mixture using an electric-spark ignition [2]. The study was conducted at various velocities, pressures, temperatures, turbulence intensities, locations, spark duration, and distances of electrodes [2]. The ideal conditions for the ignition using the electric-spark ignition were low velocity, high pressure, high gas-stream temperature, low turbulence in the gas stream, location of discharge in the best mixture composition, the optimum spark duration at gas-velocity condition, and electrode spacing maintained at quenching distance [2].

Ballal and Lefebvre investigated the ignition of propane/air mixture using an electric-spark ignition [1]. The MIE increased with increasing the flow velocity. They mentioned that heat loss by forced convection affected the MIE [1]. They proposed an empirical MIE equation that analyzed the processes the heat generation rate by combustion in an incipient spark kernel and the heat loss by thermal conduction and turbulent diffusion [7],

$$E_{ig} = c_p \rho (T_b - T_u) \frac{\pi}{6} d_q^3 \tag{1.2}$$

the quenching distance for low turbulence mixture as expressed by

$$d_q = \frac{10k}{c_p \rho (S_L - 0.16 \, u')} \tag{1.3}$$

for high turbulence mixtures

$$d_q = \frac{10k}{c_p \rho (S_T - 0.63\, u')}$$ 1.4

where c_p is a specific heat at constant pressure, ρ is a density of mixtures, T_b is a temperature of burned gas, T_u is a temperature of the unburned gas, d_q is a quenching distance, k is a thermal conductivity, S_L is a laminar flame speed, v_{rms} is a root mean square velocity, and S_T is a turbulent flame speed. From eq.(1.2), minimum ignition energy was defined as the energy required to heat a sphere volume of gas, having a quenching distance, up to the adiabatic flame temperature, T_b [7]. The MIE increased with increasing thermal diffusivity and turbulence intensity, and decreased with increasing density and flame speed [7].

Beduneau et al. studied the MIE under laminar flows using laser-induced spark [3]. The MIE for rich mixtures increased with an increase in the flow velocity since increasing the flow velocity enhanced heat convection around the flame kernel. As a result, a higher ignition energy was required at higher flow velocity. The MIE for lean mixtures decreased with increasing the flow velocity. They explained the reason that an increase in the amount of fuel available for ignition by increasing the flow velocity provided a positive influence on ignition.

Kobayashi et al. experimentally examined the MIE using laser-induced spark under low velocities ranging from 0.1 m/s to 1 m/s [4]. As flow velocity increased, the MIE initially decreased, reached a minimum value, and increased after passing the minimum values. They assumed fuel supply and convective heat loss affected the MIE. In a low-velocity flow, the effect of the fuel supply was dominant, and increasing the flow velocity facilitated combustion as supplying more fuel to the reaction zone. Consequently, the MIE in low velocity decreased with increasing the flow velocity. As velocity was faster, the energy loss by the heat convection from the flame kernel to the surrounding increased. Eventually, the heat convective loss exceeded the influence of the fuel supply. As a result, the MIE increased with the increase in the flow velocity.

Griffiths et al. measured the MIE in laser ignition of natural gas and air mixtures [5]. They found the MIE increased with increasing velocity. They estimated the high velocity necessitates the use of high energies to generate a volume of gas that can produce sufficient heat and compensate for the convective heat loss by velocity.

Lefkowitz et al. studied the minimum ignition power (MIP) using premixed methane and air [6]. When the electrodes distance was 2 mm, the MIP increased with velocity because convective losses were dominant. In contrast, at the small electrodes distance (0.5 mm), electrode quenching was dominant instead of velocity. The MIP increased with decreasing the distance of electrodes at constant velocities.

1.3.2 Minimum Ignition Energy in Constant Volume Chamber

Although many authors have studied the MIE in a constant volume chamber, the tendency of the MIE is similar to the ignition experiments conducted by Lewis and von Elbe [82]. They performed ignition experiments using the electric spark to measure the MIE and the quenching distance for various experimental conditions in terms of mixture compositions and pressures [82]. The MIE and the quenching distance increased with decreasing the pressure and the concentration of oxygen [82]. The MIE had low values at near-stoichiometric mixtures and high values at very lean and rich mixtures [82]. The tendency of the quenching distance was very similar to the trend of the MIE [82]. They suggested an empirical equation for minimum ignition energy [82],

$$E_{ig} = \frac{k}{S_L} \pi d_q^2 (T_b - T_u) \qquad 1.5$$

where d_q is a quenching distance, and k is a thermal conductivity. Equation (1.5) implied that the MIE is required energy that can grow a flame kernel having a quenching distance. However, eq.(1.5) did not agree with the experimental results [7]. The cause of the disagreement is that the MIE in eq.(1.5) is proportional to d_q^2 , but a flame kernel is proportional to d_q^3 [7].

The ignition energy also is discussed in combustion textbook [85]. In the analysis, minimum ignition energy produced by a spark requires to generate a critical gas volume having burned gas temperature [85]. The critical radius, R_{crit}, is defined as a minimum radius that can propagate to a flame from an initial state without any aid [85]. An energy balance equation between an energy generation by chemical reactions and energy loss to surrounding cold gases by heat conduction is used to determine the critical radius, R_{crit}, [85]

$$\dot{Q}'''V = \dot{Q}_{cond} \qquad\qquad 1.6$$

or

$$\overline{\dot{m}_f}\Delta h_c 4\pi \frac{R_{crit}^3}{3} = -k4\pi R_{crit}^2 \frac{(T_b - T_u)}{R_{crit}} \qquad\qquad 1.7$$

where $\overline{\dot{m}_f}$ is mean mass flux, and Δh_c is heat energy of combustion,

$$\Delta h_c = (1 + v_R)c_p(T_b - T_u) \qquad\qquad 1.8$$

where v_R is air fuel ratio. From eq.(1.7), the critical radius is

$$R_{crit}^2 = -\frac{3k(T_b - T_u)}{\overline{\dot{m}_f}\Delta h_c}. \qquad\qquad 1.9$$

The laminar flame speed is defined as

$$S_L = \left[-2\alpha(1 + v_R)\frac{\overline{\dot{m}_f}}{\rho_u}\right]^{1/2} \qquad\qquad 1.10$$

where α is thermal diffusivity, $\alpha = k/(c_p\rho_u)$. Substituting eqs.(1.8, 1.10) into eq.(1.9) yields

$$R_{crit} = \sqrt{6}\frac{\alpha}{S_L} \qquad\qquad 1.11$$

The ignition energy is assumed as the energy, added by the ignition, heats the critical mass to the burned gas temperature,

$$E_{ig} = m_{crit}c_p(T_b - T_u) \qquad\qquad 1.12$$

where the critical mass of the sphere, m_{crit}, is $\rho_b 4\pi R_{crit}^3/3$.

$$E_{ig} = \rho_b 4\pi \frac{R_{crit}^3}{3} c_p (T_b - T_u) \qquad 1.13$$

where ρ_b is the density of the burnt gas.

1.4 Effect of Turbulence Intensity on Flame Speed

Turbulent flame speed increases with an increase in the turbulence intensity [13–16]. As turbulence is higher, the wrinkling of a flame front increases. As a result, as a flame area is larger, turbulent flame speed also increases. In premixed hydrogen/air, the influence of the turbulence on the turbulence flame speed was large for lean mixtures, and was small for rich mixtures [13]. In other words, the turbulent to laminar flame speed ratios, S_T / S_L was high at lean mixtures and low at rich mixtures. However, the absolute value of S_T for rich mixtures was higher than lean mixtures. From the experimental results, Koroll et al. suggested the turbulence flame speed for premixed hydrogen/air.

$$\frac{S_T}{S_L} = \left[1 + 16 \left(\frac{u'}{S_L} \right)^2 \right]^{0.5} + \left[1 - exp \left(\frac{u'}{S_L} \right) \right] \frac{\left(\frac{\rho_u}{\rho_b} - 1 \right)}{\sqrt{3}}. \qquad 1.14$$

1.4.1 Effect of Turbulence on Flame Kernel Growth

During the timescale of 0–100 µs, the flame kernel size was nearly constant at various turbulence intensities that change by velocities, turbulence did not significantly affect the flame kernel growth [86]. After 100 µs, the flame kernel size increased with increasing the turbulence intensity because the high turbulence intensity accelerated mass burning rates and increased a flame kernel area [11,12,86]. However, at very lean conditions, an increase in the turbulence intensity decreased the flame kernel growth [11]. Flame kernel fastly grows as turbulence intensity increases regardless of experimental works and numerical studies [11,14,87-96]. They concluded that an increase in the wrinkling of the flame area by high turbulence intensity facilitates flame kernel development [71].

1.4.2 Effect of Turbulence on Flame Kernel Propogation speed

Flame kernel propagation speed was studied using Schlierne images and particle image velocimetry measurements by Mansour et al. [94-96]. As the higher jet velocity, the flame kernel propagation speed increased [94-96]. The flame kernel propagation speed decreased with a decrease in the turbulence intensity generated by the grids [94-96].

1.5 Effect of Turbulence Intensity on MIE

Swett investigated an effect of turbulence intensity on MIE in flowing gases [2]. The paper concluded that the MIE increased with increasing the turbulence intensity [2]. However, their experimental results were shown suspected points [2]. The relationship between the MIE and the turbulence intensity was not consistent [2]. The ignition experiment was conducted 10 cases at the fixed height and the various turbulence intensities [2]. However, increasing the turbulence intensity increased the MIE in only 3 cases [2]. The MIE was nearly constant or decreased with increasing the turbulence intensity in the other cases [2].

Ballal and Lefebvre performed the ignition experiment at the constant mainstream velocity and different turbulence intensities [9]. The measured MIE increased with the increase in turbulence intensity [9]. However, their experimental results were questionable [9]. The measured root-mean-square velocities had various values at the fixed perforated plate and the constant mainstream velocity [9]. If a measurement is conducted at a fixed location, a root-mean-square velocity must have one value at a constant perforated plate and velocity [9]. The various root-mean-square velocities might have implied inconsistent ignition locations in the experiment [9]. The MIE increased with an increase in the turbulence intensity in the plot [9]. However, the relation between the turbulence intensity and the MIE was not clear in the table [9]. The tabulated MIE increased, decreased or was constant with increasing the turbulence intensity [9].

Cardin at el. studied the effect of turbulence intensity on the MIE [8,10]. In the papers, increasing the turbulence intensity increased the MIE [8,10]. However, the ignition experiment did not perform at the consistent experimental condition [8,10]. The various mean velocities and ignition heights were utilized in the papers [8,10]. Mean velocity and an ignition height also provide a significant effect on MIE, respectively. They concluded the relation between the turbulence intensity and the MIE without considering the influence of the mean velocity and the

ignition height [8,10]. Therefore, the result, obtained from their experiments that conducted at inconsistent mean velocities and ignition heights, did not give sufficient trust [8,10].

However, recent ignition studies found different result with the previous papers. Law et al. examined ignition in a constant pressure chamber [97,98]. Turbulence facilitated ignition due to the increased kernel surface stretch [97,98]. The more increased turbulence above the specific values significantly dissipated the deposited energy kernel, and ignition was not possible [97,98]. Shy et al. investigated ignition energy in a large dual-chamber [99-102]. The ignition energy decreased with increasing turbulence when the electrode distance was lower than 2 mm [100-102]. In contrast, the turbulence negatively affected ignition at 2 mm of the electrode distance [100]. They estimated the flame segments intensified by the negative stretch in the intensive turbulence case might facilitate ignition [100-101].

1.6   Flame Kernel Development in Laser-induced Spark Ignition

Several researchers have investigated ignition processes from a laser pulse to flame kernel growth [71,72,75-77]. The sequence of the ignition processes is laser pulse, plasma generation, plasma expansion, shock-waves, flame kernel development, and propagating flame.
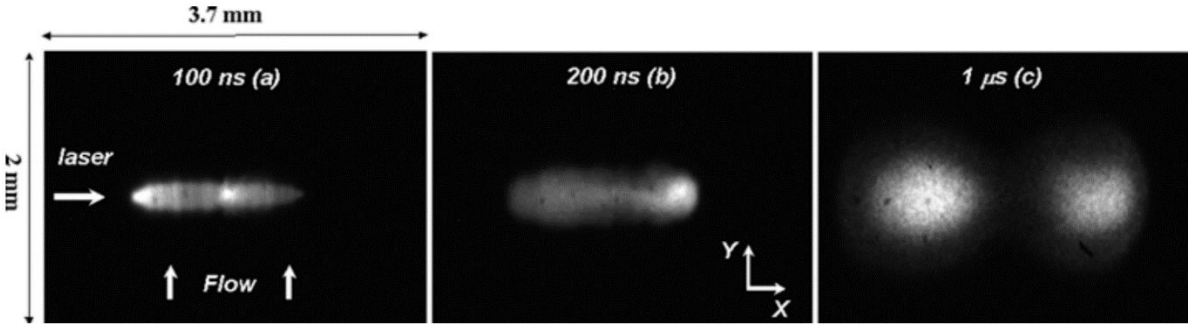
Fig.1-2. Time series of plasma to flame kernel development, premixed CH_4/air flow, equivalence ratio=0.9, flow velocity=1.15 cm/s, and E_{in}= 15.4 mJ [74].

1.6.1   Plasma Formation

The generation of laser-induced spark (plasma) in gas has been investigated since the 1960s, and the studies related to the plasma have been summarized [31,34,35,104]. A laser irradiance is increased by a focused laser beam, and multiphoton ionization is occurred by the sufficiently high

laser irradiance at the focal point. Electrons that can absorb photons by inverse bremsstrahlung process are generated by the multiphoton ionization. The ionization by the electron rapidly increases the electron density, then a breakdown occurs and a plasma (spark) is produced. The plasma heats the ambient gas by the plasma radiation, ionizes the gas, and expands. The energy transfer from the heated gas to the ambient gas leads to the absorption wave. The ionized gas absorbs the laser energy and the laser radiation via the absorption wave. The plasma expands toward the laser beam by the laser absorption. If an irradiance is sufficiently high, the plasma radiation is strong, the ambient gas is heated to high temperature by the plasma radiation prior to the shock wave arrival, and the laser absorption initiates nearby the ambient gas by the supersonic wave [35,104]. The laser-supported radiation (LSR) wave occurs at this sufficiently high irradiance, and the front edge of the plasma moves with the laser-supported radiation wave speed by the laser absorption [35,104]. At the intermediate irradiance, the shock is strong that, the shocked gas can absorb the laser radiation without heating by energy transfer from the plasma. The laser absorption occurs behind the shock wave and shows the same speed with the shock wave. This laser absorption process by the intermediate irradiance is called the laser-supported detonation wave (LSD). The laser-supported combustion wave is generated at low irradiance. The shock wave separately moves with the laser absorption zone, the front edge of the plasma. The shock wave firstly propagates, the front edge of the plasma propagates into the shocked gas zone, it is called the laser-supported combustion wave.

1.6.2 Laser-Supported Radiation Wave and Laser-Supported Detonation Wave

Many authors have experimentally studied the laser-supported radiation (LSR) wave and the laser-supported detonation (LSD) wave since 1960 [27,35-40,54,55]. Ramsden et al. used an image-converter camera to study LSD waves and estimated the wave speeds as 54-190 km/s [36]. Gatti et al. examined the laser shock wave through a digitalizing camera [37]. However, these earlier studies did not relate the wave speed with the laser irradiance [36,37]. Chen et al. measured laser irradiances and utilized an intensified CCD camera to evaluate LSR wave speeds [27]. They [27] estimated the LSR wave speeds with the scaling method, suggested by [42,104], and the one-dimensional LSR computation, studied by Bergel'son et al. [42]. Phuoc et al. measured the spark temperature through spectroscopic analysis and the wave speed using a photo-multiplier tube (2ns rise time) [48]. The measured wave speed was $110 \, km/s$ at the irradiance of $2 \times 10^{11} \, W/cm^2$

[48] and compared calculated shock speed, $133\ km/s$ at the same irradiance studied by Raizer [35]. They compared the measured wave speed with the LSD wave speed, but the irradiance in their study was sufficiently strong, which can produce an LSR wave, thus they should have considered the LSR wave instead of the LSD wave [35,48]. Recently, a lot of researchers have used an intensified CCD camera to investigate the LSR wave and the LSD wave [39,40,48,52,54,55]. The LSD wave speed is between 1 to 10 km/s at the irradiance of $10^6 \sim 10^8\ W/cm^2$ [39,40,52]. The LSR wave speed is between 10 to 200 km/s at the irradiance of $10^{10} \sim 10^{12}\ W/cm^2$ [48,54,55].

1.6.3   Plasma Temperature Measurement

The spectroscopic study has widely used to measure the plasma temperature [57-67]. Some papers utilized Rayleigh scattering to evaluate the plasma temperature [56,64,68]. The plasma temperature decreased as time elapses and increases with the laser irradiance [56-68]. The plasma temperature measured by the spectroscopic study was converged to a few thousand Kelvin by time [57-66]. The maximum plasma temperature was measured between 10,000 to 420,000 K [56-66]. The laser energy, the measurement time, and the experiment pressure contributes on the change of the maximum temperature [56-66]. Glumac et al. studied the plasma kernel using the filtered Rayleigh scattering until $1000\ \mu s$ [64]. The measured plasma temperature was higher than 2000 K at $100\ \mu s$, and the system only considered the plasma without reactants [64]. The temperature results by Glumac et al. [64] were too higher than the other works [56,105] which studied the flame kernel temperature through the Rayleigh scattering. The filter Rayleigh scattering signal was weak in their work [64], thus Glumac et al. utilized the Saha equation and the Rayleigh scattering signals to compute the temperature, not the general Rayleigh intensity equation, $T = T_0 I_{0_{Ray}}/I_{Ray}$ [56,105]. Thus, the Saha equation used in the filtered Rayleigh scattering might have calculated the high temperature [64]. There is no such study that simultaneously evaluated the plasma expansion, and the flame kernel development in terms of temperature, but Mulla et al. [71] investigated plasma and the flame kernel growth through OH PLIF images at the different velocities, equivalence ratio, and laser energy.

1.6.4 Flame Kernel Development

After plasma, flame kernel evolution initiates. The flame kernel structure starts with an elongated ellipse, changes to a spherical, then to peanut-like and finally grows to a flame [71,74, 76,77,79-81]. The flame kernel size increased with increasing the laser ignition energy [71,103]. The greater laser ignition energy led to a larger and more rapidly growing initial flame kernels [71,103]. The effect of the fuel concentration on the flame kernel growth was studied by Mulla et al. [71]. During 10-100 μs, the flame kernel perimeter was nearly constant . After 100 μs, the fuel concentration, close to the stoichiometric, showed rapid flame kernel growth. In contrast, the fuel concentration, close to the lean flammability limit, a flame was blow-off after 100 μs. Mulla et al. investigated the effect of the flow velocity on the flame kernel development [71]. The velocity did not affect the flame kernel growth during 0-100 μs. After 100 μs, increasing the flow velocity increased the flame kernel growth. They presumed the increased turbulence by the flow velocity affected the flame kernel development after 100 μs. Recently ignition in turbulent flow has examined in terms of kernel growth [106-110]. The hydrodynamic instability dominantly affected the growth of the supersonic kernel, and turbulence secondly influenced it [106]. The kernel growth in the supersonic flow during the early stages [108] was almost identical with other work examined by Mulla et al. [71]. This similarity means a universality in the early time kernel development of laser ignition [108]. The kernel rapidly developed as the reaction rate increased, and the reaction rate from the chemical composition of fuel was critical for successful ignition [110].

1.7   Diagnostics Methods

1.7.1 Schlieren Image

Schlieren image uses a difference of density [112]. When gas does not have uniform density by a change of temperature, pressure, or velocity, then the light that passes the gas is reflected by a difference of density. As a result, the direction of the light is changed due to the difference of the density. If a disturbance by temperature, pressure, or velocity occurs in a test section, a direction of a light source will be changed slightly. If the image of the light source is deflected by a knife-edge, the additional light will enter the camera which captures the additional light. The disturbance of the test section will appear as streaks of light by additional light. Many

combustion studies have used Schlieren image to exaime a flame kernel development and a flame speed [3,74,76,79,86].

1.7.2   Particle Imaging Velocimetry
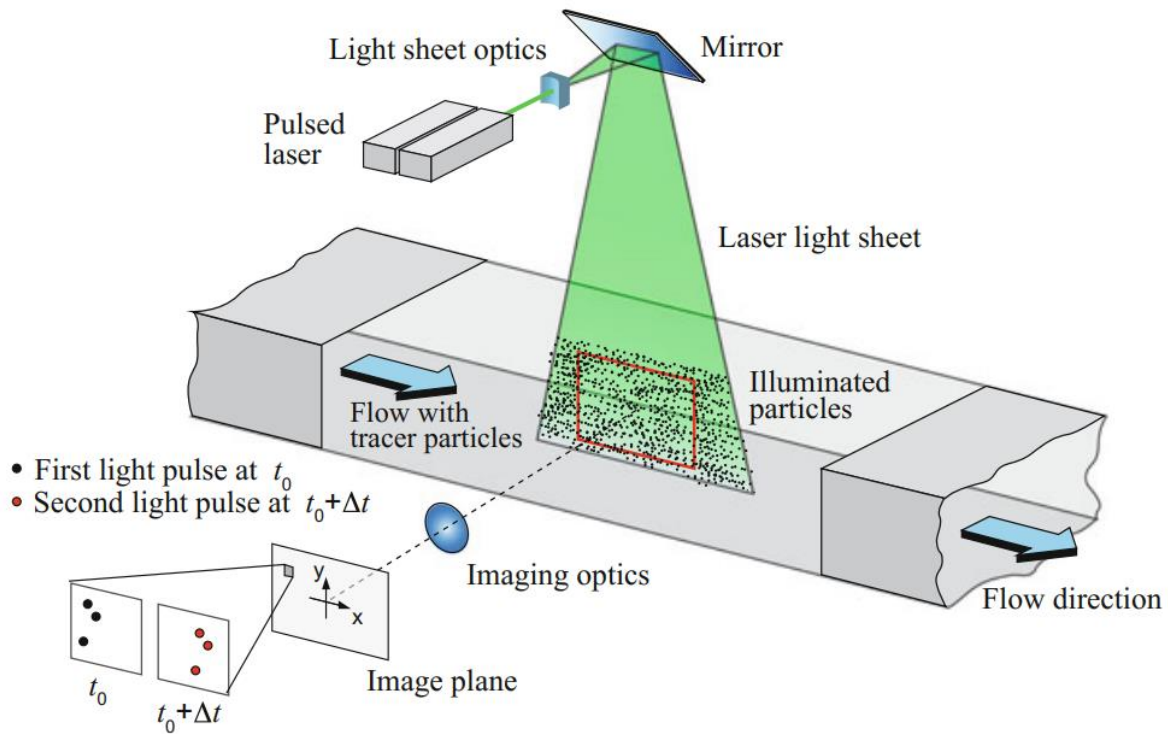
Fig.1-3. Experimental arrangement for planar 2D PIV in a wind tunnel [113].

Particle Imaging Velocimetry (PIV) is the most widely used measurement technique to investigate the flow field. A PIV system typically consists of several subsystems [113].

- Seeding: In most applications tracer particles have to be added to the flow.
- Illumination: These tracer particles have to be illuminated in a plane or volume of the flow at least twice within a short and known time interval.
- Recording: The light scattered by the tracer particles has to be recorded either on two separate frames or on a sequence of frames of a camera.

- Calibration: In order to determine the relation between the particle image displacement in the image plane and the tracer particle displacement in the flow, a calibration is required.
- Evaluation: The displacement of the particle images between the light pulses has to be determined through evaluation of the PIV recordings.
- Post-Processing: In order to detect and remove invalid measurements and to extract complex flow quantities of interest, sophisticated post-processing is required.

Tracer particles are added to a flow. A laser sheet illuminates a plane of interest within the flow twice. A time delay between the laser pulses is chosen considering the flow velocity and the magnification of the image. The tracer particles illuminated by the laser sheet become scattered signals that are captured by a camera. For simplicity it is assumed that the tracer particles move with local flow velocity between the two illuminations. The recorded PIV image is divided into small subareas called "interrogation areas" to evaluate the flow field. The local displacement vector for the images of the tracer particles collected through the first and second illumination is calculated in each interrogation area by means of statistical methods (cross-correlation). The projection of the vector of the local flow velocity into the plane of the light sheet (two-component velocity vector) is computed using the time delay between the two illuminations and the calibration of the imaging system. The flow field evaluation is repeated for all interrogation areas where captured the scattered signals.

1.7.3 Infrared Radiation Imaging

Infrared radiation imaging uses emitted infrared radiation from a substance [114]. Every substance emits radiation that has various values depending on wavelength and temperature. An IR camera (infrared camera) is used to capture emitted infrared radiation under IR ranging from 700 nm to 1000 mm. Infrared radiation imaging has advantages in terms of a simple system and non-interference measurement. When photons pass a substance, an absolute amount of absorption has been observed, and this is absorption [114]. The substance emits electromagnetic radiation at a rate depending on the local temperature and on the properties of the substance, and this is emission [114]. A direction of photons travels may be changed by interaction with particles, and this is scattering [114]. The intensity field inside a participating medium is governed by the radiative transfer equation including emission, absorption, and scattering [114],

$$\frac{dI_\lambda}{ds} = \kappa_\lambda \, I_{b\lambda} - \kappa_\lambda \, I_\lambda - \sigma_{s\lambda} \, I_\lambda + \frac{\sigma_{s\lambda}}{4\pi} \int I_\lambda(\hat{s_\iota}) \, \Phi_\lambda(\hat{s_\iota}, \hat{s}) d\Omega_i \qquad 1.15$$

where $\kappa_\lambda \, I_{b\lambda}$ is emission, $\kappa_\lambda \, I_\lambda$ is absorption, and $\hat{s}(\sigma_{s\lambda} \, I_\lambda)$ is scattering.

In the present study, mixtures are hydrogen and air. Other elements that disturb photons travels do not exist in the current experiment. Thus, scattering is neglected in the present work. Equation (1.15) can be simplified only considering emission, and absorption [114],

$$I_{\lambda_{total}} = I_\lambda(0) \cdot exp(-\tau_\lambda) + \int_0^{\tau_\lambda} I_{b\lambda}(\tau_\lambda^*) \cdot \exp\left(-(\tau_\lambda - \tau_\lambda^*)\right) d\tau_\lambda^* \; . \qquad 1.16$$

A more detailed discussion of infrared radiation imaging is given in Chapter 2.5.

1.7.4 Rayleigh Scattering

Rayleigh scattering in combustion measures Rayleigh scattered signals (Rayleigh scattering intensity). Rayleigh scattering is a result of light scattered by gas molecules and particles that are much smaller than a wavelength of incident light [115-118]. The scattered light is shifted into frequency by Doppler effect when a laser beam having a single frequency passes through a gas. In order words, the wavelength of the scattered light is the same with the wavelength of the laser beam. The signal of Rayleigh scattering is the sum of the scattered light from each individual scattered. Therefore, Rayleigh scattering is dependent on the number of density of molecules in the gas of a given volume. A density of gas and the intensity of scattered light is decreased with increasing temperature due to an expansion of the gas.

Rayleigh scattering can measure the total number of density but cannot distinguish individual species [119]. The reason is the scattered light does not shift to a specific wavelength . Rayleigh scattering does not have a method to distinguish the scattered light.

A signal of Rayleigh scattering is strong. Therefore, the signal of Rayleigh scattering can be applied to two dimensions [115,116]. However, Rayleigh scattering emitted from particles is much stronger than molecular [119]. Rayleigh scattering should be performed in a clean environment to avoid errors from Rayleigh scattering signals of unintended particles.

Rayleigh scattering signal has a linear relationship with the total number density of molecules weighed for their cross-sections [115,120-122]. From an assumption, pressure is constant, the ideal gas equation is used to calculate flame temperature [115,120-124].

$$T_{flame} = \frac{(\sum X_i \sigma_i)_{mix}}{(\sum X_i \sigma_i)_{air}} T_{air} \frac{(I_{air} - I_{back})}{(I_{flame} - I_{back})} \qquad 1.17$$

where T_{flame} is the temperature of the flame, T_{air} is the temperature of air, σ_i is Rayleigh scattering cross section for each molecule i, X_i is mole fraction of each specie, I_{flame} is Rayleigh scattering signal intensity of the flame, I_{air} is Rayleigh scattering signal intensity of air, and I_{back} is the background signal intensity, which consisted of the dark noise of the camera, the laboratory background light, and laser reflections.

As the above mentions, the signal of Rayleigh scattering is the sum of scattered light. Therefore, Rayleigh scattering can use for hydrogen-air flame to measure flame temperature or to evaluate mole fraction of hydrogen [125-131]. Flame temperature in hydrogen/air mixtures was measured through Rayleigh scattering [125,126,130,131]. Schefer et al. studied a mole fraction of hydrogen in hydrogen/air mixtures through Rayleigh scattering [127-129].

1.8   Research Object

The present research has three main purposes. The first is to understand an energy balance equation in ignition of flowing gases between MIE and energy loss under laminar flow and turbulent flow. The second is to investigate a relationship between MIE, turbulence intensity, and flame kernel propagation speed to understand an effect of the turbulence intensity on the MIE. The third is to study plasma expansion, produced by a laser-induced spark, and flame kernel temperature distribution. The ignition experiment was conducted in a jet burner using premixed hydrogen and air mixture. Chapter 2 describes experimental apparatus and test procedures regarding ignition experiments using the laser-induced spark. Used experiment diagnostics were particle image velocimetry (PIV), schlieren image, radiation intensity measurements, and Rayleigh scattering. Chapter 3 presents the results of PIV performed to examine flow fields in the experimental conditions. Chapter 4 describes the effect of the turbulence intensity on MIE. Chapter 5 explains the relationship between the MIE, the turbulence intensity, and the flame kernel

propagation speed. Chapter 6 illustrates the laser plasma expansion and the flame kernel temperature distribution. Chapter 7 explains a phenomenological model for the energy balance equation in the ignition of the flowing gases. Chapter 8 explains the energy balance equation in the ignition between the MIE and the energy loss under the turbulent flow. Chapter 9 describes the energy balance equation in the ignition between the MIE and the energy loss the under laminar flow. Finally, Chapter 10 is a conclusion.

2. EXPERIMENTAL APPARATUS

2.1 Jet burner
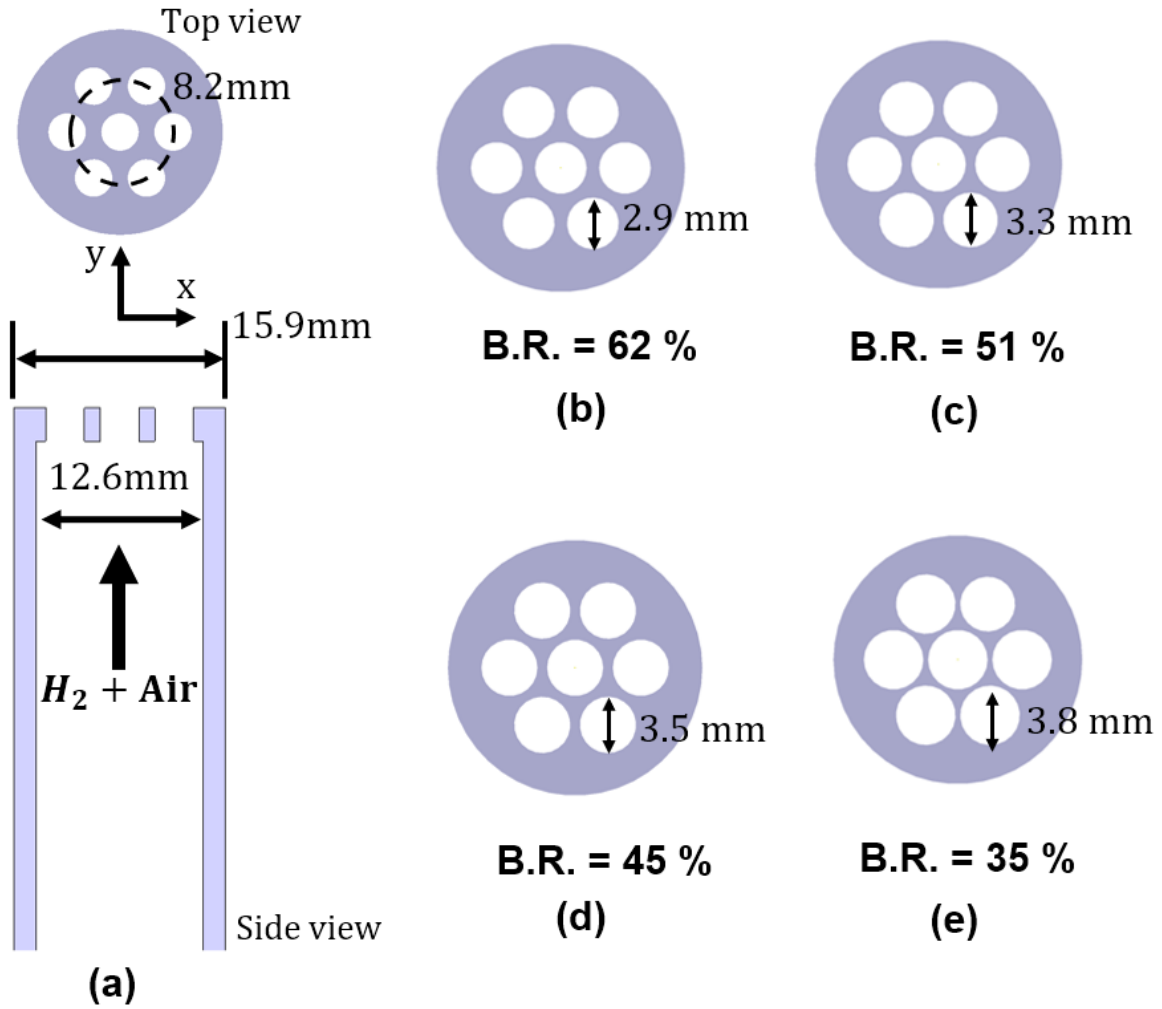
Fig. 2-1. (a) Cross schematic of the burner. (b) the perforated plate with blockage ratio 62 %, (c) the perforated plate with blockage ratio 51 %, (d) the perforated plate with blockage ratio 45 %, and (d) the perforated plate with blockage ratio 35 %.

A jet burner was used in the ignition experiment. A schematic diagram of the Jet burner was shown in Fig. 2-1. An inner diameter of the burner was 12.6 mm. An outer diameter of the burner was 15.9 mm. The burner operates at atmospheric pressure and temperature. A premixed

hydrogen/air stream flowed out through the exit. The burner generated turbulent flow through a perforated plate. The perforated plate was located on the exit of the burner. The perforated plates had circular holes in a hexagonal array. The four perforated plates selected to investigate an effect of turbulence intensity on minimum ignition energy. The coordinates of the nozzles in the perforated plates were constant regardless of a blockage ratio (B.R.). A pitch circle diameter (PCD) was 8.2 mm. The blockage ratio (B.R.) was defined as

$$\text{B. R.} = \frac{\text{Closed area}}{\text{Total area}} \qquad\qquad 2.1$$

The nozzle diameter of 2.9 mm yielded a B.R. of 62%, the nozzle diameter of 3.3 mm yielded a B.R. of 51%, the nozzle diameter of 3.5 mm yielded a B.R. of 45%, and the nozzle diameter of 3.8 mm yielded a B.R. of 35%. The thickness of the plates was 4.0 mm. The perforated plates generated four distinct turbulence flow regimes.

2.2 Laser-Induced Spark Ignition
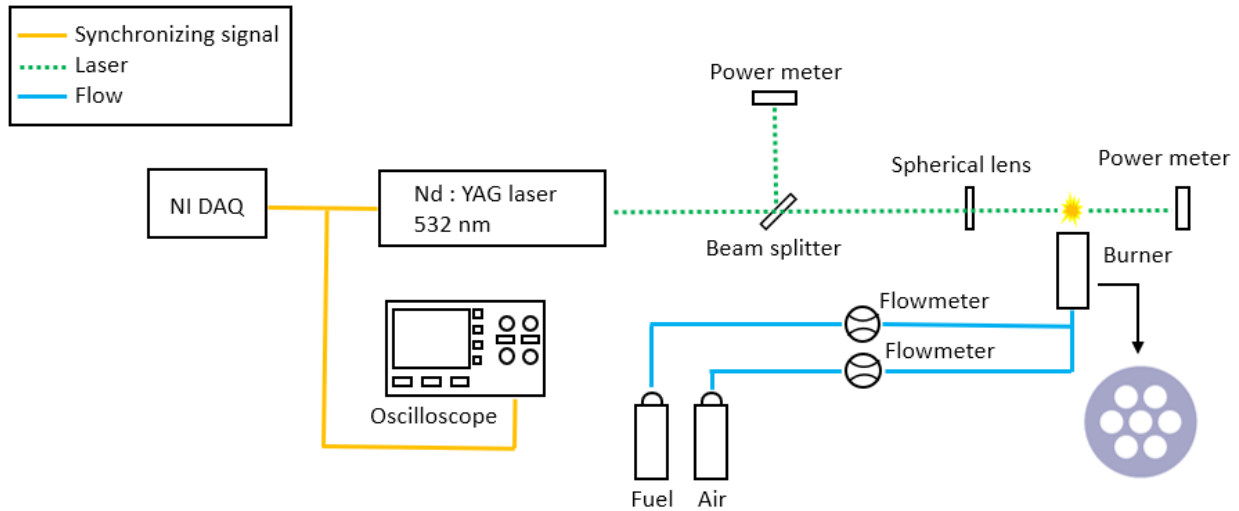
Fig. 2-2. Schematic of laser-induced spark ignition.

A laser-induced spark ignition was utilized to ignite the premixed hydrogen-air mixture. The laser-induced spark ignition system was shown in Fig. 2-2. The laser-induced spark ignition

system consisted of a double-pulsed, frequency-doubled, Q-switched Nd: YAG laser (Spectra-Physics Quanta-Ray GCR200 PIV400, 8 ns), a data acquisition board (NI USB-6343), power meters, and an optical system [Fig. 2-2]. A Labview program produced digital counters through the data acquisition board (NI USB-6343) to generate the laser-induced spark as a single shot. The Labview program is shown in Figure 2.3.
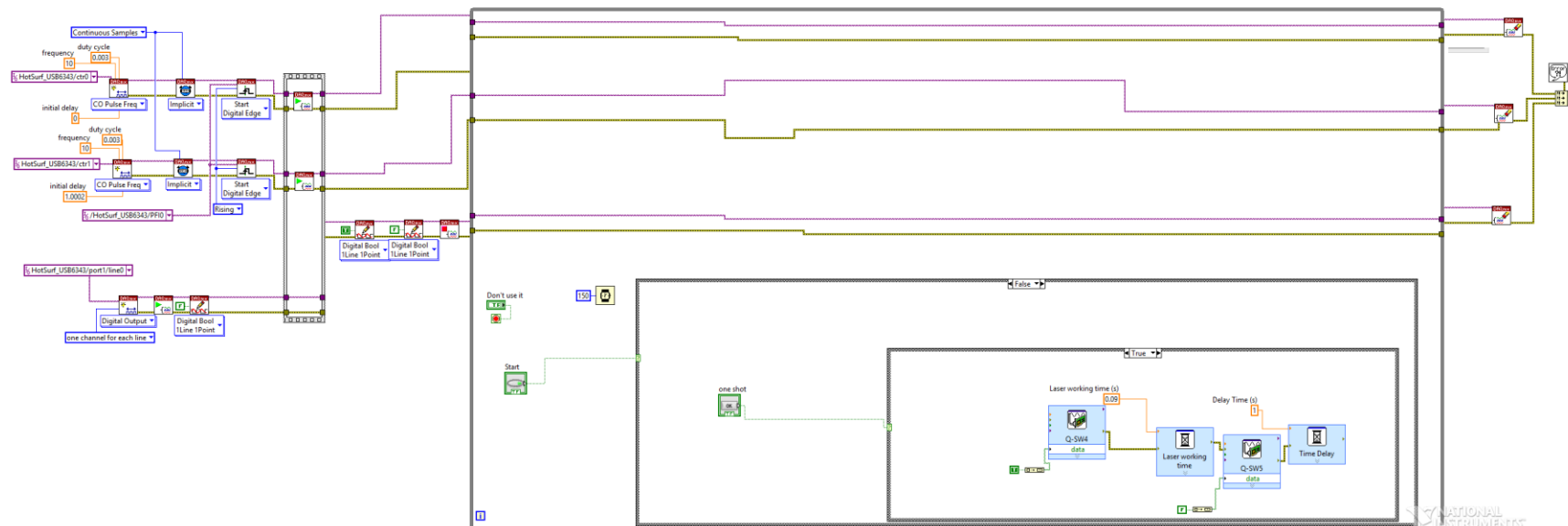
Fig. 2-3. Schematic of laser-induced spark ignition labview program to control the laser for laser-induced spark.

A process that controls the laser.

1. Two counter signals are produced from the data acquisition board. The frequency of the counters is 10 Hz. The duty cycle of the counters is 3000 μs.

2. The initial delay of the first counter (flash lamp) is 0 s. The first counter connects to the flash lamp in the laser.

3. The initial delay of the second counter (Q-switch) is 200 μs.

   The Labview program continuously produces the laser pulse. A electric circuit was designed to generate one laser pulse [Figs. 2-5,2-6]. The second counter connected to # 3 in the relay [Fig. 2-5]. # 4 in the relay connected to the Q-switch in the laser [Fig. 2-5]. A digital signal output in the data acquisition board connected to # 1 in the relay [Fig. 2-5]. # 2 in the relay was grounded [Fig. 2-5].

4. If a switch in the Labview program turns on, the digital signal output produces for 0.1 s. # 3 in the relay connects with # 4 in the relay, when the digital signal output produces.

5. As a result, the second counter enters the Q-switch in the laser for 0.1 s. Only one laser pulse produces for 0.1 s due to the frequency of the laser.

A spherical lens (f = 50 mm) was used to generate the laser-induced spark. The laser energy was measured by power meters (Newport 1916-C) in two locations before a breakdown point (E_{in}) and after the breakdown point (E_{tr}) [Figs. 2-2,2-7,2-8]. Ignition energy, E_{ig}, and laser energy difference, ΔE, were calculated by a difference between incident energy (E_{in}) and transmitted energy (E_{tr}) as

$$E_{ig} = E_{in} - E_{tr}$$
$$\Delta E = E_{in} - E_{tr.} \qquad\qquad 2.2$$

Figures 2-7 and 2-8 show the laser energy difference, ΔE, between the incident energy (E_{in}) and the transmitted energy (E_{tr}). The higher incident energy increases the difference between the incident energy and the transmitted energy. Consequently, the laser energy difference increases with increasing the incident energy. The tendency of the curve is similar to the results in the literature [3,4,74].
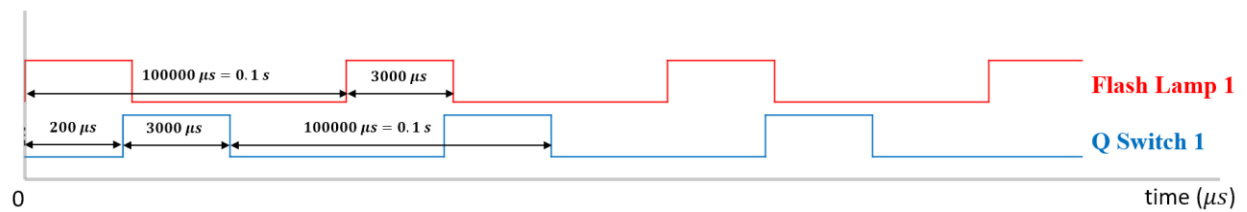
Fig. 2-4. Time sequence for laser-induced spark.
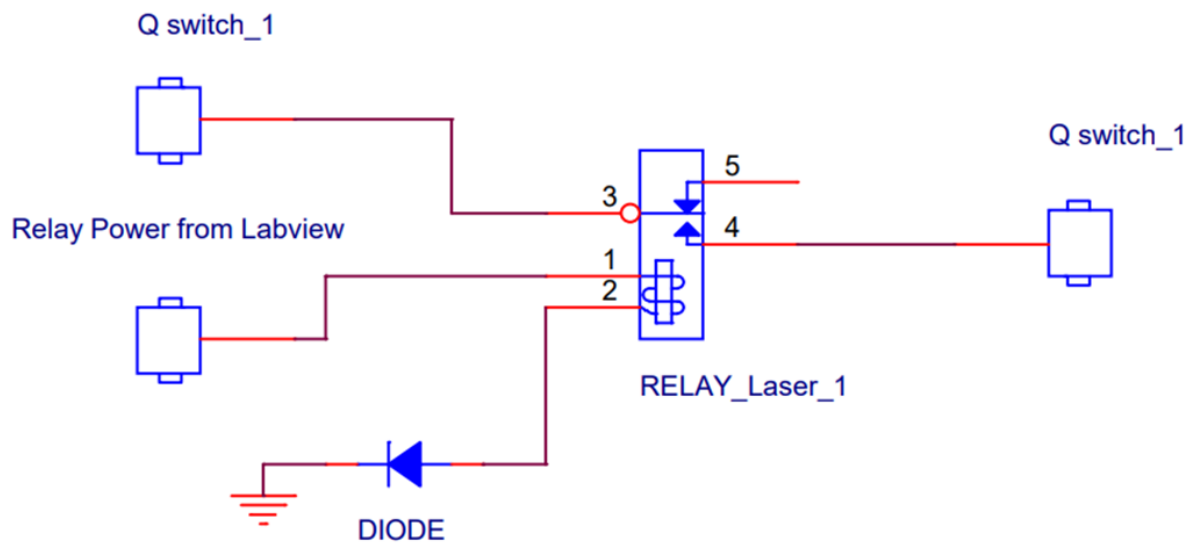
Fig. 2-5. Circuit diagram.
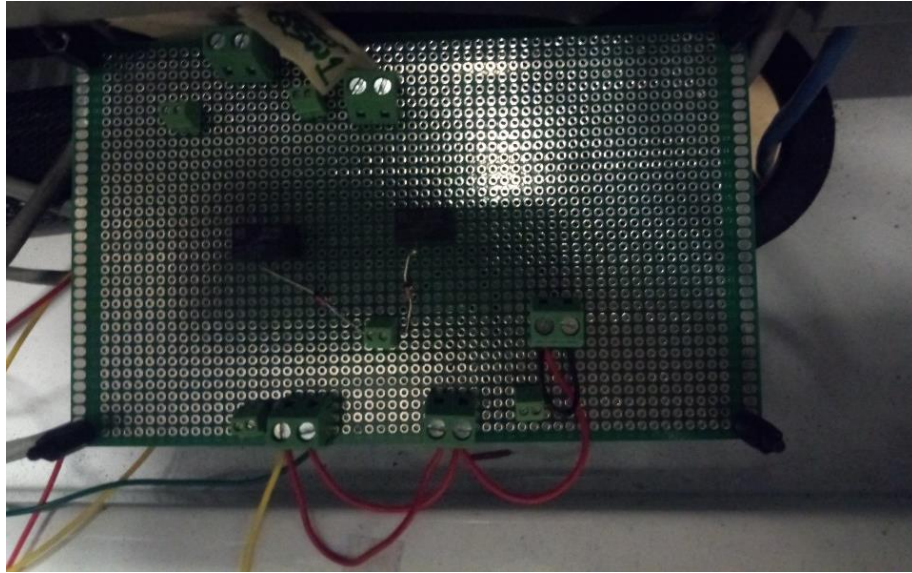
Fig. 2-6. Picture of circuit diagram.
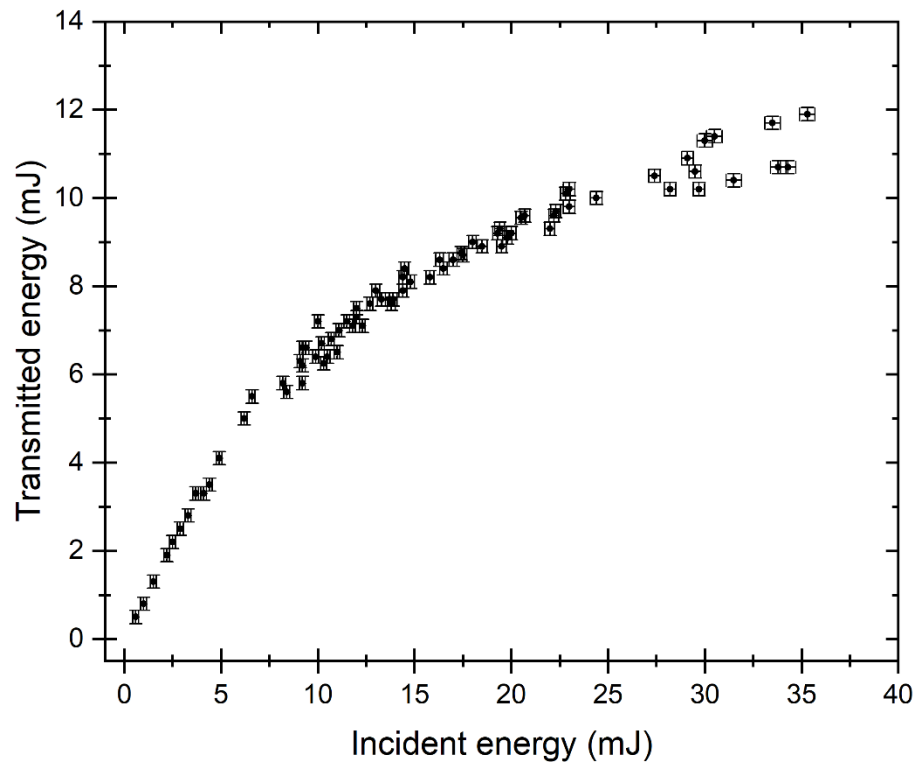
Fig. 2-7. Transmitted energy versus incident energy.
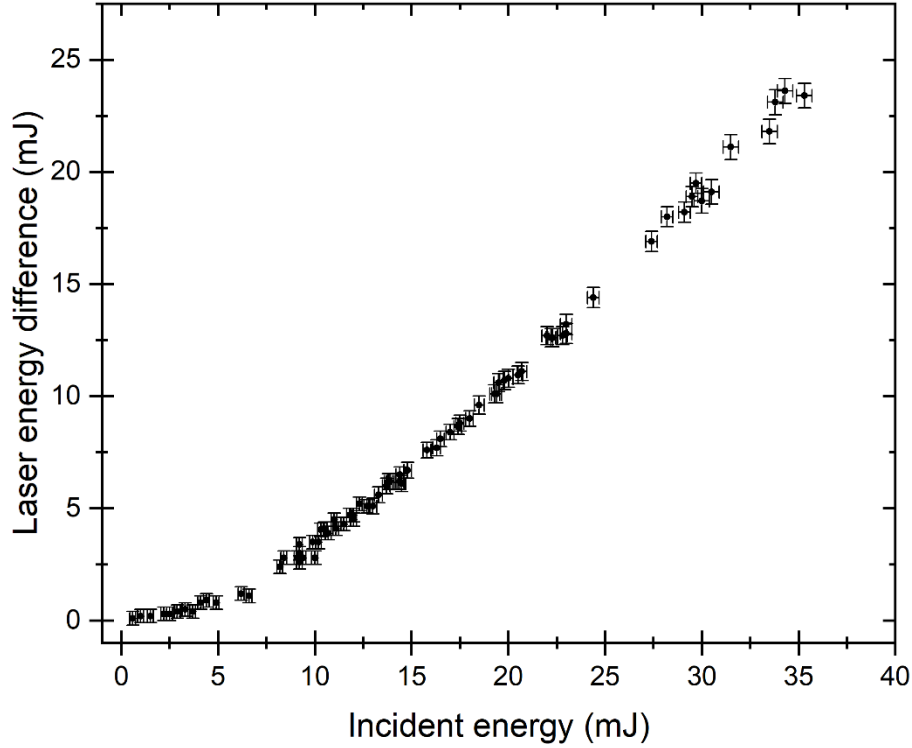
Fig. 2-8. Laser energy difference versus incident energy.

2.3 Particle Imaging Velocimetry

Particle image velocimetry (PIV) was used to study flow fileds. The 2D-PIV system consisted the double-pulsed, frequency-doubled, Q-switched Nd:YAG laser (Spectra-Physics Quanta-Ray GCR200 PIV400-10, 8 ns), a synchronizer, a camera (PIVCAM 10-30, TSI Inc.) with 300mm/F3.5 lenses (Tamron AF 28-300 mm), and optical systems. The laser operated at 532 nm and emitted a maximum of 400 mJ per pulse at 10Hz. The synchronizer (TSI laserpulse synchronizer 610034) synchronized a working time between the laser and the camera. A concave lens, $f = 50$ mm, and a cylindrical lens, $f = 200$ mm, produced a laser sheet. The thickness of the laser sheet was 240 µm at the burner center. The camera collected the light scattered images from tracer particles with a resolution of $1016 \times 1008\ Pixel^2$ at 10 fps frame-straddle mode. A calibration plate converted the dimension size of an image into meters. The time interval for the two laser pulses was varied between 6 and 11 µs corresponding to the bulk velocity. When the size of the image was $100 \times 100\ Pixel^2$, the spatial resolution of PIV was $2.9 \times 2.9\ mm^2$. The tracer

particles, Al_2O_3 having a nominal diameter of 0.5 µm, were seeded into the air flow. One thousand particle image pairs were collected to examine velocity vectors.
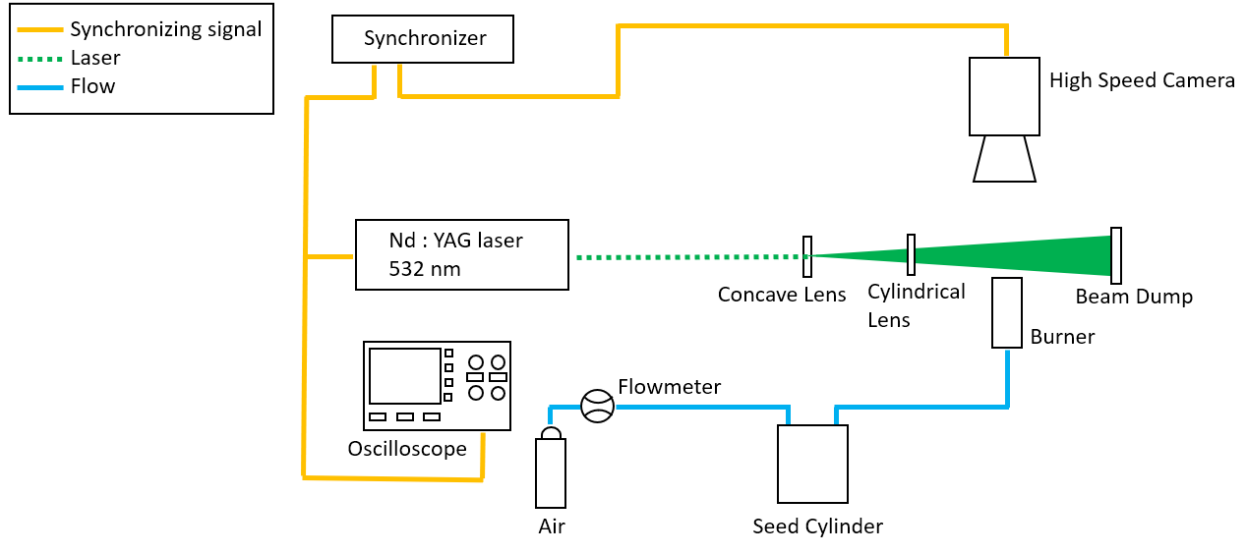
Fig. 2-9. Schematic of particle image velocimetry.

Pre-processing was conducted to remove background and noise from the captured images, before the calculation of the PIV images. PRANA software was used to compute the velocity vectors from the collected images. Multi-pass multi-grid window with discrete window offset was used to analyze the particle displacement [113]. The window resolution sizes were 64×64 Pixel^2 with 75 % window overlap (first pass) and 48×48 Pixel^2 with 83.33 % window overlap (final pass). The velocity interpolation method was a bicubic multigrid method. The image interpolation was A Sinc with Blackman filter deform method. Four-point Gaussian estimator was utilzied for subpixel correlation peak location. The particle displacement was calculated using a standard cross correlation (SCC) The root-mean-square velocity and the mean velocity obtained by the PIV computed turbulence intensity.

$$I_{tur} = \frac{\sqrt{\dfrac{u_{rms}^2 + v_{rms}^2}{2}}}{U} \qquad 2.3$$

where I_{tur} is turbulence intensity, u_{rms} is root-mean-square velocity in the x-direction, v_{rms} is root-mean-square velocity in the y-direction, and U is mean velocity.

2.4   Schlieren Image
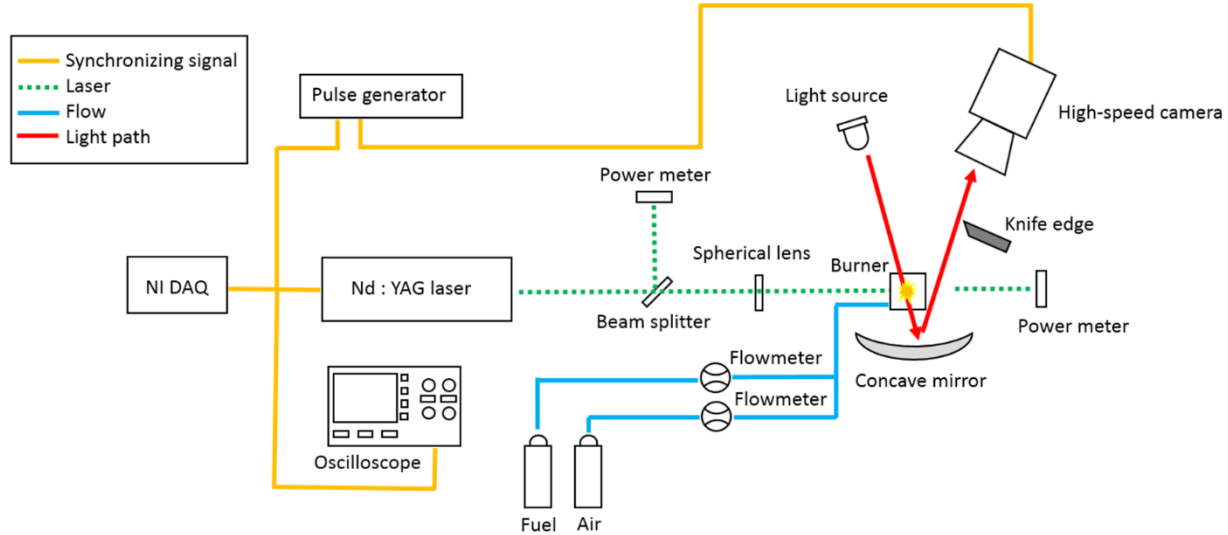
Fig. 2-10. Schematic of ignition energy experiment and Schlieren image.

A high-speed Schlieren image visualized the development of the flame kernel [Fig. 2-10]. The Schlieren system consisted of the laser, the data acquisition board, a 0.2 watt LED lamp, a pulse generator, a concave mirror (f = 250 mm), a knife edge, and a highspeed camera (Vision Research Phantom v7.1). An exposure time capturing the Schlieren images was 2 μs. An image resolution was changed by experiments. More detailed information about image resolution, and frame speed is provided in experimental conditions.

2.5   Infrared Radiation Imaging
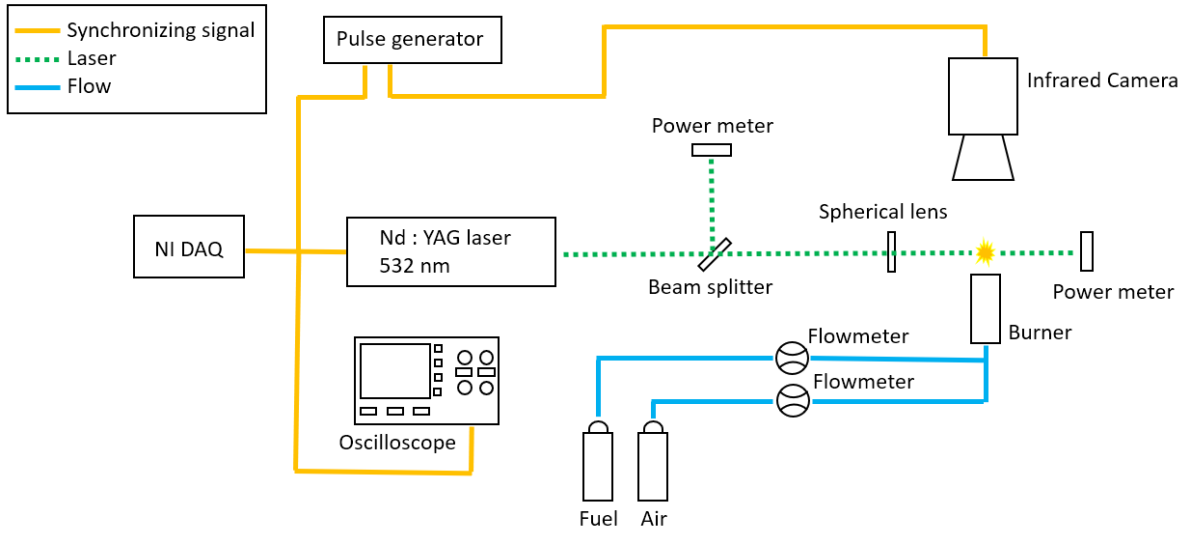
Fig. 2-11. Schematic of ignition energy experiment and radiation measurement using the IR camera.

A radiation intensity emitted from a flame kernel was measured through an infrared camera (FLIR sc6100) [Fig. 2-11]. The characteristics of the camera was: exposure time 0.01050 ms. An image resolution was changed by experiments. More detailed information about image resolution and frame speed is provided in experimental conditions.

The photon counts collected through the IR camera were converted to the radiation intensity using a blackbody calibration. The measured radiation intensity through the IR camera was [132-134]

$$I_{\Delta\lambda} = \int_{\lambda_1}^{\lambda_2} \alpha_\lambda I_{\lambda_{total}} \, d\lambda \qquad\qquad 2.4$$

where α_λ was a spectral absorption coefficient, it accounts for transmission losses corresponding to a spectral of a camera [114,132-134], and λ_1 and λ_2 are a spectral range of a filter. A spectral range of a bandpass filter that used in the present work was from $3.0 \, \mu m$ to $4.30 \, \mu m$. The IR camera was able to detect radiation emitted by water vapor (H_2O) and carbon dioxide (CO_2) in the spectral range. The fuel in the ignition experiment is hydrogen. The radiation by CO_2 can be

51

neglected from the composition of the fuel. The present work only considers the radiation emitted by H_2O. The spectral absorption coefficient is expressed as

$$\alpha_\lambda = 1 - \exp(-\tau_\lambda) \qquad\qquad 2.5$$

where τ_λ is an optical thickness defined as [114,132-134]

$$\tau_\lambda = \int_0^x \kappa_\lambda \, dx \qquad\qquad 2.6$$

where a linear absorption coefficient, κ_λ [135], is defined as an intensity attenuation of light passing through a material, and x is a path length [114,132-134]. The absorption coefficient for H_2O was tabulated by Ferriso et al. [136]. A spectral intensity, $I_{\lambda_{total}}$, emitted by a kernel or a flame is defined as [114,132-134]

$$I_{\lambda_{total}} = I_\lambda(0) \cdot exp(-\tau_\lambda) + \int_0^{\tau_\lambda} I_{b\lambda}(\tau_\lambda^*) \cdot \exp(-(\tau_\lambda - \tau_\lambda^*)) d\tau_\lambda^* \qquad\qquad 2.7$$

where I_λ is the radiative transfer equation for an isothermal gas that has a layer of a thickness, x, [114] and $I_\lambda(0)$ is a radiation intensity at a boundary, and $I_{b\lambda}$ is a blackbody spectral intensity [114],

$$I_{b\lambda} = \frac{2\bar{h} \cdot v'^3}{c_0^2} \frac{1}{\exp\left(\frac{\bar{h}v'}{k_b T}\right) - 1} \qquad\qquad 2.8$$

where $I_{b\lambda}$ is described by Planck's law [114], $\bar{h}$ is Planck's constant (6.626×10^{-34} J $\cdot$ s), v' is frequency ($c_0 = \lambda v'$), c_0 is speed of light (2.997925×10^8 m/s), k_b is Bolzmann's constant (1.381×10^{-23} J/K), and T is temperature. Eq. (2.9) implies that temperature and a wavelength determine a blackbody spectral intensity [114]. An isothermal uniform gas is considered as a blackbody enclosure [114]. Therefore, the radiation intensity for blackbody can be applied to an isothermal uniform gas [114].
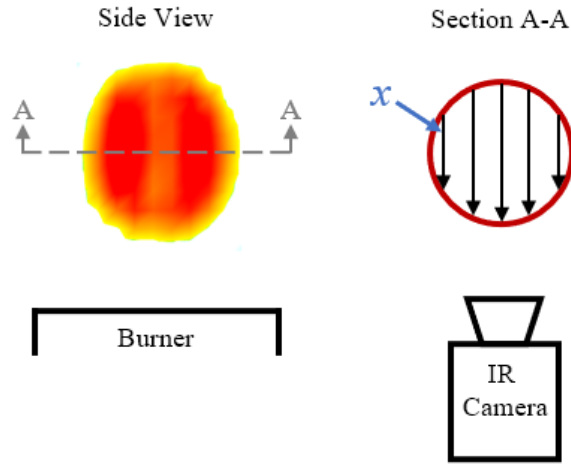
Fig. 2-12. Schematic of deconvolution for estimation of temperature.

2.5.1 Temperature Deconvolution

A deconvolution technique had been used to estimate temperatures [114,132-134]. Radiation intensity measurements using the deconvolution technique estimated the temperature of a flame kernel. The flame kernel was divided into 30-160 pixels to implement the deconvolution technique. The temperature of the flame kernel was calculated via the following procedures.

1. A photon count measured through the IR camera in a pixel is converted to a radiation intensity, $I_{\Delta\lambda m}$.

2. The temperature in the pixel is guessed. A thickness of the flame kernel in the pixel is found from the captured images. A minimum wavelength and a maximum wavelength are defined from a range of a filter in the IR camera.

3. An optical thickness is calculated at the minimum wavelength from Eq. (2.6), where κ_λ is a linear absorption coefficient at the minimum wavelength, and x is the thickness of the flame kernel in the pixel.

4. A spectral absorption coefficient is computed at the minimum wavelength using Eq. (2.5).

5. A blackbody spectral intensity is calculated at the guessed temperature and the minimum wavelength from Eq. (2.8).

6. A spectral intensity is computed using eq.(2.7).

53

7. $\alpha_\lambda I_{\lambda_{total}}$ is calculated at the guessed temperature and the minimum wavelength.

8. Steps 3-7 are repeated from the minimum wavelength to the maximum wavelength in order to calculate a radiation intensity, $I_{\Delta\lambda_c} = \int_{\lambda_1}^{\lambda_2} \alpha_\lambda I_{\lambda_{total}} d\lambda$.

9. The calculated radiation intensity, $I_{\Delta\lambda_c}$, is compared with the measured radiation intensity, $I_{\Delta\lambda m}$. The guessed temperature is changed, and steps 2-8 are repeated until the radiation intensity value is converged (an error is lower than 1 %).

10. Temperatures in other pixels are estimated using steps 1-9.

50 images at each experimental condition were captured and used to estimate the temperature.

2.6   Evaluation of Deconvolution

2.6.1   Thermocouple Error Correction

Thermocouples have been used to measure temperature in many applications. However, measuring a flame temperature by a thermocouple is prone to errors by conduction and radiation losses [137-140].
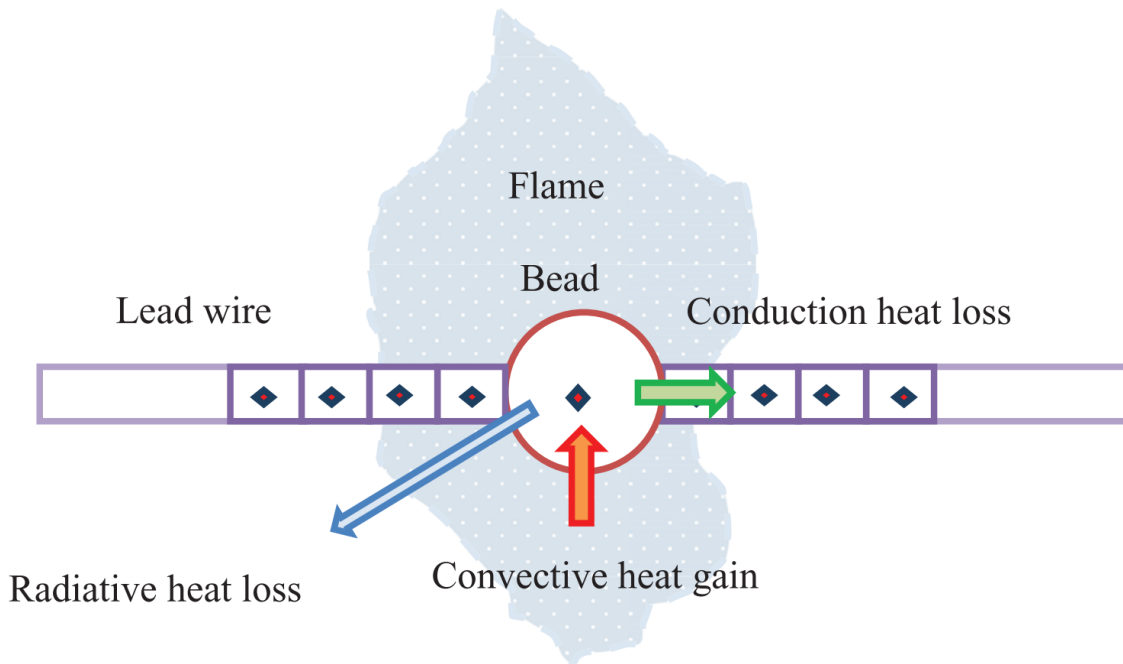
Fig. 2-13. Schematic of the Heat Exchange Process for the Thermocouple with a Flame [138].

The measured temperature using a thermocouple has to be corrected for heat losses. An energy balance equation of a thermocouple is [137,140]

$$h_{conv}(T_f - T_{TC}) = \epsilon\sigma(T_{TC}^4 - T_s^4)$$
2.9

where T_f is a flame temperature, T_{TC} is a thermocouple temperature, T_s is a surrounding temperature, h_{conv} is heat convection coefficient, ϵ is an emissivity of a thermocouple, and σ is the Stefan-Boltzmann constant ($5.67 \times 10^{-8}\text{W/(m}^2\text{K}^4$)). Brundage et al. measured flame temperature using a type K thermocouple and compared the obtained values with Coherent anti-Stokes Raman Spectroscopy (CARS) measurements and thermochemical equilibrium calculation [Fig. 2-14][137]. The measured temperature using the thermocouple showed significant difference with the obtained temperature from CARS and Equilibrium [Fig. 2-14][137]. They corrected the meausred temperature using the energy balanace equation [Eq.(2.9)].
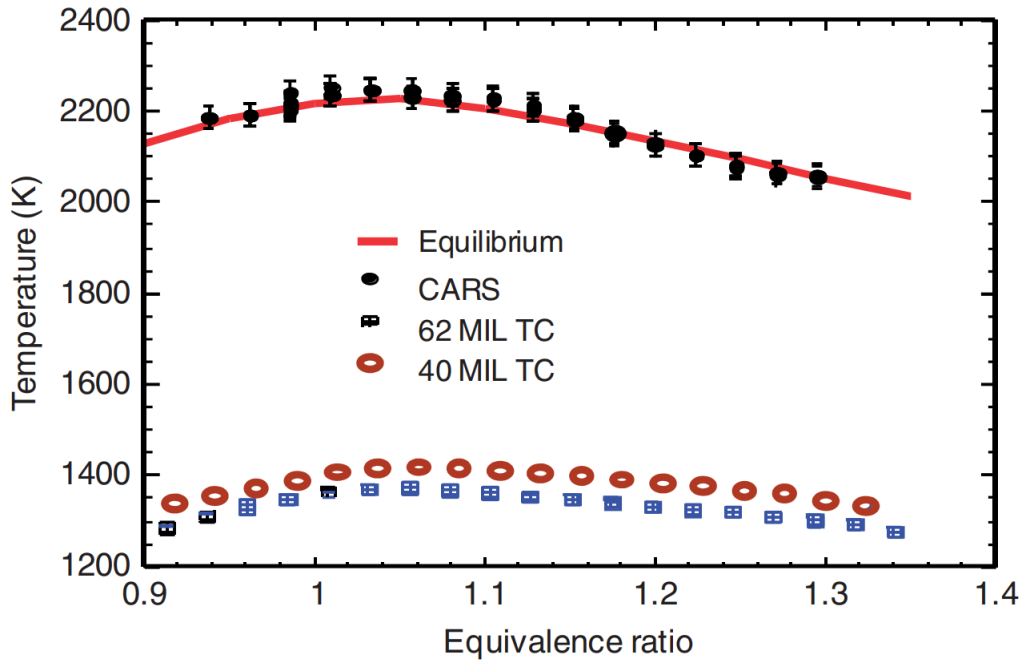
Fig. 2-14. CARS and Thermocouple Temperatures for a Clean Methane-Air Flame From a Hencken Burner [137].

The heat convection coefficient is calculated from the Nusselt number for a thermocouple [141]

$$Nu = 0.42\, Pr^{0.2} + 0.57 Re^{0.5} Pr^{1/3} \qquad\qquad 2.10$$

where Pr is Prandtl number, and Re is Reynolds number. The temperature of the hydrogen/air flame was measured using 0.062" diameter, 304 Stainless Steel sheathed, a type K thermocouple (Omega-GKMQSS-062G-6) when the equivalence ratio was 0.4 and the bulk velocity was 11 m/s [Fig. 2-15]. The measurements were performed 5 locations in a radial direction [Fig. 2-15]. The emissivity of the thermocouple was 0.85 [142]. From Eq.(2.9), the flame temperature was corrected [Fig. 2-15].

2.6.2   Evaluation of Deconvolution

To evaluate the deconvolution technique, radiation intensity measurements were conducted through the IR camera in the hydrogen/air flame when equivalence ratio was 0.4 and the bulk velocity was 11 m/s [Fig. 2-15]. The obtained radiation intensity converted to temperature using the deconvolution technique. The flame temperature measured by the thermocouple and the estimated temperature from the infrared camera measurement agreed within 6 % [Fig. 2-15]. The estimated temperature using the radiation intensity through the IR camera is underestimated [132, 133]. The reason is that the equation of the radiation intensity assumes a flame as isothermal uniform gas in a pixel [114].
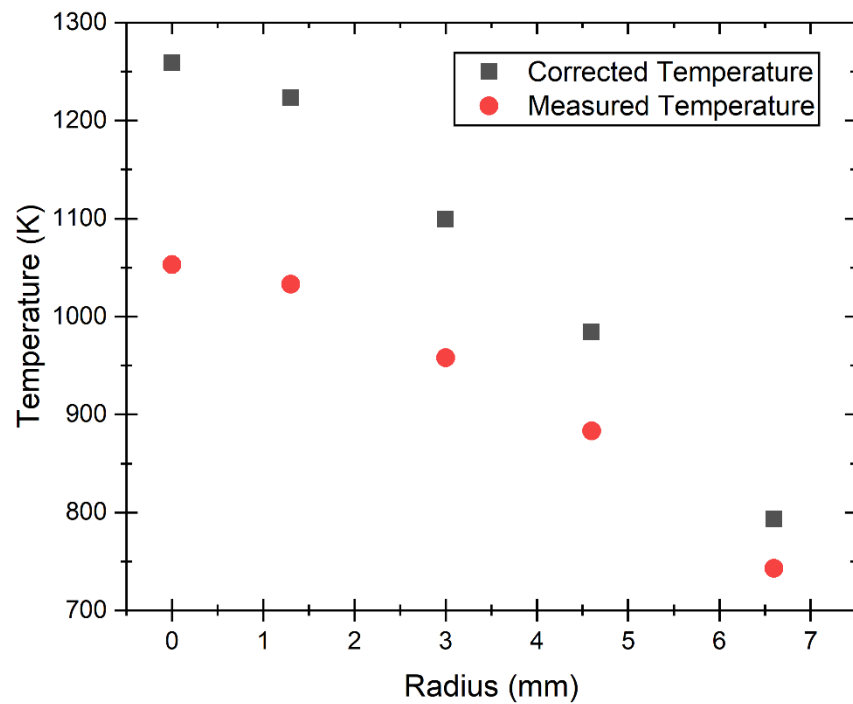
(a)
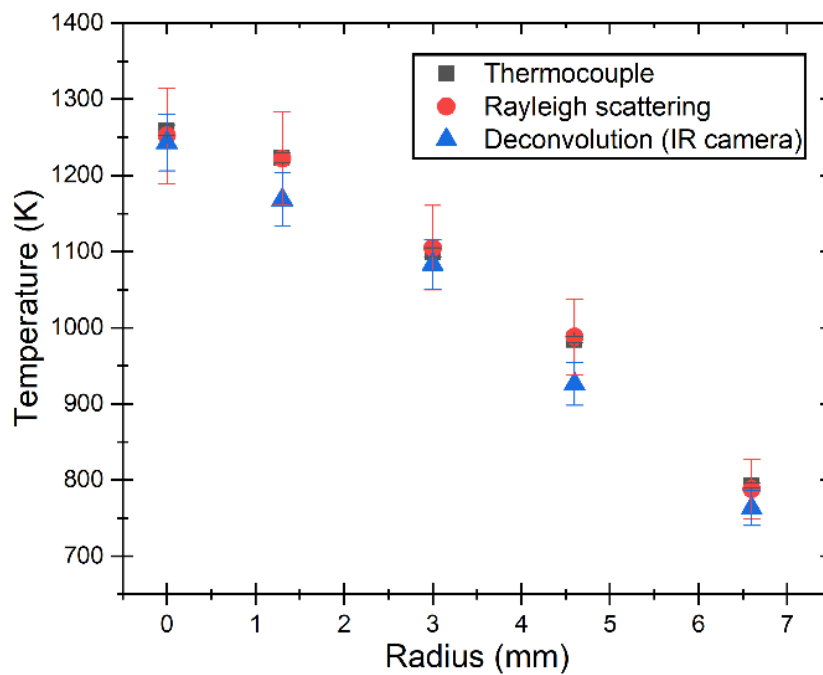
(b)

Fig. 2-15. (a) Comparison of flame temperature between the measured temperature and corrected temperature, (b) comparison of flame temperature between the thermocouple and IR camera, and Rayleigh scattering.

2.7 Rayleigh Scattering
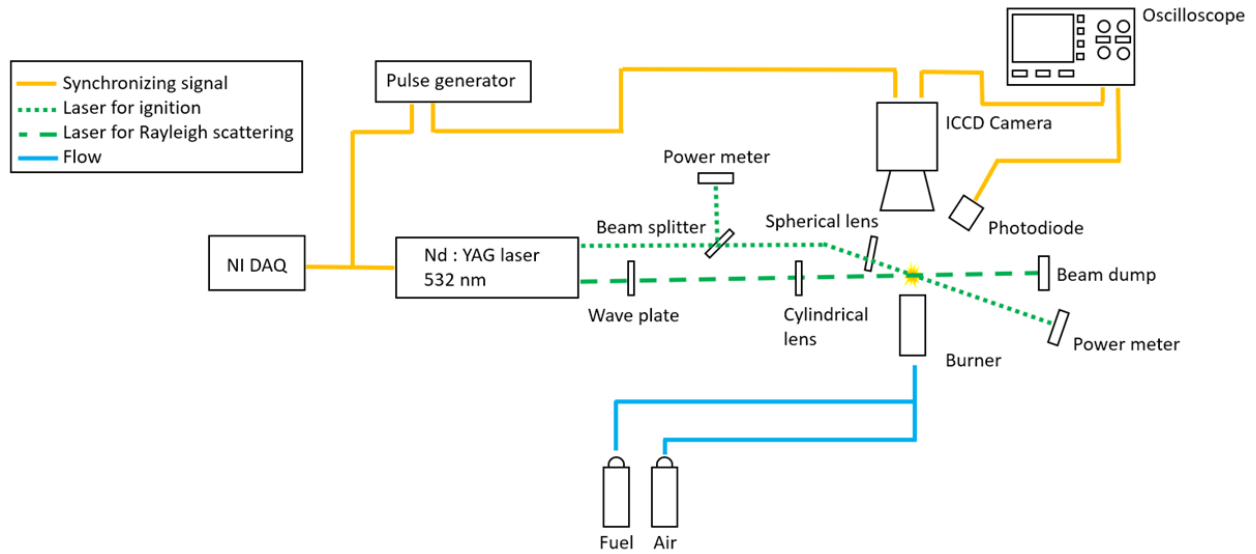
Fig. 2-16. Schematic diagram of the ignition experiment for Rayleigh scattering.
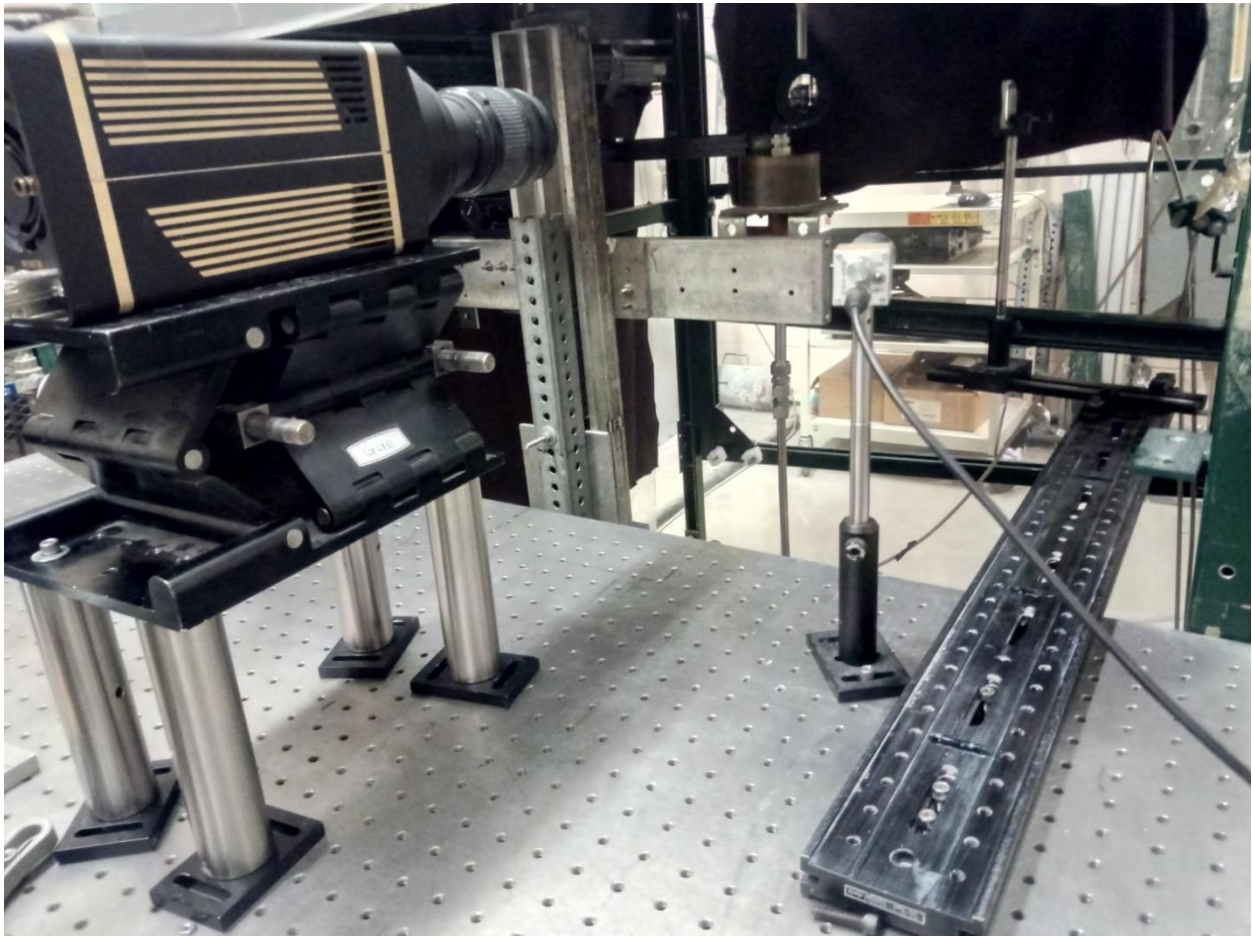
Fig. 2-17. Photograph of the Rayleigh scattering and the ignition system.

Flame kernel images were captured using the Rayleigh scattering. This experimental device consisted of optics, the data acquisition board, a photodiode, the pulse generator, an intensified CCD camera (PI-MAX2), the laser used in the ignition experiment.

The first laser head in the laser and the spherical lens, $f = 50$ mm, generated the laser-induced spark. The second laser head in the laser and a cylindrical lens, $f = 200$ mm, produced a laser sheet of 13 mm height and 350 µm thickness. The ICCD camera positioned at 90° to the scattered light. An array size of the ICCD camera was 512×512 pixel^2. An image resolution was changed by experiments. More detailed information about image resolution and gate time is provided in experimental conditions.

A Labview program and the data acquisition board (NI USB-6343) were used to generate count signals in order to control the laser. The ignition experiments were performed 50 times at each experimental condition.

The Labview program designed to produce the laser-induced spark and the laser sheet for Rayleigh scattering [Fig. 2-16]. The big structure of the LabView program is the same with the Labview program used for the generation of the laser-induced spark [Figs. 2-3,2-18].

A process that controls the laser.

1. Four counter signals are produced. The frequency of the counters is 10 Hz. The duty cycle of the counters is 3000 µs.

2. The initial delay of the first counter (flash lamp 1) is 0 s. The first counter connects to the first flash lamp in the laser.

3. The initial delay of the second counter (Q-switch 1) is 200 µs. 4. The initial delay of the third counter (flash lamp 2) is dt µs. The third counter connects to the second flash lamp in the laser.

4. The initial delay of the third counter (flash lamp 2) is dt µs. The third counter connects to the second flash lamp in the laser.

5. The initial delay of the fourth counter (Q-switch 2) is dt + 200 µs.

    Previously mentioned, the Labview program continuously produces the laser pulse. The electric circuit was designed to generate one laser pulse [Figs. 2-5,2-19]. The second counter and fourth counter connected to # 3 in the relay [Fig. 2-5]. # 4 in the relay connected to the first Q-switch and the second Q-switch in the laser [Fig. 2-5]. A digital

signal output connected to # 1 in the relay [Fig. 2-5]. # 2 in the relay was grounded [Fig. 2-5].

6. The fourth counter also connected to the pulse generator [Fig. 2-16]. The pulse generator generates the counter signal after the delay time, dt. The produced counter signal connected to the ICCD camera.As a result, the ICCD camera synchronizes working time with the laser sheet.

7. If a switch in the Labview program turns on, the digital signal output from the data acquisition board produces for 0.1 s. # 3 in the relay connects with # 4 in the relay, when the digital signal output produces.

8. As a result, the second counter and the fourth counter enter the first Q-switch and the second Q-switch respectively for 0.1 s. The laser-induced spark is generated by the first head in the laser. After the delay time, dt, the laser sheet is produced by the second head in the laser. When the laser sheet is produced, the ICCD camera captured the Rayleigh scattering image.
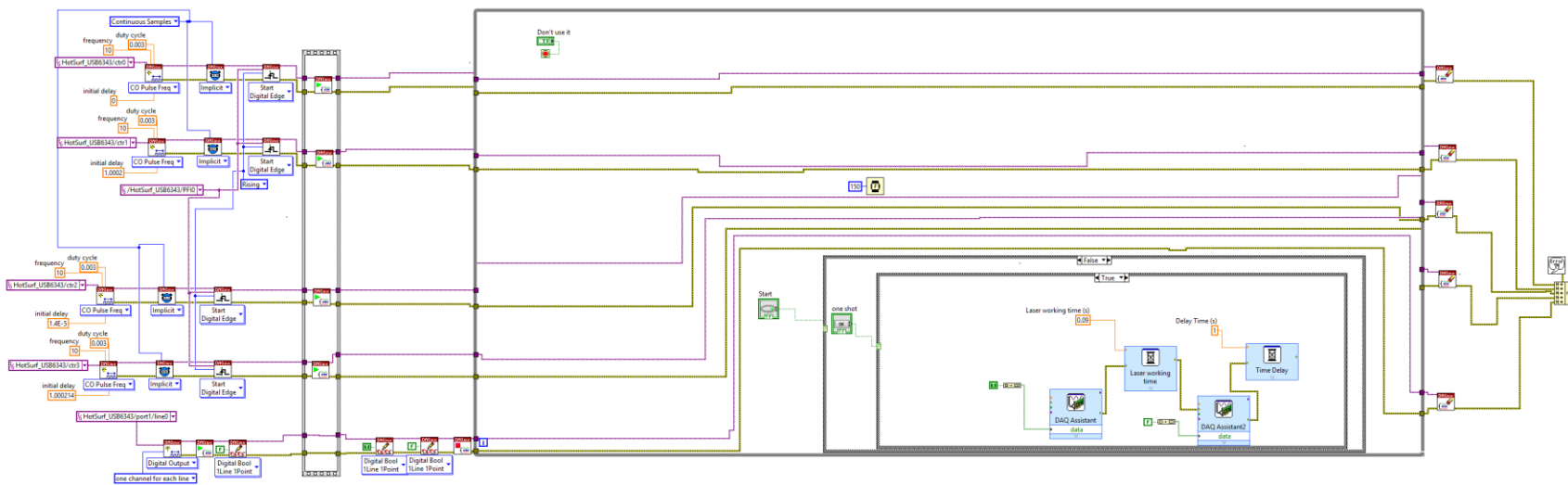
Fig. 2-18. Labview program to control the laser for Rayleigh scattering
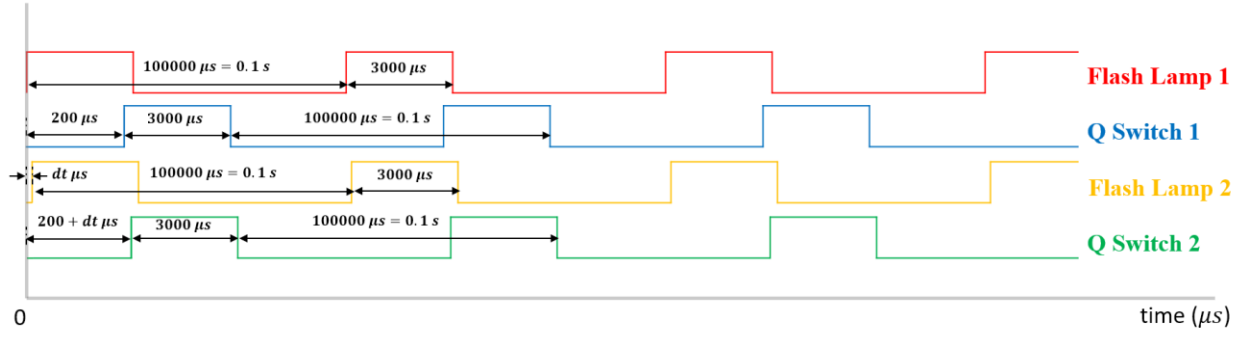
Fig. 2-19. Time sequence for Rayleigh scattering

The total Rayleigh scattering intensity, I_r, in a perpendicular direction from a laser source, I_0, passing through mixtures of ideal gas can be expressed as

$$I_r = CI_0 \Omega l N \sum_i \sigma_i X_i \qquad 2.11$$

where C is a system calibration constant which accounts for the optical collection and transmission efficiencies, N is the total molecular number density $(1/\text{cm}^3)$, σ_i is Rayleigh scattering cross section for each molecule i, X_i is mole fraction of each specie, Ω is the solid angle between a laser sheet and a collection optic, and l is the length of the laser beam segment imaged onto the detector [115]. For a consistent experiment environment, I_0, Ω , l, and C are invariable. N, and $\sum_i \sigma_i X_i$ are variable in Rayleigh scattered light intensity. From ideal gas equation,

$$N = \frac{PA_0}{R_u T} \qquad 2.12$$

where A_0 is the Avogadro's number, and R_u is the universal gas constant. From Eqs. (2.11) and (2.12), the Rayleigh scattered intensity can be written as

$$I_r = CI_0 \Omega l \frac{PA_0}{R_u T} \sum_i \sigma_i X_i . \qquad 2.13$$

Eq. (2.13) is re-written considering the invariable and variable as

62

$$\frac{I_r T}{P \sum_i \sigma_i X_i} = C I_0 \Omega l \frac{A_0}{R_u} .$$

2.14

Denoting the standard condition with the subscript s, the temperature T can be obtained from the following equation:

$$T = \frac{P}{P_s} \frac{I_{r_s}}{I_r} \frac{\sum_i \sigma_i X_i}{\sum_i (\sigma_i X_i)_s} T_s .$$

2.15

Generally, the standard condition is the room temperature and atmospheric pressure. If the pressure in an experiment is the same with the standard pressure, the Eq. (2.15) can be written as

$$T = \frac{I_{r_s}}{I_r} \frac{\sum_i \sigma_i X_i}{\sum_i (\sigma_i X_i)_s} T_s .$$

2.16
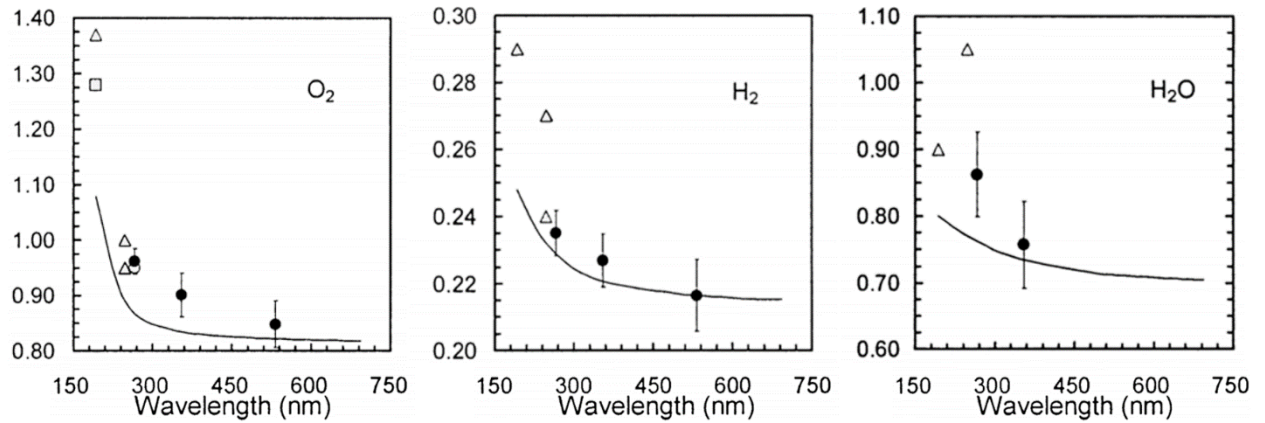
Fig. 2-20. Relative Rayleigh scattering cross sections at 295 K for wavelengths of 266, 355, and 532 nm. Also shown are calculations with Eq.(2.19) [143].

From Eq. (2.16), the temperature of the flame kernel is estimated using this equation [56]

$$T_{flame} = \frac{(\sum \sigma_i X_i)_{mix}}{(\sum \sigma_i X_i)_{air}} T_{air} \frac{(I_{air} - I_{back})}{(I_{flame} - I_{spark} - I_{back})}$$

2.17

where I_{spark} is the intensity of the laser-induced spark, σ_i is Rayleigh scattering cross section for each molecule i. Sutton et al. experimentally investigated Rayleigh scattering cross section [143]. The differential Rayleigh scattering cross section, $\sigma_i{'}$ is written as [115,143]

$$\sigma_i' = \frac{4\pi^2(n_i - 1)^2}{\lambda^4 N^2} sin^2\theta \frac{3}{3 - 4\rho_v} \qquad 2.18$$

where n_i is the refractive index for each species, N is the molecular number density, λ is the wavelength of the laser light, θ is the angle between the incident laser and the scattered light, and ρ_v is the depolarization ratio for light polarized perpendicular to the observation plane that accounts for the anisotropy of nonspherical molecules.

Visible laser beams can neglect the depolarization ratio [143,144]. At a specific wavelength, the Rayleigh scattering cross section of each species can be normalized by the Raleigh scattering cross section of nitrogen. Eq.(2.18) can be rewritten [143],

$$\sigma_{i\,N,i}' = \frac{\sigma_i'}{\sigma_{N_2}'} \simeq \frac{(n_i - 1)^2}{\left(n_{N_2} - 1\right)^2} = \sigma_{i\,N,i,calc}' . \qquad 2.19$$

In the current study, the products are the reactants are O_2, N_2, and H_2O. $\sigma_{i\,N,O_2,calc}'$, $\sigma_{i\,N,N_2,calc}'$, and $\sigma_{i\,N,H_2O,calc}'$ are 0.83, 1, and 0.73 respectively from Fig. 2-20 [143,145] when the wavelength is 532 nm. $\sigma_{i\,N,N_2,calc}'$ is 1 because $\sigma_{i\,N,i}'$ divides σ_i' by σ_{N_2}' [Eq. (2.19)][143]. The mole fraction, X_i, is computed using NASA CEA [146]. σ ratio, $(\sum \sigma_i X_i)_{mix} / (\sum \sigma_i X_i)_{air}$ is

$$\frac{(\sum \sigma_i X_i)_{mix}}{(\sum \sigma_i X_i)_{air}} = \frac{\sigma_{O_2} X_{O_2} + \sigma_{N_2} X_{N_2} + \sigma_{H_2O} X_{H_2O}}{\sigma_{O_2} X_{O_2} + \sigma_{N_2} X_{N_2}} . \qquad 2.20$$

Temperature affects on Rayleigh scattering cross sections [115,143]. Sutton et al. experimentally examined an effect of temperature on the cross sections [143]. Rayleigh cross sections increases with increasing temperature. O_2, and N_2 increases the most than other species. An increase of the Rayleigh cross sections in the present study is assumed as 5 % referring to the result of Sutton's

research [143]. σ ratio, $(\sum \sigma_i X_i)_{\text{mix}} / (\sum \sigma_i X_i)_{\text{air}}$, is calculated using the effect of temperature on the Rayleigh scattering cross sections

$$\frac{(\sum \sigma_i X_i)_{\text{mix}}}{(\sum \sigma_i X_i)_{\text{air}}} = \frac{\sigma_{O_2} X_{O_2} + \sigma_{N_2} X_{N_2} + \sigma_{H_2O} X_{H_2O}}{\sigma_{O_2} X_{O_2} + \sigma_{N_2} X_{N_2}} \cdot \sigma_T = 0.992 \simeq 1 \qquad 2.21$$

where σ_T is a calibration factor for the effect of temperature on the Rayleigh scattering cross sections. Many studies using air as an oxidizer have used the σ ratio, $(\sum \sigma_i X_i)_{\text{mix}} / (\sum \sigma_i X_i)_{\text{air}}$, as 1 [120,147-150]. The reason is nitrogen, N_2, is major species in reactants, products, and intermediates and has a large mole fraction. Equation (2.21) is the calculation result at 0.9 of the equivalence ratio. The σ ratios at the equivalence ratios of 0.4 and 0.9 are 1.

Eq. (2.17) subtracts the intensity of the spark that captured by the ICCD camera. The current Rayleigh scattering experiment does not use a band-pass filter. When a band-pass filter having 50 % of transmission was employed, the intensity of the measured scattering signals was too weak. Thus, clear images were not able to obtain with the band-pass filter. Many experimental works studying hydrogen collected images without a band-pass filter [127-129]. If we do not use a band-pass filter, signals that unwanted wavelength are also captured through the ICCD camera [Fig. 2-21]. A spark of the laser pulse is a strong intensity [Fig. 2-21]. The Rayleigh scattering images collected the flame kernel subtracts the intensity of the spark to avoid an influence of the unwanted wavelength [Fig. 2-21]. Experiments were performed to capture the intensity of the spark. The used laser energy difference to produce the laser-induced spark was the same with the minimum ignition energy at each experimental condition. Fig. 2-21 shows the process that the subtraction of the spark from the flame kernel. Fig. 2-21(a) visualizes the flame kernel and the spark. Fig. 2-21(b) is the spark. The subtraction work changes the intensity of the flame kernel, specifically in the center [Fig. 2-21].
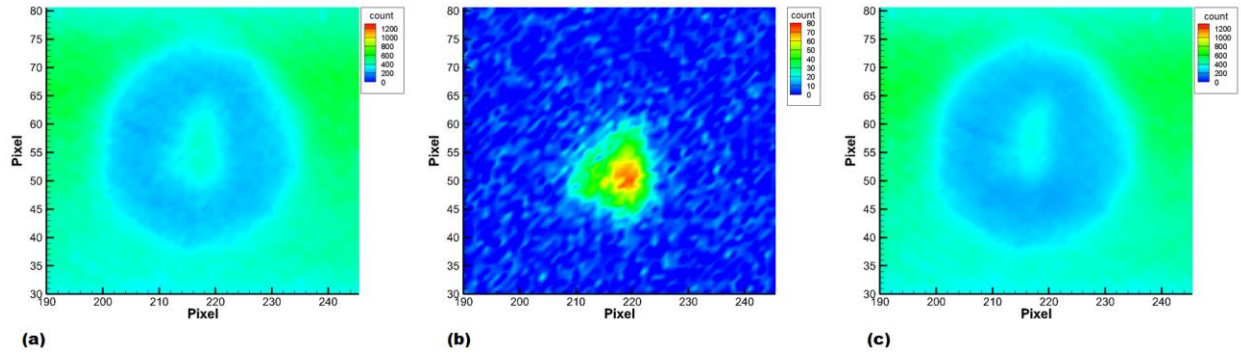
Fig. 2-21. Subtraction of spark intensity, (a) flame kernel with spark, (b) spark, (c) flame kernel without spark.

A scattering spectrum from molecules is broadened by a combination of thermal and acoustic motion and is called as Rayleigh-Brillouin lineshape [Fig. 2-22] [151-154]. An iodine filter can absorb unwanted light scattering from surfaces or particles [Fig. 2-22] [151-154]. The reason is the unwanted light scattering dose not relate to thermal or acoustic motion, thus it is narrow [Fig. 2-22] [151-154]. The narrow unwanted light scattering is absorbed by the iodine filter [Fig. 2-22] [151-154]. In contrast, the scattering spectrum of the absorption band, the hatched regions in Fig. 2-22, will be transmitted to a detector (ICCD camera) [151-154]. However, the Rayleigh scattering in the present study does not use an iodine filter that can reduce an effect of mie scattering. As previously mentioned, when the band-pass filter with 50 % of transmission was used, the collected intensity was too weak. Transmission of an iodine filter is lower than 50 %. If an iodine filter is used for the ignition experiment, it will be hard that to obtain clear images.

The heights of the ignition are 9 mm and 17 mm from the burner exit to reduce the effect of mie scattering by the surface of the burner. The ignition experiments in the Rayleigh scattering were conducted 60 times. The clear 50 images having the low mie scattering effect were chosen.
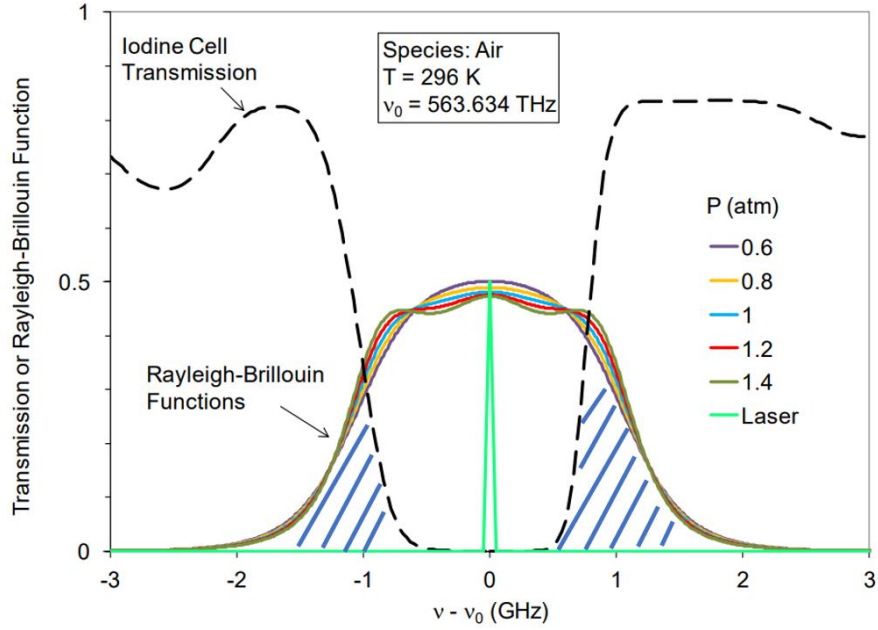
Fig. 2-22. Simulated iodine filter transmission and Rayleigh-Brillouin functions at various air pressures [151].

2.7.1   Evaluation of Rayleigh Scattering

To evaluate the Rayleigh scattering, flame temperatures were examined through the Rayleigh scattering in the hydrogen/air flame when the equivalence ratio was 0.4 and the bulk velocity was 11 m/s [Fig. 2-15]. The Rayleigh scattering signals were converted to the temperatures using Eq. (2.17). The calculated temperatures from the Rayleigh scattering were compared with the flame temperatures measured using the thermocouple [Chapter 2.6.1][Fig. 2-15]. The difference of the temperatures between the Rayleigh scattering results and the thermocouple is lower than 2 %.

3. FLOW FIELD

3.1 Experimental Conditions

Table 3-1. Experimental conditions for PIV

V_{bulk} (m/s)	B. R. (%)	V_{bulk} (m/s)	B. R. (%)	V_{bulk} (m/s)	B. R. (%)	V_{bulk} (m/s)	B. R. (%)
20.6	35	20.6	45	20.6	51	20.6	62
23.3		23.3		23.3		23.3	
25.5		25.5		25.5		25.5	
28.4		28.4		28.4		28.4	

The particle image velocimetry (PIV) was conducted to study velocity vectors and turbulence intensity. The experimental conditions used in this experiment were tabulated in Table 3-1. The experiments were performed at room temperature and atmospheric pressure. The blockage ratio (B.R.) of 35 %, 45 %, 51 %, and 62 % were utilized for the bulk velocity of 20.6 m/s, 23.3 m/s, 25.5 m/s, and 28.4 m/s. The bulk velocity was calculated using the opened area of the perforated plate and the flowrate measured through flowmeters (DTM325, and Bios DryCal DC-1). The Reynolds number is calculated at the exit of the burner, based on the bulk velocity, V_{bulk}, and the nozzle diameter, D, as

$$Re = \frac{V_{bulk}D}{\nu}.$$
3.1

The integral length scale of the velocity defined as

$$l_0 = \int_0^\infty R_{ii}(r,t)dr$$
3.2

where the double-i subscript, $R_{ii}(r,t)$ indicates the autocorrelation function defined by

$$R_{ii}(r,t) = \frac{<u_i(x_i,t)u_i(x_i+r,t)>}{<u_i^2>}$$
3.3

where r is the distance between two points in the flow [155]. The autocorrelation function is longitudinal if r is parallel to u_i , and transverse if r is perpendicular to u_i , where u_i is the root-mean-square velocity in the i-direction [155]. The mean and the root-mean-square velocities measured by the PIV are used to calculate the turbulence intensity [Eq. (3.4)].

$$I_{tur} = \frac{\sqrt{\dfrac{u_{rms}^2 + v_{rms}^2}{2}}}{U}. \tag{3.4}$$

3.2   Flow Field

The flow field for the B.R. 35 %, B.R. 45 %, B.R. 51 %, and B.R. 62 % was examined through cold flow PIV [Table 3-1]. The purpose of the present work is to study the effect of turbulence on minimum ignition energy. Therefore, it is important to analyze the non-reacting flow before an ignition.

There is a large change in mean velocity for the highest blockage ratio burner followed by the other three burners. A decrease in the velocity resulting from the wake of the turbulence generation plate exists for all four burners. For the burner with a large blockage ratio, the jets emanating from the seven openings expand, entrain and merge to reduce the deficit velocity in the wakes. Figures 3-2(a) through 3-2(d) illustrate three of the seven jet flows resulting from the openings. The highest blockage ratio burner (Fig.3-2(a)) depicts the deepest wake velocity deficits and correspondingly the highest peak jet velocities and the maximum velocities and the minimum velocities decrease progressively with reductions in the blockage ratios represented by Figs.3-2(b), 3-2(c), and 3-2(d) [17].
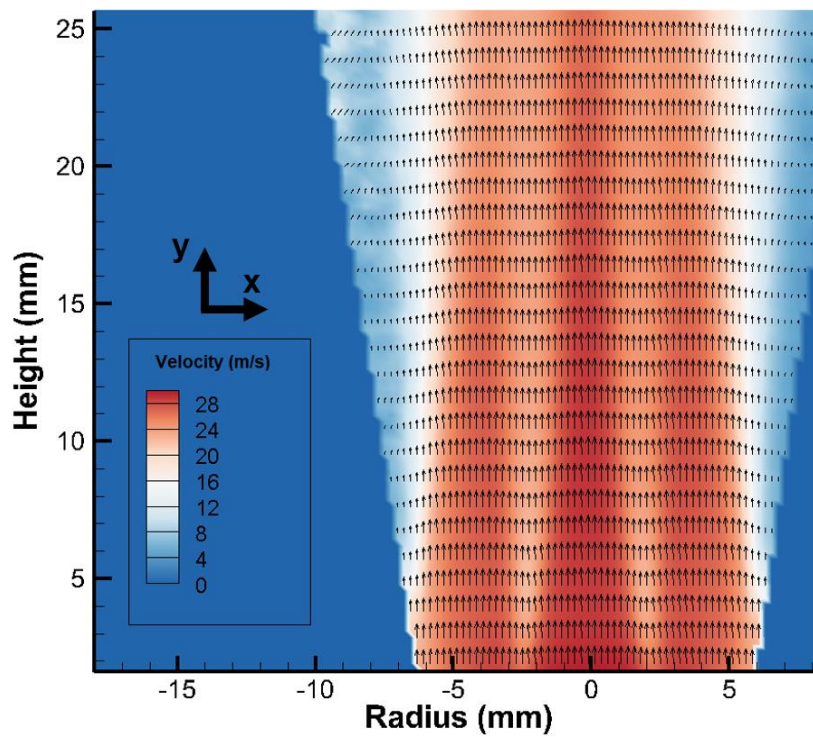
Fig.3-1. Averaged velocity profiles, when bulk velocity is 25.5 m/s and blockage ratio is 45 %.
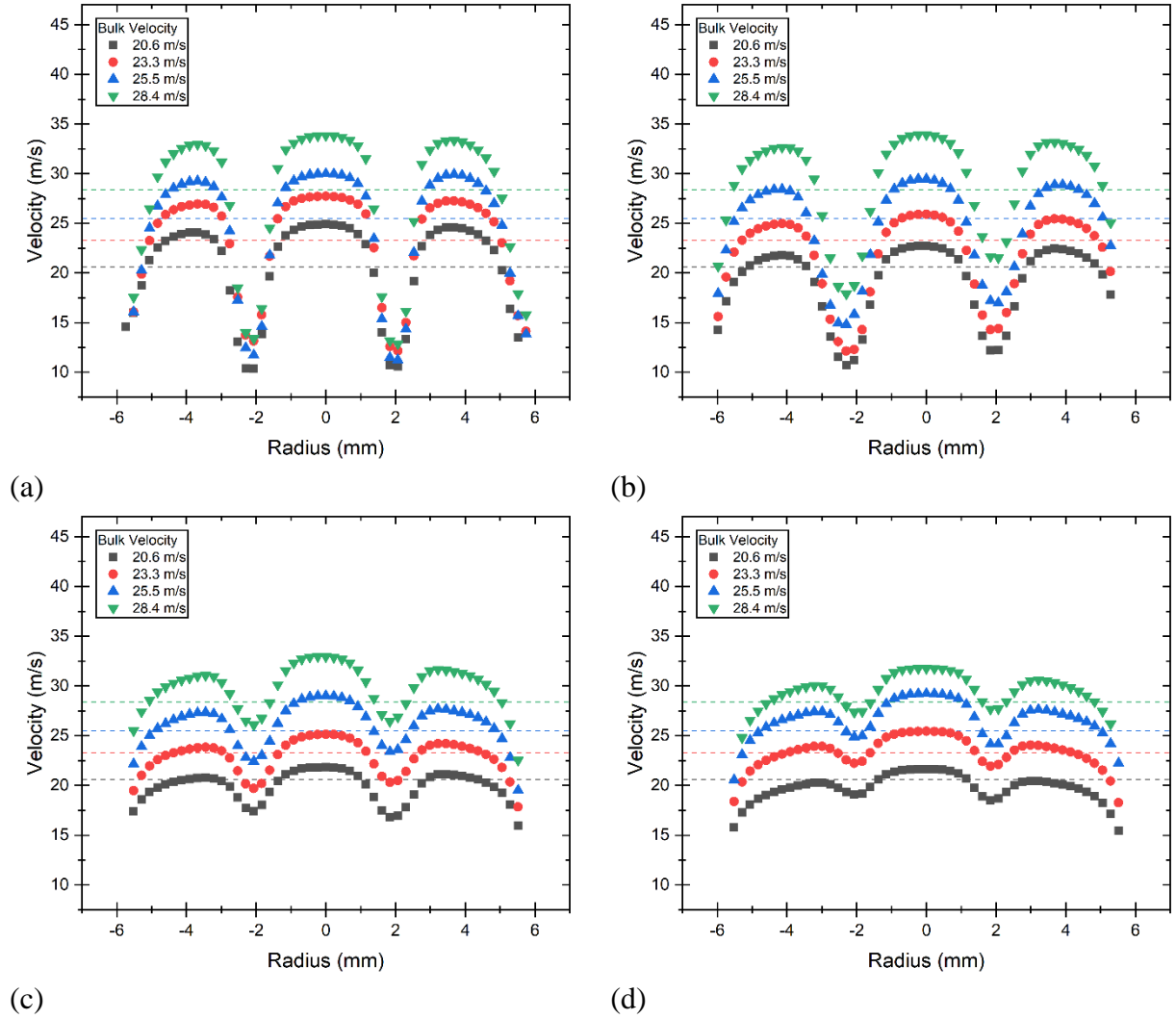
Fig.3-2. Mean velocity, *U*, height is 7.1 mm from the burner exit (a) blockage ratio is 62 %, (b) blockage ratio is 51 %, (c) blockage ratio is 45 %, and (d) blockage ratio is 35 %.

Figures 3-3(a) through 3-3(d) are the axial components of the measured root-mean-square (RMS) velocities, u', corresponding to the burners and operating conditions for which the mean axial velocities were illustrated in Figures 3-2(a) through 3-2(d). The velocity fluctuations for all four bulk velocities are relatively low at radial locations corresponding to the openings in the turbulence generating plates. As expected the RMS velocity fluctuations increase significantly in the annular shear layers forming around the seven openings. The size of the wakes varies inversely with the blockage ratios. While the rate at which the velocity fluctuations increase are similar, the peak fluctuations near the central portion increase with increasing bloackage ratios reaching values as high as 10 m/s for the blockage ratio of 62% and reducing to a lower value of 2 m/s for the

central portion of the blockage ratio of 35%. The RMS velocities reach very high values in the annular wake region outside of the central openings for all four turbulence generators.

(a)

(b)

(c)

(d)
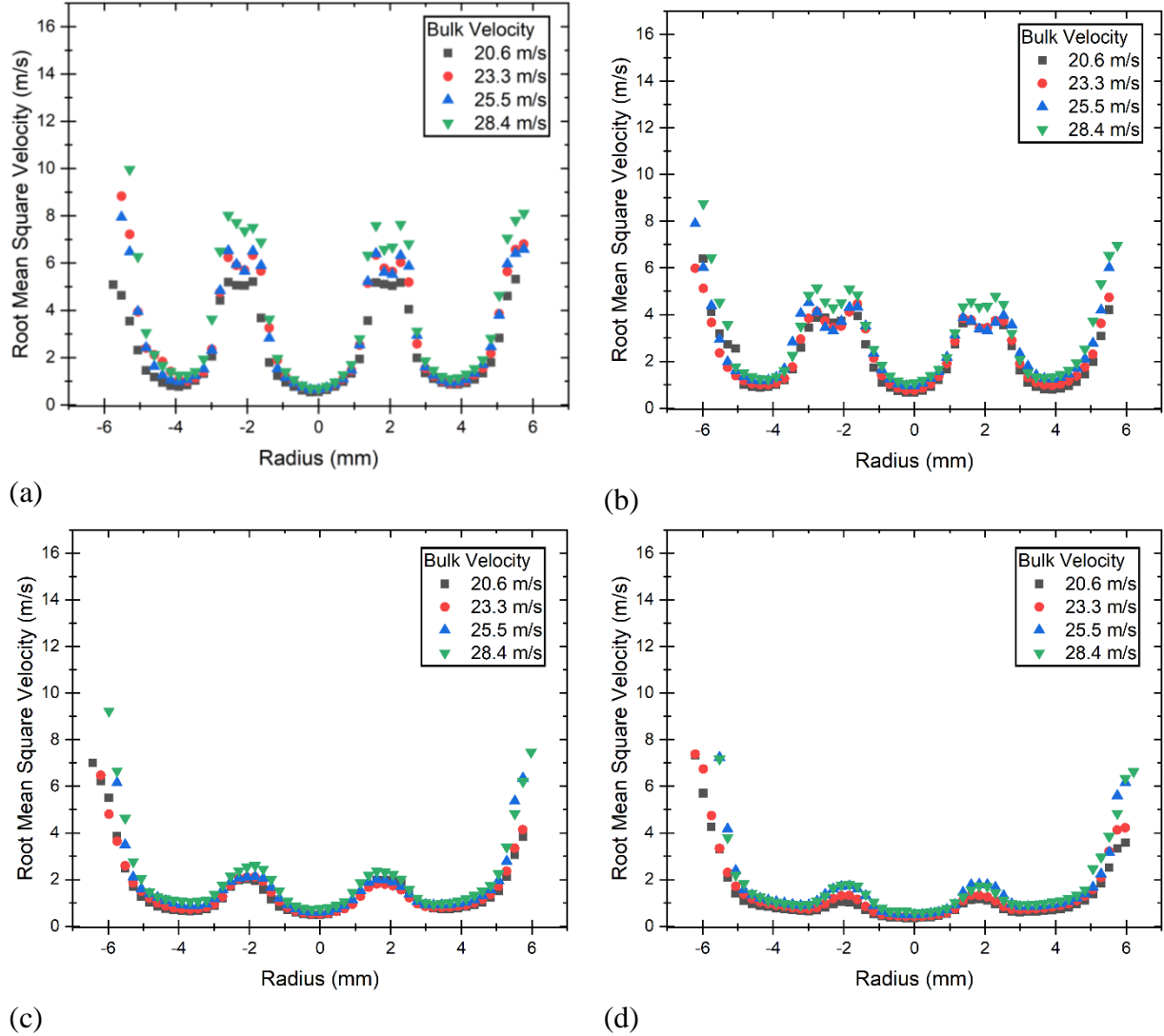
Fig.3-3. Root mean square velocity at 7.1 mm from the burner exit (a) blockage ratio is 62 %, (b) blockage ratio is 51 %, (c) blockage ratio is 45 %, and (d) blockage ratio is 35 %.

Figures 3-4(a) through 3-4(d) show the turbulence intensity corresponding to the burners and operating conditions for which the mean axial velocities and the RMS velocities were depicted in Figs.3-2(a) and Figs.3-3(a) through 3-2(d) and 3-3(d). The turbulence intensity has the lowest values in the core of the seven openings in the turbulence generation plates and increases in regions corresponding to the wakes of the blocked areas between these openings. The turbulence intensity also increases significantly in the blocked annular area at radial locations for all bulk velocities

and blockage ratios. These measurements are consistent with the those of Liu et al. [17] who studied the effects of Reynolds number on the turbulence generated by perforated plats. The present measurements of turbulence intensity showing increases with increasing blockage ratio are also in agreement with those discussed in Refs. [17,18].

(a)

(b)

(c)

(d)
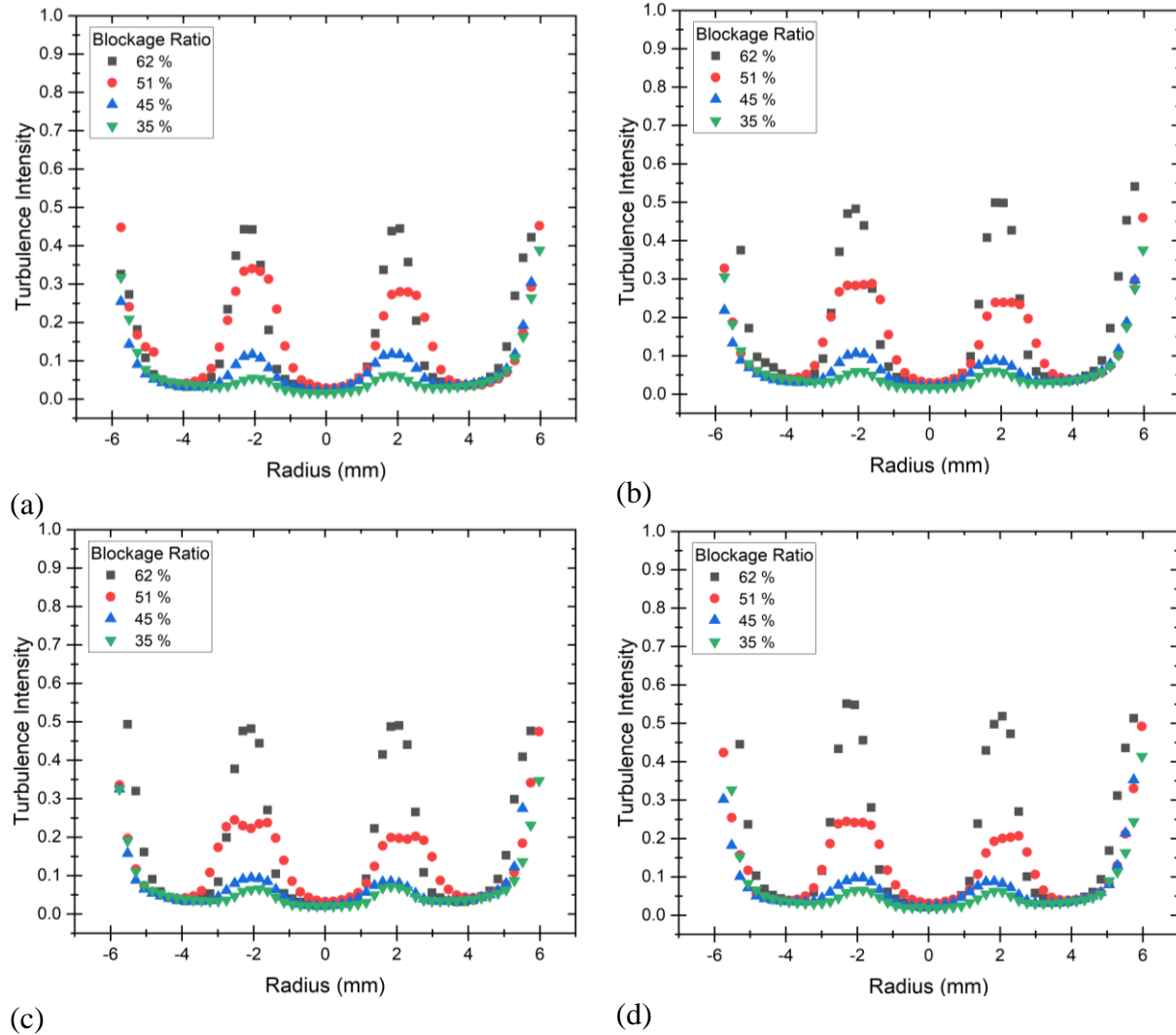
Fig.3-4. Turbulence intensity at 7.1 mm from the burner exit (a) bulk velocity is 20.59 m/s, (b) bulk velocity is 23.26 m/s, (c) bulk velocity is 25.49 m/s, and (d) bulk velocity is 28.35 m/s.

Figs.3-5 through 3-7 illustrate an evaluation of the turbulence intensity for the height and the blockage ratio. The turbulence intensity has different trends by the variation of blockage ratio and the height. Generally, as the blockage ratio is higher, the turbulence intensity has high values [Figs.3-5-3-7]. With an increase in the height, the turbulence intensity increases until the maximum values and reduces after the maximum values [Figs.3-5-3-7]. When the blockage ratio is constant,

73

the turbulence intensity at the center is nearly constant with the height [Fig.3-5]. In contrast, the turbulence intensity at 2.1 mm from the axis changes with the height [Fig.3-7]. As previously mentioned, the mixing of the expanded jets has actively occurred between the nozzles.

Table 3-2. Experimental results for PIV

V_{bulk} (m/s)	B. R (%)	Ignition location from the center (mm)	u' (m/s)	I_{tur}	l_0 (mm)
20.6	35	0	0.36	0.017	12.73
		1.05	0.70	0.034	8.79
		2.10	1.11	0.059	6.11
23.3	35	0	0.42	0.017	11.07
		1.05	0.75	0.030	9.41
		2.10	1.26	0.057	5.35
25.5	35	0	0.50	0.021	9.62
		1.05	0.93	0.031	9.53
		2.10	1.78	0.069	5.02
28.4	35	0	0.58	0.019	9.28
		1.05	1.01	0.033	8.80
		2.10	1.71	0.062	4.99
20.6	45	0	0.49	0.022	13.61
		1.05	1.37	0.068	6.01
		2.10	1.96	0.116	4.67
23.3	45	0	0.52	0.021	15.53
		1.05	1.29	0.055	6.52
		2.10	1.73	0.084	4.94
25.5	45	0	0.61	0.021	14.44
		1.05	1.53	0.057	7.36
		2.10	1.90	0.080	5.60
28.4	45	0	0.75	0.023	12.6
		1.05	1.86	0.061	5.94
		2.10	2.22	0.082	5.44
20.6	51	0	0.66	0.029	18.75
		1.05	1.67	0.078	6.81
		2.10	3.42	0.280	3.50
23.3	51	0	0.77	0.030	17.23
		1.05	1.90	0.079	5.51
		2.10	3.42	0.239	3.38
25.5	51	0	0.96	0.033	15.48
		1.05	2.18	0.080	5.75
		2.10	3.39	0.198	3.62

Table 3 2. continued

28.4	51	0	1.07	0.031	15.35
		1.05	2.17	0.067	7.35
		2.10	4.33	0.200	3.93
20.6	62	0	0.55	0.022	25.59
		1.05	1.94	0.084	5.81
		2.10	5.03	0.445	2.62
23.3	62	0	0.60	0.022	26.13
		1.05	2.27	0.088	6.76
		2.10	6.06	0.499	2.19
25.5	62	0	0.64	0.021	27.45
		1.05	2.54	0.092	4.68
		2.10	5.52	0.490	2.14
28.4	62	0	0.70	0.021	26.03
		1.05	2.80	0.089	5.17
		2.10	6.68	0.518	2.33
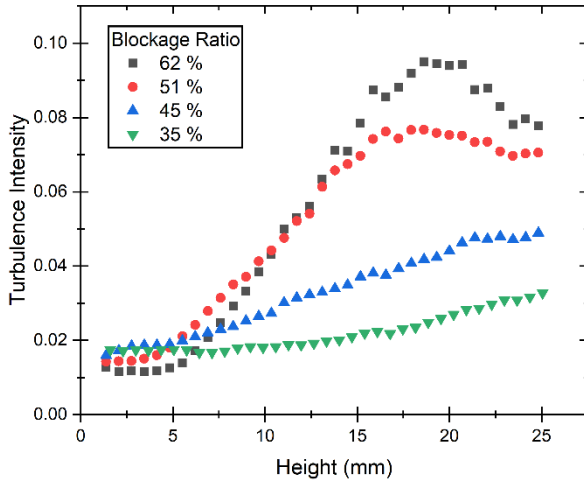
(a)
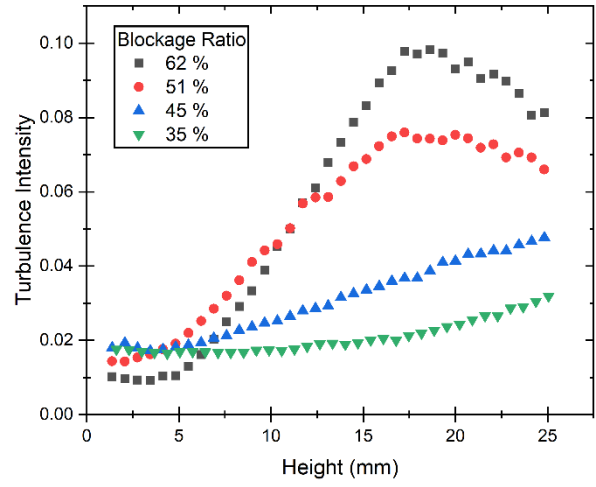
(b)
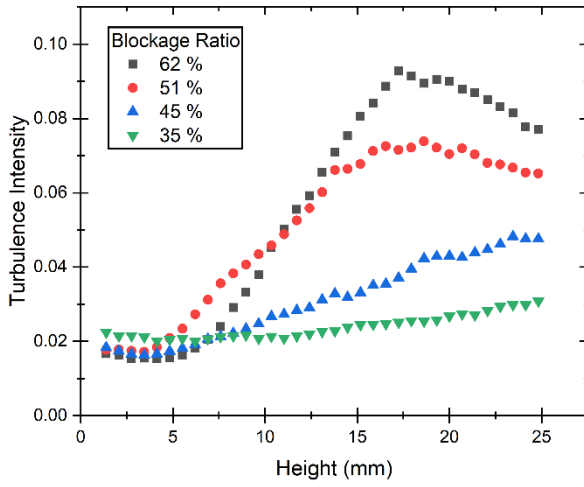
(c)
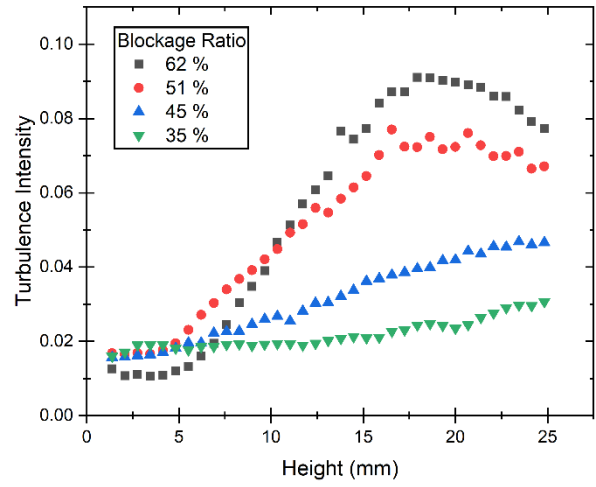
(d)

Fig.3-5. Turbulence intensity at the center (a) bulk velocity is 20.59 m/s, (b) bulk velocity is 23.26 m/s, (c) bulk velocity is 25.49 m/s, and (d) bulk velocity is 28.35 m/s.
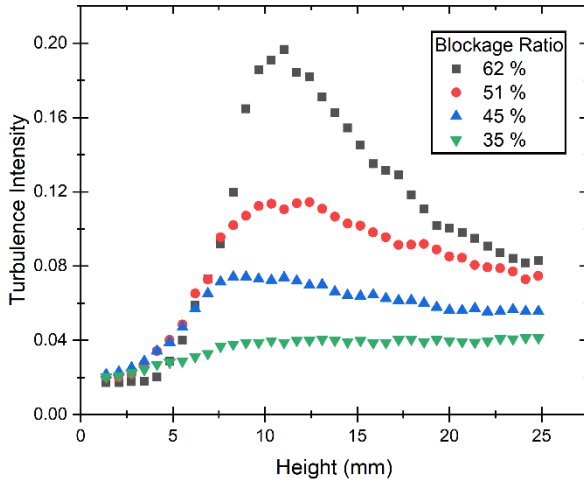
(a)
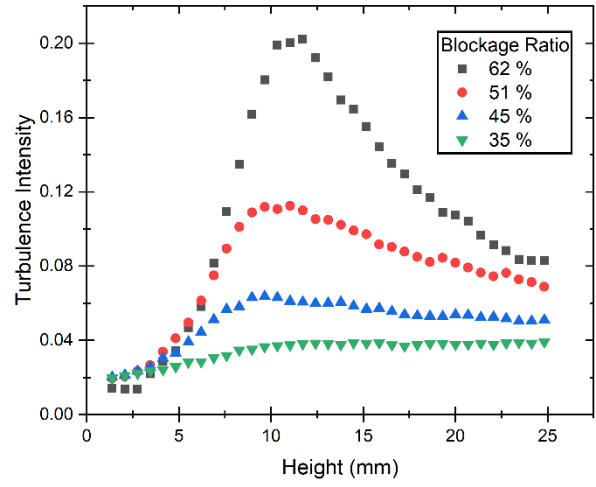
(b)
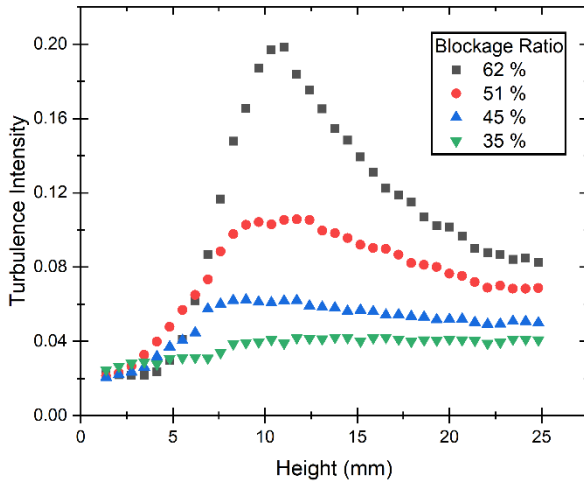
(c)
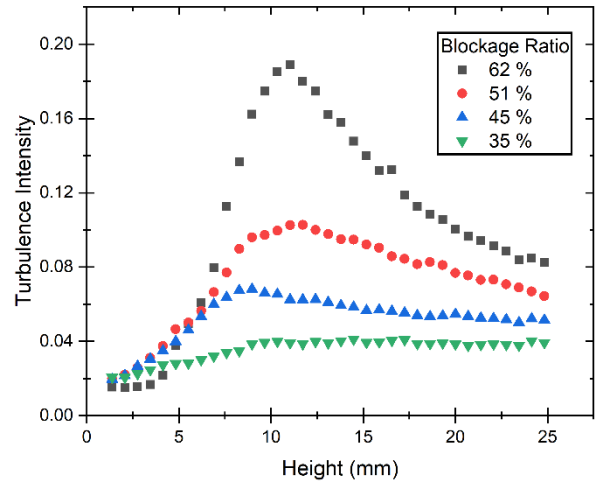
(d)

Fig.3-6. Turbulence intensity at 1.05 mm from the center in the radial direction (a) bulk velocity is 20.59 m/s, (b) bulk velocity is 23.26 m/s, (c) bulk velocity is 25.49 m/s, and (d) bulk velocity is 28.35 m/s.

(a)

(b)

(c)

(d)
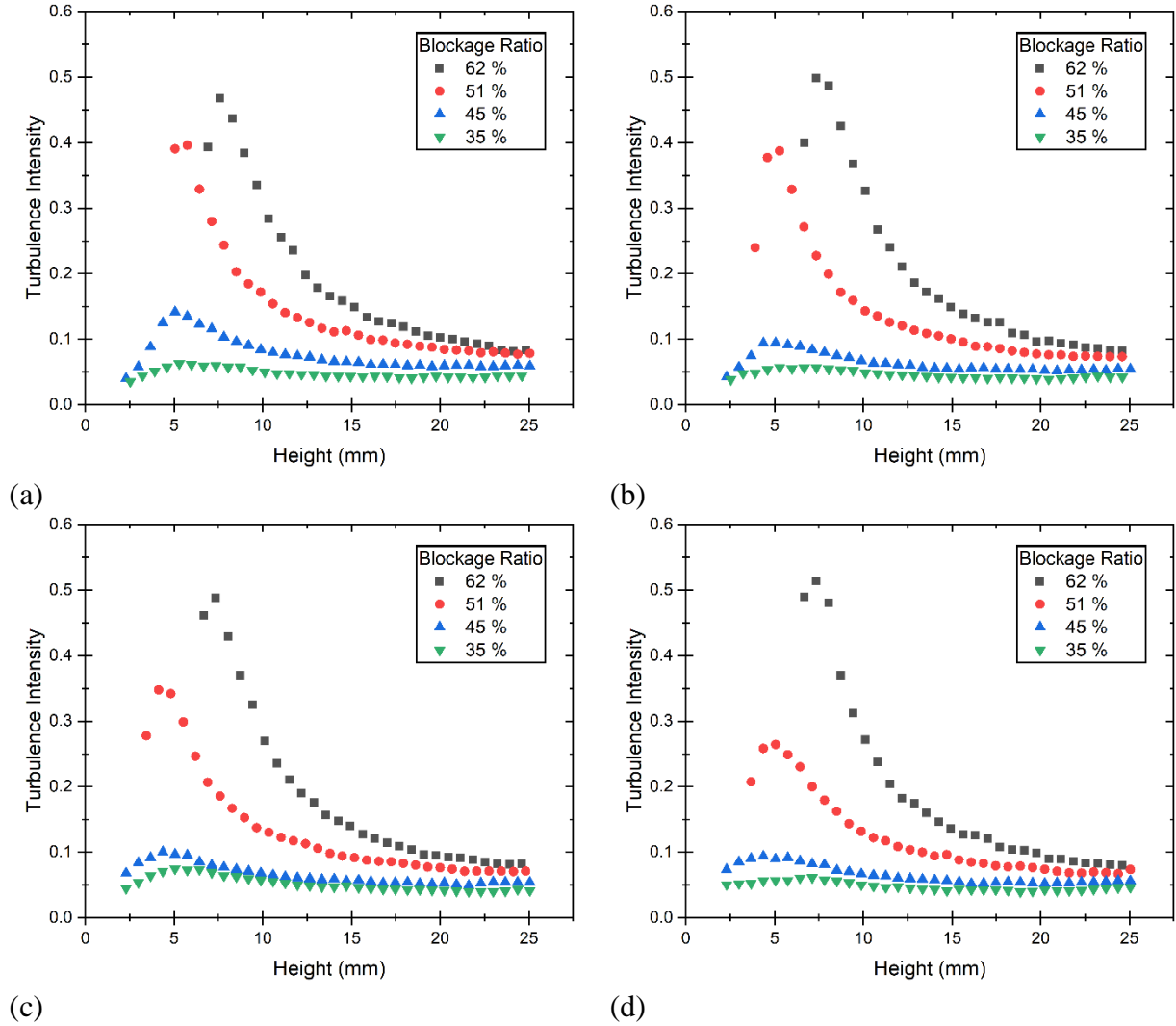
Fig.3-7. Turbulence intensity at 2.10 mm from the center in the radial direction (a) bulk velocity is 20.59 m/s, (b) bulk velocity is 23.26 m/s, (c) bulk velocity is 25.49 m/s, and (d) bulk velocity is 28.35 m/s.

4. EFFECT OF TURBULENCE ON MINIMUM IGNITION ENERGY

4.1 Experimental Conditions

Ignition experiments were performed to study the effect of turbulence intensity on minimum ignition energy (MIE). The premixed hydrogen/air mixture at an equivalence ratio, ϕ=0.9, was issued through the burner exit. The blockage ratio (B.R.) of 35 %, 45 %, 51 %, and 62 % were used for the bulk velocity of 20.6 m/s, 23.3 m/s, 25.5 m/s, and 28.4 m/s [Fig. 2-1][Table 4-1]. The height of the ignition was fixed as 7.1 mm from the exit of the burner [Fig.4-1]. Three ignition locations, 0 mm from the center, 1.05 mm from the center in a radial direction, and 2.10 mm from the center in the radial direction were utilized to compare the influence of the turbulence intensity on the MIE [Fig.4-1]. The turbulence intensities at the ignition locations are the results of the PIV experiments [Fig.3-4][Table 4-1]. The ignition probability at the experimental conditions was 100 %. In order to measure the MIE, the ignition experiments using the ignition probability were conducted 20 times at each condition.

(a) (b)
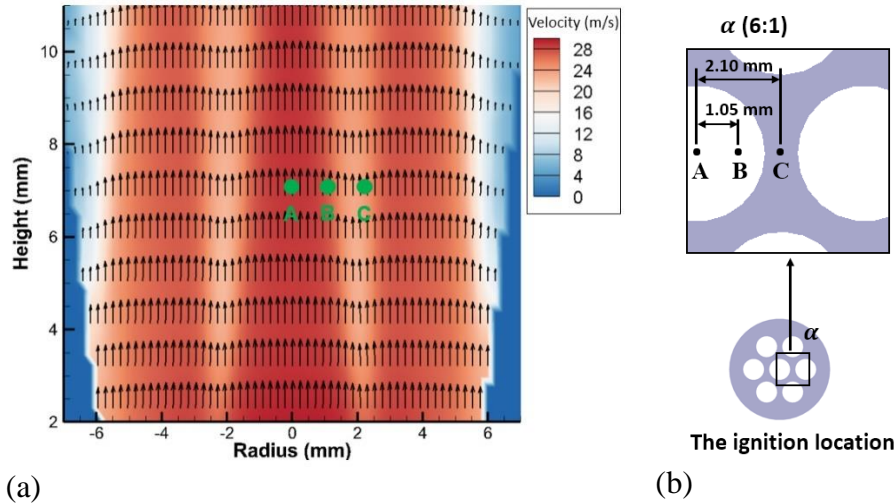
Fig.4-1. (a) The ignition locations, side view, A: 0 mm from the axis (0 mm, 7.1 mm), U is 29.0 m/s, u' is 0.61 m/s, B: 1.05 mm from the axis (1.05 mm, 7.1 mm), U is 26.9 m/s, u' is 1.53 m/s, C: 2.1 mm from the axis (2.1 mm, 7.1 mm), U is 23.6 m/s, u' is 1.9 m/s when V_{bulk} is 25.5 m/s and B.R. is 45 %, (b) the ignition locations, top view, A: 0 mm from the axis (0 mm, 7.1 mm), B: 1.05 mm from the axis (1.05 mm, 7.1 mm), and C: 2.1 mm from the axis (2.1 mm, 7.1 mm).

Table 4-1. Experimental conditions

V_{bulk} (m/s)	B.R. (%)	Re	Ignition location from the center (mm)	u' (m/s)	I_{tur}	l_0 (mm)	η (μm)	τ_η (ms)
20.6	35	3850	0	0.36	0.017	12.73	197.61	1.922
			1.05	0.70	0.034	8.79	109.4	0.589
			2.10	1.11	0.059	6.11	70.69	0.246
23.3	35	4360	0	0.42	0.017	11.07	169.99	1.423
			1.05	0.75	0.030	9.41	105.66	0.55
			2.10	1.26	0.057	5.35	62.18	0.19
20.6	45	3550	0	0.49	0.022	13.61	159.46	1.252
			1.05	1.37	0.068	6.01	60.12	0.178
			2.10	1.96	0.116	4.67	43.15	0.092
23.3	45	4010	0	0.52	0.021	15.53	157.62	1.223
			1.05	1.29	0.055	6.52	64.19	0.203
			2.10	1.73	0.084	4.94	48.05	0.114
25.5	45	4390	0	0.61	0.021	14.44	137.32	0.928
			1.05	1.53	0.057	7.36	58.21	0.167
			2.10	1.90	0.080	5.60	46.22	0.105
20.6	51	3350	0	0.66	0.029	18.75	138.17	0.94
			1.05	1.67	0.078	6.81	53.47	0.141
			2.10	3.42	0.280	3.50	26.44	0.034
23.3	51	3790	0	0.77	0.030	17.23	120.51	0.715
			1.05	1.90	0.079	5.51	46.03	0.104
			2.10	3.42	0.239	3.38	26.21	0.034
25.5	51	4140	0	0.96	0.033	15.48	99.44	0.487
			1.05	2.18	0.080	5.75	41.97	0.087
			2.10	3.39	0.198	3.62	26.84	0.035
28.4	51	4610	0	1.07	0.031	15.35	91.48	0.412
			1.05	2.17	0.067	7.35	44.78	0.099
			2.10	4.33	0.200	3.93	22.81	0.026
20.6	62	2940	0	0.55	0.022	25.59	171.23	1.443
			1.05	1.94	0.084	5.81	45.92	0.104
			2.10	5.03	0.445	2.62	18.42	0.017
23.3	62	3330	0	0.60	0.022	26.13	139.05	0.952
			1.05	2.27	0.088	6.76	37.75	0.07
			2.10	6.06	0.499	2.19	13.63	0.009
25.5	62	3640	0	0.64	0.021	27.45	157.1	1.215
			1.05	2.54	0.092	4.68	35.54	0.062
			2.10	5.52	0.490	2.14	16.33	0.013
28.4	62	4050	0	0.70	0.021	26.03	143.51	1.014
			1.05	2.80	0.089	5.17	33.87	0.056
			2.10	6.68	0.518	2.33	14.46	0.01

4.2   Experimental Results
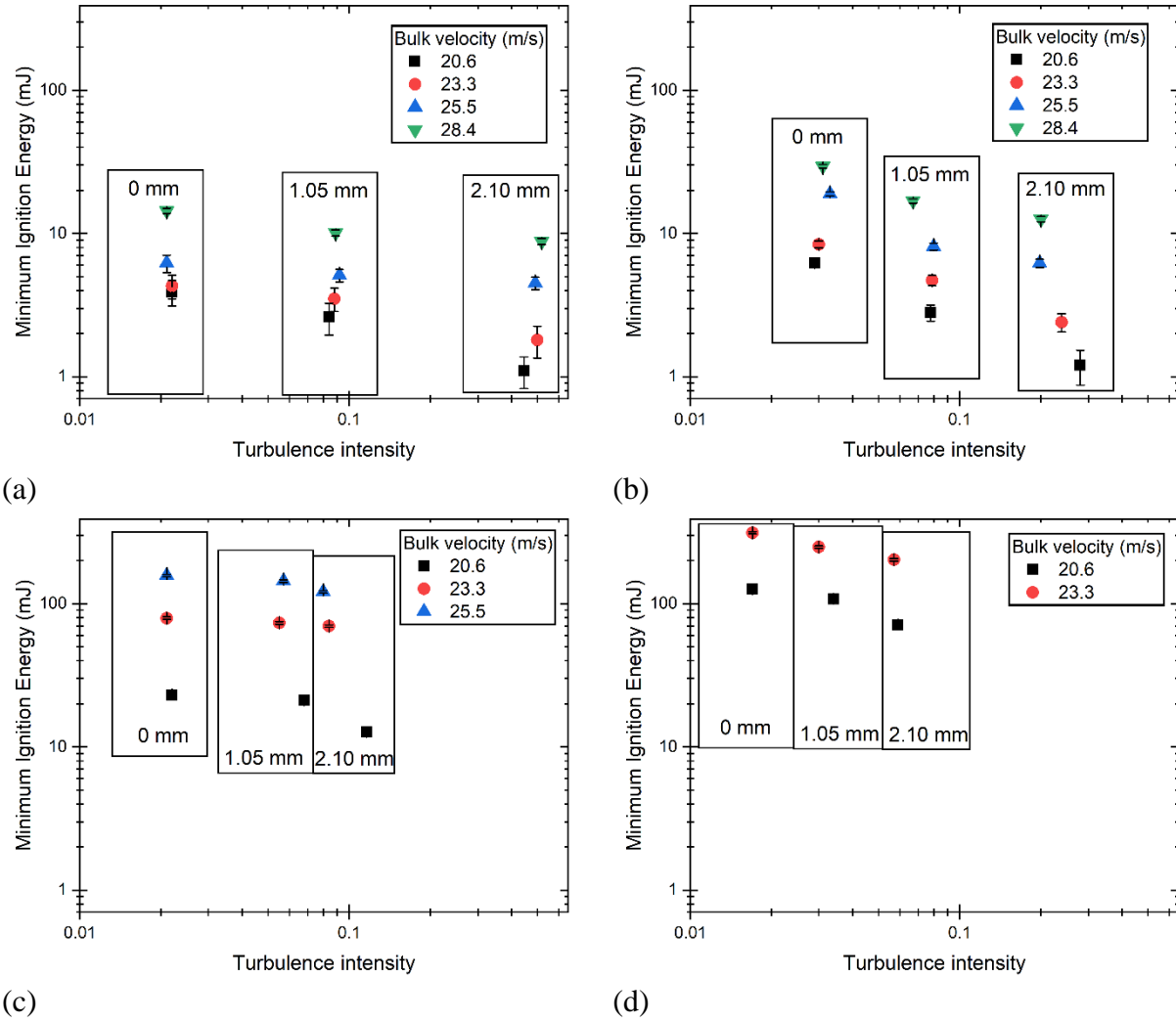
Fig.4-2. Effect of the turbulence intensity on the MIE at the constant blockage ratio, (a) the blockage ratio is 62 %, (b) the blockage ratio is 51 %, (c) the blockage ratio is 45 %, and (d) the blockage ratio is 35 %.

Figure 4-2 shows the effect of turbulence intensity on the MIE at the constant blockage ratio. The variation of the ignition location changes the turbulence intensity [Fig.4-2][Table 4-1]. The more detailed experimental conditions related to the turbulence intensity are illustrated in Table 4-1. The MIE decreases with an increase in the turbulence intensity at the constant bulk velocity [Fig.4-2]. These data are not consistent with the results reported in Refs. [2,8-10]. However, the present results support the recent experimental studies that discovered turbulence facilitates ignition [97-102]. The decrease in the MIE with increasing turbulence intensely most likely results

from the enhancement of kernel propagation speed, and kernel growth by turbulence. In other words, the increase in kernel propagation speed and the kernel development may provide a favorable condition that can rapidly become sustainable flame before blowing away the growing kernel.
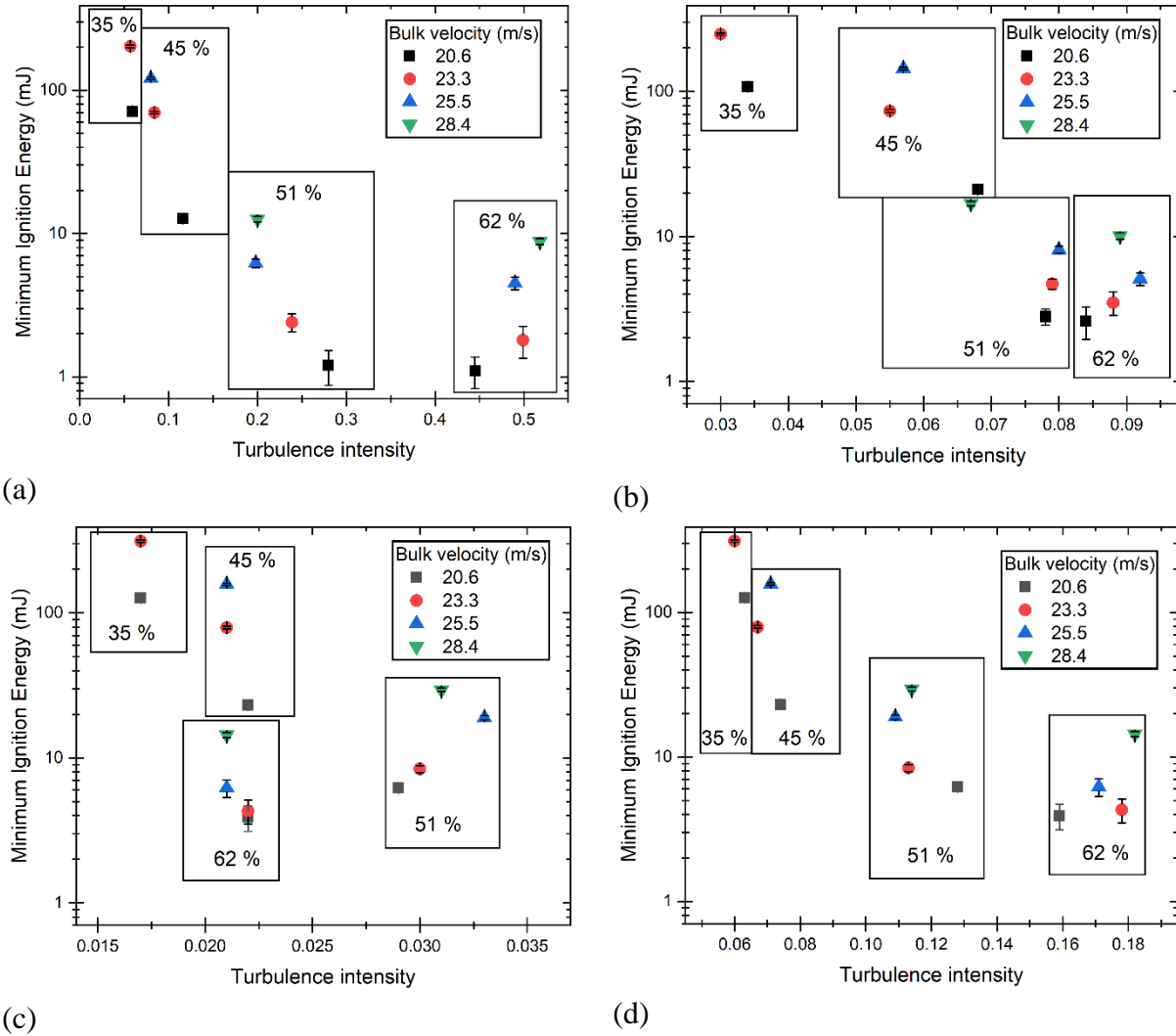
Fig.4-3. Effect of the turbulence intensity on minimum ignition energy at the fixed ignition location, (a) the ignition location is 2.10 mm from the center, (b) the ignition location is 1.05 mm from the center, (c) the ignition location is 0 mm from the center, (d) the ignition location is 0 mm from the center, and the turbulence intensities are the average values in the entire flow field.

Figure 4-3 illustrates the effect of turbulence intensity on the MIE at the fixed ignition location. The blockage ratios of 62%, 51%, 45%, and 35% yield distinct flow regimes in terms of turbulence intensity [Table 4-1]. Generally, the MIE decreases with an increase in the turbulence intensity

[Figs.4-3(a)-(c)]. However, the MIE does not have a clear relationship with the turbulence intensity, when the ignition location is 0 mm from the center [Figs.4-3(c)]. The turbulence intensity in the blockage ratio of 51 % is higher than the turbulence intensity in the blockage ratio of 62 % [Fig.4-3(c)]. However, the MIE in the blockage ratio of 62 % is lower than the the blockage ratio of 51 % [Fig.4-3(c)]. The turbulence of a specific location influence a kernel in very early time growth of kernel. As time elapses, the kernel size increases, then the turbulence of the entire flow field affects the kernel. Thus, when turbulence intensity is changed by a blockage ratio, the turbulence intensity of the entire flow field should also be considered. Fig.4-3(d) depicts the relationship between the MIE in the center location and the average turbulence intensity of the entire flow field [Table 4-2]. The MIE decreases as the turbulence intensity increases [Fig.4-3(d)].

Table 4-2 Experimental conditions for the entire flow field.

V_{bulk} (m/s)	B.R (%)	Re	u' (m/s)	I_{tur}	l_0 (mm)	η (μm)	τ_η (ms)
20.6	35	3850	1.1	0.063	5.39	68.92	0.234
23.3	35	4360	1.24	0.060	5.21	62.53	0.192
20.6	45	3550	1.34	0.074	5.23	58.97	0.171
23.3	45	4010	1.4	0.067	5.28	57.24	0.161
25.5	45	4390	1.69	0.071	5.22	49.61	0.121
20.6	51	3350	2.15	0.128	4.56	40.02	0.079
23.3	51	3790	2.19	0.113	4.25	38.73	0.074
25.5	51	4140	2.44	0.109	4.30	35.86	0.063
28.4	51	4610	2.94	0.114	4.43	31.4	0.049
20.6	62	2940	2.54	0.159	4.50	35.22	0.061
23.3	62	3330	3.13	0.178	4.76	30.50	0.046
25.5	62	3640	3.23	0.171	4.46	29.29	0.042
28.4	62	4050	3.84	0.182	4.47	25.77	0.033

Koroll et al. [13] measured the turbulent flame speed from the growth of two kernels and defined the flame speed ratio between turbulence flame and laminar flame in hydrogen and air mixture as:

$$\frac{S_T}{S_L} = \left[1 + 16\left(\frac{u'}{S_L}\right)^2\right]^{0.5} + \left[1 - exp\left(-\frac{u'}{S_L}\right)\right] \cdot \frac{\frac{\rho_u}{\rho_b} - 1}{\sqrt{3}}. \tag{4.1}$$

(a)

(b)

(c)

(d)
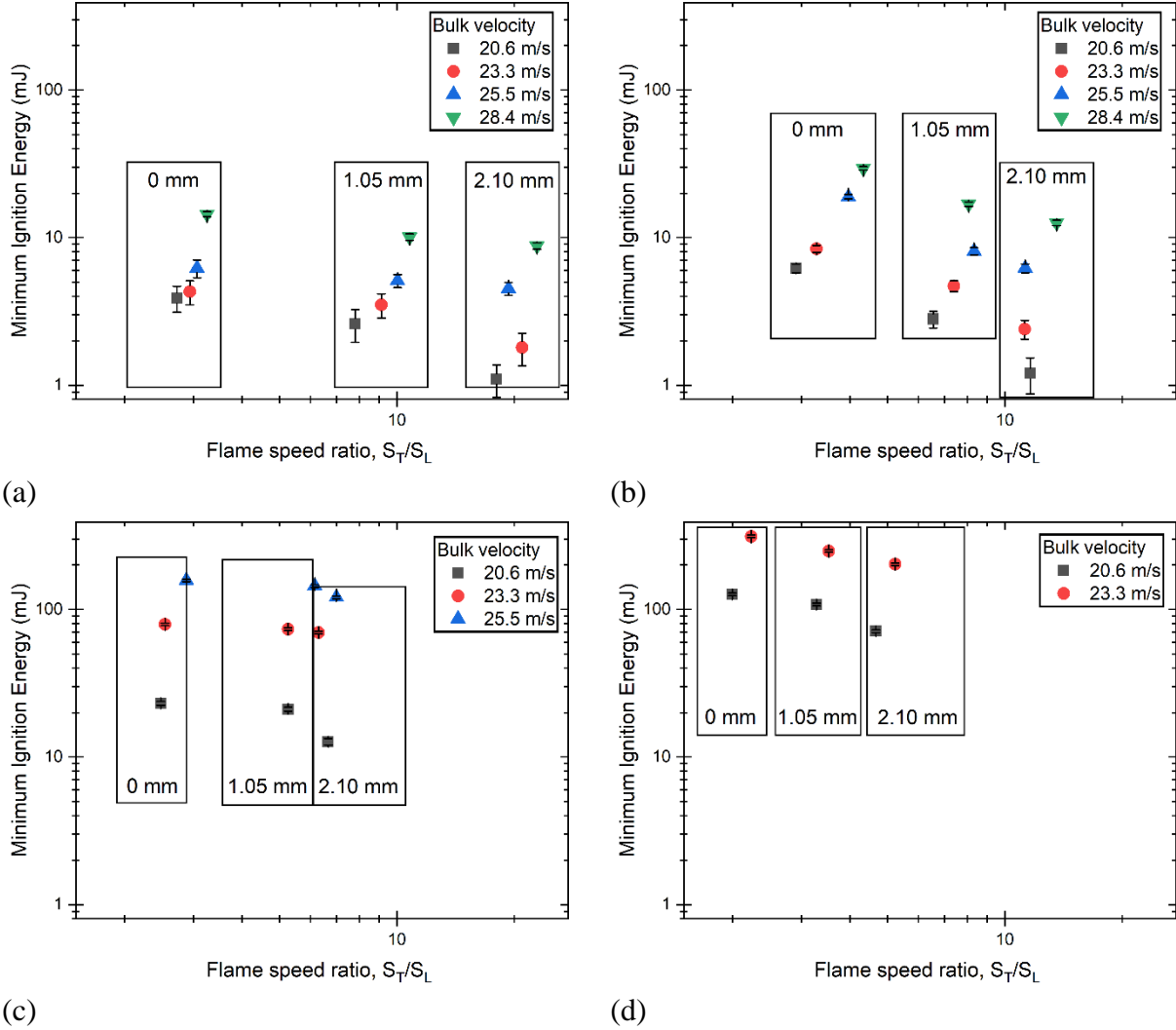
Fig.4-4. Effect of turbulence flame speed on MIE at the constant blockage ratio, (a) the blockage ratio is 62 %, (b) the blockage ratio is 51 %, (c) the blockage ratio is 45 %, and (d) the blockage ratio is 35 %.

A flame speed ratio between the turbulent flame speed and the laminar flame speed is calculated using Eq. (4.1). The laminar flame speed in Eq. (4.1) is 1.79 m/s obtained from

experimental studies [13,156-160]. The MIE decreases with increasing the turbulent flame speed [Fig.4-4]. The result suggests that the fast turbulent flame speed provides a positive effect on the decrease of the MIE [Fig.4-4].
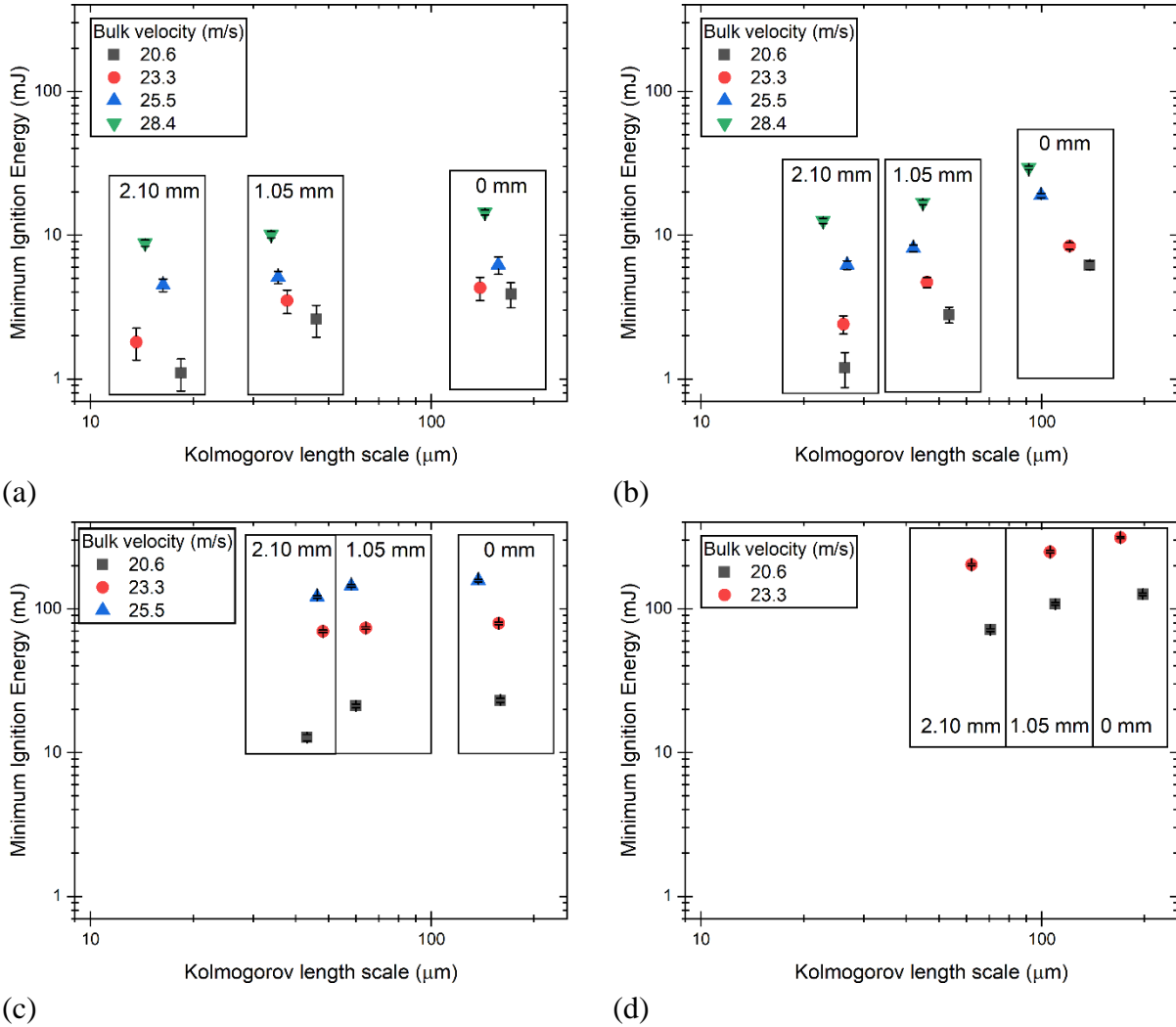
Fig.4-5. Effect of the Kolmogorov length scale on MIE at the constant blockage ratio, (a) the blockage ratio is 62 %, (b) the blockage ratio is 51 %, (c) the blockage ratio is 45 %, and (d) the blockage ratio is 35 %.

The characteristic scales of the smallest turbulent motions are the Kolmogorov scales [161]. The dissipation rate, ε_d, and the kinematic viscosity form the length scale, η, and the time scale, τ_η [161]:

$$\eta \approx \left(\frac{\upsilon^3}{\varepsilon_d}\right)^{1/4} \qquad\qquad 4.2$$

$$\tau_\eta = \left(\frac{\upsilon}{\varepsilon_d}\right)^{1/2} \qquad\qquad 4.3$$

$$\varepsilon_d \approx \frac{3u'^2/2}{l_0/u'} \;. \qquad\qquad 4.4$$
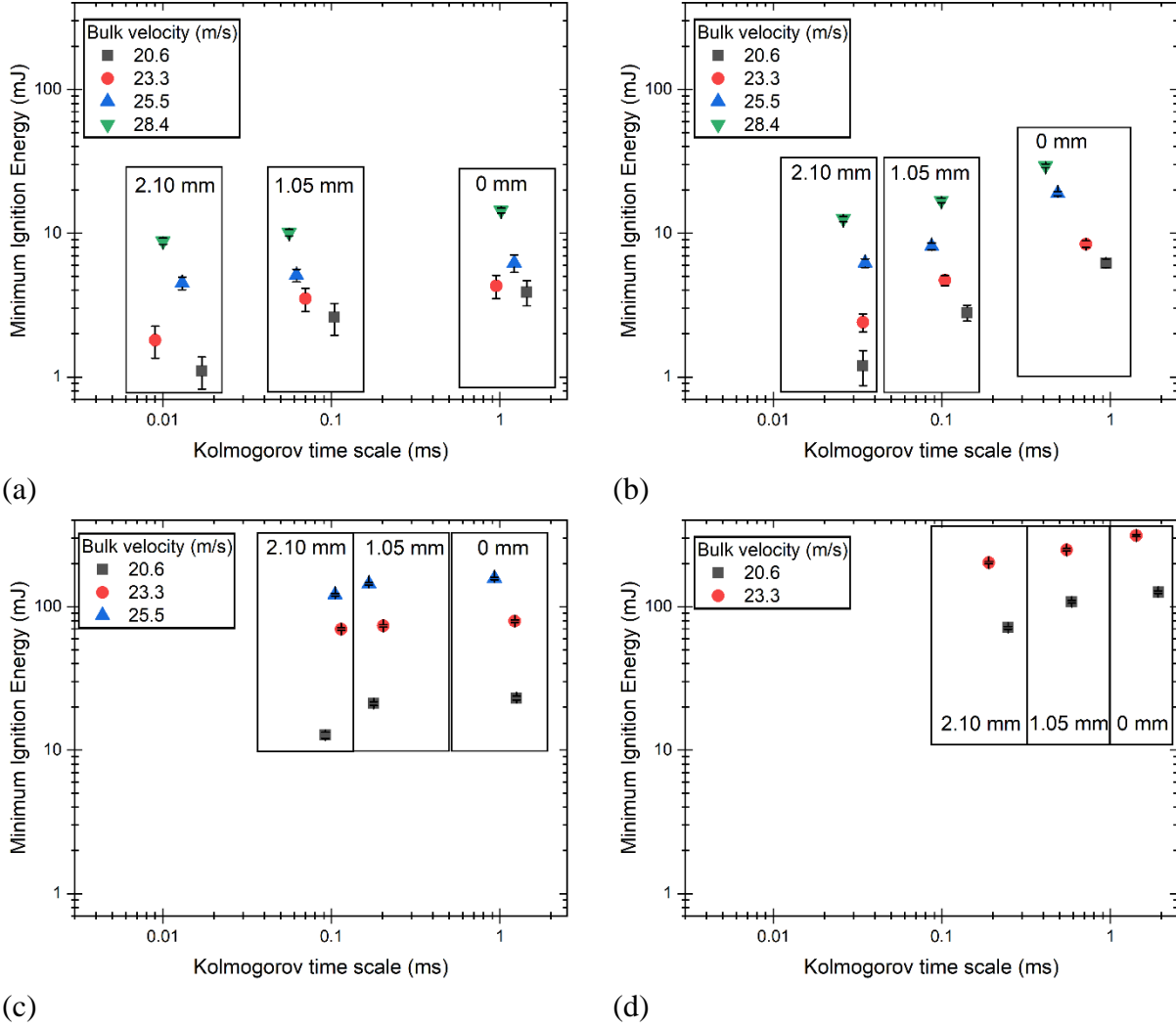
Fig.4-6. Effect of the Kolmogorov time scale on MIE at the constant blockage ratio, (a) the blockage ratio is 62 %, (b) the blockage ratio is 51 %, (c) the blockage ratio is 45 %, and (d) the blockage ratio is 35 %.

The MIE decreases with a decrease in the Kolmogorov scale (the Kolmogorov length scale or the Kolmogorov time scale) [Figs.4-5,4-6]. A reduction in the Kolmogorov scale changed by

the blockage ratio decreases the MIE when the ignition locations are 1.05 mm and 2.10 mm from the center of the burner [Figs.4-5,4-6]. But, the Kolmogorov length scale and the Kolmogorov time scale does not show clear results at 0 mm of the ignition location from the center of the burner [Figs.4-5,4-6]. The Kolmogorov length scale and the Kolmogorov time scale in the entire flow field decrease as the blockage ratio increases [Table 4-2]. The kernel grows as time elapses. Thus, the kernel first receives the effect of the local flow field, then and the influence of the entire flow field as time elapses. Therefore, the MIE decrease as the Kolmogorov scale of the entire flow field reduces [Figs.4-5,4-6] [Table 4-2]. A decrease in the size of the edges (the size of the length scale) increases mixing rates [85,161]. Thus, the enhancement of the mixing rates in the flow fields positively affects a decrease in the MIE since a reaction between a kernel and unburned mixture may be increased by the high mixing rates [Figs.4-5,4-6].

$$Da = \frac{l_0}{\delta_L} \frac{S_L}{u'} \qquad\qquad 4.5$$
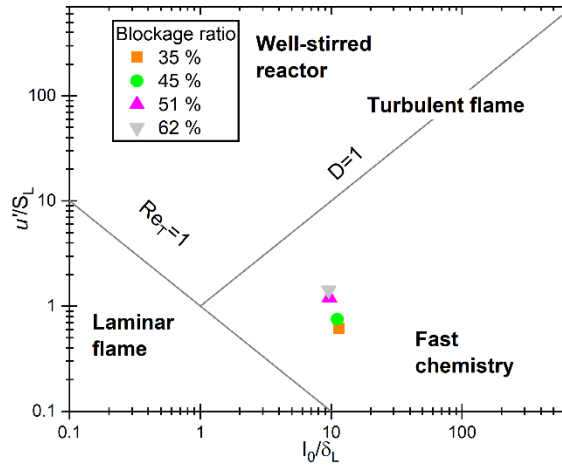
Fig.4-7. Dakmköhler number in the entire flow field, when the bulk velocity is 20.6 m/s.

Figure 4-7 shows the Dakmköhler number of the entire flow field at the bulk velocity of 20.6 m/s. The Dakmköhler number decreases as turbulence intensity is higher [Eq.4.5][85]. As the Dakmköhler number is lower , the mixing rate is fast, and the MIE decreases [Figs.4-2,4-3, 4-5,4-7]. In other words, the improved mixing by the high turbulence intensity decreases the MIE [Figs.4-2,4-3,4-5,4-7]. The enhancement of the mixing rate in Dakmköhler number is

corresponding to the result of the Kolmogorov scale. Turbulence promotes ignition by the increase in mixing. However, more increased turbulence above the specific values may lead to suppressing ignition due to the enhanced dissipation of kernel and the heat loss by diffusion to the surrounding unburned gas like reference papers [2,8-10,98].

(a)

(b)

(c)

(d)
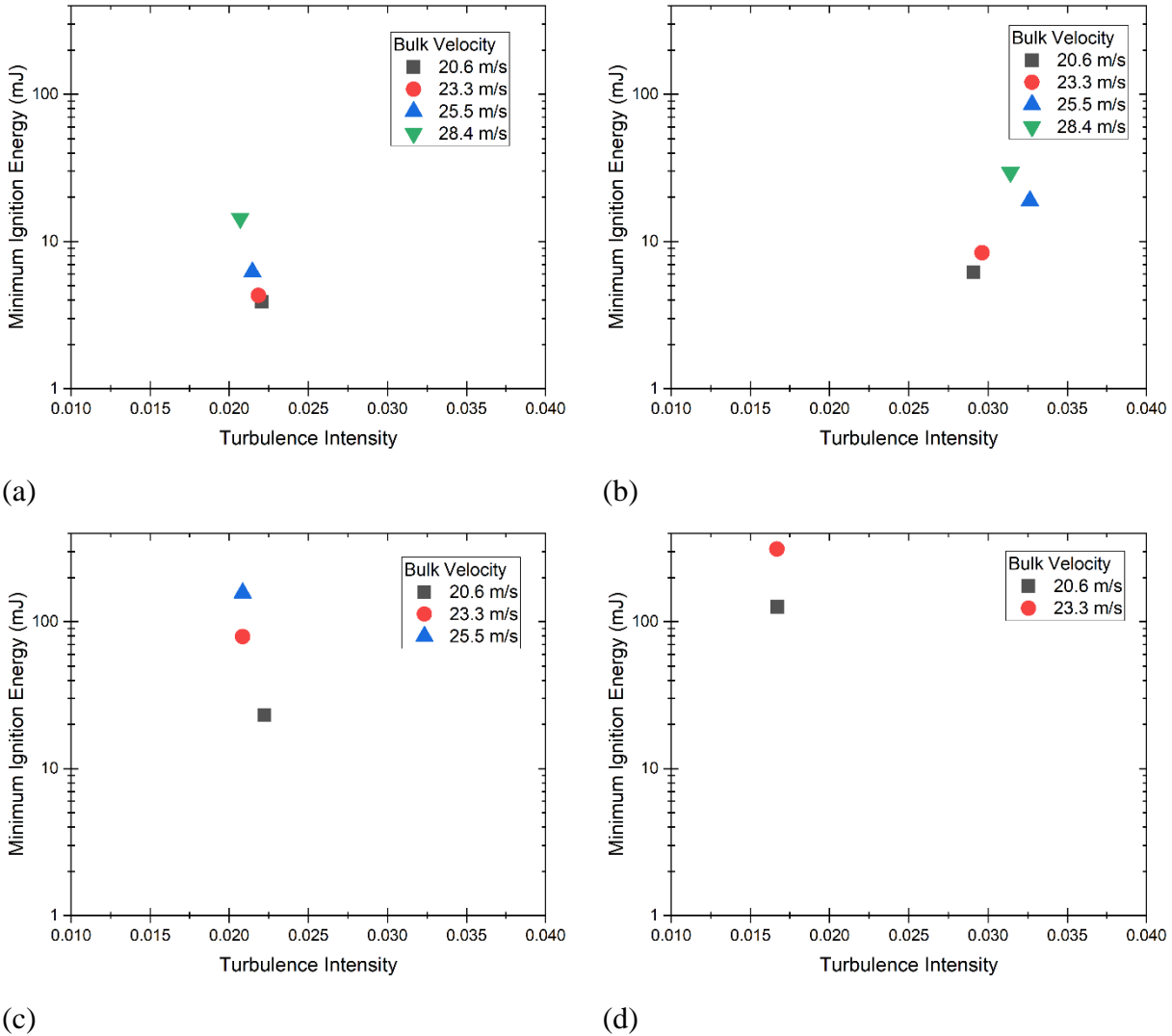
Fig.4-8. Effect of bulk velocity on MIE, (a) the blockage ratio is 62 %, (b) the blockage ratio is 51 %, (c) the blockage ratio is 45 %, and (d) the blockage ratio is 35 %.

Where the ignition location is the center, the turbulence intensities are nearly constant at the different bulk velocities for the fixed perforated plates [Fig.4-8]. It means that the ignition condition at the given experimental conditions is only dependent on the bulk velocity and

independent on the turbulence intensity. The MIE increases with increasing the bulk velocity [Fig.4-8]. Heat convection between a flame kernel and unburnt mixtures increases with an increase in bulk velocity [1,3-6]. Therefore, the increased ignition energy is required to compensate for the enhanced heat loss at the higher bulk velocity. A more detailed explanation about the effect of bulk velocity on MIE will discuss in Chapters 8,9.

5. RELATIONSHIP BETWEEN MINIMUM IGNITION ENERGY, TURBULENCE INTENSITY, AND KERNEL PROPAGATION SPEED

5.1 Experimental Conditions

The blockage ratio of 35 %, 45 %, 51 %, and 62 % were used for the bulk velocity of 23.3 m/s to study the effect of the turbulence intensity on kernel propagation speed. The blockage ratio of 45 % was utilized for the bulk velocity of 20.6 m/s, and 23.3 m/s to examine the effect of bulk velocity on the kernel propagation speed. An equivalence ratio of the hydrogen/air mixture was 0.9. The height of the ignition was constant as 7.1 mm above the burner exit. The ignition experiments used three ignition locations, 0 mm from the center, 1.05 mm from the center, and 2.10 mm from the center in the radial direction to compare the effect of turbulence intensity on the kernel propagation speed [Fig.4-1].

The laser-induced spark was applied as an ignition source in the present study [Fig. 2-10]. The more detailed information about the laser-induced spark is given Chapter 2.2. An laser energy difference was calculated by the difference between the incident energy (E_{in}) and the transmitted energy (E_{tr}) as $\Delta E = E_{in} - E_{tr}$ [3,4,74]. The laser energy difference used in the present research was constant as 2.0 mJ to avoid an influence of ignition energy on the kernel propagation speed. In other words, the kernel generated by the constant laser energy is studied at the different ignition locations and perforated plates that vary the turbulence intensity to understand the relation between the turbulence intensity, the kernel propagation speed, and the ignition energy. The turbulence intensity was measured through the particle imaging velocity (PIV) [Chapter 3]. The more detailed experimental conditions are provided in Table 5-1.

The Schlieren image visualized the kernel development to study the kernel propagation speed [Fig. 2-10]. The Schlieren image system consisted of the 0.2 watt LED lamp, the concave mirror ($f = 250$ mm), the knife-edge, and the high-speed camera (Vision Research Phantom v7.1). An exposure time of the camera was 2 µs. A sample rate of the high-speed camera was 20000 fps. An array size of the high-speed camera was $256 \times 512 \ pixel^2$. A resolution of capture images was 0.188 mm/pix.

Table 5-1. Experimental conditions for ignition test

Case 1					
V_{bulk} (m/s)	ΔE (mJ)	ϕ	Blockage ratio (%)	Ignition location from the center (mm)	Turbulence intensity (%)
23.3	2.0	0.9	62	0	2.2
23.3	2.0	0.9	62	1.05	8.8
23.3	2.0	0.9	62	2.10	49.9
Case 2					
V_{bulk} (m/s)	ΔE (mJ)	ϕ	Blockage ratio (%)	Ignition location from the center (mm)	Turbulence intensity (%)
23.3	2.0	0.9	51	0	3.0
23.3	2.0	0.9	51	1.05	7.9
23.3	2.0	0.9	51	2.10	23.9
Case 3					
V_{bulk} (m/s)	ΔE (mJ)	ϕ	Blockage ratio (%)	Ignition location from the center (mm)	Turbulence intensity (%)
23.3	2.0	0.9	45	0	2.1
23.3	2.0	0.9	45	1.05	5.5
23.3	2.0	0.9	45	2.10	8.4
Case 4					
V_{bulk} (m/s)	ΔE (mJ)	ϕ	Blockage ratio (%)	Ignition location from the center (mm)	Turbulence intensity (%)
23.3	2.0	0.9	35	0	1.7
23.3	2.0	0.9	35	1.05	3.0
23.3	2.0	0.9	35	2.10	5.7
Case 5					
V_{bulk} (m/s)	ΔE (mJ)	ϕ	Blockage ratio (%)	Ignition location from the center (mm)	Turbulence intensity (%)
20.6	2.0	0.9	45	0	2.2
20.6	2.0	0.9	45	1.05	6.8
20.6	2.0	0.9	45	2.10	11.6

5.2   Experimental Results

The analysis of the kernel has studied until 1000 μs after the laser pulse. A kernel center velocity means a movement speed of a kernel center. The kernel propagation speed is calculated by

$$S_F = \frac{dL}{dt} \qquad\qquad 5.1$$

where dL is the change of kernel length in the x-direction or the y-direction [Fig.5-1(a)], dt is a time interval between the Schlieren images. The kernel propagation speed is divided into four directions [Fig.5-1(b)]. The experiments for each case were performed 25-30 times using the Schlieren image [Table 5-1]. The experimental results like the kernel location, the kernel length, the kernel propagation speed, and the kernel center velocity, are the average results. The uncertainties of the measurements are 12 %.

(a)   (b)
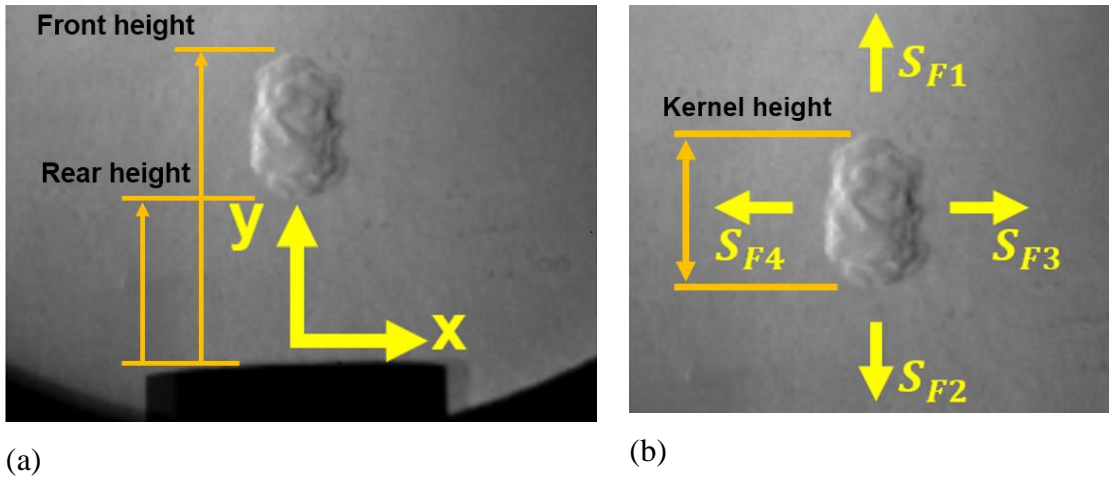
Fig.5-1. (a) Schlieren image, (b) Kernel propagation speed.

5.2.1   Kernel Propagation Speed in y-direction
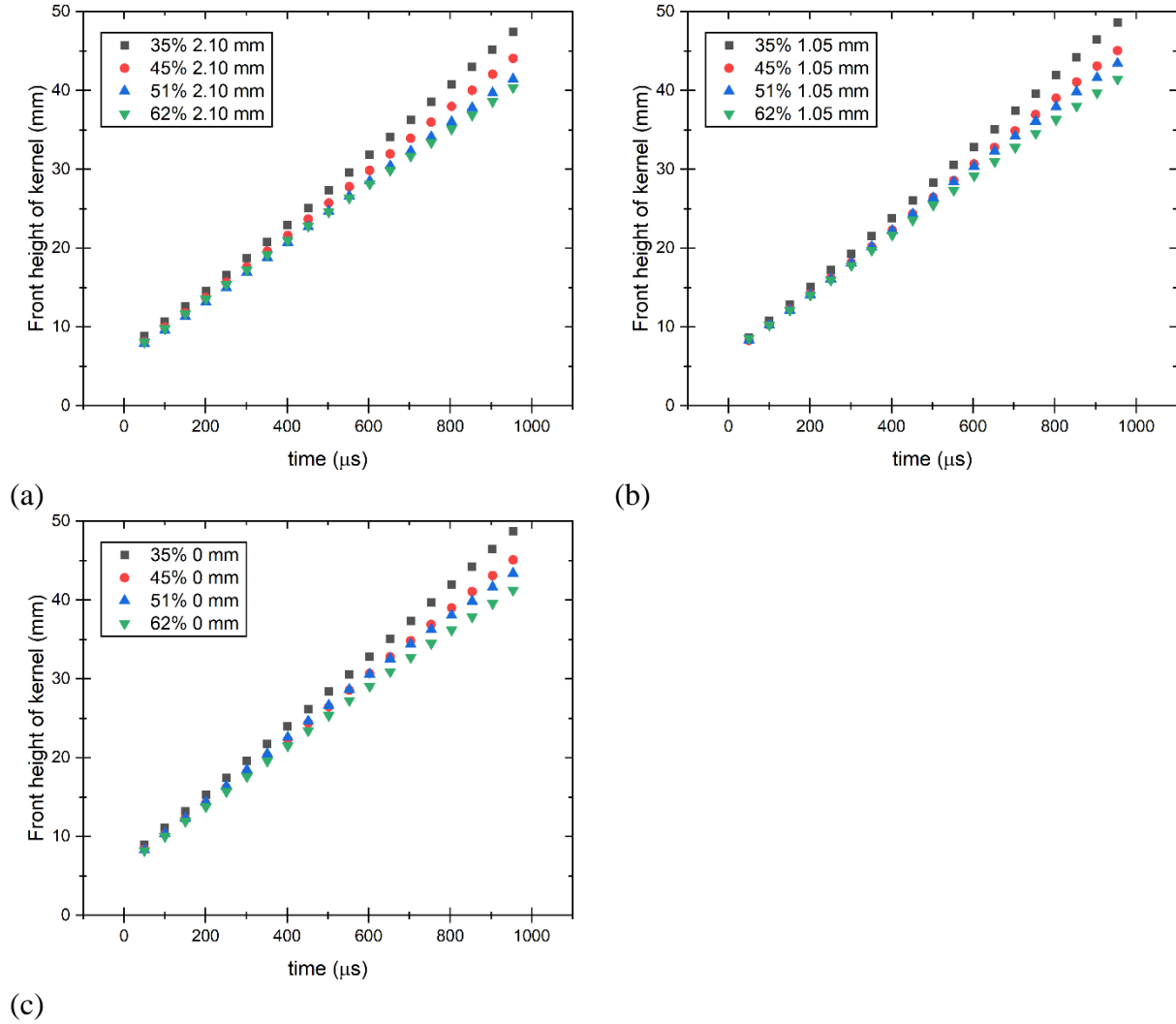
Fig.5-2. The front height of the kernel from the burner exit (a) the ignition location is 2.10 mm from the center, (b) the ignition location is 1.05 mm from the center, and (c) the ignition location is 0 mm from the center, (d) the blockage ratio is 62 %, (e) the blockage ratio is 51 %, (f) the blockage ratio is 45 %, and (e) the blockage ratio is 35 %.

Fig. 5-2 continued

(d)

(e)

(f)

(g)
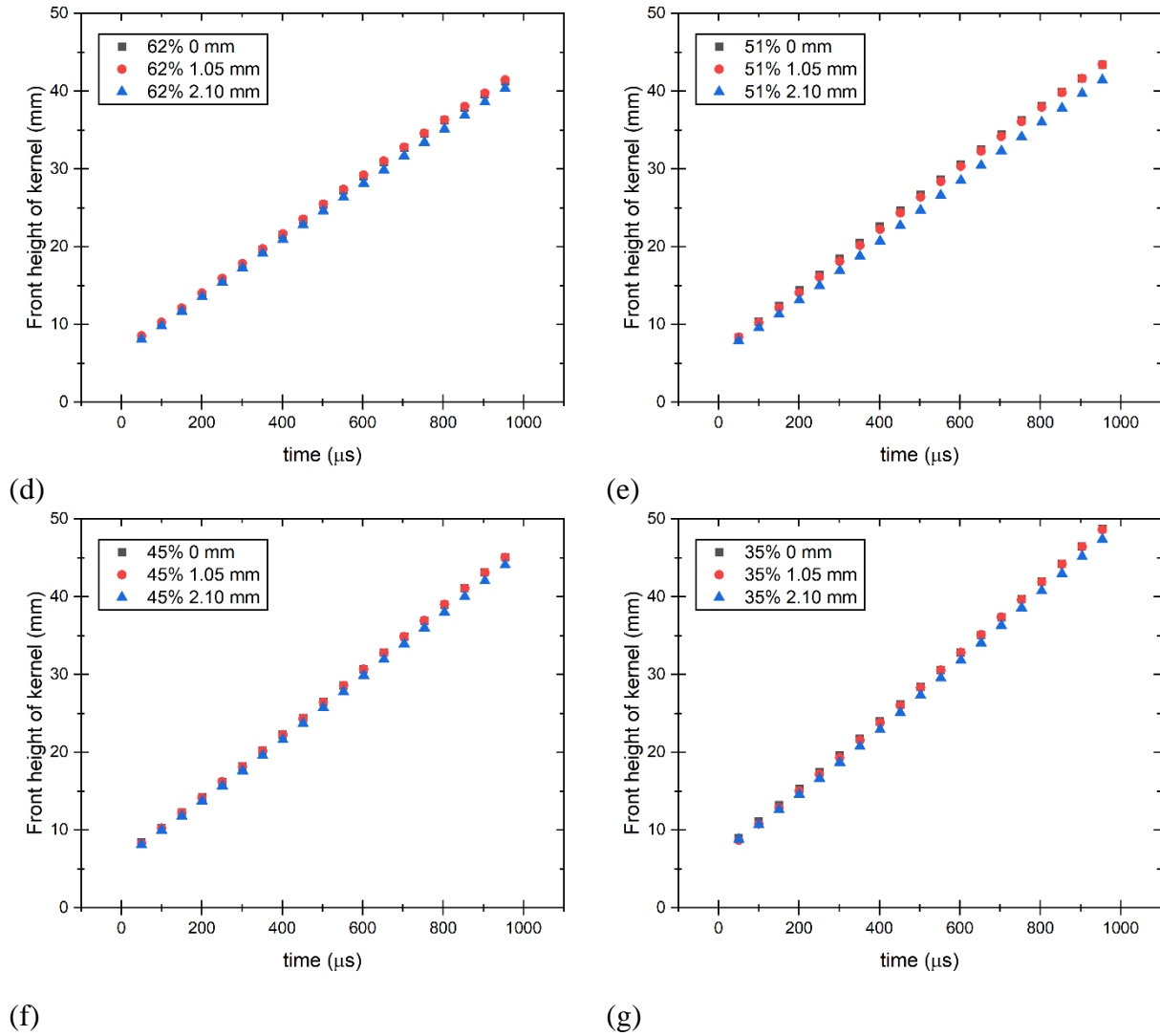
Figures 5-2 and 5-3 show the flame kernel heights from the burner exit for the time interval 0-1000 μs after the laser pulse. The front height of the kernel from the burner exit increases as time elapses since the kernel grows with time [Fig.5-2]. The front height of the kernel increases with a decrease in the turbulence intensity (the blockage ratio) [Fig.5-2 (a)-(c),Fig.5-4]. Similarly, the rear height of the kernel increases with a decrease in the turbulence intensity (the blockage ratio) [Fig.5-3 (a)-(c),5-4]. The relationship between the kernel heights and the turbulence intensity means that the high turbulence intensity negatively affects the kernel movement and thus is able to provide a condition that can hold the kernel instead of blowing off. In other words, the kernel generated in the low turbulence intensity easily blows off instead of becoming a sustainable flame

since the low turbulence intensity facilitates the kernel movement [Fig.5-3 (a)-(c),5-4]. For the high turbulence like the blockage ratio of 62 % [Fig.5-3 (a)] [Table 5-1], the rear height of the kernel continuously decreases by the kernel growth, approaches zero, and develops into a sustainable flame. The reason is the measured minimum ignition energy for the blockage ratio of 62 % is 1.8 mJ, this value is lower than the used laser energy difference (2 mJ) [Table 5-2]. In contrast, the rear height of the kernel for the blockage ratios of 45 % and 35 % increases for times less than 400 μs and decreases for times longer than 400 μs [Fig.5-3]. The momentum energy of the jet flow pushes the kernel from the burner exit. The kernel travel by the momentum energy reduces with time since the kernel continuously grows but the momentum energy is consistent. The kernel growth becomes larger than the kernel travel by the momentum energy of the jet flow for times longer than 400 μs. Therefore, the rear height of the kernel for the blockage ratios of 45 % and 35 % also decreases with time due to the kernel development [Fig.5-3].

(a)   (b)
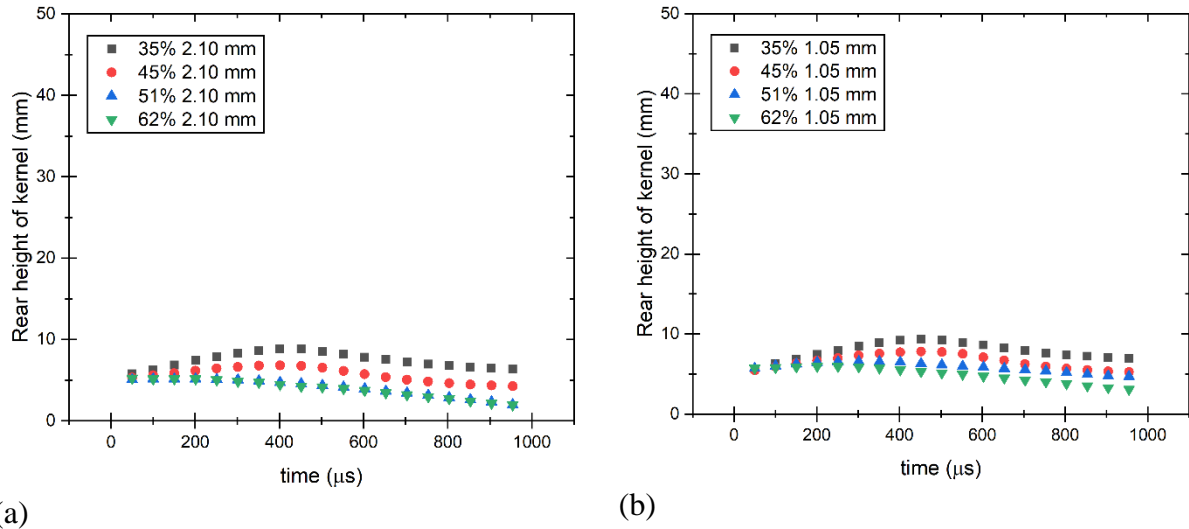
Fig.5-3. The Rear height of kernel from the burner exit (a) the ignition location is 2.10 mm from the center, (b) the ignition location is 1.05 mm from the center, and (c) the ignition location is 0 mm from the center, (d) the blockage ratio is 62 %, (e) the blockage ratio is 51 %, (f) the blockage ratio is 45 %, and (e) the blockage ratio is 35 %.

Fig.5-3 continued

(c)

(d)

(e)
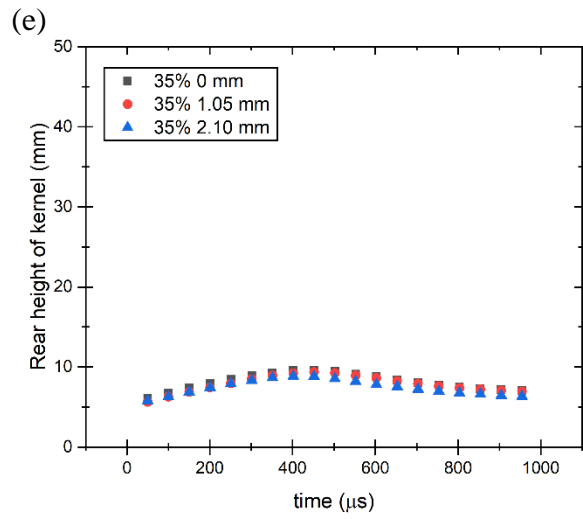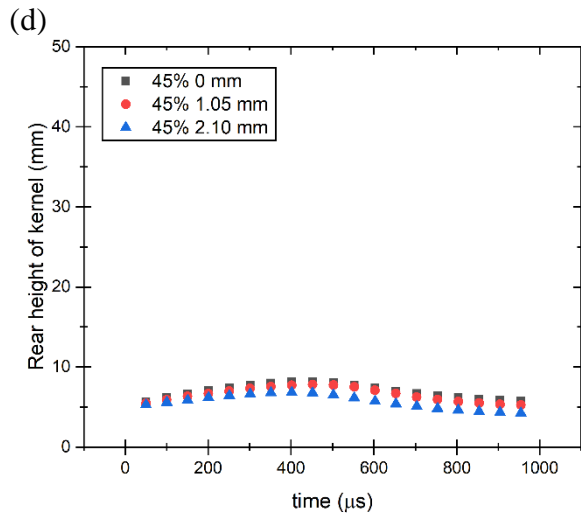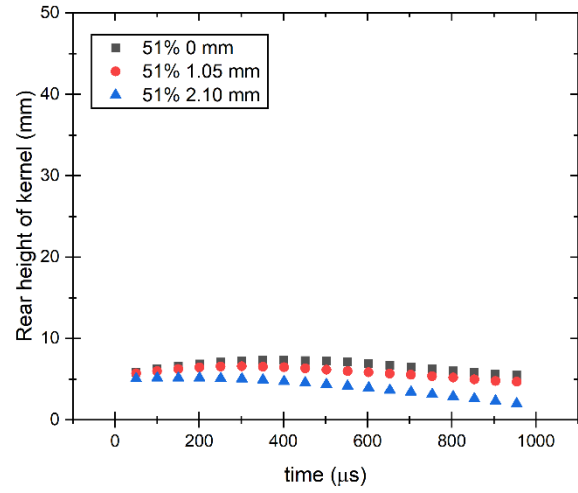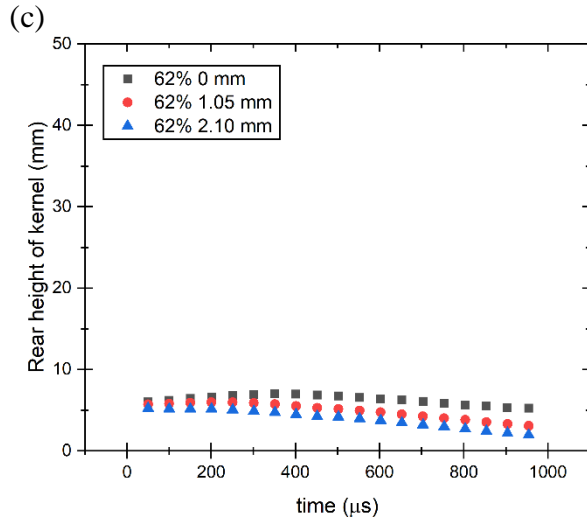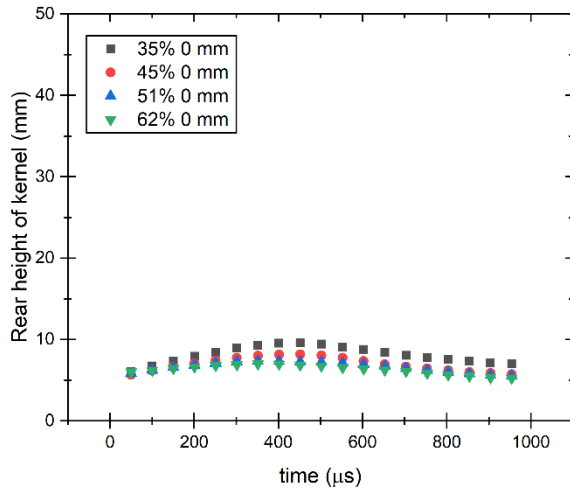
(f)

(g)

The kernel height decreases as the turbulence intensity increases for the fixed blockage ratios [Fig.5-2 (d)-(g), Fig.5-3 (d)-(g),Fig.5-5]. The rear height of the kernel more clearly illustrates the difference in the kernel height by the turbulence than the kernel front height [Fig.5-2 (d)-(g), Fig.5-3 (d)-(g),Fig.5-5]. The reason is turbulence in the flow field becomes stronger as the height is closer to the burner. The kernel produced at the high turbulence intensity relatively rapidly expands to the burner and decreases the rear height.

(a)   (b)   (c)   (d)
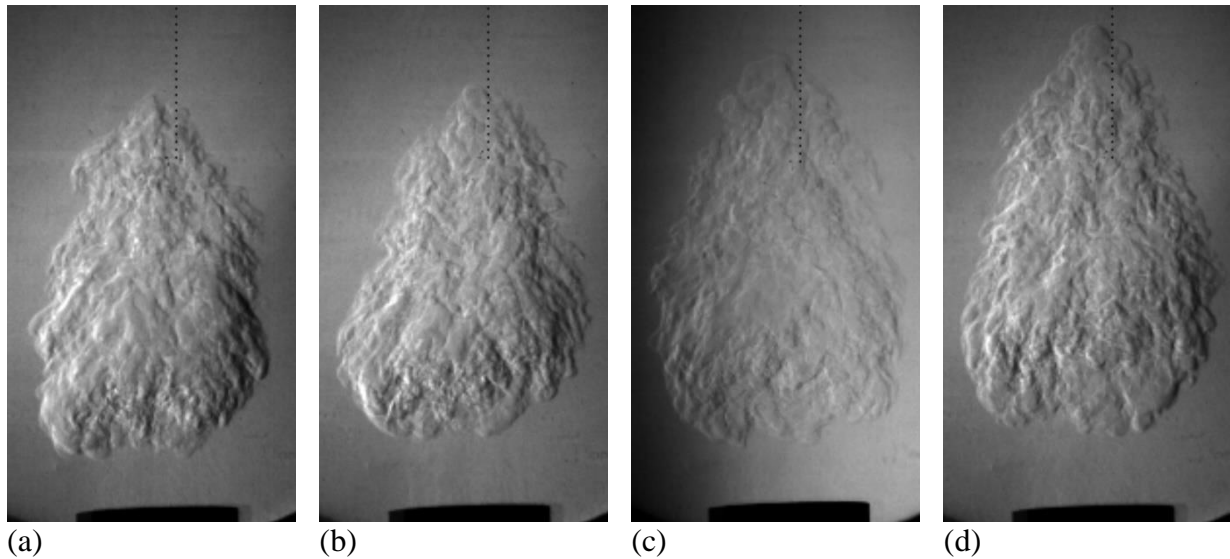
Fig.5-4. Schlieren image of the kernel (at 875 μs) (a) the blockage ratio is 62 %, and the ignition location is 1.05 mm from the center, (b) the blockage ratio is 51 %, and the ignition location is 1.05 mm from the center, (c) the blockage ratio is 45 %, and the ignition location is 1.05 mm from the center, and (d) the blockage ratio is 35 %, and the ignition location is 1.05 mm from the center.

(a) (b) (c)
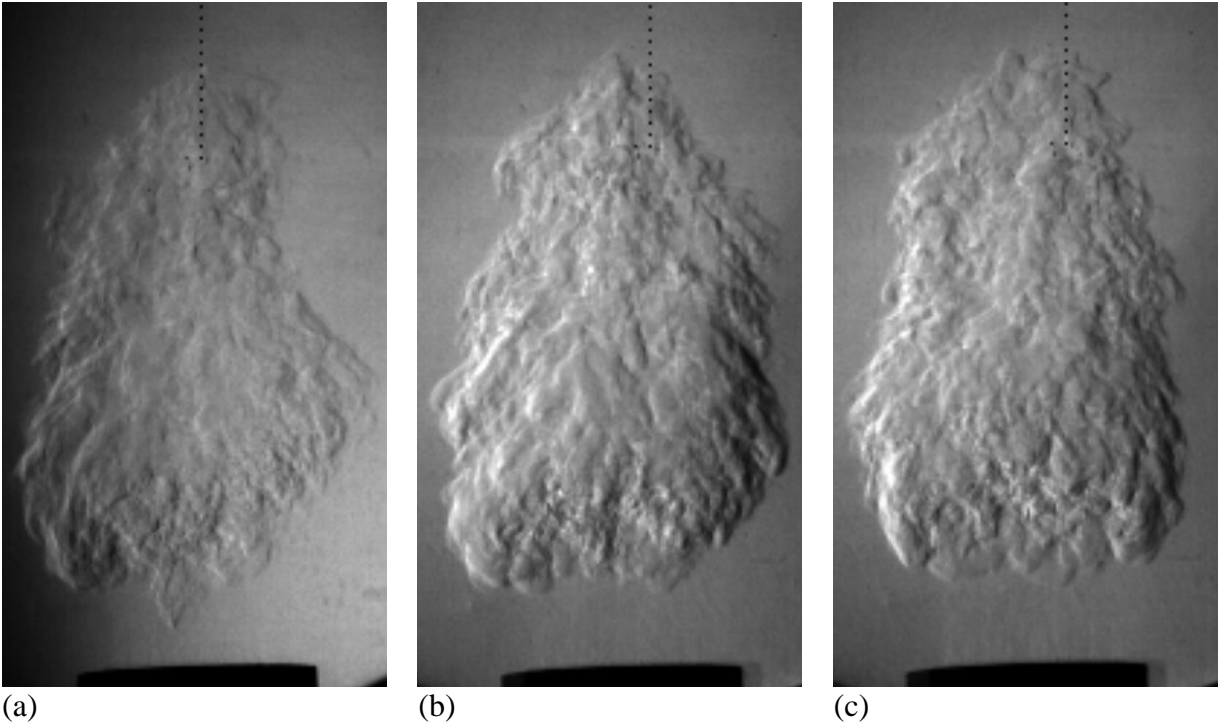
Fig.5-5. Schlieren image of the kernel (at 875 μs) (a) the blockage ratio is 62 %, and the ignition location is 2.10 mm from the center, (b) the blockage ratio is 62 %, and the ignition location is 1.05 mm from the center, and (c) the blockage ratio is 62 %, and the ignition location is 0 mm from the center.

(a)

(b)

(c)

(d)
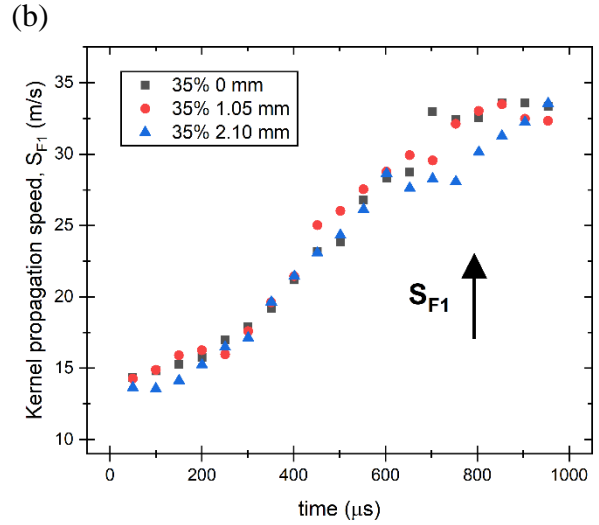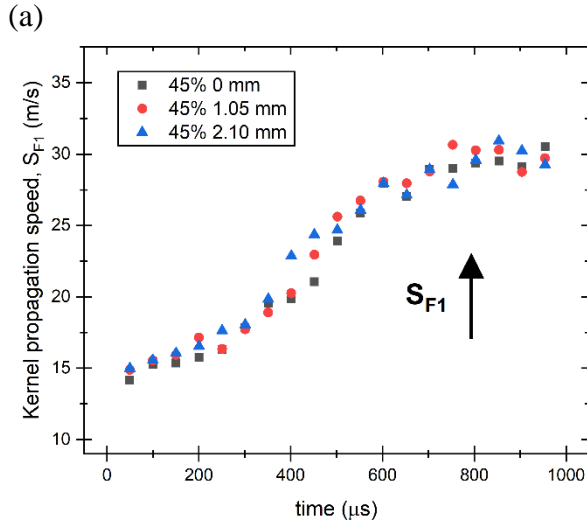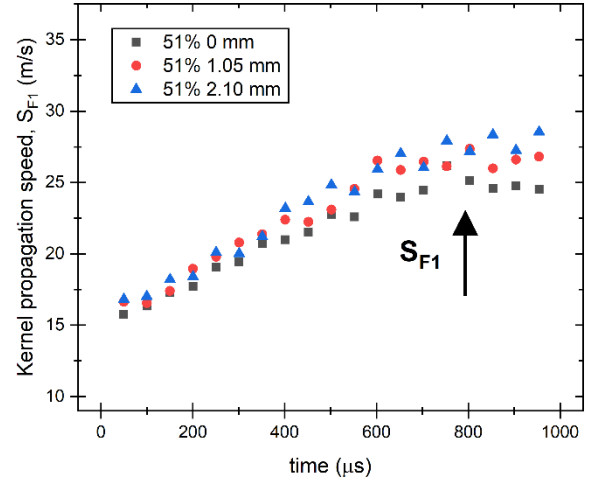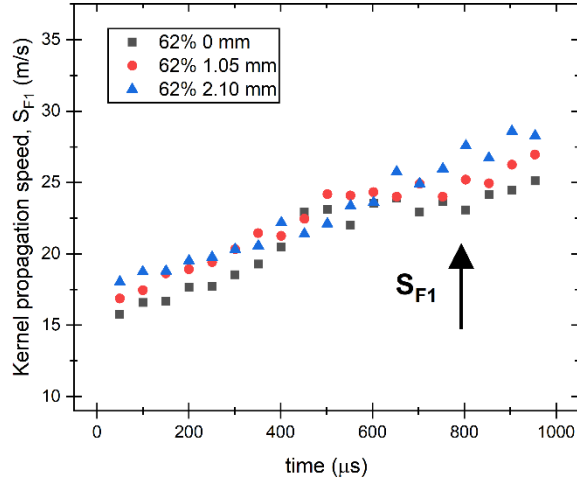
Fig.5-6. Kernel propagation speed toward up, S_{F1} (a) the blockage ratio is 62 %, (b) the blockage ratio is 51 %, (c) the blockage ratio is 45 %, (d) the blockage ratio is 35 %. (e) the ignition location is 2.10 mm from the center, (f) the ignition location is 1.05 mm from the center, and (g) the ignition location is 0 mm from the center.

Fig.5-6 continued

(e)

(f)

(g)
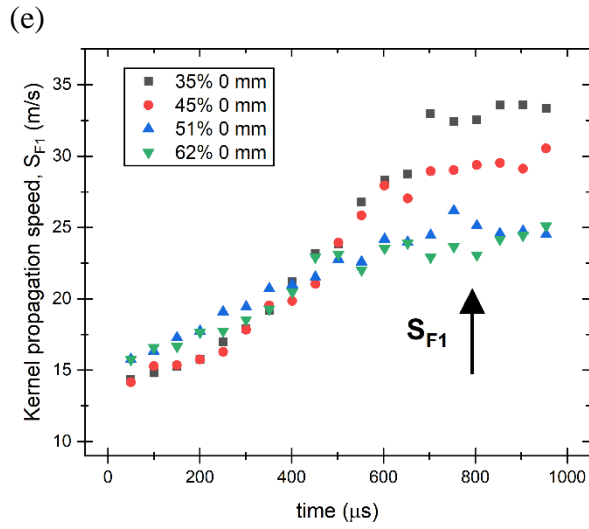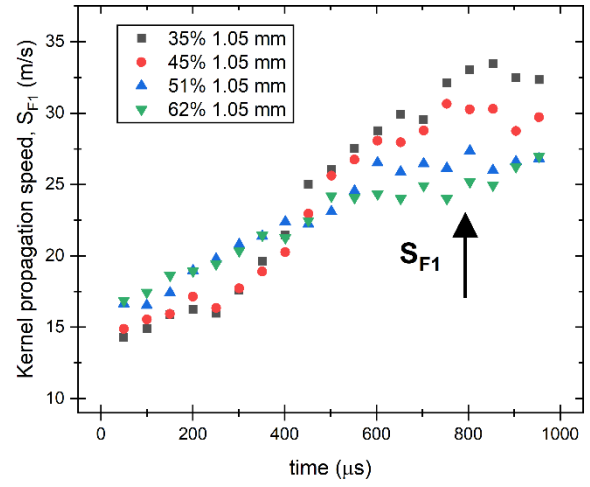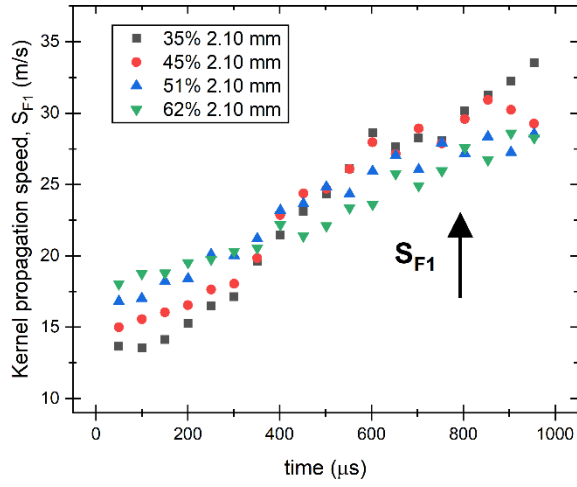
Figures 5-6(a)-(d) illustrate the relation between the kernel propagation speed toward up, S_{F1}, and the turbulence changed by the ignition locations [Table 5-1]. The kernel propagation speed toward up, S_{F1}, at the constant blockage ratios increases with increasing the turbulence [Fig.5-6(a)-(d)]. The high turbulence intensity increases wrinkles in the kernel surface [Figs.5-6,5-7][87-89]. Therefore, the increased kernel surface at the high turbulence leads to an increase in the contact between the kernel and the reactant in the surrounding and the kernel propagation speed, S_{F1} [Figs.5-6(a)-(d),5-7]. However, as the blockage ratio is lower, the tendency, the increase in the kernel propagation speed, S_{F1}, due to the turbulence intensity which changed by the ignition location, is weaker because the difference of the turbulence intensity between the ignition locations is small [Figs.5-6(a)-(d),5-7][Table 5-1]. This observation is similar to the relationship between the kernel growth and the turbulence intensity [11,14,87-96].

The relation between the kernel propagation speed, S_{F1}, and the turbulence intensity shows slightly different results for the constant ignition locations [Figs.5-6(e)-(g)]. The kernel propagation speed, S_{F1}, increases with increasing the turbulence intensity (blockage ratio) for times less than 400 μs and decreases with increasing the turbulence intensity (blockage ratio) for times longer than 400 μs [Figs.5-6(e)-(g)]. The front height of the kernel increaes with the decrease in the turbulence intensity (blockage ratio) and as time elapses [Figs.5-4(a)-(c)]. The front height of the kernel for the low turbulence (blockage ratio) is located in a high position than in the high turbulence intensity [Figs.5-4 (a)-(c)]. The flame speed is fast with an increase in the axial height due to the thermal expansion of hot gases since the more hot gases exist as farther away from the burner exit [111]. The kernel propagation speed, S_{F1}, in the low turbulence intensity (the blockage ratio) is rapidly increased with time due to the thermal expansion by the raised front height of the kernel [Figs.5-6(e)-(g)]. Eventually, the kernel propagation speed, S_{F1}, in the low turbulence intensity becomes faster than in the high turbulence intensity for times longer than 400 μs [Figs.5-6(e)-(g)]. Figure 5-7 shows that the kernel is more wrinkled and close to the burner as the turbulence intensity and the blockage ratio are higher.

Fig.5-7. Schlieren image of the flame kernel (at 225 μs) (a) the blockage ratio is 62 %, and the ignition location is 2.10 mm from the center, (b) the blockage ratio is 62 %, and the ignition location is 1.05 mm from the center, (c) the blockage ratio is 62 %, and the ignition location is 0 mm from the center, (d) the blockage ratio is 51 %, and the ignition location is 2.10 mm from the center, (e) the blockage ratio is 51 %, and the ignition location is 1.05 mm from the center, (f) the blockage ratio is 51 %, and the ignition location is 0 mm from the center, (g) the blockage ratio is 45 %, and the ignition location is 2.10 mm from the center, (h) the blockage ratio is 45 %, and the ignition location is 1.05 mm from the center, (i) the blockage ratio is 45 %, and the ignition location is 0 mm from the center, (j) the blockage ratio is 35 %, and the ignition location is 2.10 mm from the center, (k) the blockage ratio is 35 %, and the ignition location is 1.05 mm from the center, and (l) the blockage ratio is 35 %, and the ignition location is 0 mm from the center.

Fig. 5-7. continued

(a)

(b)

(c)

(d)

(e)

(f)

(g)

(h)

(i)

(j)

(k)
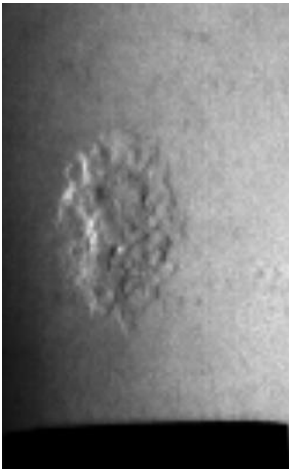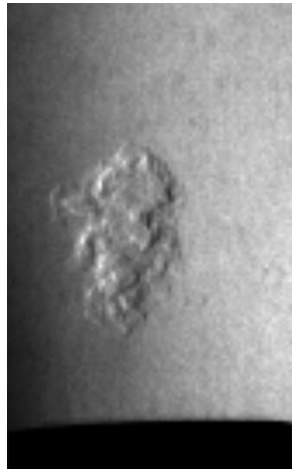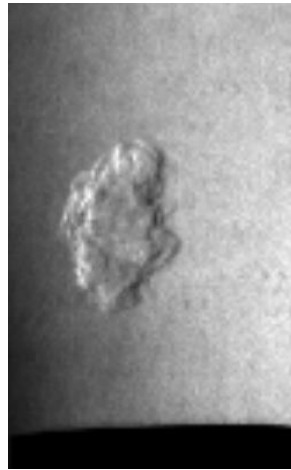
(l)
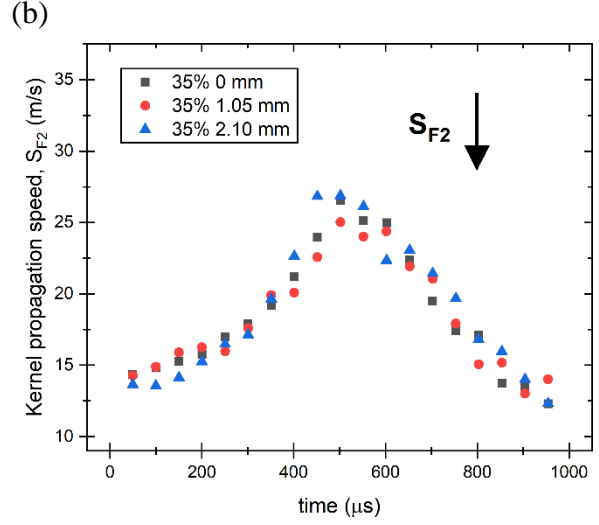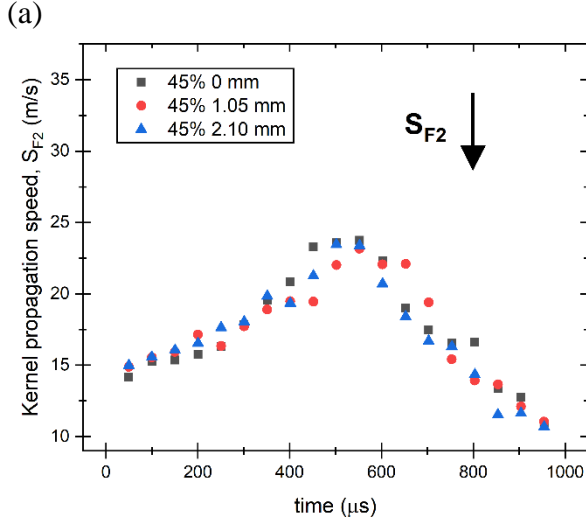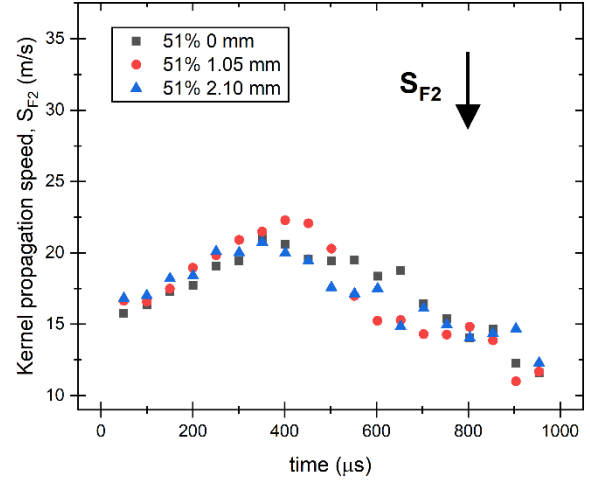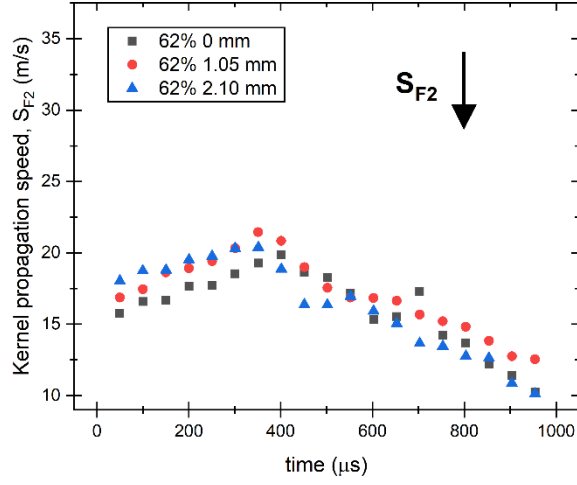
Fig.5-8. Kernel propagation speed toward down, S_{F2}, (a) the blockage ratio is 62 %, (b) the blockage ratio is 51 %, (c) the blockage ratio is 45 %, (d) the blockage ratio is 35 %, (e) the ignition location is 2.10 mm from the center, (f) the ignition location is 1.05 mm from the center, and (g) the ignition location is 0 mm from the center.

Fig.5-8 continued
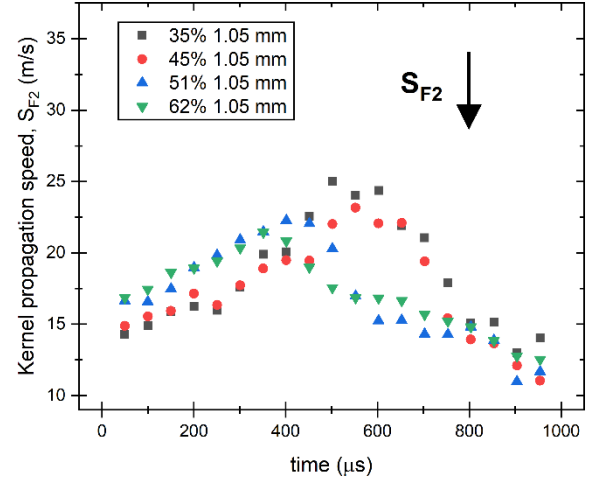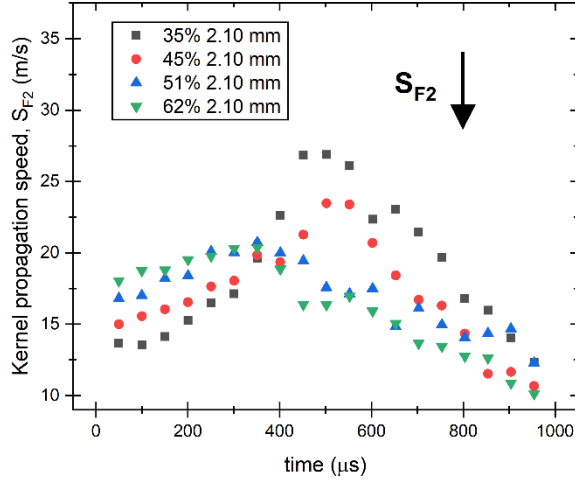
(e)

(f)

(g)
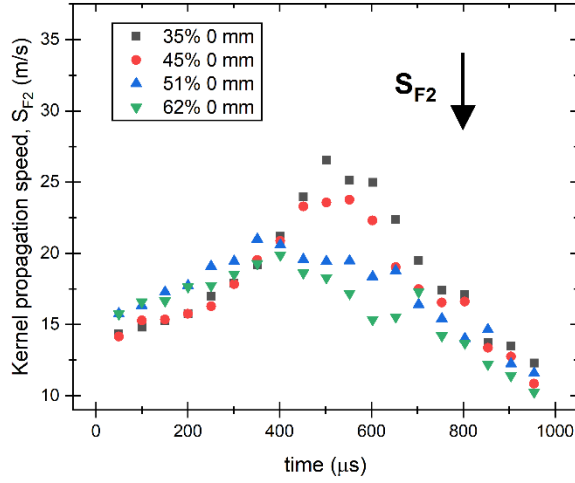
The kernel propagation speed toward down, S_{F2}, increases until specific times and decreases after the specific times [Fig.5-8]. The kernel propagation speed, S_{F2}, increases with increasing the turbulence intensity that grows the wrinkle and the kernel surface for times lower than $400\ \mu s$ [Figs.5-7,5-8]. As the turbulence intensity is higher, the rear height of the kernel is closer to the burner exit [Figs.5-3,5-9]. Therefore, the momentum energy of the jet flow that influences the kernel is stronger as the rear height of the kernel is lower. As a result, the kernel propagation speed, S_{F2}, decreases with the turbulence intensity for times longer than $400\ \mu s$ since the lowering of the kernel growth by the momentum energy of the flow becomes stronger [Figs.5-8,5-9]. Figure 5-9 illustrates the jet flow negatively affects the kernel development as the kernel is closer to the burner. This obervation supports the experimental results reported by Mansour et al.

that the kernel propagation speed decreases with time after the specific time [94-96]. The tendency between the kernel propagation speed, S_{F2}, and the turbulence intensity, measured in the ignition location, is weaker with time for the fixed blockage ratios [Figs.5-8(a)-(c)]. The reason is, as time elapses, the kernel size grows, thus the kernel receives an effect from the turbulence intensity of the entire flow field not the turbulence intensity of the local region.

The enhancement of 430 % in the turbulence intensity for the ignition location of 2.1 mm from the burner axis increases 32 % of the kernel propagation speed at 50 μs after the laser pulse. The increment of 2380 % in the turbulence intensity for the blockage ratio of 62 % increases the 14 % of the kernel propagation speed at 50 μs after the laser pulse. The enhancement of the turbulence improves the kernel propagation speed. The change of the turbulence by the blockage ratio is more critical on the kernel propagation speed.

(a)   (b)   (c)   (d)   (e)

(f)   (g)   (h)   (i)   (j)
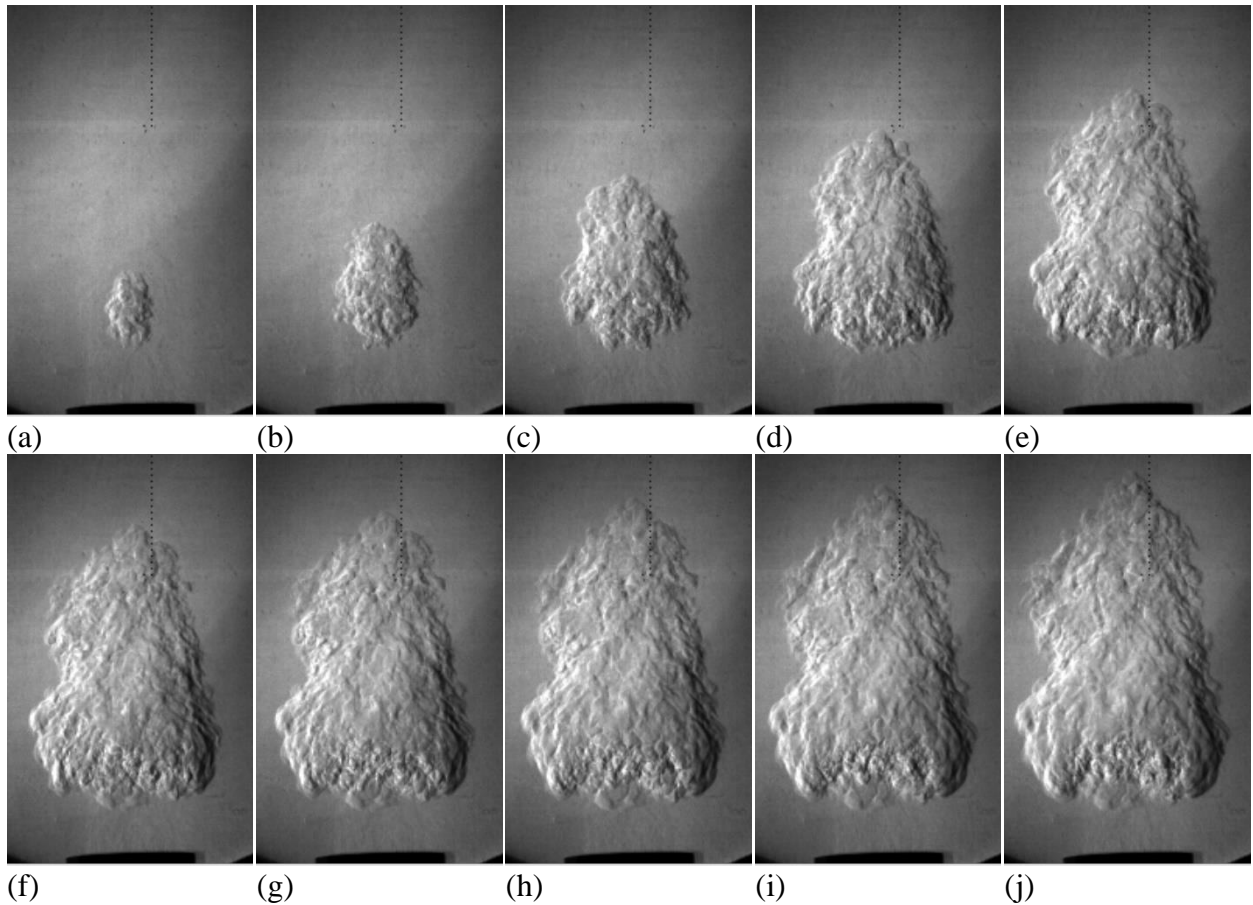
Fig.5-9. Kernel development with time when the blockage ratio is 62 %, and the ignition location is 0 mm from the center (a) 225 μs, (b) 375 μs (c) 525 μs, (d) 675 μs, (e) 825 μs, (f) 875 μs, (g) 925 μs, (h) 975 μs, (i) 1025 μs, (j) 1075 μs.
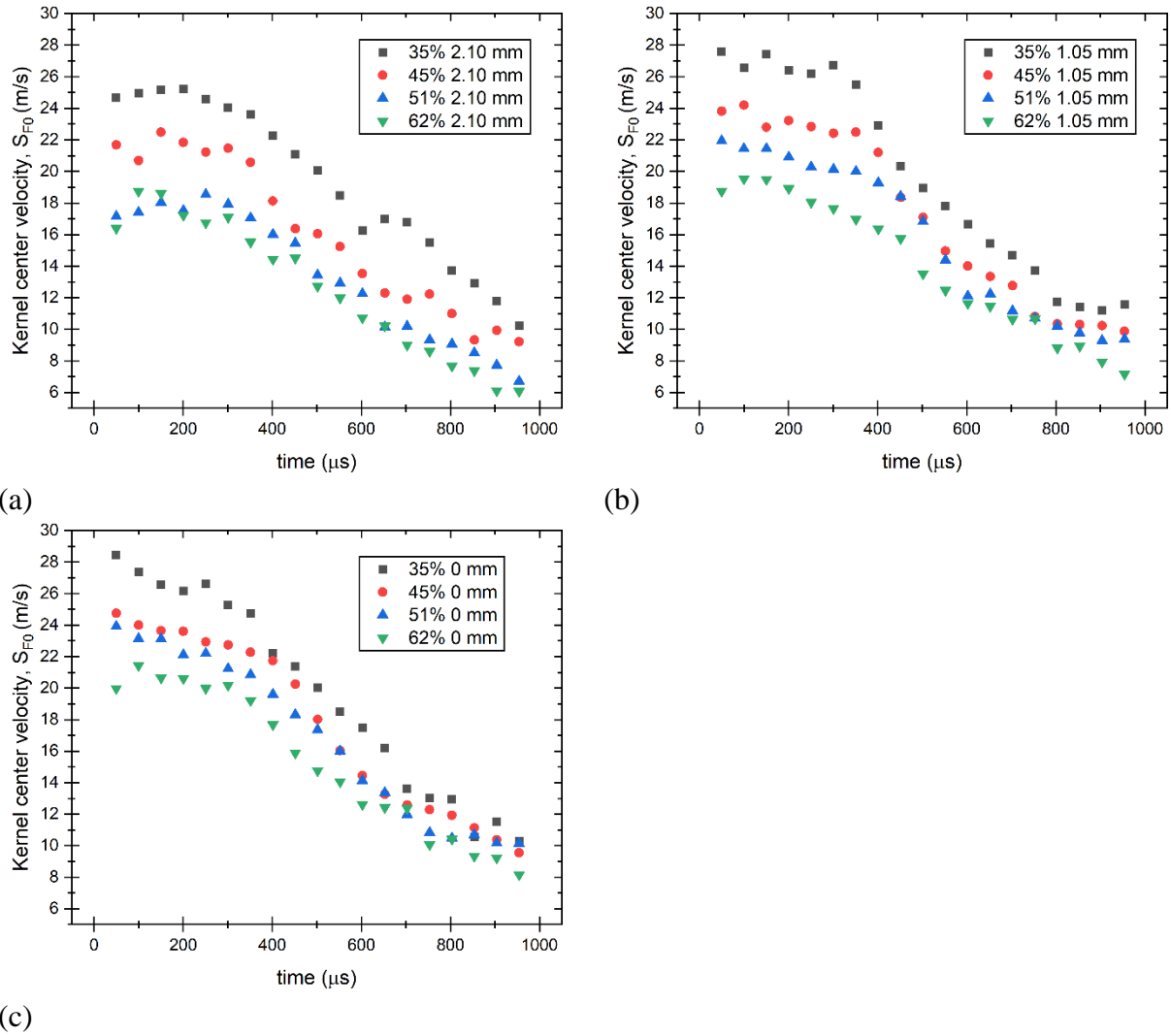
Fig.5-10. Kernel center velocity (a) the ignition location is 2.10 mm from the center, (b) the ignition location is 1.05 mm from the center, and (c) the ignition location is 0 mm from the center.

Figure 5-10 illustrates the kernel center velocity in the y-direction for the different flow fields. The kernel center velocity in the y-direction decreases with an increase in the turbulence intensity [Fig.5-10]. This is because the high turbulence negatively affects the kernel movement and reduces the kernel center velocity. The kernel center velocity decreases with time [Fig.5-10]. The momentum energy of the flow causes the kernel movement. The kernel size develops as time elapses, but the momentum energy of the flow is almost identical with time at a consistent height. Therefore, the kernel movement by the momentum energy of the flow reduces with time. The

enhancement of 430 % in the turbulence intensity for the ignition location of 2.1 mm from the burner axis decreases 33 % of the kernel center velocity at 50 μs after the laser pulse.

5.2.2 Flame Kernel Propagation Speed in x-direction

(a)

(b)

(c)

(d)
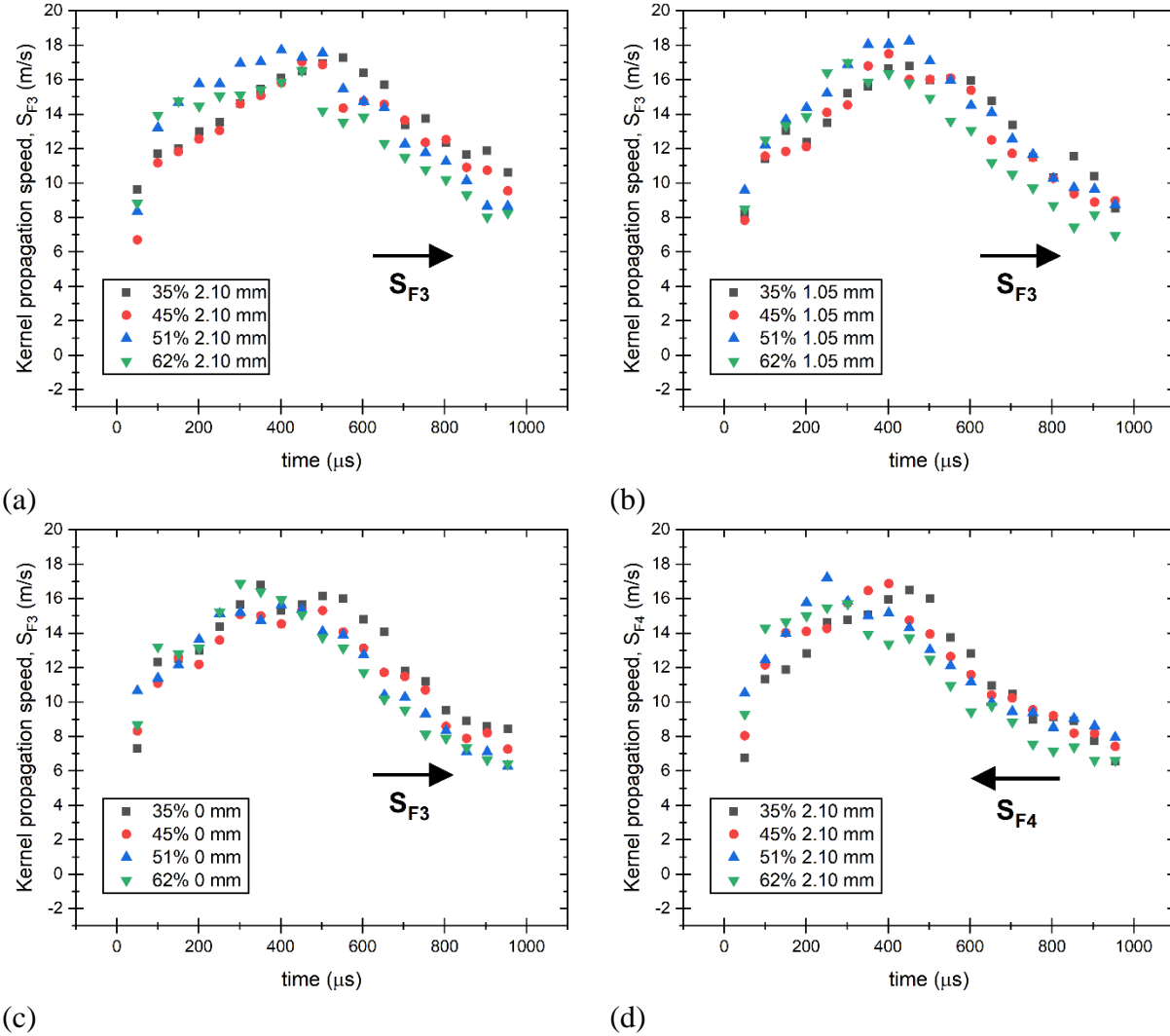
Fig.5-11. The speed of the flame kernel propagation toward the right direction, S_{F3}, (a) the ignition location is 2.10 mm from the center of the burner, (b) the ignition location is 1.05 mm from the center of the burner, and (c) the ignition location is 0 mm from the center of the burner, the speed of the flame kernel propagation toward the left direction, S_{F4}, (d) the ignition location is 2.10 mm from the center of the burner, (e) the ignition location is 1.05 mm from the center of the burner, and (f) the ignition location is 0 mm from the center of the burner.

Fig.5-11 continued
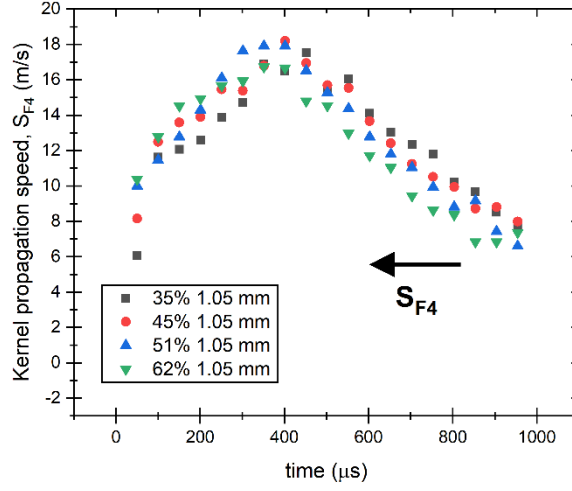
(e)

(f)
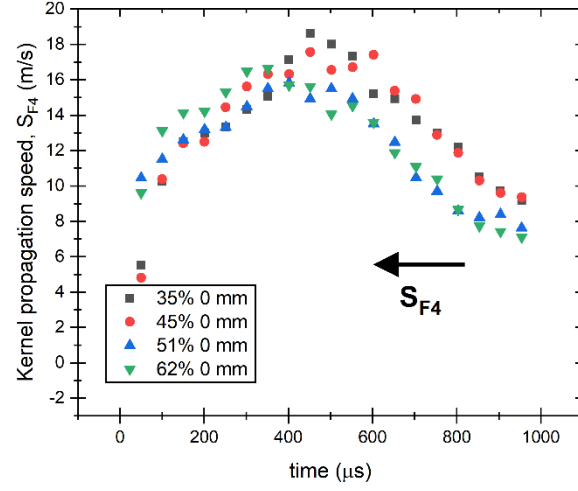
The kernel propagation speeds, S_{F3}, and S_{F4}, in the x-direction increase until the maximum values and decreases after the maximum values [Fig.5-11]. Farther away from the burner axis in the x-direction, the reactant becomes the leaner. In other words, when further away from the center of the burner in the x-direction, the kernel in the right edge and the left edge cannot meet the sufficient reactant. Thus, the kernel propagation speeds, S_{F3}, and S_{F4}, reduces after the maximum values due to decreasing the reactant in the edges of the right and the left [Fig.5-11]. The blockage ratio is higher, the kernel propagation speeds, S_{F3}, and S_{F4}, rapidly reach the maximum value [Fig.5-11]. The first reason is the kernel propagation speeds, S_{F3}, and S_{F4}, increase since the kernel surface grows by the high turbulence intensity of the higher blockage ratio. The second reason is the reactant is widely distributed in the radial direction as the more low blockage ratio due to the nozzle diameter of the perforated plate. Therefore, a kernel in the high blockage ratio rapidly reaches regions where insufficient reactants exist. After the maximum values, the kernel propagation speeds, S_{F3}, and S_{F4}, reduce with an increase in the blockage ratio [Fig.5-11]. The distribution of the reactant in the radial direction increases with decreasing the blockage ratio due to the nozzle diameter of the perforated plate. Over time, the right edge and the left edge of the kernel are farther away from the center of the burner [Fig.5-9]. Thus, as time elapses, the edges of the kernel in the high blockage ratio than in the low blockage ratio meet a relatively lean reactant and are hard to react with the reactant sufficiently. As a result, after the maximum values, the kernel propagation speeds, S_{F3}, and S_{F4}, decrease with increasing the blockage ratio due to the

distribution of the reactant [Fig.5-11]. The speed of the kernel propagation in the right, S_{F3}, and the speed of the kernel propagation in the left, S_{F4}, does not show a huge difference [Fig.5-11]. This is because the kernel almost evenly grows in the radial direction [Fig.5-9].

(a)

(b)

(c)

(d)
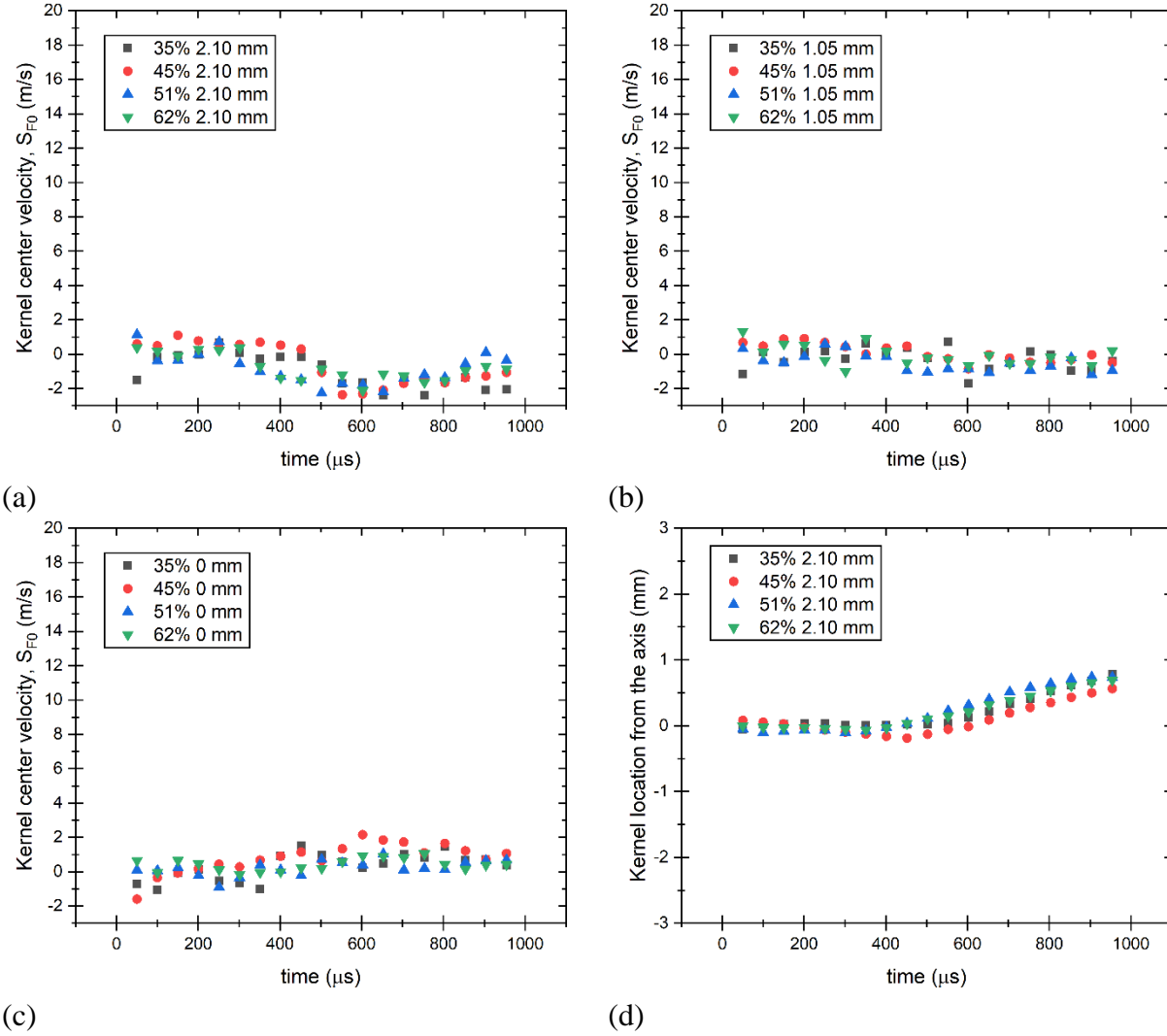
Fig.5-12. The speed of the flame kernel movement in the x-direction (a) the ignition location is 2.10 mm from the center of the burner, (b) the ignition location is 1.05 mm from the center of the burner, and (c) the ignition location is 0 mm from the center of the burner, the location of the flame kernel center from the center of the burner in the x-direction (d) the ignition location is 2.10 mm from the center of the burner, (e) the ignition location is 1.05 mm from the center of the burner, and (f) the ignition location is 0 mm from the center of the burner.

Fig.5-12 continued

(e)

(f)
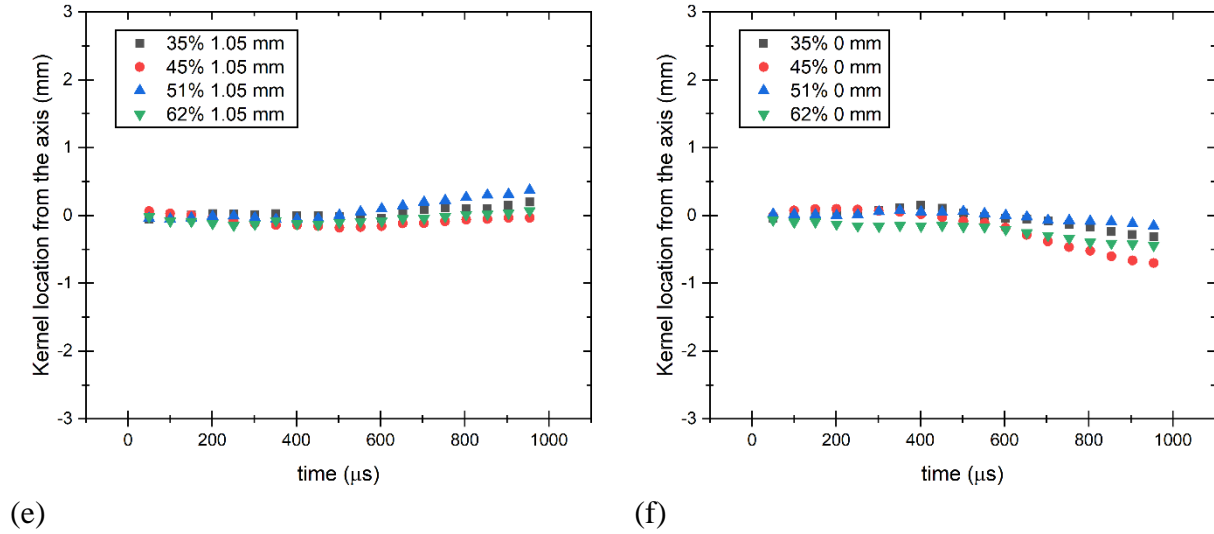
The kernel center velocity in the x-direction is slow [Figs.5-12(a)-(c)]. The kernel expands forward in both directions, the right, and the left. Thus, the speed of the kernel movement in the x-direction does not show a huge difference for both directions [Figs.5-12(a)-(c)]. Similarly, the center of the kernel in the x-direction only slightly moves with time [Figs.5-12(d)-(f)].

5.2.3   Effect of Bulk Velocity on the Flame Kernel Development

The speeds of the kernel propagation, S_{F1} and S_{F2}, increase as the bulk velocity increases [Fig.5-13]. The effect of the bulk velocity on the kernel propagation speeds is in good agreement with ignition experiments studied by Mansour et al. [94-96]. An increase of the bulk velocity increases a supply of the reactant into the kernel. Thus, the increased supply of the reactant may contribute to the increase in the speed of the kernel propagation.

The kernel center velocity in the y-direction increases with increasing the bulk velocity [Fig.5-14]. The reason is the momentum energy of the flow increases with the bulk velocity and pushes away the kernel from the burner exit. Therefore, as the bulk velocity is slower, the kernel displacement is slow [Fig.5-14]. An increase in the bulk velocity by 13 % increases the kernel propagation speed by 7 % and the kernel center velocity by 16 % for the time interval 0-1000 μs after the laser pulse. The increase in the bulk velocity negatively affects ignition since the kernel is easily farther away from the burner instead of attaching into the burner lip. The bulk velocity

111

also increases the kernel propagation speed. However, the effect of the increment of the kernel propagation speed by the bulk velocity is weak than the kernel center velocity.

(a)

(b)

(c)

(d)
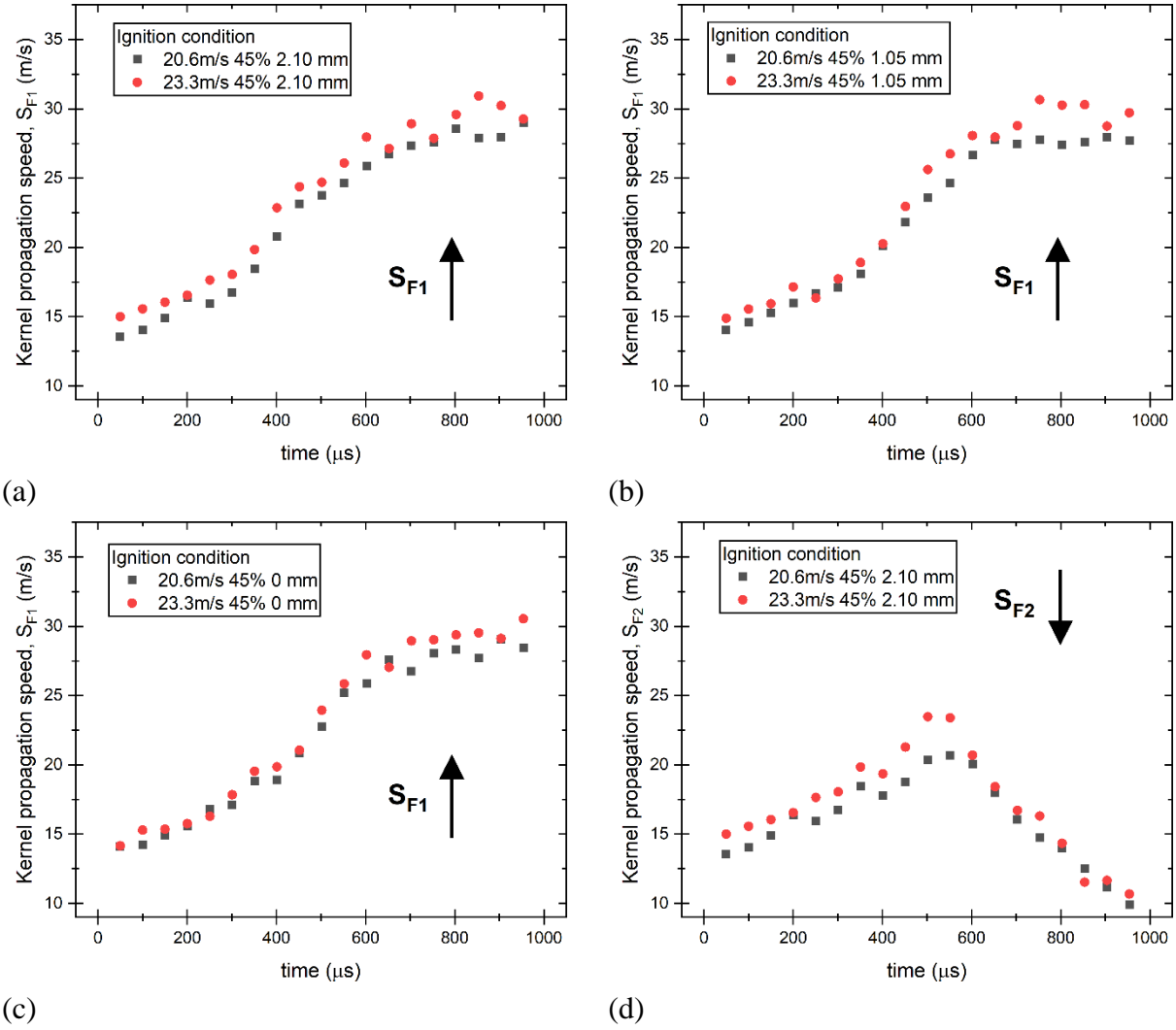
Fig.5-13. The speed of the flame kernel toward up, S_{F1}, (a) the ignition location is 2.10 mm from the center of the burner, (b) the ignition location is 1.05 mm from the center of the burner, and (c) the ignition location is 0 mm from the center of the burner, the speed of the flame kernel toward down, S_{F2}, (d) the ignition location is 2.10 mm from the center of the burner, (e) the ignition location is 1.05 mm from the center of the burner, and (f) the ignition location is 0 mm from the center of the burner.

Fig.5-13 continued

(e)

(f)

(a)

(b)
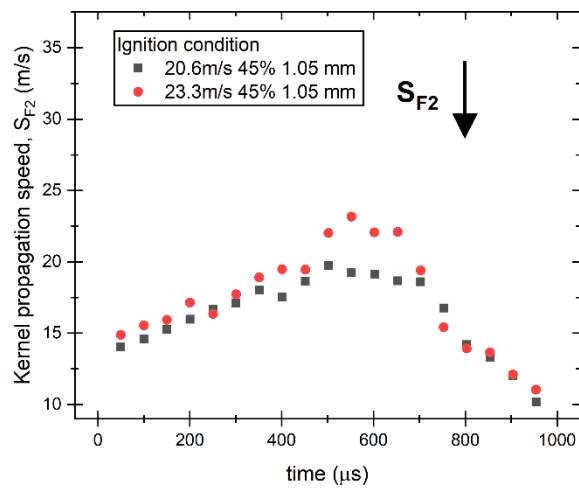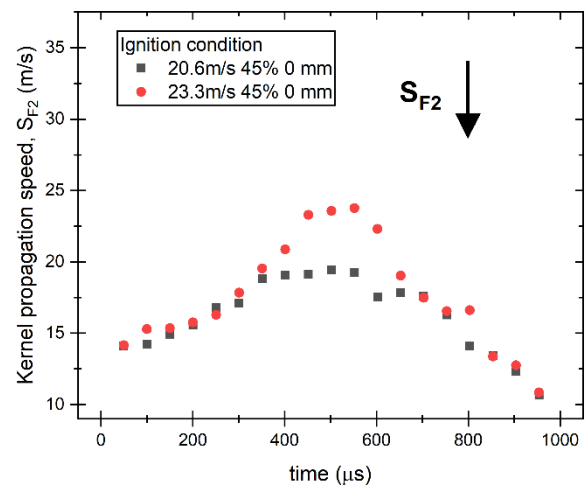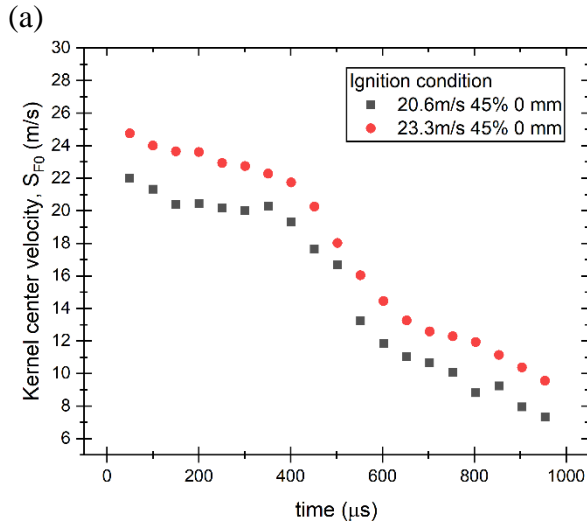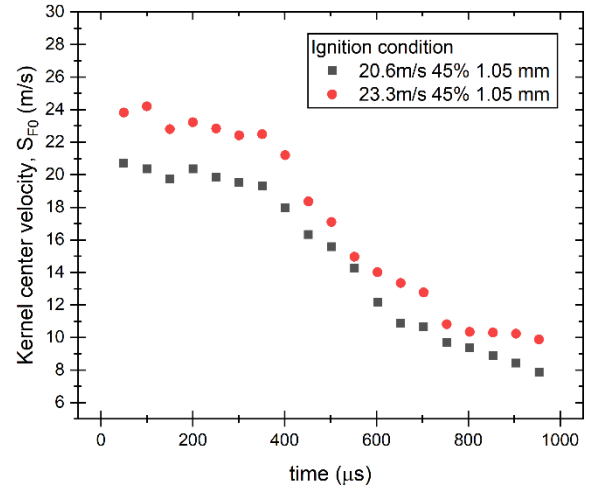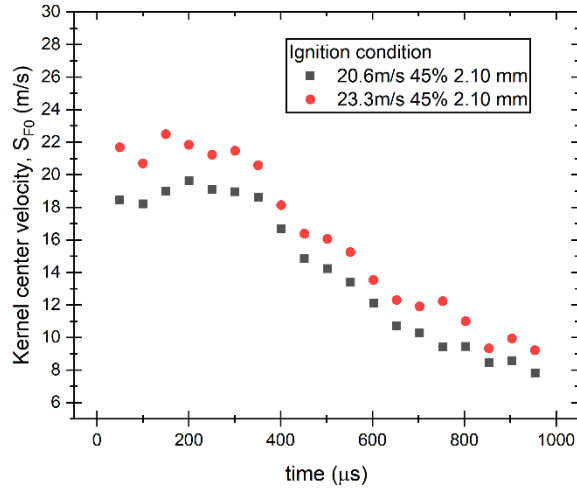
(c)

Fig.5-14. The kernel center velocity in the y-direction (a) the ignition location is 2.10 mm from the center of the burner, (b) the ignition location is 1.05 mm from the center of the burner, and (c) the ignition location is 0 mm from the center of the burner.

(a)

(b)

(c)

(d)
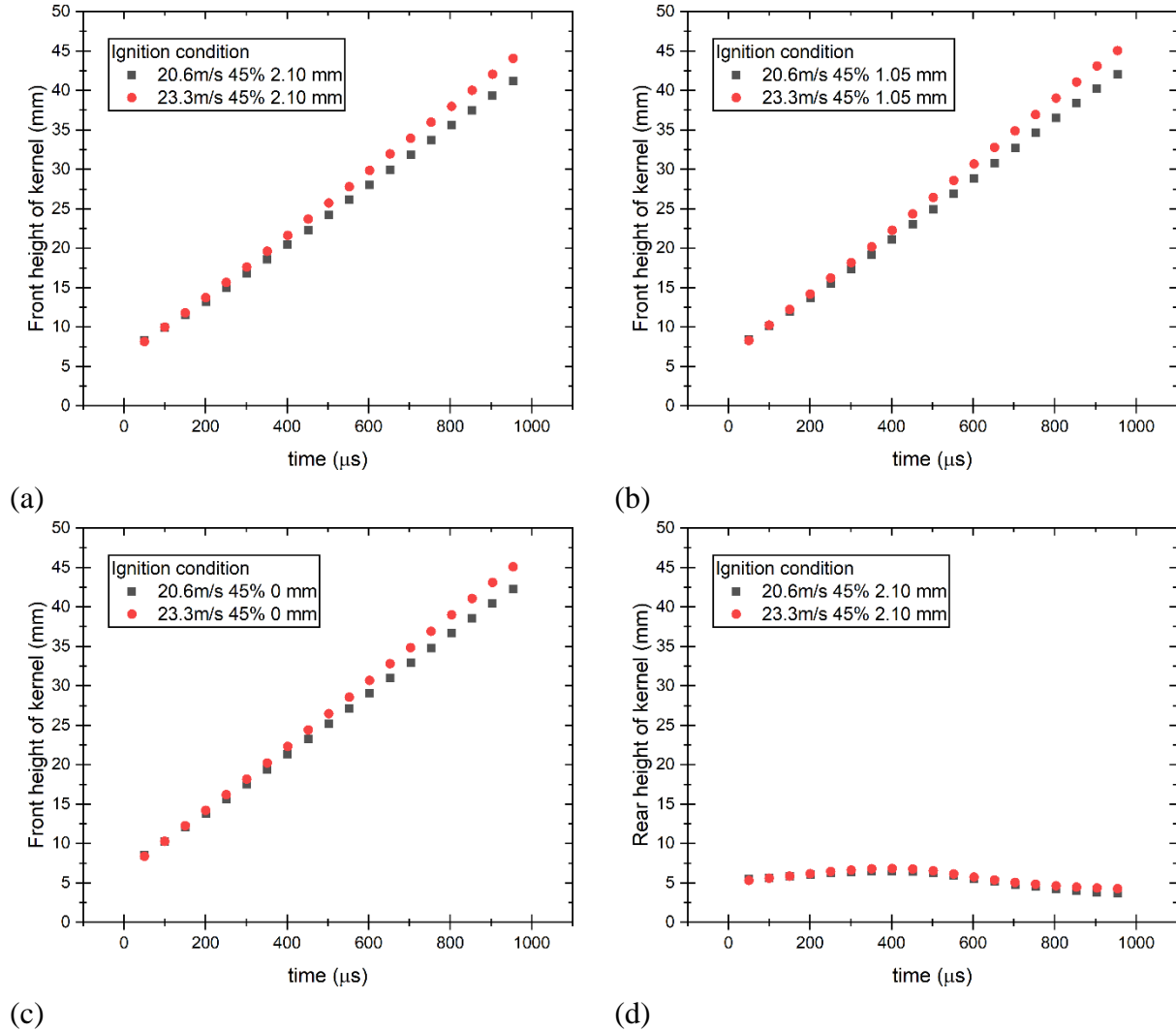
Fig.5-15 The front height of the flame kernel (a) the ignition location is 2.10 mm from the center of the burner, (b) the ignition location is 1.05 mm from the center of the burner, and (c) the ignition location is 0 mm from the center of the burner, the rear height of the flame kernel (d) the ignition location is 2.10 mm from the center of the burner, (e) the ignition location is 1.05 mm from the center of the burner, and (f) the ignition location is 0 mm from the center of the burner.

Fig.5-15 continued
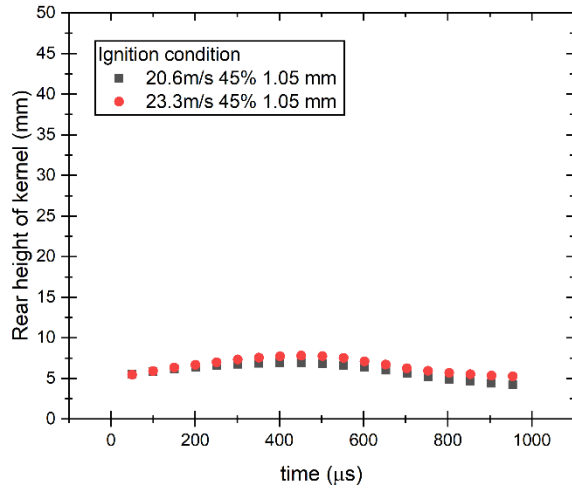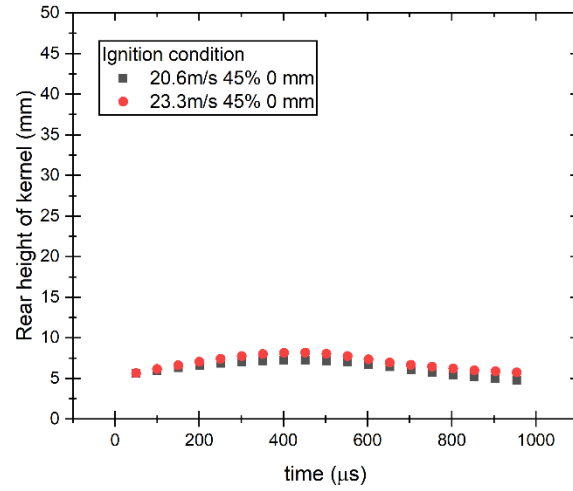
(e)   (f)

The rear height of the flame kernel and the front height of the flame kernel increase with the bulk velocity [Fig.5-15]. The momentum energy of the jet increases with increasing the bulk velocity. Thus, as the bulk velocity is faster, the momentum energy of the flow farther pushes the flame kernel from the burner exit [Fig.5-15].

5.2.4 Relationship between Minimum Ignition Energy, Turbulence Intensity, and Flame Kernel Propagation Speed
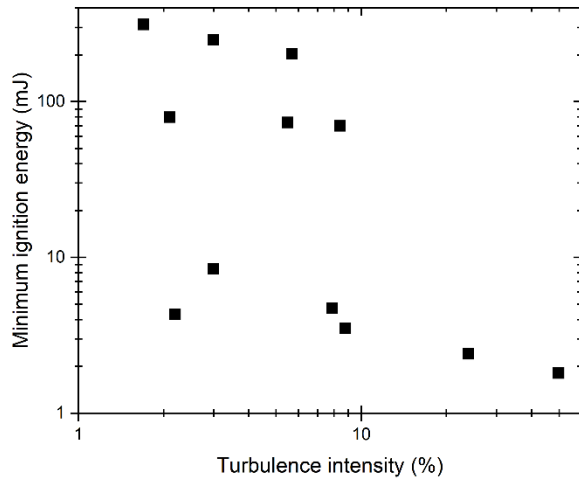
(a)
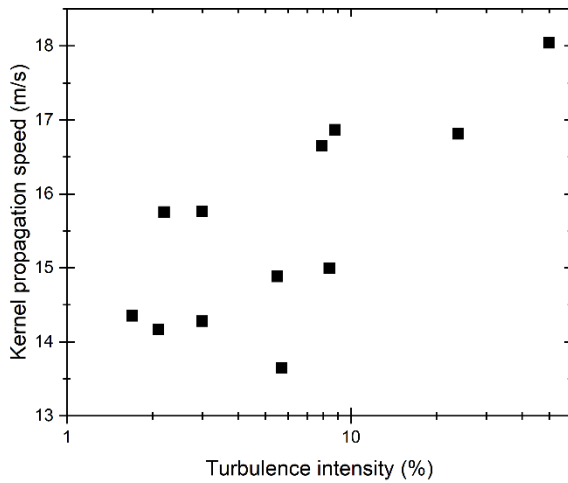
(b)
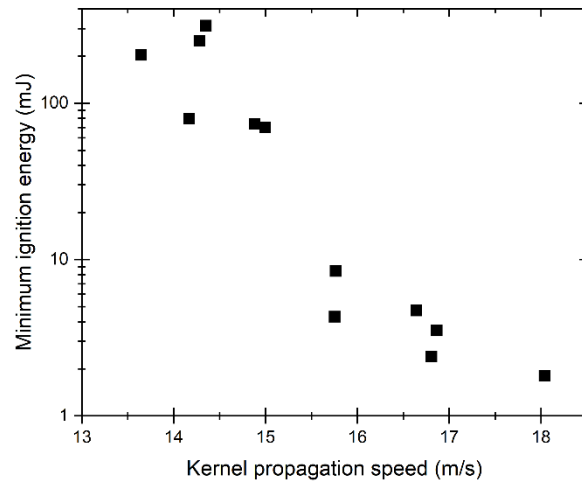
(c)

Fig.5-16. Relationship between the minimum ignition energy, the turbulence intensity, and the flame kernel development in the y-direction when the time elapsed after laser pulse is 50 μs (a) The minimum ignition energy versus the turbulence intensity, (b) the flame kernel propagation speed in the y-direction versus the turbulence intensity, (c) the minimum ignition energy versus the flame kernel propagation speed in the y-direction, (d) kerenl center velocity in the y-direction versus the turbulence intensity, and (e) the minimum ignition energy versus the kernel center velocity in the y-direction.

Fig.5-16 continued

(d)

(e)
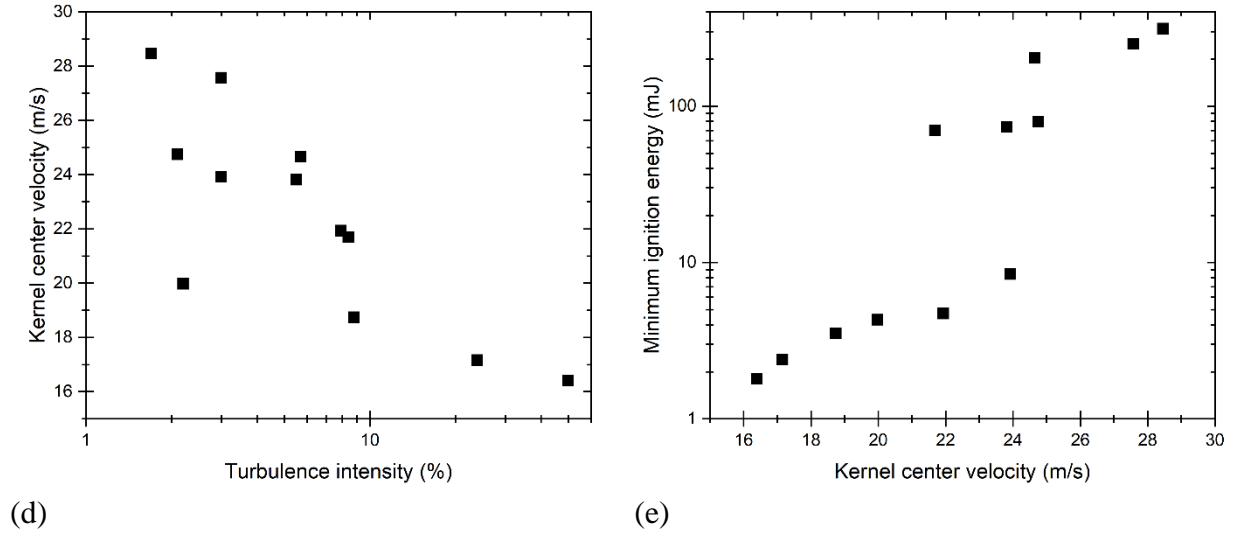
In the previous study (Charpter 4) that performed the ignition test at the same experimental conditions with the present work, the minimum ignition energy (MIE) decreases as the turbulence intensity increases [Table 5-2]. The measured MIE is utilized to compare the MIE, the turbulence intensity, and the kernel propagation speed. Figures 5-16 (b)(c) and 5-17 (a) show the relationship between the MIE, the turbulence intensity, and the kernel propagation speed in the y-direction at 50 μs after the laser pulse. S_{F1} is almost identical with S_{F2} at 50 μs. Hence only one kernel propagation speed is illustrated in Figs.5-16(b)(c),17(a). The kernel propagation speed in the y-direction is faster with the increase in the turbulence intensity since the wrinkled on the kernel affecting the kernel surface area increases [Figs.5-16(b)(c),17(a)]. The MIE decreases as the kernel propagation speed in the y-direction is faster [Figs.5-16(b)(c),17(a)]. The kernel generated at the high turbulence intensity leading to the fast kernel propagation speed can rapidly become a sustainable flame by anchoring into the burner lip even low ignition energy before blowing off. In contrast, the kernel generated at the low turbulence intensity needs higher ignition energy than the kernel at the high turbulence intensity to increase the kernel propagation for becoming a sustainable flame before blowing off. The reason is if the ignition energy at the low turbulence intensity is the same as the high turbulence intensity condition, the kernel may blow off due to low kernel propagation speed. Another interesting factor is the relationship between the MIE, turbulence intensity, and the kernel center velocity in the y-direction [Figs.5-16(d)(e),17(b)]. Increasing the turbulence intensity reduces the kernel center velocity in the y-direction since the

118

high turbulence intensity negatively affects the kernel movement [Figs.5-16(d)(e),17(b)]. The MIE decreases with decreasing the kernel center velocity in the y-direction [Figs.5-16(d)(e),17(b)]. As the kernel center velocity in the y-direction is slower, the kernel is closer to the burner exit and thus can rapidly anchor into the burner exit by the kernel development. Therefore, the MIE decreases as the turbulence intensity increases when the ignition conditions, including the bulk velocity, ignition height, are constant because the high turbulence intensity increases the kernel propagation speed and decreases the kernel center velocity [Figs.5-16,17][Table 5-2].

Table 5-2. Minimum ignition energy in the ignition experiments [Chapter 4.2].

Blockage ratio (%)	Ignition location from the center (mm)	Turbulence intensity at the ignition location (%)	Minimum ignition energy (mJ)
62	0	2.2	4.3
62	1.05	8.8	3.5
62	2.10	49.9	1.8
51	0	3.0	8.4
51	1.05	7.9	4.7
51	2.10	23.9	2.4
45	0	2.1	79.3
45	1.05	5.5	73.5
45	2.10	8.4	69.8
35	0	1.7	313
35	1.05	3	249.2
35	2.10	5.7	202.8
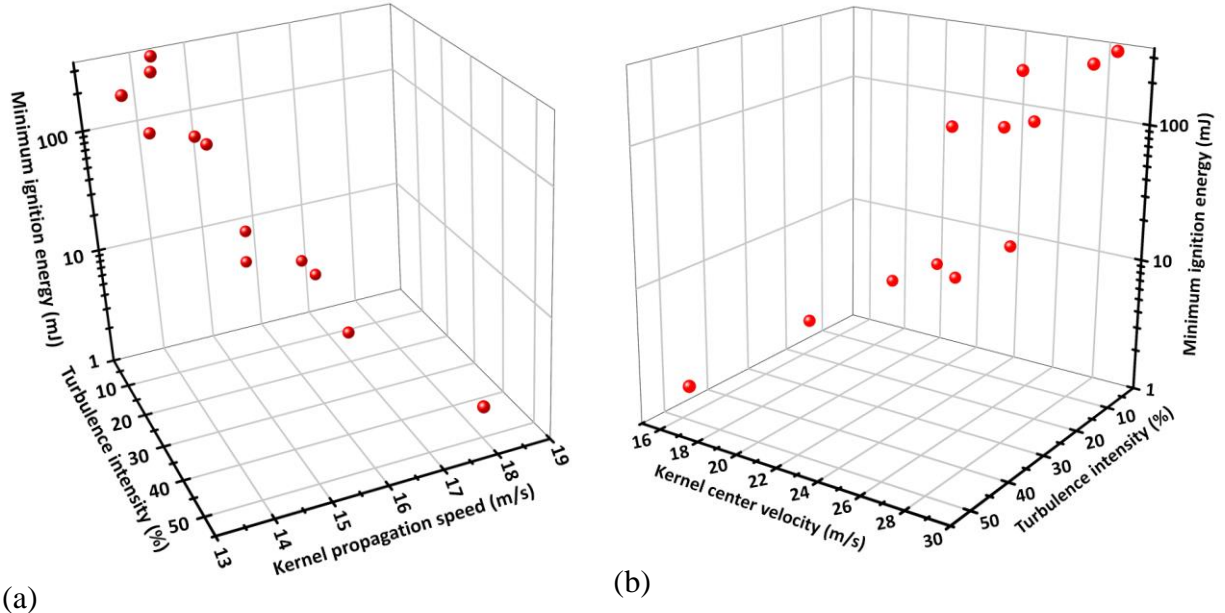
Fig.5-17. (a) Relationship between the minimum ignition energy, the turbulence intensity, and the flame kernel propagation speed in the y-direction at the time delay of 50 μs, and (b) relationship between the minimum ignition energy, the turbulence intensity, and the kernel center velocity in the y-direction at the time delay of 50 μs.
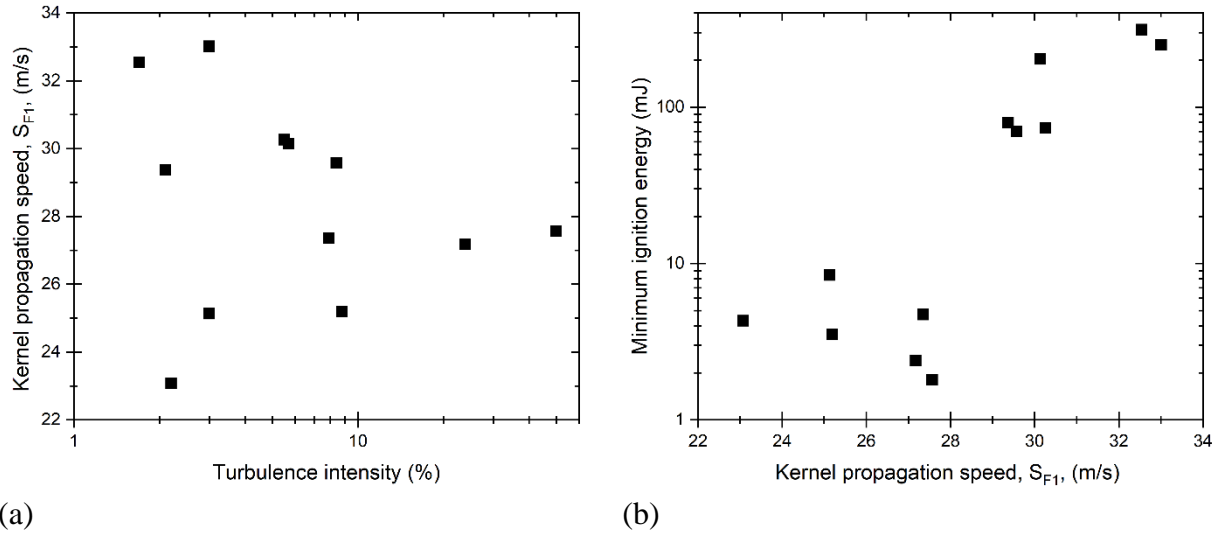
Fig.5-18. Relationship between the minimum ignition energy, the turbulence intensity, and the flame kernel development in the y-direction when the time elapsed after the laser pulse is 800 μs, (a) the flame kernel propagation speed in the y-direction, S_{F1}, versus the turbulence intensity, (b) the minimum ignition energy versus the flame kernel propagation speed in the y-direction, S_{F1}, (c) the flame kernel propagation speed in the y-direction, S_{F2}, versus the turbulence intensity, (d) the minimum ignition energy versus the flame kernel propagation speed in the y-direction, S_{F2}, (e) flame kernel center velocity in the y-direction versus the turbulence intensity, and (f) the minimum ignition energy versus the flame kernel center velocity in the y-direction.

Fig.5-18 continued

(c)

(d)

(e)

(f)
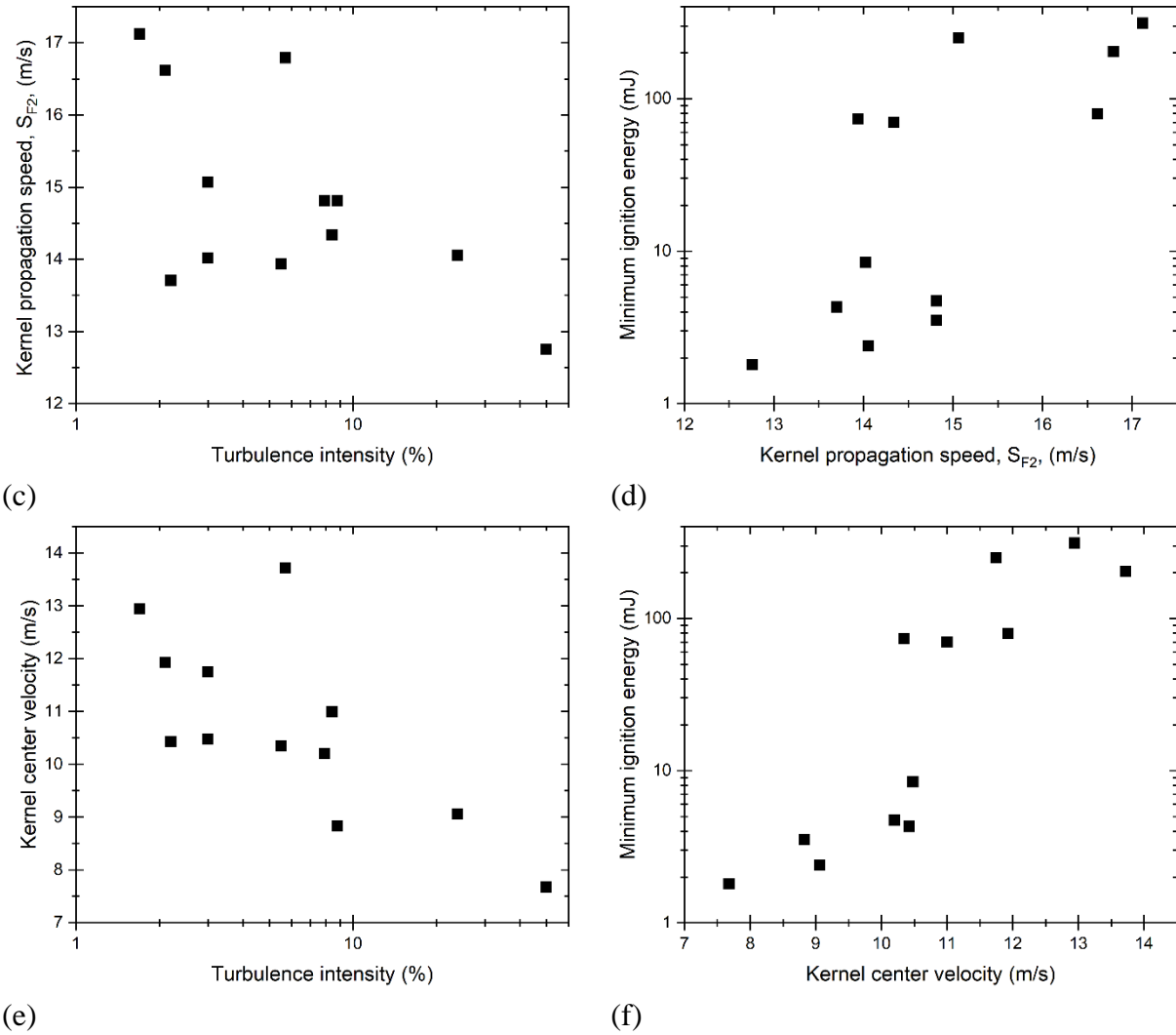
The kernel at the high turbulence intensity condition has the high kernel propagation speed, and the low kernel center velocity during the early time after the laser pulse [Figs.5-16,17]. Therefore, if ignition energy is constant, the kernel at the high turbulence intensity condition can fastly attach to the burner exit and easily develop into a flame than the other kernel at the low turbulence intensity condition. In other words, the minimum ignition energy will be decreased by increasing the turbulence intensity. When we performed the ignition experiments at the different turbulent intensities, the minimum ignition energy decreased as the turbulence intensity increases [Table 5-2]. The experimental result is agreed with the recent ignition studies that reported that turbulence facilitates ignition [97-102].

Figure 5-18 shows the relation between the MIE, the turbulence intensity, and the kernel propagation speeds in the y-direction at 800 μs after the laser pulse. The relationship between the turbulence intensity and the kernel propagation speeds, S_{F1} and S_{F2}, is not clear. The kernel size increases with time. When the time is 800 μs, the kernel is affected by the turbulence intensity of the entire flow field not the local turbulence intensity of the ignition locations. Thus, the kernel propagation speeds, S_{F1} and S_{F2}, at 800 μs do not largely receive the influence of the turbulence intensity, measured in the ignition locations. Increasing the front speed of the kernel propagation, S_{F1}, increases the MIE [Fig.5-18(b)]. For times longer than 400 μs, the kernel propagation speed, S_{F1}, rises as the turbulence intensity (the blockage ratio) decreases. As the turbulence intensity (the blockage ratio) is lower, the front height of the kernel is farther away from the burner exit. Therefore, the kernel propagation speed, S_{F1}, is faster due to the thermal expansion of the hot gas [111]. The MIE increases as the rear speed of the kernel propagation, S_{F2}, increases [Fig.5-18(d)]. The rear height of the kernel reduces with increasing the turbulence intensity because the high turbulence intensity negatively influences the kernel movement. As the turbulence intensity is higher, the rear height of the kernel is closer to the burner exit. Therefore, the kernel propagation speed, S_{F2}, is slower since the kernel growth is suppressed by the momentum energy of the flow nearby the burner exit. As time elapses, the influence of the local turbulence intensity measured in the ignition locations on the kernel speeds, S_{F1} and S_{F2}, becomes weaker since the kernel grows. Thus, it is hard to define the relationship between the MIE, the turbulence intensity, and the kernel propagation speeds at 800 μs after the laser pulse.

Figure 5-19 illustrates the relationship between the MIE and the kernel propagation speeds, S_{F3}, and S_{F4} in the x-direction. It is hard to define a characteristic of the tendency between the MIE and the kernel propagation speeds, S_{F3}, and S_{F4} in the x-direction [Fig.5-19]. It means the kernel propagation speed, S_{F3}, and S_{F4} in the x-direction does not affect the MIE.
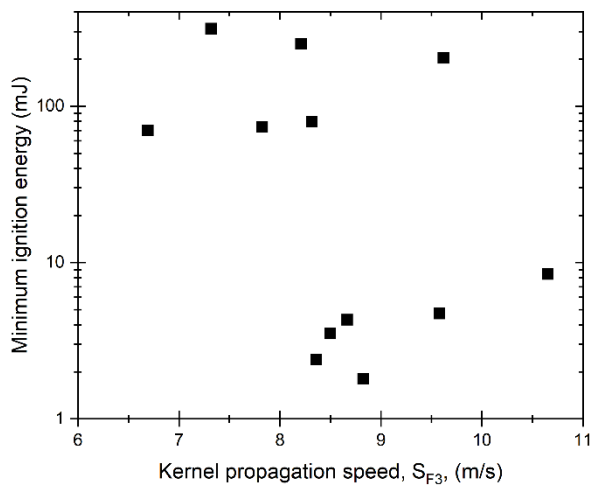
(a)
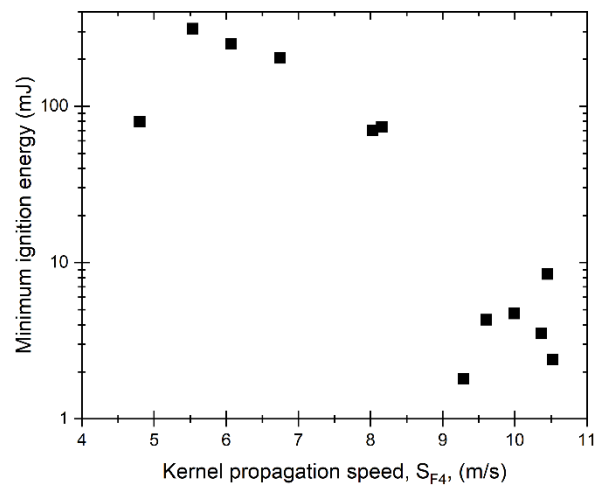
(b)

Fig.5-19. (a) The minimum ignition energy versus the flame kernel propagation speed in the x-direction, S_{F3}, and (b) the minimum ignition energy versus the flame kernel propagation speed in the x-direction, S_{F4}.

6. LASER PLASMA EXPANSION AND FLAME KERNEL TEMPERATURE DISTRIBUTION

6.1 Experimental Conditions

Ignition experiments were conducted to study the plasma emission generated by the laser-induced spark. The ignition system was consisted of the double-pulsed, frequency-doubled, Q-switched Nd:YAG laser (Spectra-Physics Quanta-Ray GCR200 PIV400-10, 8 ns), the data acquisition board (NI USB – 6343), the power meter (Newport 1916-C) and an optical system [Fig. 6-1]. The laser operated at 532 nm. The maximum energy of the laser was 400 mJ per pulse at 10 Hz. Six laser energies were used to study the effect of laser incident energy on plasma emission (spark emission) [Table 6-1]. In this experiment, forced flow or reactant was not used to avoid the influence of flow and reactants [Fig. 6-1]. The ignition experiment ran at atmospheric pressure and room temperature. The laser-induced spark ignition system used a spherical lens, $f = 50$ mm, to focus the spark. The laser energy difference, ΔE, is defined as the difference between the incident energy (E_{in}) and the transmitted energy (E_{tr}) as $\Delta E = E_{in} - E_{tr}$ [3,4,74]. The Labview program generated digital counts through the data acquisition board to control the laser.
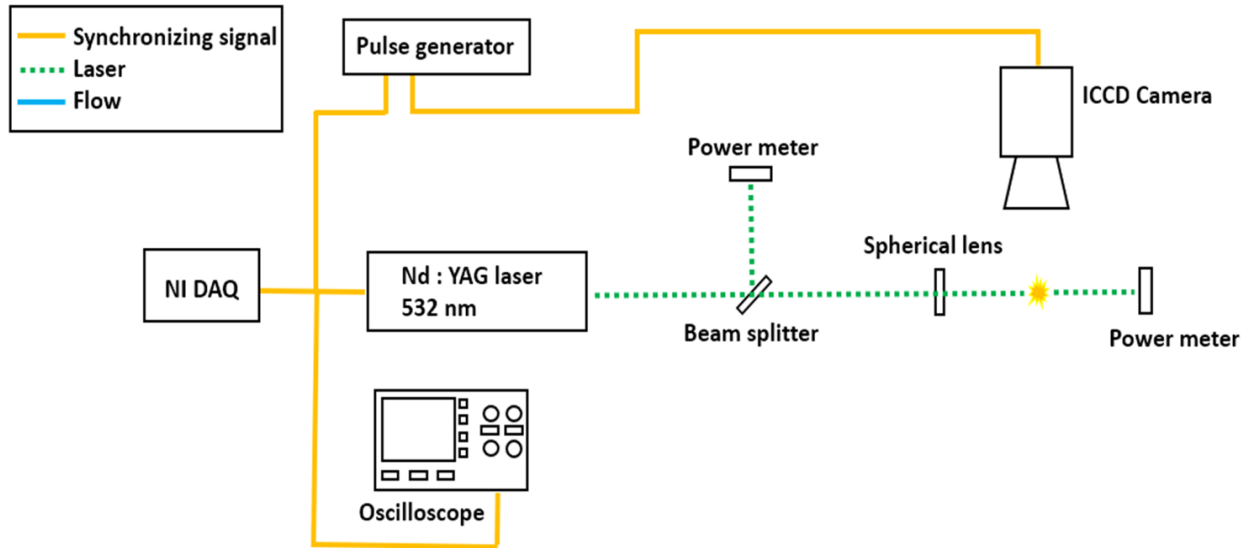
Fig. 6-1. The schematic of the experimental device for the plasma emission.

The intensified camera (PI-MAX 2, ICCD camera) visualized the plasma emission [Fig. 6-1]. The gate time of the ICCD camera was 2.6 ns. The gate time was from 2 ns to 5 ns from the reference papers that studied the plasma emission using the ICCD cameras [22-30]. The gain rate was 1. The time captured the images were changed through the pulse generator. The resolution of the image was 0.082 mm/pix. The ignition experiments were performed 20 times at each time step. The figures are the average results at each time step [Figs.6-2-6-7].

Table 6-1. Laser energy.

E_{in} (mJ)	E_{tr} (mJ)	ΔE (mJ)
6.8	4.2	2.6
12.2	6.1	6.1
16.2	7.8	8.4
20.7	8.4	12.3
27.0	9.2	17.8
32.3	11.4	20.9

The ignition experiments were performed to investigate the effect of velocity on kernel temperature distribution. The jet burner with 62 % blockage ratio was used [Fig.2-1]. The perforated plate was located on the burner exit. The structure of the perforations on the plate involves fixed diameter circular holes in a multi-hole hexagonal array [Fig.2-1]. The premixed hydrogen and air flowed out the burner exit. Three bulk velocities (8, 14, and 23 m/s) were used. Three laser energy differences (2.6, 12.3, and 20.9 mJ) were utilized [Table 6-1]. The equivalence ratio was 0.7. The plasma (spark) produced by the laser was located 17 mm above the burner exit. The plasma location was the axis of the burner. The time captured the kernel was varied (1, 2, 3, 5, 7, 10, 15, 20, 50, and 100 μs). The more detailed experimental conditions were shown in Table 6-2. The air and hydrogen flow rates were respectively measured with the flowmeters (DTM325, and Bios DryCal DC-1) and controlled through the regulator (Schrader bellows H80) and the rotameter (Matheson FM 604) respectively.

Table 6-2. The experimental conditions for the effect of velocity on the flame kernel temperature distribution.

Case 1			
ΔE (mJ)	V_{bulk} (m/s)	ϕ	Plasma (Spark) height (mm)
2.6	8	0.7	17
2.6	14	0.7	17
2.6	23	0.7	17
Case 2			
ΔE (mJ)	V_{bulk} (m/s)	ϕ	Plasma (Spark) height (mm)
12.3	8	0.7	17
12.3	14	0.7	17
12.3	23	0.7	17
Case 3			
ΔE (mJ)	V_{bulk} (m/s)	ϕ	Plasma (Spark) height (mm)
20.9	8	0.7	17
20.9	14	0.7	17
20.9	23	0.7	17

The infrared camera (FLIR sc6100) was utilized to study the kernel development in terms of the kernel temperature [Fig. 2-11]. The characteristics of the camera were: exposure time- 0.01056 ms (10.56 μs) ; frame rate- 661 fps; pixel count- 128×288 pixel^2. A captured area of 42 mm $\times$ 94 mm and a resolution of 0.325 mm/pixel were archived. The measured photon count was converted to the temperature using the deconvolution method [132,133]. The more detailed process regarding the deconvolution method for the infrared images was written in Chapter 2.5.

6.2   Experimental Results

6.2.1 Plasma Expansion
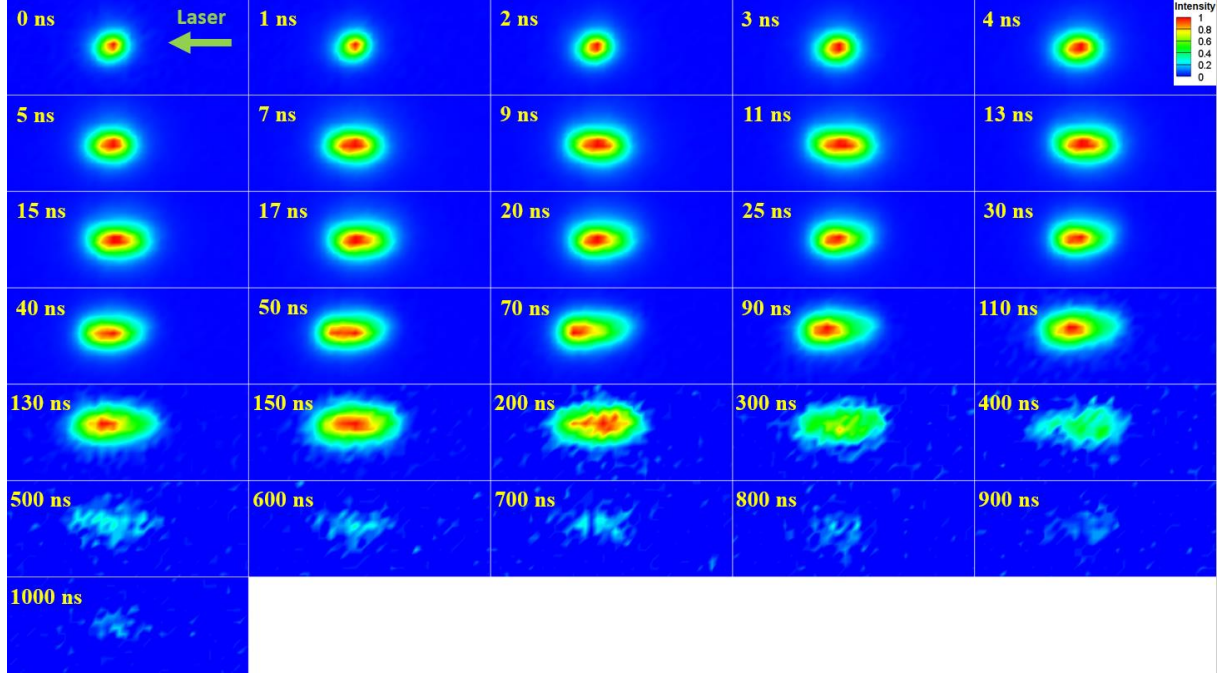
(a)
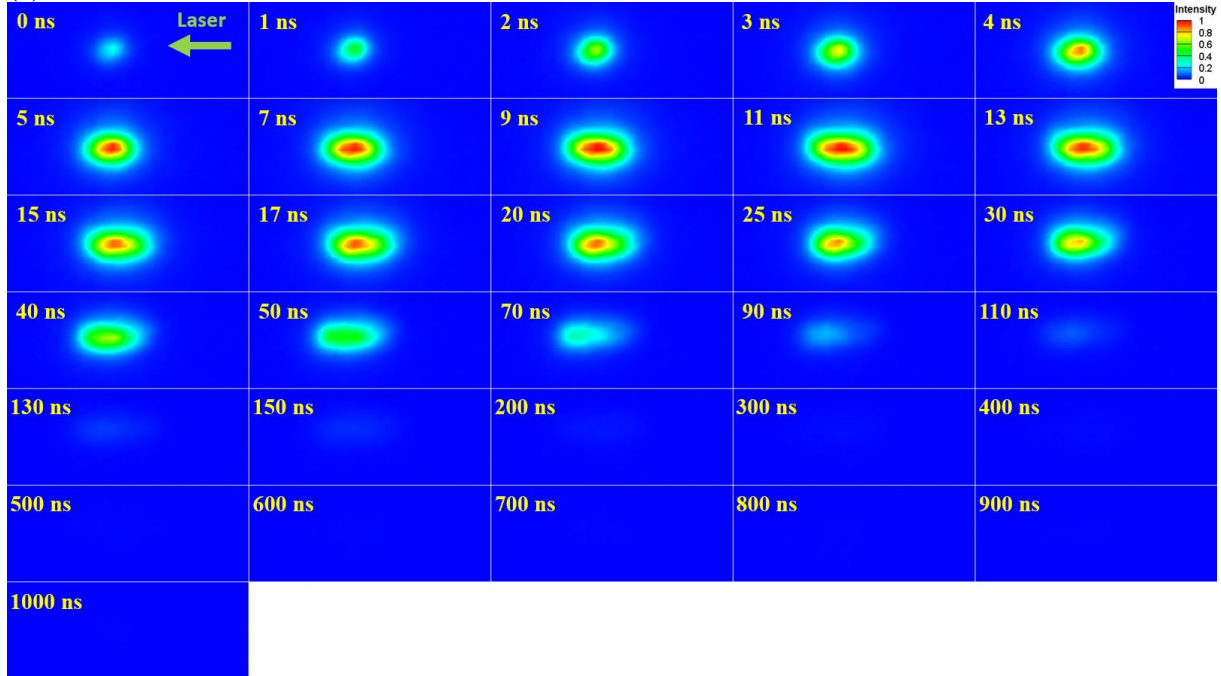
(b)

Fig.6-2. ICCD images of the time evolution of emission from a laser-induced spark in air, E_{in} = 6.8 mJ, the image size is 1.3 mm × 3.1 mm, (a) all of the images are normalized to their maximum intensity, (b) all of the images are normalized to maximum intensity in the images.
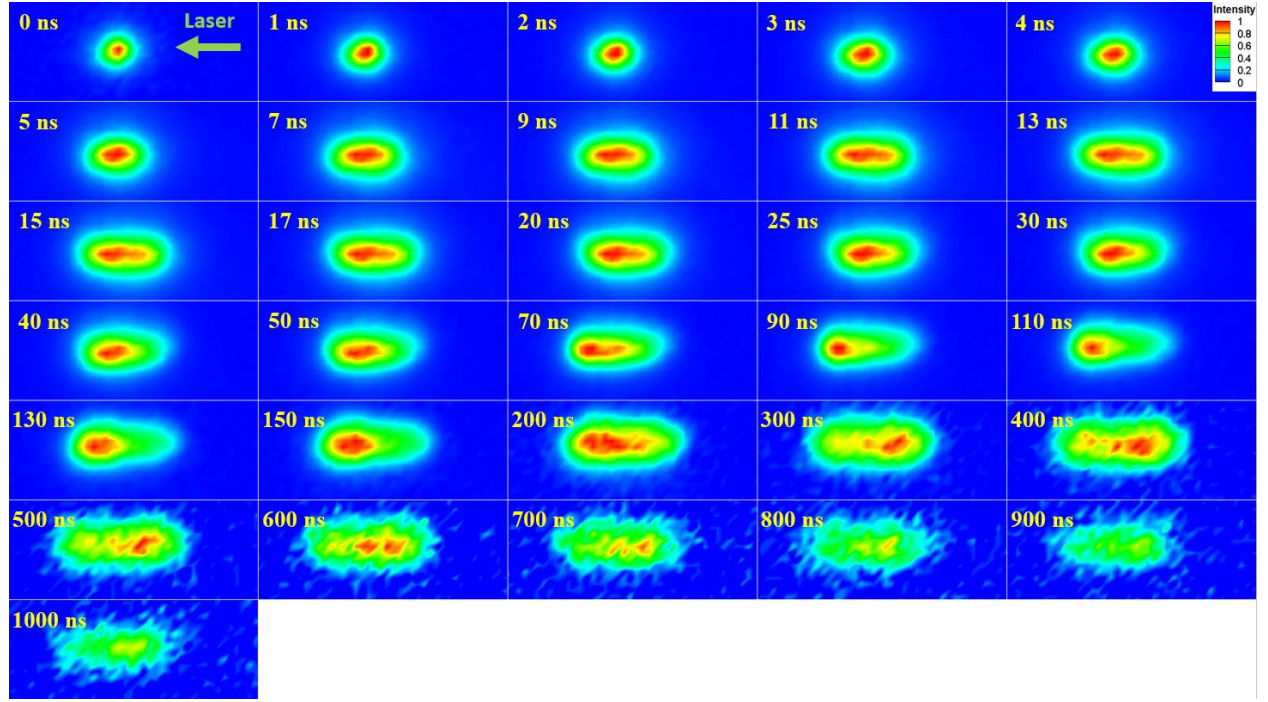
(a)
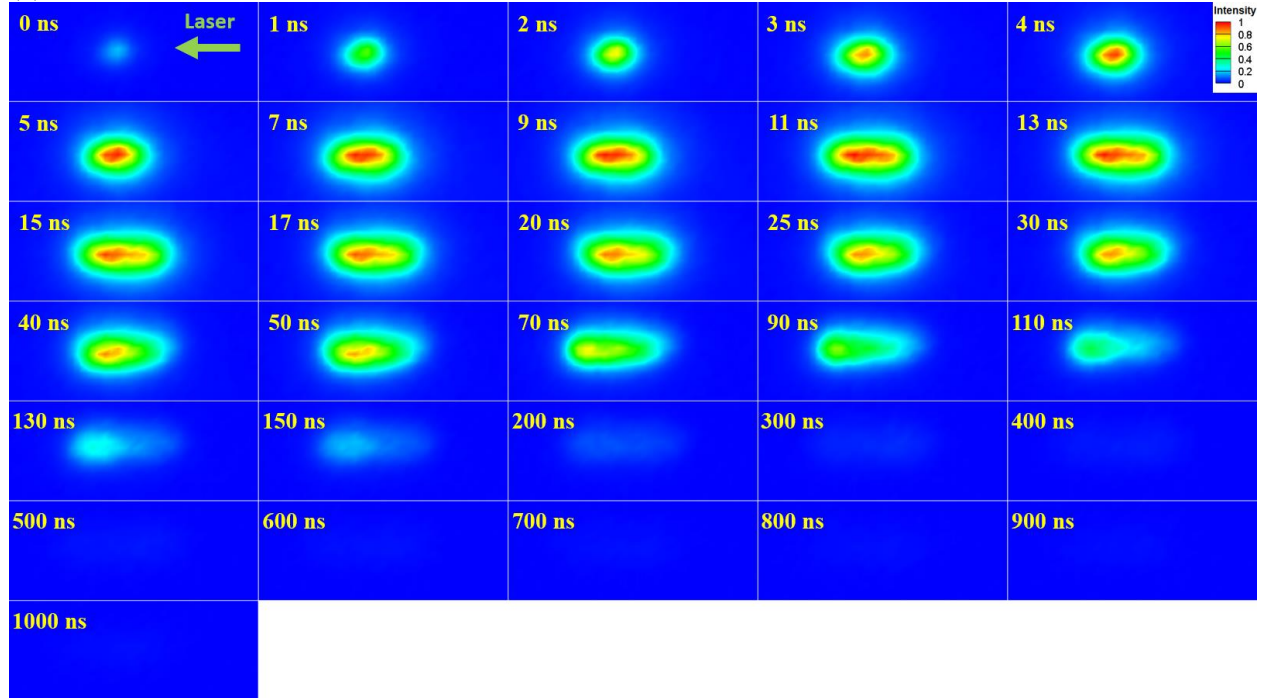
(b)

Fig.6-3. ICCD images of the time evolution of emission from a laser-induced spark in air, $E_{in} = 12.2$ mJ, the image size is 1.3 mm $\times$ 3.1 mm, (a) all of the images are normalized to their maximum intensity, (b) all of the images are normalized to maximum intensity in the images.
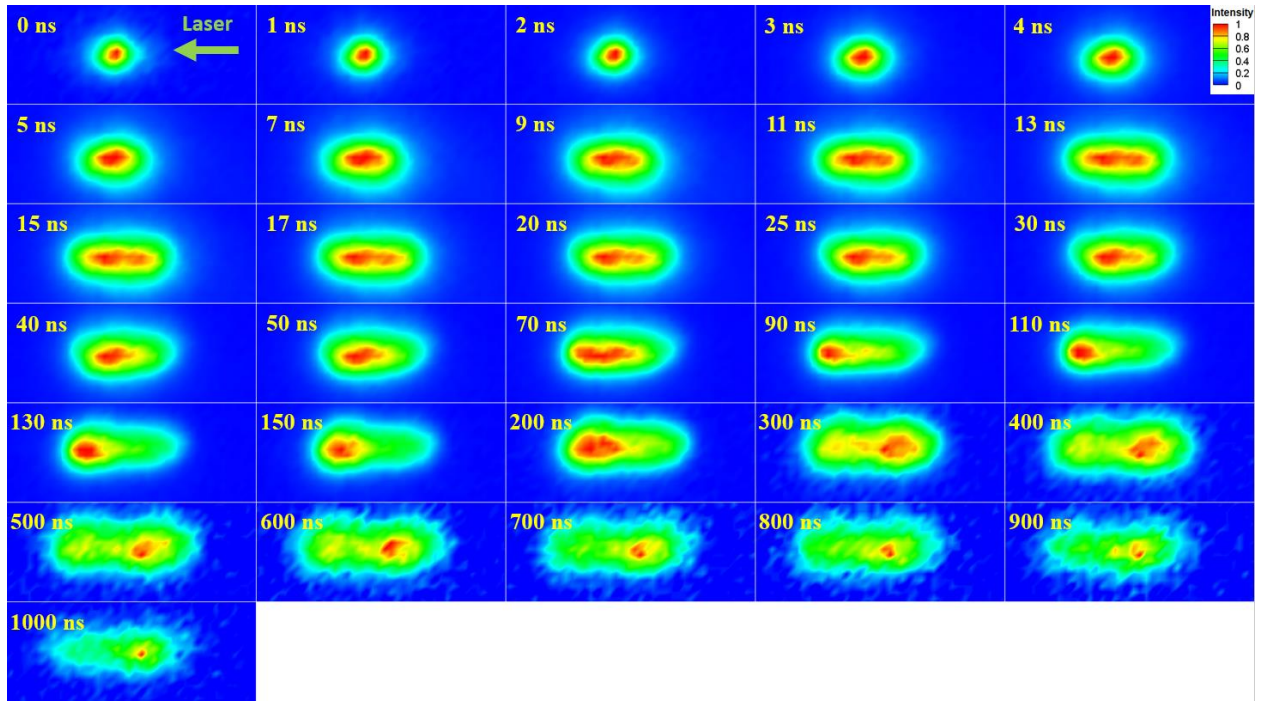
(a)
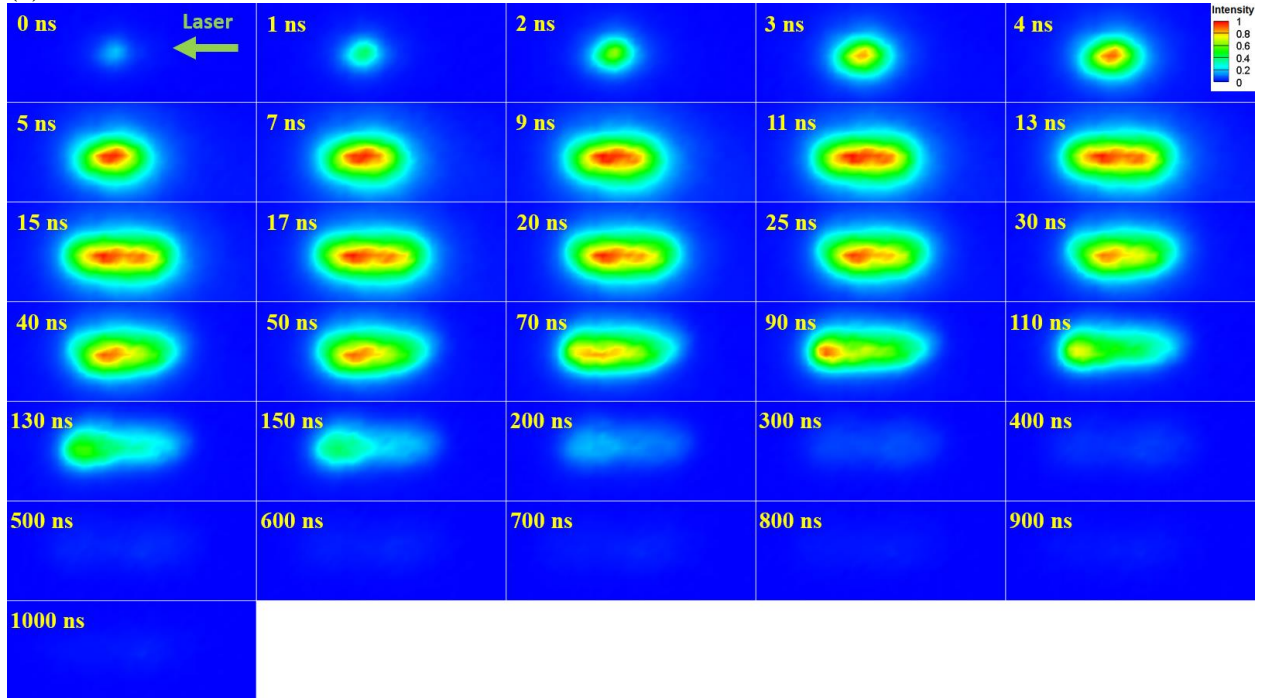
(b)

Fig.6-4. ICCD images of the time evolution of emission from a laser-induced spark in air, $E_{in} = $ 16.2 mJ, the image size is 1.3 mm $\times$ 3.1 mm, (a) all of the images are normalized to their maximum intensity, (b) all of the images are normalized to maximum intensity in the images.
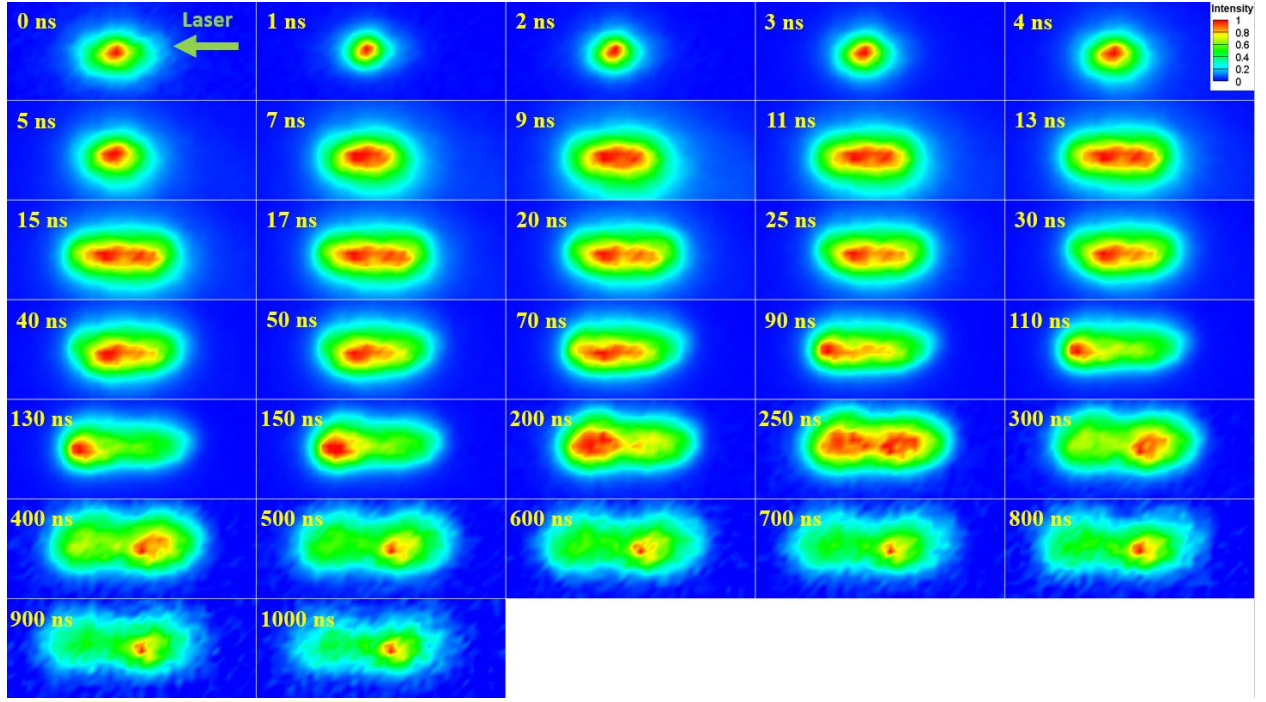
(a)
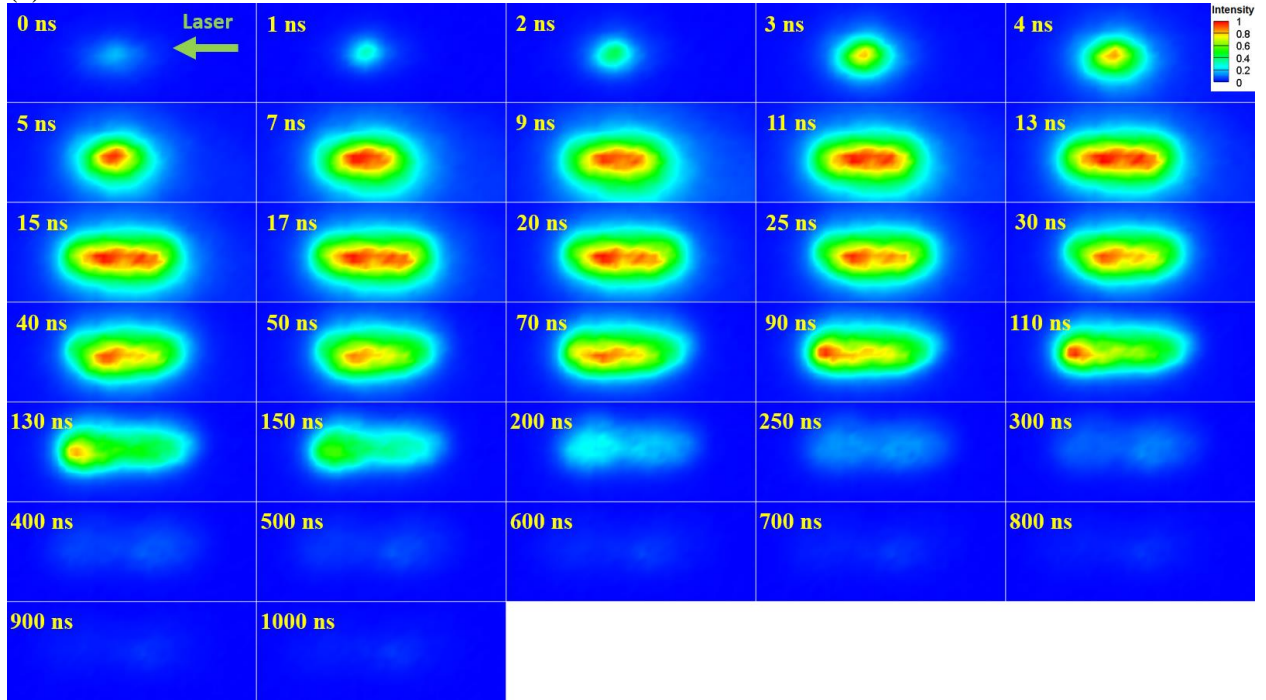
(b)

Fig.6-5. ICCD images of the time evolution of emission from a laser-induced spark in air, $E_{in} = 20.7$ mJ, the image size is 1.3 mm $\times$ 3.1 mm, (a) all of the images are normalized to their maximum intensity, (b) all of the images are normalized to maximum intensity in the images.
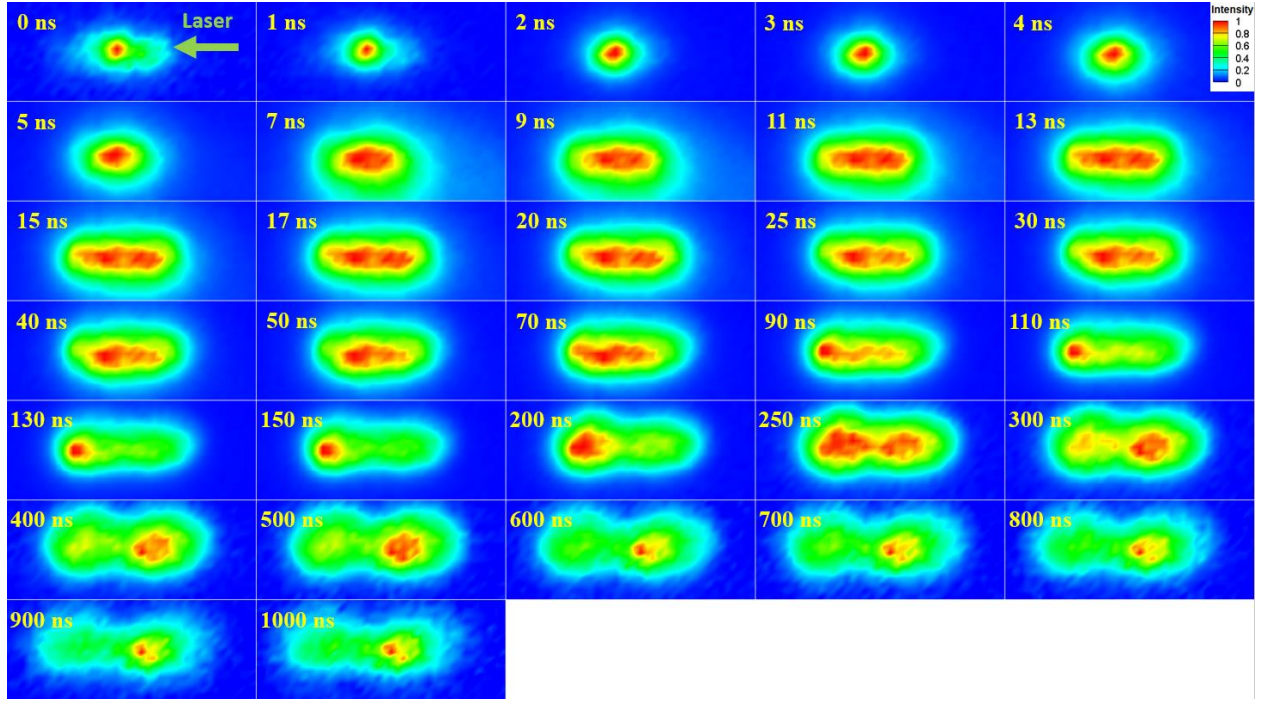
(a)
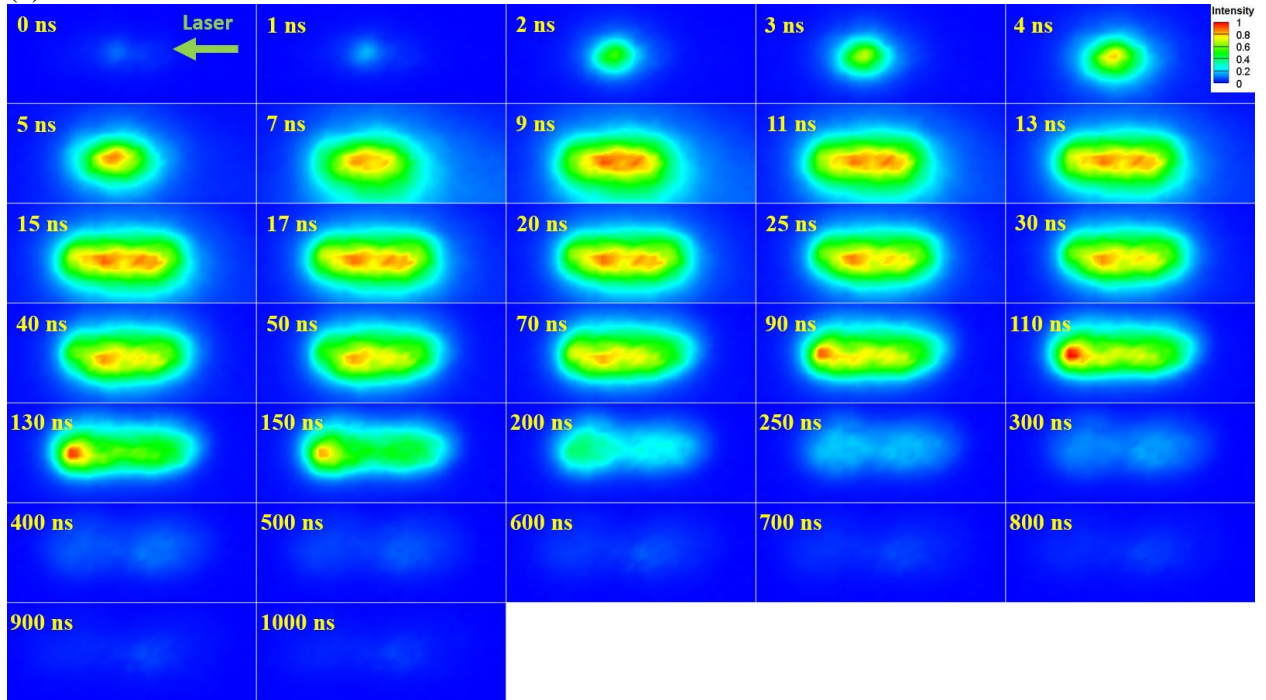
(b)

Fig.6-6. ICCD images of the time evolution of emission from a laser-induced spark in air, $E_{in} = 27.0$ mJ, the image size is 1.3 mm $\times$ 3.1 mm, (a) all of the images are normalized to their maximum intensity, (b) all of the images are normalized to maximum intensity in the images.
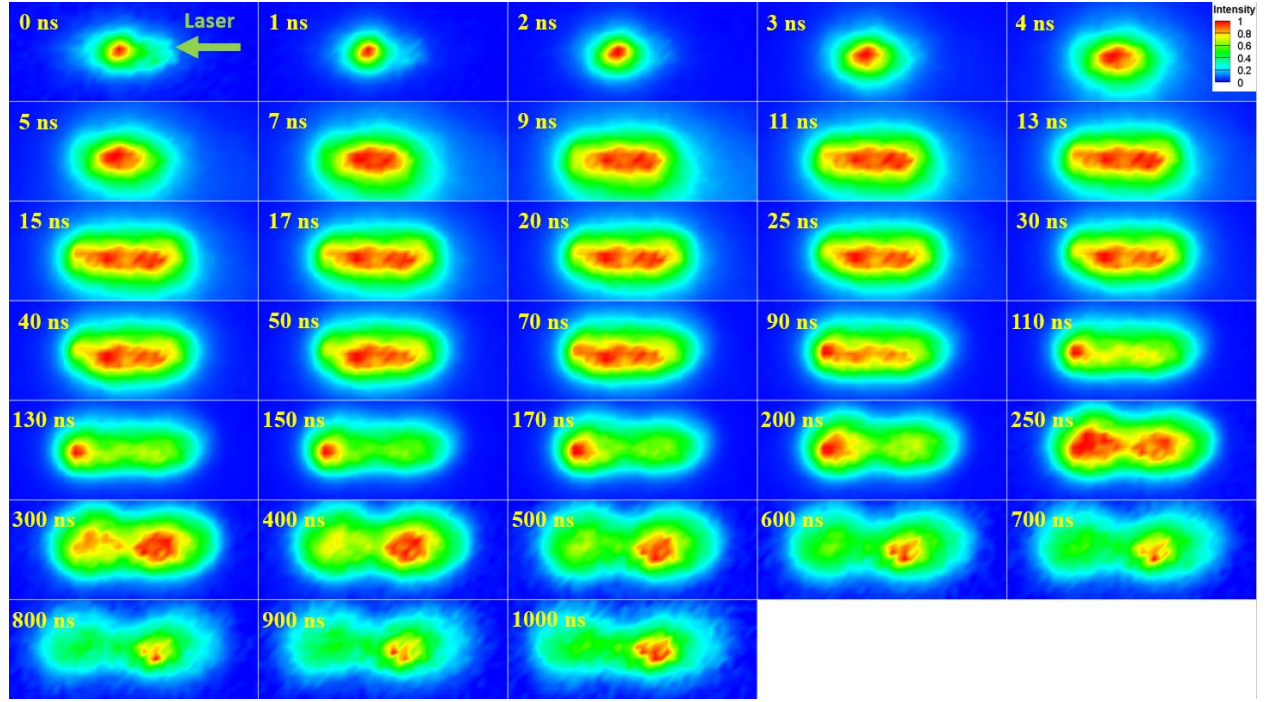
(a)
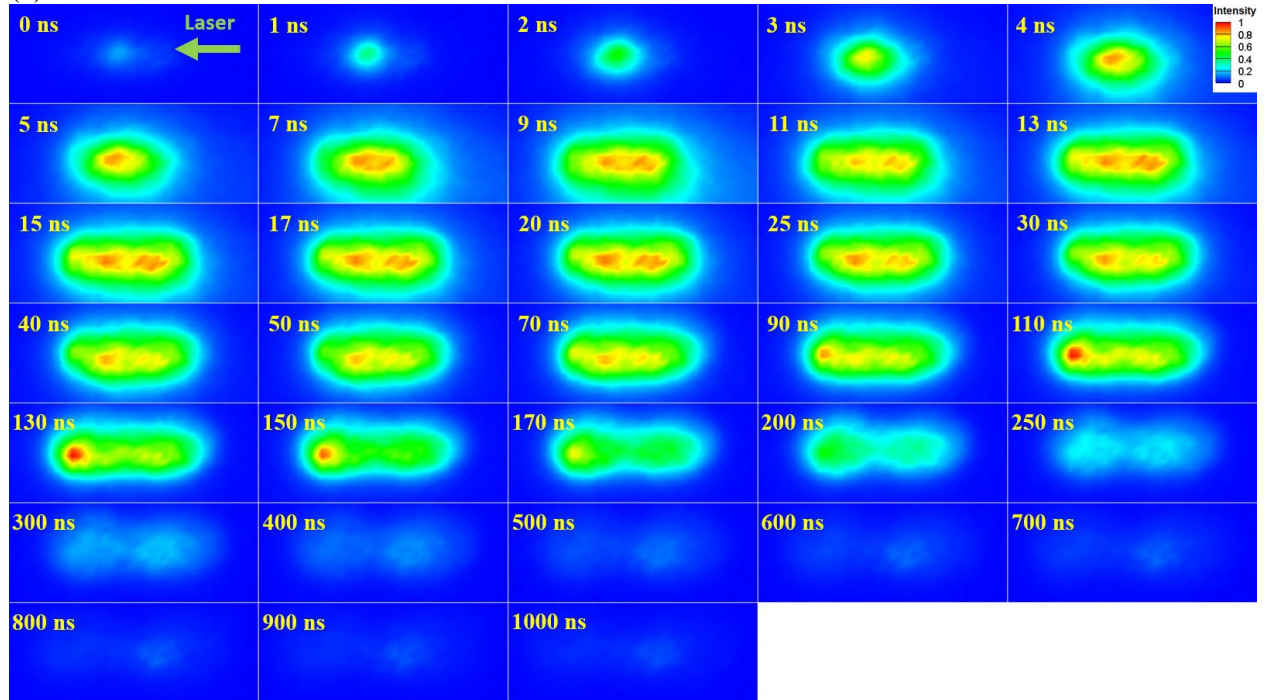
(b)

Fig.6-7. ICCD images of the time evolution of emission from a laser-induced spark in air, $E_{in} = 32.3$ mJ, the image size is 1.3 mm $\times$ 3.1 mm, (a) all of the images are normalized to their maximum intensity, (b) all of the images are normalized to maximum intensity in the images.

If a laser beam is focused at a focal point, and the laser irradiance is high enough, then multiphoton ionization occurs at the focal point [35,104]. Multiphoton ionization generates electrons that can easily absorb more photons by inverse bremsstrahlung process. The liberated electrons collide with other molecules located the surrounding of the focal point and ionize the molecules. Thus, the electron density is increased by the ionization and reaches a critical value. After that, a breakdown occurs and a plasma (spark) is generated [Figs. 6-2-6-7]. The surrounding gas of the plasma is heated by the plasma radiation, thus is ionized and the temperature of the gas increases. The ionized gas absorbs the laser photons. The inverse bremsstrahlung process that leads to a laser supported radiation wave is the main reason for the absorption of the laser photons. The plasma moves toward the laser by the laser absorption [Figs. 6-2-6-7] [35,104]. Therefore, the structure of the plasma is changed by time [Figs. 6-2-6-7] [22-30]. This is laser supported radiation wave [35,104]. In other words, if the plasma radiation is strong at the sufficiently high irradiance, the surrounding gas is rapidly heated to a high temperature by the plasma radiation prior to the shock wave arrival, the laser absorption initiates nearby the surrounding gas by the supersonic wave, and the plasma front edge moves with the laser-supported radiation (LSR) wave speed by the laser absorption [35,104]. At the low incident energy, 6.8 mJ, the plasma structure at early times is spherical [Fig. 6-2]. The plasma shape is changed to an elliptical structure as time elapses [Fig. 6-2]. The shape of the plasma is spherical at early times even the laser energy (the incident energy) is high [Figs. 6-2-6-7]. As time elapses, the plasma expands toward the laser by the laser absorption. Thus, the length of the elliptical increases. The plasma shape is changed to an infinity symbol structure along the laser beam as the laser energy is higher [Figs. 6-3-6-7]. These results support the observation by [23,25,26,29].

The average laser irradiance is defined as this equation [162]

$$I_{irr} = P_{laser}/A_{laser} \qquad\qquad 6.1$$

where P_{laser} is a power, and A_{laser} is an area of a laser beam. High laser energy generates strong laser irradiance [Eq. (6.1)]. Thus, generated electrons and the plasma size increase as the laser energy is stronger [Figs.6-2-6-7]. The laser absorption occurs widely toward the laser beam by the strong laser irradiance and the large plasma size [Figs.6-2-6-7]. The laser absorption leads to the plasma expansion toward the laser beam [Figs.6-2-6-7]. The plasma shape is changed to the

infinity symbol structure by the laser absorption [Figs.6-2-6-7]. In contrast, low laser energy forms low laser irradiance. Therefore, generated electrons and the plasma size decrease as the laser energy is weaker [Figs.6-2-6-7]. The laser absorption occurs narrowly toward the laser by the weak laser irradiance and the small plasma size [Figs.6-2-6-7]. The plasma expands toward the laser by the laser absorption, but the expansion is weak [Figs.6-2-6-7]. The plasma structure does not change significantly due to the short distance of the laser absorption [Figs.6-2-6-7].
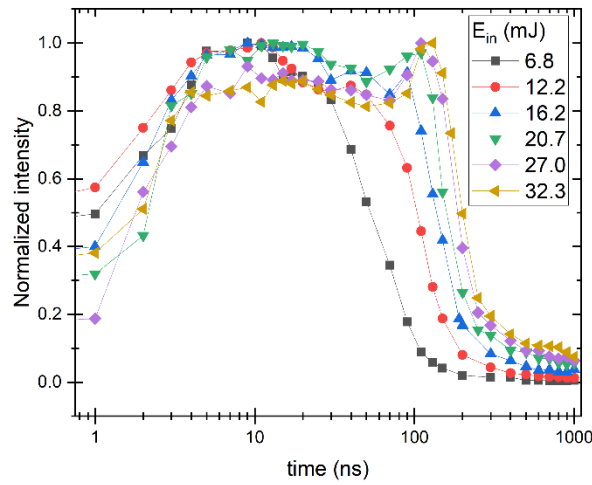
Fig.6-8. Normalized intensity of the plasma as time elapses.

Figure 6-8 illustrates the normalized intensity of the plasma. As the incident energy is higher, the time that keeps the high intensity in the plasma is longer [Fig.6-8]. High laser energy increases the generation of electrons leading a plasma, plasma intensity, and plasma radiation [30,31]. Therefore, plasma intensity at high incident energy may maintain for a relatively long time with a high value than low incident energy since high plasma radiation and high laser irradiance may positively affect plasma survival for a relatively long time. Difficult ignition conditions like high velocity, low pressure, and low temperature require high ignition energy. As the laser incident energy, E_{in}, and the laser energy difference, ΔE, are higher, the plasma intensity is keeping for a long time with a high value, and the plasma length increases due to the laser absorption [Figs.6-2-6-8]. Thus, the plasma heats a mixture for a long time, which leads to high temperature, and a large flame kernel that brings fast flame kernel propagation speed is generated due to the increased plasma length. Therefore, high laser energy for ignition increases a chance that can ignite a mixture in difficult ignition conditions.

134

Gaussian beam is widely used for the beam produced by a laser source. The irradiance is related to the magnitude of the complex electric field and is expressed as [162]

$$I_{irr}(z,r) = \frac{2P_{laser}}{\pi w(z)^2} \exp\left(-\frac{2r^2}{w(z)^2}\right) \qquad 6.2$$

where P_{laser} is the laser beam power, and $w(z)$ is the beam radius [162]. The irradiance decreases as farther away from the focal point [Eq. (6.2)]. Fig.6-9 illustrates the calculated irradiance in the current experimental conditions. As the laser incient energy is higher, the irradiance nearby the focal point increases, and the region having the high irradiance expands [Eq. (6.2)]. Therefore, the plasma expansion toward the laser by the laser absorption increases with the increasing the laser energy due to the high irradiance. However, plasma will not expand continuously as laser energy increases since an irradiance rapidly decreases farther away from a focal point due to an increase in a beam radius. In other words, a plasma length will converge to a specific size from a focal point with increasing laser energy.
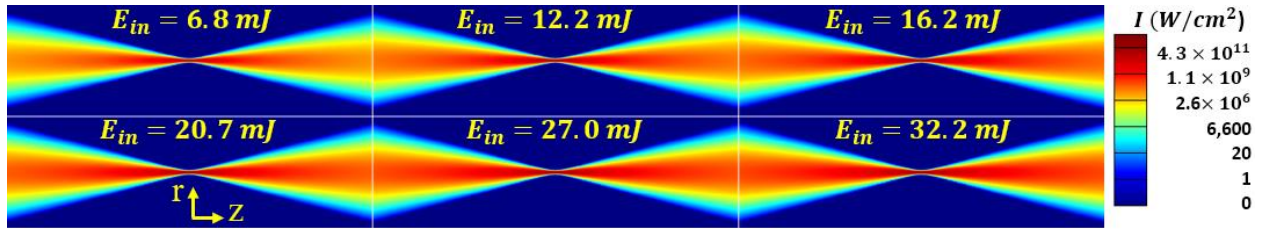
Fig.6-9. The laser irradiance, the image size is $0.24\ mm \times 0.80\ mm$.

6.2.2 Laser-Supported Radiation Wave
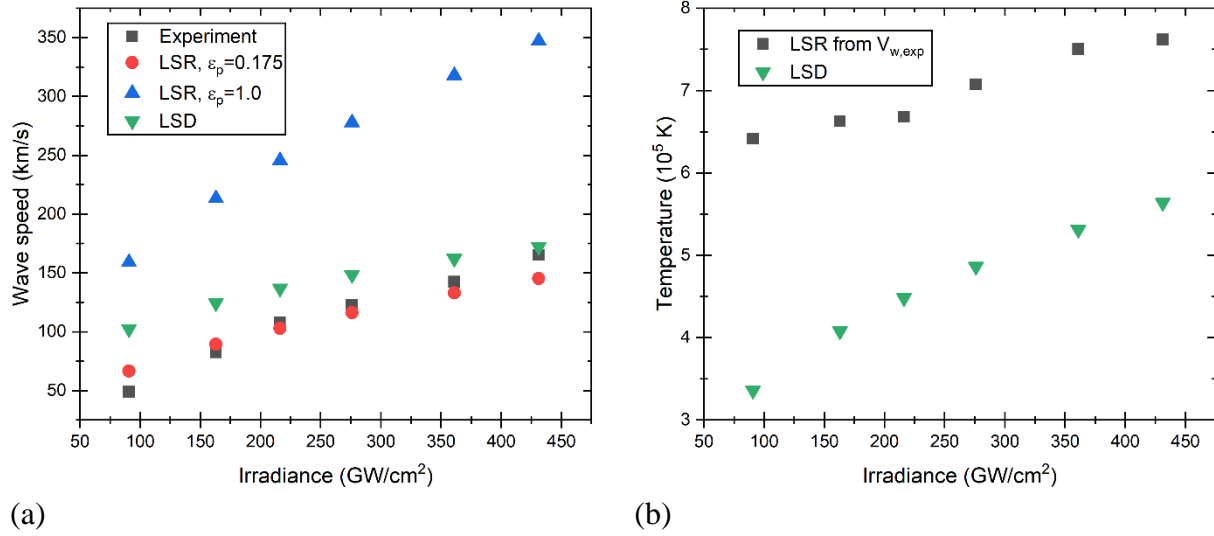
Fig.6-10. (a) Wave speed versus irradiance, (b) temperature versus irradiance.

The expansion wave speed by the laser supported radiation (LSR) was measured using the captured images at 3 ns after the plasma generation [Figs.6-2-6-7]. The LSR wave increases with an increase in the irradiance [Fig.6-10(a)]. As the laser energy is stronger, then plasma temperature is higher, thus LSR wave speed is faster because the internal energy is converted to velocity energy [35,42,163,164]. The energy balance equation in LSR wave between the LSR wave speed, V_w, the internal energy of the plasma, u_p, and the laser irradiance, I_{irr} is written by [35,163,164]

$$I_{irr} = \rho_0 u_p V_w \qquad\qquad 6.3$$

where ρ_0 is the ambient density. The spectral radiance of a blackbody is expressed as [114,165]

$$I_{b\lambda} = \frac{2\bar{h} \cdot v'^3}{c_0^2} \frac{1}{\exp\left(\frac{\bar{h}v'}{k_b T}\right) - 1} \qquad\qquad 6.4$$

where $\bar{h}$ is Planck's constant (6.626×10^{-34} J $\cdot$ s), v' is frequency ($c_0 = \lambda v'$), c_0 is speed of light (2.997925×10^8 m/s), k_b is Bolzmann's constant (1.381×10^{-23} J/K), and T is temperature. The irradiance of a blackbody is calculated integrating the spectral radiance [Eq. (6.4)] as [114,165]

$$\int I_{b\lambda} \, d\lambda = \sigma T^4 \qquad\qquad 6.5$$

where σ is Stefan-Boltzmann constant. Plasma does not emit radiation like a blackbody. An emissivity is applied to Eq. (6.5) to explain radiation emission from a real substance as

$$E_{PR} = \varepsilon_p \sigma T_p^4 \ . \qquad\qquad 6.6$$

In Eq. (6.6), E_{PR} is radiation emission from a plasma, ε_p is the emissivity of the plasma, and T_p is the plasma temperature. The temperature profile of the plasma, right after the plasma generation by a laser, is uniform [42,44,104]. Therefore, Eq. (6.6) can be used for the LSR. The plasma emissivity, ε_p, in Eq. (6.6) is an unknown value. Phuoc mentioned [31] citing Hughes's work [45] that if the plasma is thick, the emissivity of the plasma is 1 because the plasma emits radiation like a blackbody. However, it is not clear that what is a sufficient plasma thickness which can emit radiation like a blackbody. The plasma thickness is changed by temperature, and plasma length [46,47]. If the plasma length was longer than 100 cm [46] or 70 cm [47], the emissivity of the plasma was 1 [46,47]. The plasma length in the laser-induced spark is shorter than 10 cm and is generally below 1 cm [Fig.6-2-6-7][22-31]. Thus, we cannot assume the plasma in the laser-induced spark as a blackbody due to the short length of the plasma [Fig.6-2-6-7][22-31].
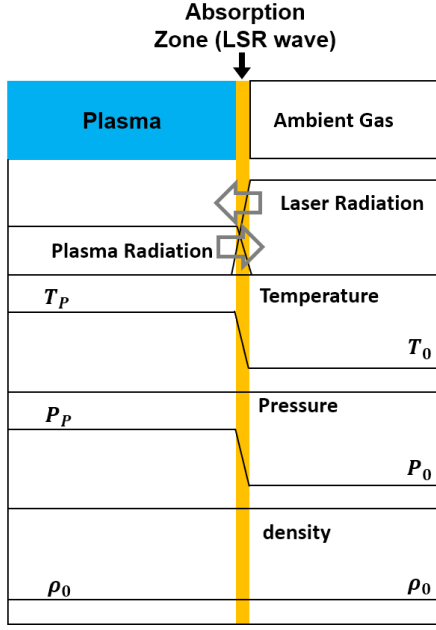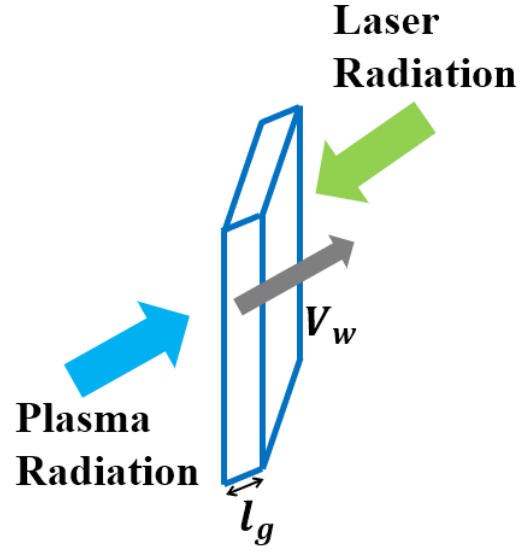
Fig.6-11. (a) One dimensional propagating plasma produced by laser-supported radiation wave, (b) schematic in absorption zone.

The plasma radiation increases the temperature of the ambient gas [Fig.6-11][104,166]. The temperature of the gas rapidly increases and the absorption zone is moved toward the laser beam with the wave speed [Fig.6-11][35,42,163]. The internal energy change of the gas for Δt and the heated gas length, l_g, is [Fig.6-11]

$$
\begin{aligned}
&(u_g - u_0)\rho_0 \forall_g \frac{1}{\Delta t} \\
&(u_g - u_0)\rho_0 A_g \frac{l_g}{\Delta t}
\end{aligned}
\qquad 6.7
$$

where u_g is the internal energy of the heated gas, u_0 is the internal energy of the gas at the initial temperature, ρ_0, is the initial density of the gas, A_g is the surface area, and $\forall_g$ is the volume of the heated gas expressed as $A_g l_g$. $\frac{l_g}{\Delta t}$ is the wave speed, V_w. Hence, the energy balance equation per the unit area between the heated gas and the plasma radiation is

$$\varepsilon_p \sigma T_p^4 = (u_g - u_0)\rho_0 V_w. \qquad\qquad 6.8$$

If we assume the gas temperature is very rapidly increased by the plasma radiation, and the heated gas temperature is similar to the plasma temperature ($T_p \approx T_g$), then we can rewrite Eq. (6.8) as

$$\varepsilon_p \sigma T_p^4 = (u_p - u_0)\rho_0 V_w. \qquad\qquad 6.9$$

where u_g is the internal energy of the gas at the plasma temperature. The plasma temperature, T_p, is calculated using the measured LSR wave speed and EES (Engineering Equation Solver) because the internal energy, u_p, is determined by temperature [Eq. (6.3)]. The plasma temperature increases with increasing the irradiance because the focused laser energy is stronger as the irradiance is higher [Fig.6-10(b)][Table 6-3]. The plasma emissivity is calculated by Eq. (6.9) [Table 6-3]. The calculated emissivities are between 0.09 and 0.23 [Table 6-3]. As the temperature is higher and the plasma length is longer, the plasma emissivity increases [46,47] [Table 6-3]. In the current work, the plasma temperature and the plasma length increase with an increase in the irradiance [Figs.6-2-6-7,6-10] [Table 6-3]. Therefore, the change of the plasma temperature and the plasma length leads to the variation of the emissivity [Table 6-3]. The tendency between the laser irradiance, the plasma temperature, and the wave speed are the same with the experimental papers [40-42,54,55].

Table 6-3. LSR wave speed, plasma temperature, plasma emissivity.

I_{irr} (GW/cm^2)	$V_{w,exp}$ (km/s)	$T_{p,cal}$ (K)	$\varepsilon_{p,cal}$
91	49	6.4×10^5	0.094
163	83	6.6×10^5	0.149
216	108	6.7×10^5	0.191
276	123	7.1×10^5	0.194
361	143	7.5×10^5	0.201
431	165	7.6×10^5	0.226

Bergel'son et al. [42] suggested three balance equations in the LSR wave as

$$\rho_0 V_w (u_f - u_0) = I_{irr} \qquad \text{6.10}$$

$$\rho_0 V_w u_0 = \sigma T_p^4 \varepsilon_p (1 - \chi) \qquad \text{6.11}$$

$$\rho_0 V_w u_p = I_{irr} - \sigma T_p^4 \varepsilon_p \chi. \qquad \text{6.12}$$

One equation was derived by the three equations as [42]

$$u_f - u_0 = \frac{u_0 I_{irr}}{\sigma T_p^4 \varepsilon_p (1 - \chi)}. \qquad \text{6.13}$$

Eq. (6.13) was expressed as the scaling equations, $T_f \approx A_T I_{irr}^{\alpha_T}$, and $V_w \approx B_v I_{irr}^{\beta_v}$ [42], and the scaling equations have wildly used in LSR wave [27,28,40,42,104,167-173]. However, Eqs. (6.10)-(6.12) have reset each other and cannot derive Eq. (6.13). Therefore, the suggested equation by Bergel'son et al. is questionable [42]. The more detailed explaination regarding to the equations, suggested by Bergel'son et al., is shown in 6.2.2.1.

The laser supported detonation (LSD) wave with the hydrodynamic model has used in the laser ignition research to calculate the wave velocity and the plasma temperature [31,35,48,51-53,104]. The laser irradiance determines the detonation wave speed, V_D, from the energy equation and momentum equation [35,51,104,174]

$$V_D = \left[\frac{2(\gamma_k^2 - 1) I_{irr}}{\rho_0} \right]^{1/3} \qquad \text{6.14}$$

where γ_k is specific heat ratio. The energy balance equation in the detonation wave zone is [35,51]

$$I_{irr} = \rho_0 V_D u_p. \qquad \text{6.15}$$

The energy balance equation in the LSD is the similar with the LSR [Eqs. (6.3),(6.14)]. The temperature behind the detonation wave is calculated using the energy balance equation, the pressure at the Chapman-Jouget point [35,104]

$$T_p = \frac{2\gamma_k I_{irr}}{c_v \rho_0 V_D (\gamma + 1)}$$

<div align="right">6.16</div>

where c_v is the specific heat at the plasma temperature. For laser irradiance of $2 \times 10^{11} \, W/cm^2$, Raizer [35] utilized the LSD wave by the hydrodynamic model to compute the wave velocity of $133 \, km/s$ and the plasma temperature of $9.1 \times 10^5 \, K$. At the same laser irradiance, Phuoc et al. [48] measured the wave speed of $110 \, km/s$ and the plasma temperature of $6.0 \times 10^5 \, K$, and Mandel'shtam and Raizer et al. [51,163] measured the wave speed of 110 km/s, and the plasma temperature of 6.0×10^5 [Table 6-4]. Eqs. (6.3) and (6.9) are calculated the wave speed of $103 \, km/s$ and the plasma temperature of $6.56 \times 10^5 \, K$ at the laser irradiance of $2 \times 10^{11} \, W/cm^2$ and the emissivity of 0.19 obtained from our experimental results [Table 6-4]. From the wave speed of the $110 \, km/s$ and the laser energy of $2 \times 10^{11} \, W/cm^2$, the calculated temperature is $6.36 \times 10^5 \, K$ [Eqs. (6.3),(6.9)]. The wave velocity and the temperature that computed using Eqs. (6.3) and (6.9) are similar to the experimental results studied by Phuoc et al. [48] and Mandel'shtam and Razier et al. [51,163] but different from the detonation model suggested by Raizer [35] since the detonation model of Raizer is not proper in the LSR wave. Therefore, the newly suggested equation, Eq. (6.9), in LSR wave is a valid method. Fig.6-10(a) compares the measured wave speeds with the calculated wave speeds. The experimental results in the wave speed are a good agreement with the LSR wave speed at the emissivity of 0.175 and are significantly lower than the LSR wave speed at the emissivity of 1.0 [Fig.6-10(a)]. It means that assuming the plasma emissivity like a blackbody is not a good approach method in the laser-induced spark. The LSD wave speed using Eq. (6.14) is overestimated than the measured wave speed [Fig.6-10(a)]. The difference between the LSD and the LSR decreases with an increase in the irradiance [Fig.6-10(a)]. The LSR wave speed more rapidly increases with the irradiance and the plasma temperature slowly rises than the LSD wave [Fig.6-10]. This is because the absorbed energy in the LSR wave effectively used for heating gas than increasing local energy [104]. Table 6-4 illustrates the comparison between the measured wave speed and the calculated LSR wave speed [Eqs. (6.3),(6.9)] [48,51,54,55]. For the irradiance is higher than $10 \, GW/cm^2$, the calculation of the LSR wave speed is a good agreement with the experimental results even the emissivity is assumed using the present experimental results [Table 6-4]. Therefore, the calculation

of the LSR wave speed using the energy balance equations is valid at the high irradiance [Eqs. (6.3),(6.9)][Table 6-4].

Table 6-4. Comparison between the measured wave speed and the calculated laser supported radiation wave speed.

	Present study	Mandel'shtam et al. [51]	Phuoc et al. [48]	Harilal et al. [54]	Qiu et al. [55]	Qiu et al. [55]
I_{irr} (GW/cm^2)	216	200	200	654[a]	19	10
$V_{w,exp}$ (km/s)	108	110	110	178[b]	25	20
$V_{w,LSR}$ (km/s)[c]	107	103[d]	103[d]	186[d]	25[e]	18[e]

[a]The irradiance was calculated using the given values from the paper [54].
[b]The wave speed was calculated at 3 ns from the ICCD images [54].
[c]Eq.(3) and Eq.(9) used to compute the LSR wave speed.
[d]The plasma emissivity was 0.19 in the calculation.
[e]The plasma emissivity was 0.12 in the calculation.

6.2.2.1 Equations suggested by Bergel'son et al. [42].

Bergel'son et al. used the balance equations in the LSR wave [42]

$$\rho_0 V_w (u_f - u_0) = I_{irr} \qquad \text{6.17}$$

$$\rho_0 V_w u_0 = \sigma T_p^4 \varepsilon_p (1 - \chi) \qquad \text{6.18}$$

$$\rho_0 V_w u_\infty = I_{irr} - \sigma T_p^4 \varepsilon_p \chi . \qquad \text{6.19}$$

ρ_0 (kg/m^3)	Initial density	V_w (m/s)	Wave speed
$u_f (J/kg)$	Internal energy of the front in the wave	u_0 (J/kg)	Initial internal energy
$I_{irr}(W/m^2)$	Irradiance	$\sigma(W/m^2/K^4)$	Stefan–Boltzmann constant
T_p (K)	Plasma temperature	ε_p	Emissivity of hot layer (plasma)
χ	Fraction of the radiation loss	u_p	Plasma internal energy

| T_f (K) | Temperature of the front in the wave | T_0 (K) | Initial temperature |

I think Eq. (6.17) explains the expansion of the wave, Eq. (6.19) explains the expansion of the wave considering the radiation loss. However, I cannot understand Eq. (6.18). Bergel'son et al. found the two equations from Eqs. (6.17)-(6.19)

$$u_f - u_0 = \frac{u_0 I_{irr}}{\sigma T_p^4 \varepsilon_p (1 - \chi)} \qquad \text{6.20}$$

$$u_f - u_p = u_0/(1 - \chi). \qquad \text{6.21}$$

When I followed the explanation of Bergel'son et al., $u_f - u_p = u_0 + u_0/(1 - \chi)$. Bergel'son et al. may have missed the calculation, but their explanation for Eq. (6.21) is still valid. Bergel'son et al. said the energy emitted by the hot plasma is absorbed at the front, thus $\chi \ll 1$. Hence, Eq. (6.21) becomes

$$u_f - u_p = u_0. \qquad \text{6.22}$$

The internal energy at the flame temperature, u_f, is very high than the internal energy at the initial temperature, u_0. Thus, $u_f - u_p \approx 0$, $u_f \approx u_p$, and $T_f \approx T_p$. These procedures look reasonable, but this method is wrong.

$$\rho_0 V_w u_p = I_{irr} - \sigma T_p^4 \varepsilon_p \chi$$
$$I_{irr} = \rho_0 V_w (u_f - u_0)$$

>>

$$\rho_0 V_w u_p = \rho_0 V_w (u_f - u_0) - \sigma T_p^4 \varepsilon_p \chi$$
$$\rho_0 V_w u_p - \rho_0 V_w (u_f - u_0) = -\sigma T_p^4 \varepsilon_p \chi$$
$$\rho_0 V_w (u_p - u_f + u_0) = -\sigma T_p^4 \varepsilon_p \chi$$
$$\rho_0 V_w u_0 = \sigma T_p^4 \varepsilon_p (1 - \chi) = \sigma T_p^4 \varepsilon_p - \sigma T_p^4 \varepsilon_p \chi$$

\>>

$$\rho_0 V_w u_0 = \sigma T_p^4 \varepsilon_p + \rho_0 V_w (u_p - u_f + u_0)$$

$$\rho_0 V_w u_0 - \rho_0 V_w (u_p - u_f + u_0) = \sigma T_p^4 \varepsilon_p$$

$$\rho_0 V_w (u_f - u_p) = \sigma T_p^4 \varepsilon_p$$

But, $u_f \approx u_p$, and $T_f \approx T_p$ from their paper [42], this equation becomes

$$0 = \sigma T_p^4 \varepsilon_p.$$

Therefore, these equations are unreasonable.

However, Bergel'son et al. used Eq.(6.20) to calculate the plasma temperature and the wave speed and Eq. (6.20) is changed as

$$\frac{u_f}{u_0} = \frac{I_{irr}}{\sigma T_f^4 \varepsilon_p}. \qquad \qquad 6.23$$

Bergel'son et al. mentioned that $T_f \gg T_0$, and $e_f \gg e_0$, thus the plasma temperature (=the front temperature) and the wave speed are respectively expressed as $T_f \approx A_T I_{irr}^{\alpha_T}$, and $V_w \approx B_v I_{irr}^{\beta_v}$. However, the balance equations used by Bergel'son et al. resets each other. Therefore, the suggested equations are questionable.

6.2.3   Effect of Velocity on the Kernel Temperature Distribution

(a)

(b)

(c)
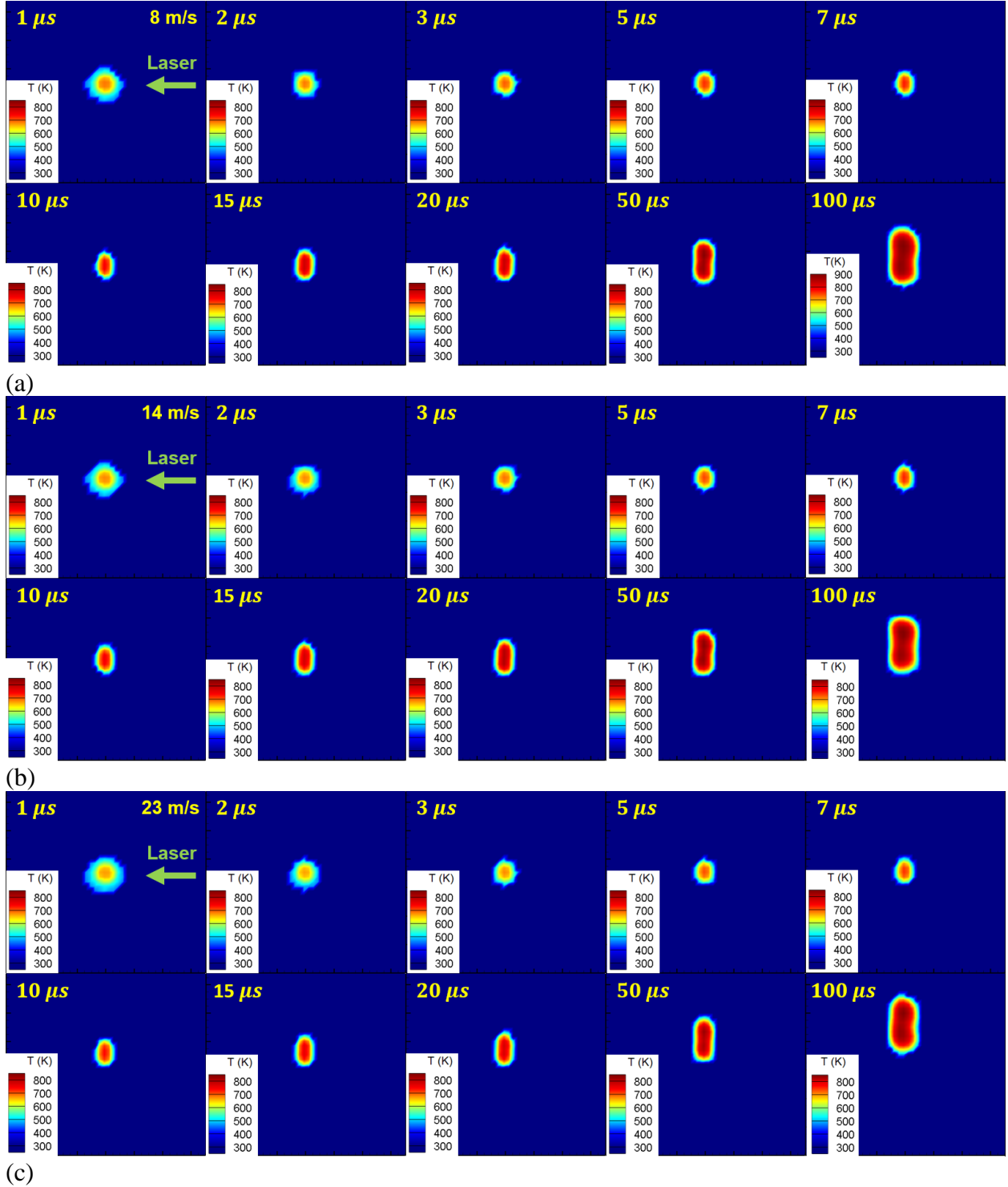
Fig. 6-12. Kernel development, (a) $\Delta E = 2.6$ mJ, and $V_{bulk} = 8$ m/s, (b) $\Delta E = 2.6$ mJ, and $V_{bulk} = 14$ m/s, and (c) $\Delta E = 2.6$ mJ, and $V_{bulk} = 23$ m/s, the image size is 4.55 mm $\times$ 4.15 mm.
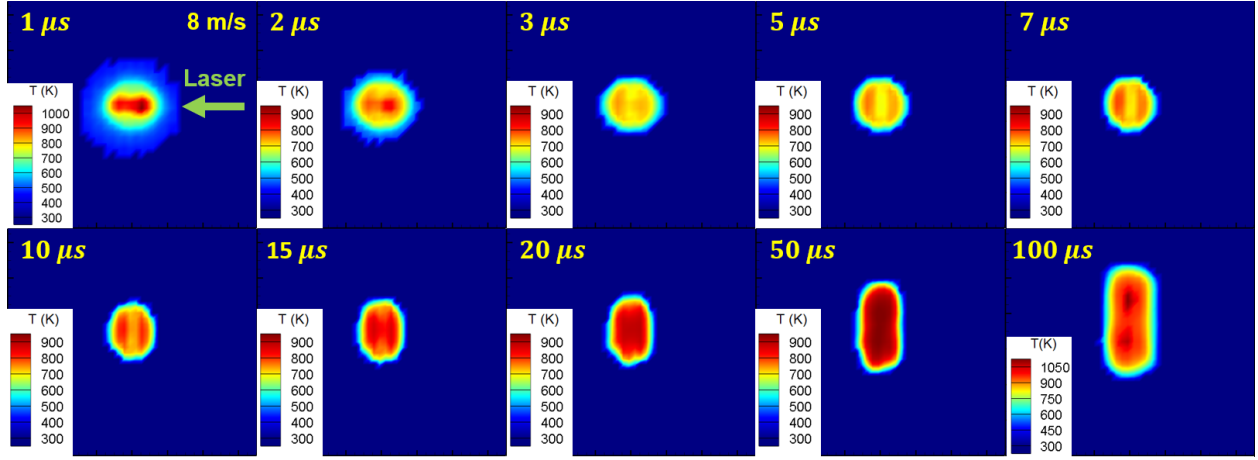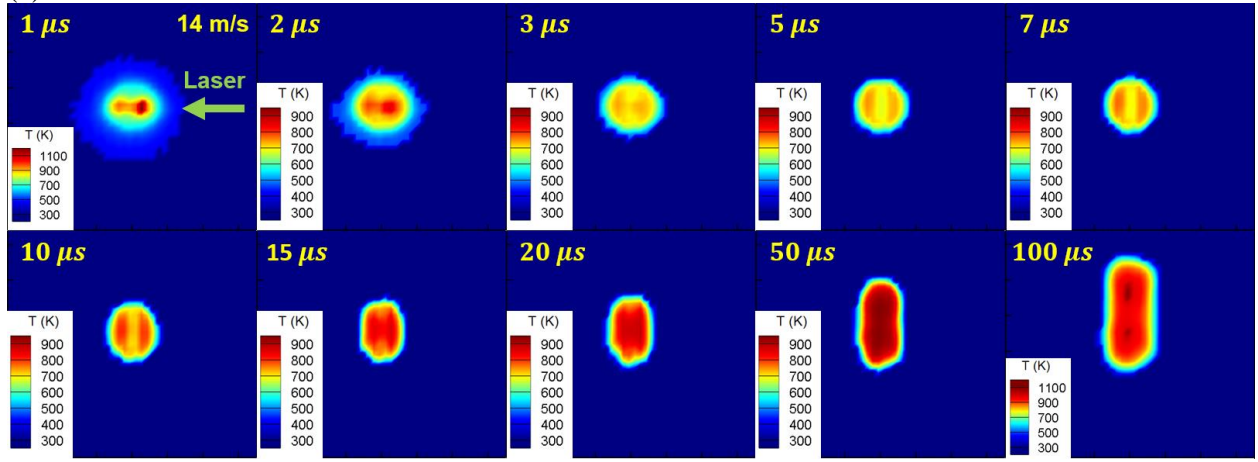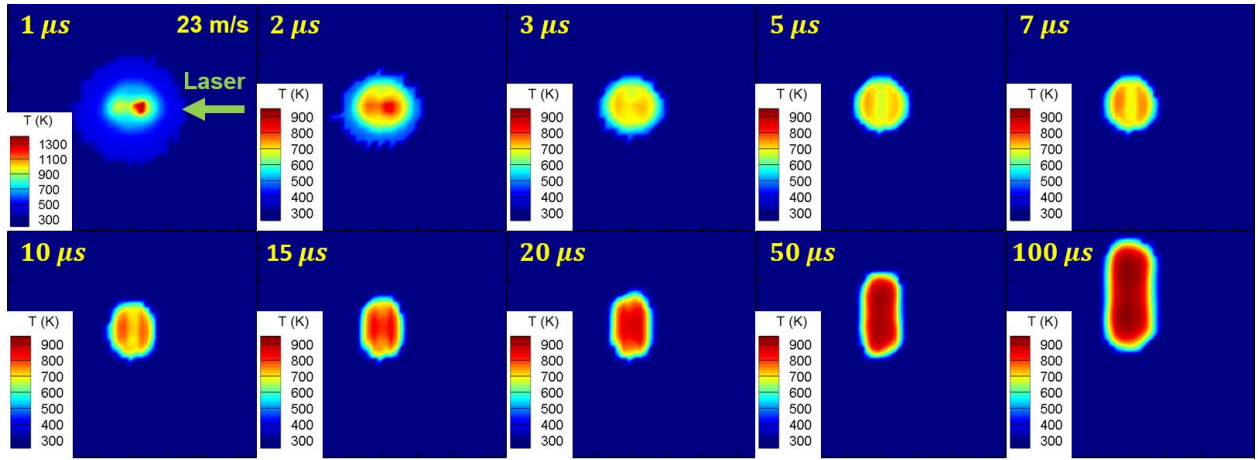
Fig. 6-13. Kernel development, (a) $\Delta E = 12.3$ mJ, and $V_{bulk} = 8$ m/s, (b) $\Delta E = 12.3$ mJ, and $V_{bulk} = 14$ m/s, and (c) $\Delta E = 12.3$ mJ, and $V_{bulk} = 23$ m/s, the image size is 4.55 mm $\times$ 4.15 mm.
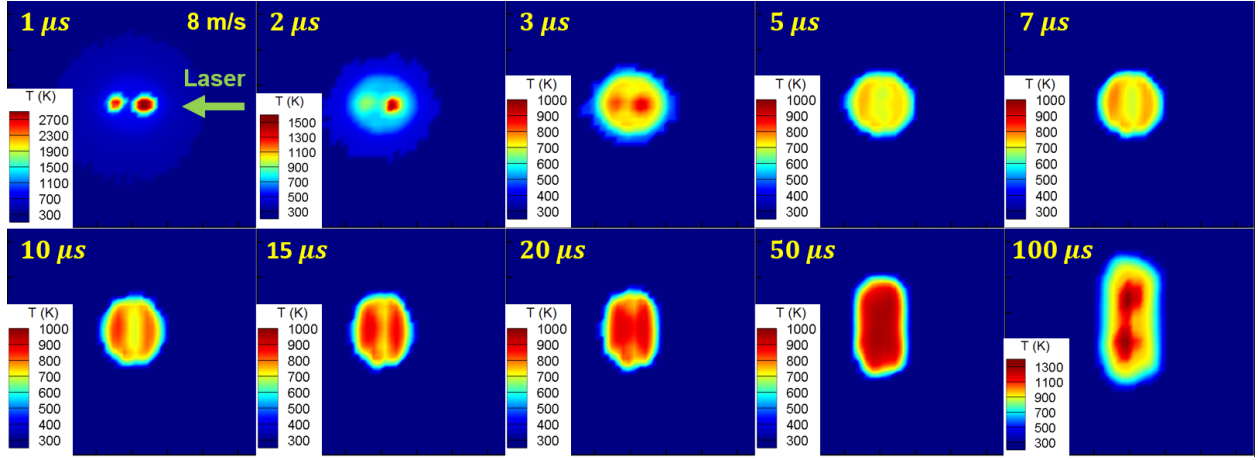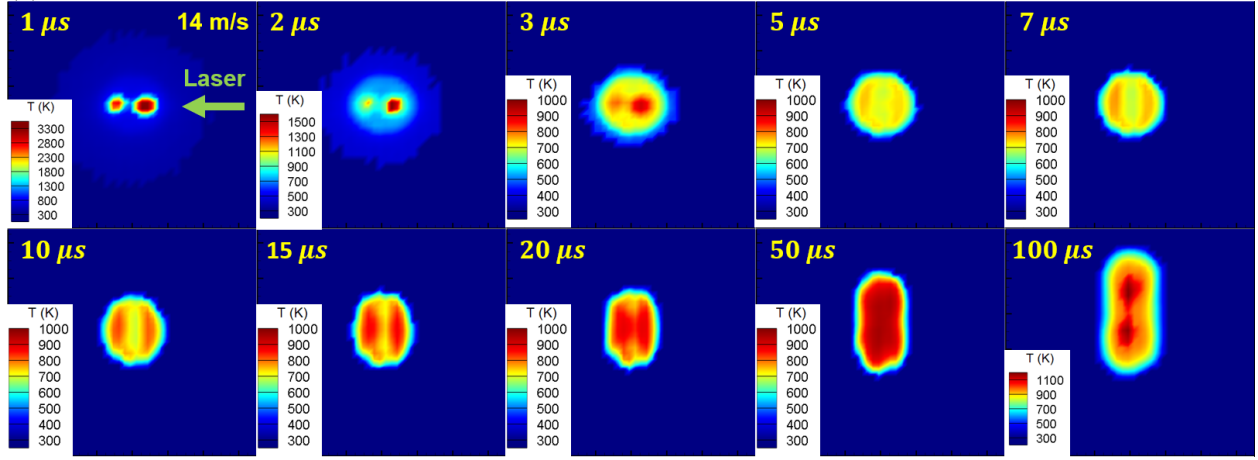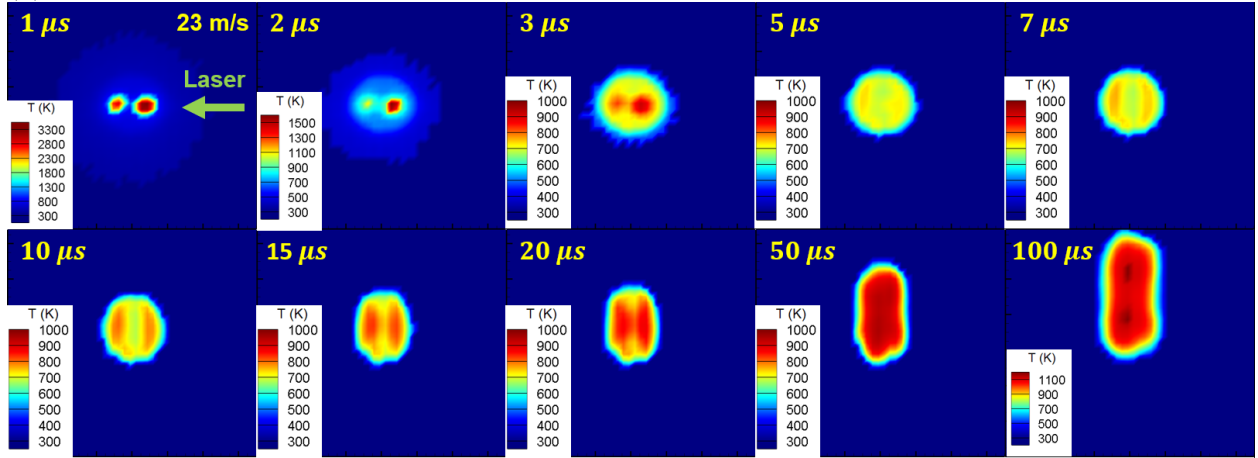
Fig.6-14. Kernel development, (a) $\Delta E = 20.9$ mJ, and $V_{bulk} = 8$ m/s, (b) $\Delta E = 20.9$ mJ, and $V_{bulk} = 14$ m/s, and (c) $\Delta E = 20.9$ mJ, and $V_{bulk} = 23$ m/s, the image size is 4.55 mm $\times$ 4.15 mm. The kernel temperature at 1 µs was an extrapolation result.

When the laser energy difference, ΔE, is 2.6 mJ, the temperature of the kernel center is higher than the other regions at 1 μs after the laser pulse [Fig.6-12]. The low laser energy generates the low laser irradiance. Thus, the laser absorption at the low laser energy is weak due to the low laser irradiance. The plasma shape does not significantly change and the small change of the plasma occurs near the focal point because the plasma cannot sufficiently expand toward the laser due to the weak laser absorption [Fig.6-2]. Therefore, the plasma energy is concentrated on the focal point [Fig.6-2]. The mixture at the focal point is heated by the plasma [Fig.6-12]. Hence, the kernel temperature increases from the kernel center to the kernel edge as time elapses [Fig.6-12].

As the laser energy difference, ΔE, is higher, the irradiance increases and the plasma widely expands toward the laser by the laser absorption due to the high laser irradiance [Figs.6-2-6-7]. The plasma size expands toward both sides, the coming direction of the laser beam and the leaving direction of the laser beam, from the focal point since the laser beam passes the focal point [Figs.6-2-6-7]. As time elapses, the plasma shape changes to an infinity symbol structure similar to the laser beam passing the focal point due to the laser absorption [Figs.6-2-6-7]. The mixture at the circle centers of the plasma with the infinity symbol geometry, not the focal point, is heated because the plasma shape is kept as the infinity symbol structure for a longer time than the circle or the ellipse [Figs.6-5,6-7,6-13,6-14]. We can discover the relevance between the location of the heated mixture and the plasma circles in Fig.6-15. The plasma shape at 1 μs after the laser pulse is corresponding to the heated mixture location [Fig.6-15]. The kernel temperature increases from the kernel edge to the kernel center as time elapses [Figs.6-13,6-14].

Figures.6-12-6-14 illustrate the effect of velocity on the kernel temperature distribution. The velocity does not affect the kernel temperature distribution during the early stage [Figs.6-12-6-14]. A strong energy source increases mixture temperature and creates a kernel. In a laser-induced spark, a plasma roles the high energy source that increases mixture temperature and produces a kernel. The plasma expansion is determined by the laser energy and does not relate to a jet [22-30]. Therefore, the kernel temperature distribution during the early stage is dependent on the laser energy and is independent of the bulk velocity [Figs.6-12-6-14].
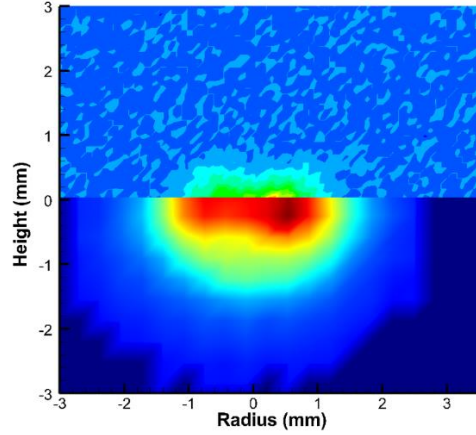
Fig.6-15. Comparison between the plasma and the generated kernel at 1 μs after the laser pulse, $\Delta E = 12.3\ mJ$, and $V_{bulk} = 8\ m/s$.

The bulk velocity affectes the kernel temperature [Figs.6-12-6-14,6-16(d)-(f)]. With increasing the bulk velocity, the kernel temperature increases until 3 μs and decreases after 3 μs [Figs.6-12-6-14,6-16(d)-(f)]. Especially, the time between 3 μs and 100 μs clearly shows the effect of the velocity on the kernel temperature [Figs.6-12-6-14,6-16(d)-(f)]. As the bulk velocity is faster, the forced convection heat transfer between the kernel and the mixture in the surrounding enhances. The energy loss from the kernel to the surrounding at the high velocity is higher than at the low velocity. Thus, the increased energy loss by the forced convection heat transfer decreases the kernel temperature as the bulk velocity increases [Figs.6-12-6-14,6-16(d)-(f)]. The kernel size is very small immediately after the kernel generation by the plasma [Figs.6-12-6-14]. If the kernel size is very small, the high velocity may positively affect the kernel since the supply of mixture into the kernel increases with velocity. Therefore, the kernel temperature decrease with the velocity until 3 μs after the laser pulse. In other words, an increase in the mixture supplement into the kernel by the velocity may contribute to the relatively high kernel temperature because of the increased reaction. As the incident energy is stronger, the plasma temperature is higher; thus, the high temperature can deal with a lot of reactants. Therefore, this phenomenon is more clear with an increase in the laser energy. As time elapses, the kernel grows, and the energy loss by the velocity increases due to an increase in the kernel size, thus the forced convection heat transfer by the velocity is dominant than the supply of the reactant by the velocity [Figs.6-12-6-14,6-16(d)-(f)]. Eventually, kernel temperature decreases with increasing the velocity after a specific time [Figs.6-12-6-14,6-16(d)-(f)].

149

Figures 6-13, and 6-14 illustrate the two high-intensity bowls in the kernel. The temperature at the right bowl is higher than the temperature at the left bowl [Figs.6-13,6-14]. A plasma expands toward a laser beam due to the laser absorption [Figs.6-2-6-7] [31,34,104]. The energy of a laser beam before a focal point is higher than the laser beam energy after the focal point since some amount of the energy is used to generate a plasma [Table 6-1] [27,28,31]. We can estimate the circle of the plasma at the right side will be a high intensity than the circle of the plasma at the left side because the laser irradiance at the right side is strong than the irradiance at the left side. Therefore, the mixture at the right intensity bowl is more heated by the relatively high energy of the plasma at the right side than the left side. It brings to the temperature difference between the two high-intensity bowls [Figs.6-13,6-14].

(a)   (d)
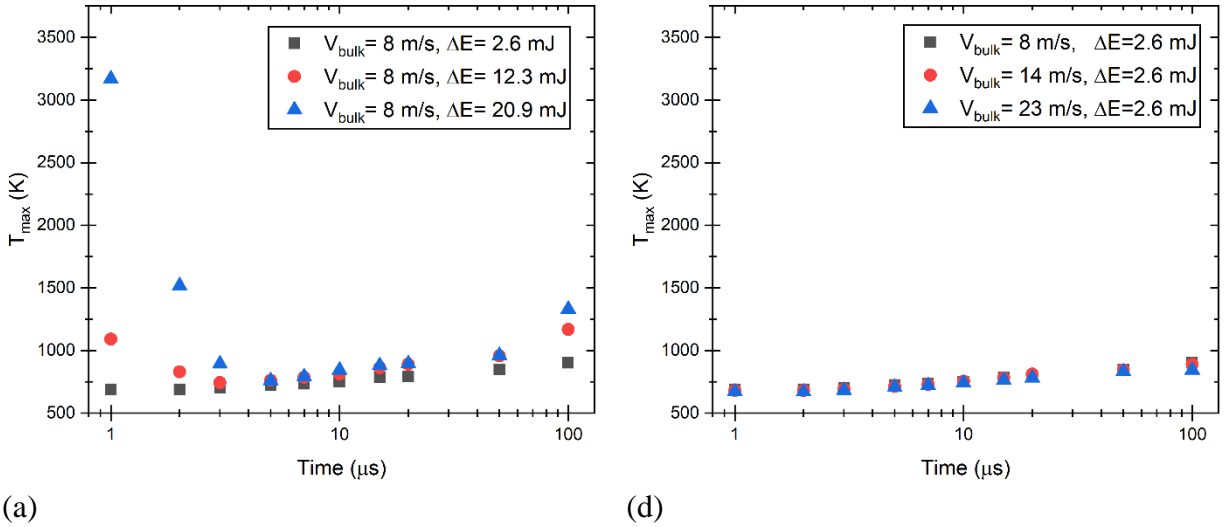
Fig.6-16. The maiximum kernel temperature, (a) the bulk velocity is 8 m/s, (b) the bulk velocity is 14 m/s, (c) the bulk velocity is 23 m/s, (d) ΔE is 2.6 mJ, (e) ΔE is 12.3 mJ, and (f) ΔE is 20.9 mJ.

Fig.6-16 continued

(b)

(c)

(e)

(f)
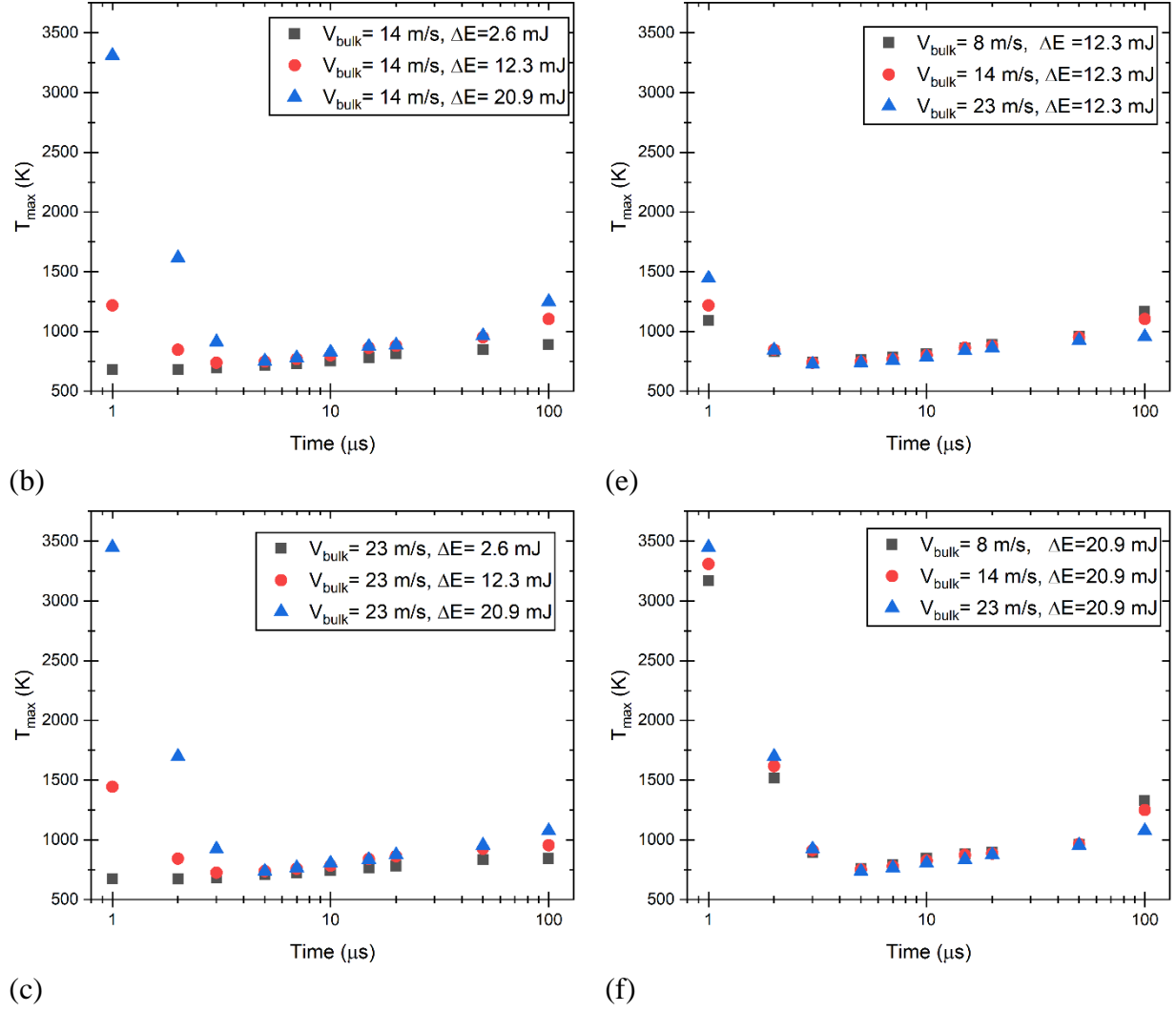
The temporal evolution of the kernel temperature is shown in Fig.6-16. The kernel temperature rapidly decreases after the plasma generation since the surounding temperature is very low than the plasma temperature [Fig.6-16]. As time elapses, the reaction in the kernel increases, thus the kernel temperature also rises [Fig.6-16]. Kernel temperature or plasma temperature have studied by experimental measurements [56-66]. However, only Dumitrache et al. [56], who measured the kernel temperature through the Rayleigh scattering, showed similar results with the present study. The kernel temperature was below 4,000 K at 1 μs after the laser pulse and rapidly decreased to 500 K [56]. Other researchers, who investigate the plasma temperature using the spectroscopic analysis, evaluated the plasma temperature is higher than 10,000 K until 1 μs after the laser pulse [57-66]. The paper, measured the temperature until 10 μs after the laser pulse,

evaluated the temperature was above 5,000 K, and converged to the specific values [62]. The temperature studied by the spectroscopic analysis converged to the specific value as time elapses [57-66]. Thus, the measurement limitation in the spectroscopic method may contribute to the temperature above 5,000 K at 10 μs [62].

Mulla et al. and Bedenue et al. have found that the kernel size increases with increasing E_{in} and ΔE [3,71]. The relationship between the kernel size and E_{in} and ΔE at their experiments is the same as the present work [Figs.6-12-6-14] [3,71]. The plasma length increases with increasing E_{in} and ΔE since the plasma expands toward the laser beam by the laser absorption due to the laser irradiance [Figs.6-2-6-7]. The high temperature of the plasma heats the mixture nearby the plasma [Figs.6-2-6-7,6-12-6-14]. Therefore, the initial size of the kernel expands with an increase in E_{in} and ΔE due to the increased plasma length [Figs.6-2-6-7,6-12-6-14]. Consequently, as E_{in} and ΔE are higher, the kernel size increases because the larger plasma widely heats the mixture [Figs.6-2-6-7,6-12-6-14]. However, the kernel size will not continuously increase with increasing E_{in} and ΔE and will converge to a specific size. Laser irradiance suddenly reduces since to increasing a laser beam diameter as the location is farther away from a focal point. If a laser beam diameter is sufficiently large that cannot bring laser absorption by laser irradiance, a plasma will not expand moreover.

From our ignition experiments and Mulla et al.'s work [71], if the E_{in} and ΔE are constant, the kernel size is almost constant during the early stage even the velocity increases [Figs.6-12-6-14]. Mulla et al. have found that the kernel development is identical at the constant E_{in} and ΔE and the different equivalence ratios during the early stage (0-100 μs) [71]. The initial size of the kernel is determined by E_{in} and ΔE [Figs.6-2-6-7,6-12-6-14]. The reason is a plasma heats a mixture and generates a kernel, and E_{in} and ΔE determine a plasma length. Thus, the kernel size during the early stage at the constant E_{in} and ΔE is identical even with different flow conditions [Figs.6-12-6-14] [71]. This is because the plasma size determines the initial kernel size, and the flow conditions do not significantly affect the kernel growth due to the small kernel surface area during the early stage.

7. PHENOMENOLOGICAL MODEL IN IGNITION OF FLOWING GASES

An energy balance involving the high temperature kernel generated by the volumetric deposition of energy and heat transfer to the flowing gases at a lower temperature is recognized to be complex. As a first step, we utilize the experimental data to understand these complex processes in conjunction with the energy balance described by Eq. (7.1).

$$E_{ig} = E_{loss}.$$
<div align="right">7.1</div>

In Eq. (7), E_{ig} is the ignition energy (the deposited energy), and E_{loss} is the energy loss by heat transfer. We compare energy losses with the measured MIE using Eq. (7.1) to understand the dominant energy loss in the ignition [Chapters 8 and 9]. The energy loss mechanisms from the ignition kernel include conduction, convection, and radiation. Lewis and von Elbe [82], Williams [84], and Turns [85] consider the energy loss to be from the surface of the spherical volume of hot gas (ignition kernel) generated by the ignition process. The heat transfer from the ignition kernel is through the temperature gradient established by the flowing gases at the surface. However, as a first step, as shown in Eq. (7.2), these complexities are folded into the definition of a coefficient h relating the energy loss by conduction, convection, and radiation across the kernel surface area, the temperature difference, and a time scale $\frac{dr}{dS}$ defined by the rate of outward propagation of the incipient ignition front.

$$E_{loss} = hA(T_k - T_u)\frac{dr}{dS}$$
<div align="right">7.2</div>

In Eq. (7.2), r is the kernel radius, and S is the flame speed (kernel propagation speed). We assume that the flame speed, S, is the same as the laminar flame speed when the kernel size is near its minimum radius (critical radius). Once the ignition is successful, the rate of outward propagation is assumed to be equal to the flame speed as described below in Eq. (7.3). The coefficient h is a multimode heat transfer coefficient including molecular conduction and radiation. The molecular conduction heat transfer is enhanced by the increase in temperature gradient caused by the free

stream flow. The heat transfer from the kernel to the surrounding flow is significantly enhanced by the low gradient within the kernel followed by the sharp gradient in the flow around the kernel. The contributions of conduction are estimated using the thermal conductivity of the mixture as discussed below and the contributions of radiation are estimated using an equivalent emissivity of the mixture based on the partial pressures of the participating species in the mixture. As a further approximation, the measured average temperature is designated to be the kernel temperature, T_k. Equation (7.2) includes a time scale of energy exchange approximately defined by the rate at which the kernel radius increases with respect to the rate of outward propagation $\frac{dr}{dS}$. The quantitative value for this time scale is approximated as:

$$\frac{dr}{dS} = \frac{R_{crit}}{S_L} \qquad 7.3$$

where R_{crit} is the minimum (critical) radius and S_L is the kernel propagation speed approximated to be the laminar premixed flame speed. The physical meaning of Eq. (7.3) is that the time scales of the ignition process is comparable to the time scale of the flame propagation process. The energy loss considering the molecular conduction heat transfer enhanced by the increase in temperature gradient caused by the free stream flow and substituting Eq. (7.3) into Eq. (7.2) is:

$$E_{loss,conv} = h_{conv}(4\pi R_{crit}^2)(T_k - T_u)\frac{R_{crit}}{S_L} = \frac{(k)Nu}{2R_{crit}}(4\pi R_{crit}^2)(T_k - T_u)\frac{R_{crit}}{S_L}. \qquad 7.4$$

The laminar flame speeds for the current operating conditions based on past experimental studies are utilized [156-160]. In order to calculate the forced convection heat transfer coefficient for the ignition process, a Nusselt number correlation applicable to all Prandtl numbers and for the current Reynolds number range of Re $< 10^5$ was utilized [175-178].

$$Nu = 2 + 0.5505Re^{0.5}Pr^{\frac{1}{3}}/[1 + (0.45/Pr)^{\frac{2}{3}}]^{\frac{1}{4}} \text{ for Laminar flow, and } 0 < Pr < \infty \qquad 7.5$$

$$Nu = 2 + 0.775Re^{0.5}\frac{Pr^{\frac{1}{3}}/(2\gamma + 1)^{0.5}}{\left[1 + \left(\frac{1}{(2\gamma + 1)^3 Pr}\right)\right]^{1/6}} \text{ for } Re < 10^5 \text{ and } 0 < Pr < \infty \qquad 7.6$$

$$\gamma = 1/Re^{0.25} \qquad\qquad 7.7$$

where Re is calculated using the minimum (critical) diameter ($2R_{crit}$) of the flame kernel, the bulk velocity, and the properties of the unburned mixture.

For significantly lower Reynolds numbers, natural convection influences the minimum ignition energy . In the absence of gravity or neglecting body forces, the limiting minimum value of the heat loss results from heat conduction. The heat conduction loss is estimated as [84,85]:

$$E_{loss,cond} = h_{cond} 4\pi R_{crit}^2 (T_k - T_u) \frac{R_{crit}}{S_L} = (k) 4\pi R_{crit}^2 \frac{(T_k - T_u)}{R_{crit}} \frac{R_{crit}}{S_L} \qquad 7.8$$

where, $h_{cond} = \left(\frac{k}{R_{crit}} \right)$ is the coefficient of heat transfer by conduction, k being the thermal conductivity of the flowing gas mixture.

Equations (7.4) and (7.8) are combined to yield Eq. (7.9):

$$E_{loss,cond} + E_{loss,conv} \qquad\qquad 7.9$$

$$= \frac{k}{R_{crit}} (4\pi R_{crit}^2)(T_k - T_u)\frac{R_{crit}}{S_L} + \frac{(k)Nu}{2R_{crit}} (4\pi R_{crit}^2)(T_k - T_u)\frac{R_{crit}}{S_L}$$

$$= \frac{k}{R_{crit}} (4\pi R_{crit}^2)(T_k - T_u)\frac{R_{crit}}{S_L}\left(1 + \frac{Nu}{2}\right).$$

Equation (7.9) includes heat transfer by natural convection in the limit of the ignition kernel and the molecular conduction heat transfer by the increase in temperature gradient caused by the free stream flow. Equation (7.9) represents the heat flux per unit time in the thermal boundary layer formed around the ignition kernel multiplied by its surface area.

For hydrocarbon fueled mixtures, participating gases such as CO_2, CO, and H_2O within the flame kernel emit radiation. For the present hydrogen air mixture, the radiative loss is solely from the H_2O molecules. For the hydrocarbon flames considered later in Chapter 8.5, the radiative loss includes emission from the product gas mixture containing both H_2O, CO_2, and CO. The radiative loss per unit volume in an optically thin limit is expressed as [179]:

$$q = 4\,\sigma(T_k^4 - T_u^4) \sum_i (p_i a_{pi})$$

<div align="right">7.10</div>

where σ is the Stefan-Boltzmann constant, p_i is the partial pressure of the participating species $i\ (= H_2O)$, and a_{pi} is the Planck mean absorption coefficient of the species $i\,(=H_2O,\ CO_2,$ and $CO)$ [179]. The radiative energy loss from the flame kernel to the surroundings is approximated as:

$$E_{loss,rad} = h_{rad} 4\pi R_{crit}^2 (T_k - T_u) \frac{R_{crit}}{S_L} = q\left(\frac{4\pi R_{crit}^3}{3}\right)\frac{R_{crit}}{S_L}$$

<div align="right">7.11</div>

where, $h_{rad} = \frac{4R_{crit}}{3}\sigma(T_k + T_u)\left(T_k^2 + T_u^2\right)\sum_i(p_i a_{pi})$ is the coefficient of heat transfer by radiation in the optically thin limit. The strong nonlinear dependence of the heat loss and the coefficient of heat transfer by radiation are noted.

Table 7-1. Froude number

V_{bulk} (m/s)	Fr
20.6	22,500
23.3	16,200
25.5	14,900
28.4	17,000
6	2,300
7	2,000
8	1,800
10	7,700
11	8,500
12	7,700
13	7,600
14	8,100

Froude number is defined as:

$$Fr = \frac{V_{bulk}^2}{gD_k} \qquad 7.12$$

where D_k is the kernel diameter ($2R_{crit}$). Table 7.1 illustrates the Froude number in the experimental conditions. The calculated Froude number is much larger than 1. Therefore, the effect of natural convection in the flow regime is very weak.

Radiative flux is expressed as [114]:

$$\nabla \cdot q_\eta = 4\pi \kappa_\eta I_{b\eta} - \beta_\eta \int_{4\pi} I_\eta(\hat{s})d\Omega + \sigma_{s\eta} \int_{4\pi} I_\eta(\hat{s}_i)d\Omega_i. \qquad 7.13$$

In the right-hand side, the first term is radiative energy stored in a control volume, the second term is radiation energy emitted from the control volume, and the third term is the radiation energy absorbed in the control volume. Using $\kappa_\eta = \beta_\eta - \sigma_{s\eta}$:

$$\nabla \cdot q_\eta = \kappa_\eta \left(4\pi I_{b\eta} - \int_{4\pi} I_\eta \, d\Omega \right) = \kappa_\eta \left(4\pi I_{b\eta} - G_\eta \right). \qquad 7.14$$

Equation (7.14) explains the radiative energy loss from a control volume is equal to emitted energy minus absorbed irradiation. If we consider the entire wavelength, the equation is expressed as:

$$\nabla \cdot q = \int_0^\infty q_\eta \, d\eta = \int_0^\infty \kappa_\eta \left(4\pi I_{b\eta} - G_\eta \right)d\eta = \kappa(4\sigma T^4 - G). \qquad 7.15$$

The Planck mean absorption coefficient, κ, is frequently used as a_p. The radiation loss between the temperature, T, and the surrounding temperature, T_{sur}, is:

$$q = 4 \, \sigma \cdot a_p (T^4 - T_{sur}^4). \qquad 7.16$$

The overall Planck mean absorption coefficient for gas mixture is calculated as

$$a_p = \sum_i a_{pi}(T)P_i \, .$$

<div align="right">7.17</div>

Substituting Eq. (7.17) into Eq. (7.16) is:

$$q = 4\,\sigma(T^4 - T_{sur}^4) \sum_i (P_i a_{pi}) = [W/m^3] \, .$$

<div align="right">7.10</div>

This equation including Planck mean absorption coefficient has most popularly used for optically thin flame instead of complicated band models to calculate radiative values [179]. Thus, this paper is applied the optically thin flame model to calculate the radiation loss.

8. ENERGY BALANCE BETWEEN MINIMUM IGNITION ENERGY AND ENERGY LOSS UNDER TURBULENT FLOW

8.1 Experimental Conditions

Ignition experiments performed to study the effect of bulk velocity on minimum ignition energy (MIE) in the jet burner [Fig.2-2]. The turbulence intensities are nearly constant at the experimental conditions to avoid the impact of turbulence intensity on MIE [Table 8-1]. The laser-induced spark is located in the axis of the burner. Premixed air and hydrogen flow out through the burner exit. The ignition experiment was conducted at atmospheric pressure and temperature. A height of the laser-induced spark is 9 mm from the burner exit. The equivalence ratio, ϕ, is 0.9. The ignition probability at the experimental conditions was 100 %. The four bulk velocities are used (20.6, 23.3, 25.5, and 28.4 m/s) [Table 8-1]. The corresponding turbulence intensities in the bulk velocities are 3.3± 0.2 % [Table 8-1]. This flow condition permits to study the ignition experiments without the effect of the turbulence intensity. The turbulence intensities were measured through the PIV in the current study [Chapter 3]. The detailed experimental conditions are shown in Table 8-1.

Table 8-1. Experimental conditions for ignition test

Jet	V_{bulk} (m/s)	ϕ	Blockage ratio (%)	Ignition height (mm)	Re	Turbulence intensity (%)
1	20.6	0.9	62	9.0	2940	3.32
2	23.3	0.9	62	9.0	3330	3.33
3	25.5	0.9	62	9.0	3640	3.32
4	28.4	0.9	62	9.0	4050	3.48

8.2 Effect of Velocity on Minimum Ignition Energy

Figure 8-1 shows the effect of the flow velocity on the MIE. The flow velocity is varied between 20 m/s and 29 m/s [Table 8-1]. Increasing the flow velocity increases the MIE [Fig.8-1]. The trend of the MIE indicates that the higher laser energy needs to ignite the mixture as the flow velocity is faster. The relationship between the ignition energy and the velocity is consistent with the results reported in Refs. [1,3-6]. The measured MIE values in the present work are greater than

the experimental result, 0.15 mJ, studied by Syage et al. [73]. They performed the experiments in a constant volume chamber [73]. The difference between the present study and their work means that the flow velocity significantly affects the MIE.
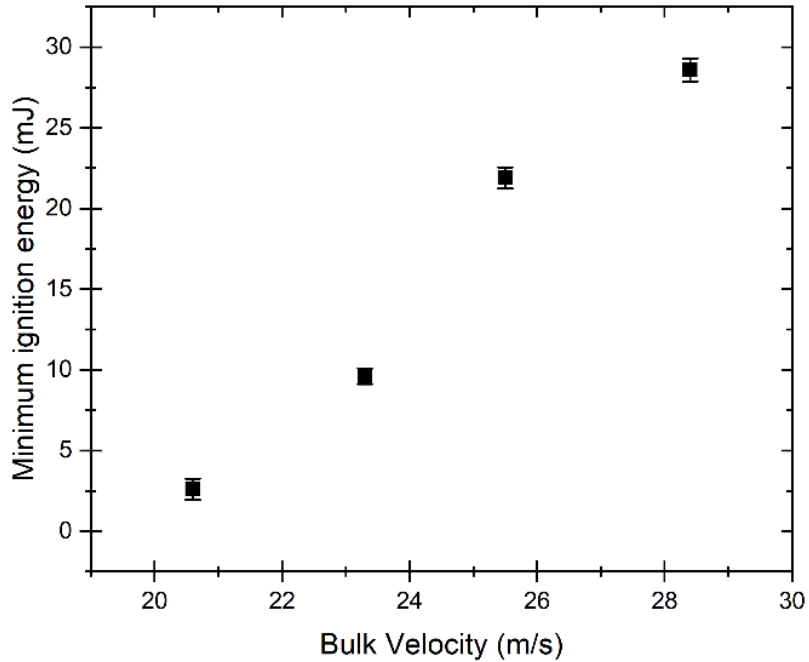
Fig.8-1. Effect of bulk velocity on MIE.

8.3   Kernel Growth

8.3.1   Experimental Conditions

Ignition experiments were performed to investigate a minimum (critical) radius and kernel growth. Experimental conditions were the same with the MIE experiments under the turbulent flows [Table 8-2]. The measured MIE was used for the ignition tests [Table 8-2]. The kernel growth was visualized through the Schlieren images and the IR camera [Figs.8-2-8-9]. The characteristics of the high speed camera for the Schlierne images were: frame rate-100,000 fps; resolution- 0.2 mm/pixel. The characteristics of the IR camera were: frame rate- 924 fps; resolution- 0.314 mm/pixel. The visualized images in Figs.8-2-8-9 were obtained from a single event. The experiments ran 20 times at each time step.

Table 8-2. Experimental conditions for kernel development.

Jet	V_{bulk} (m/s)	ф	Blockage ratio (%)	Ignition height (mm)	Re	Turbulence intensity (%)	E_{ig} (mJ)
1	20.6	0.9	62	9.0	2940	3.32	2.6
2	23.3	0.9	62	9.0	3330	3.33	9.6
3	25.5	0.9	62	9.0	3640	3.32	21.9
4	28.4	0.9	62	9.0	4050	3.48	28.6

8.3.2 Experimental Results

After the laser pulse, the laser irradiance increases and the plasma is generated by the laser pulse [35,104]. The more detailed procedure regarding the plasma generation is explained in Chapters 1.6.1 and 6.2.1. As the laser energy difference, ΔE, is lower, the plasma size decreases due to the weak laser absorption, and the plasma structure is close to a spherical [Figs.6-2-6-7]. In contrast, as the laser energy difference, ΔE, is higher, the plasma increases the size and expands toward the laser beam due to the strong laser absorption, and the plasma shape is similar to an infinity symbol structure [Figs.6-2-6-7]. A plasma has a high temperature, heats reactants, and generates a kernel. Therefore, a plasma structure and size determine an initial kernel size and a kernel temperature distribution during the early reaction steps [Figs.6-12-6-14].

In jet 1, a kernel is produced with one high-intensity bowl having a high temperature [Figs.8-2,8-3]. The kernel temperature increases from the center to the edges as time elapses because the energy transfer between the high-intensity bowl and reactants of the surrounding [Figs.8-2,8-3].

In jets 2-4, kernels are generated with two high-intensity bowls [Figs.8-4-8-9]. The plasma shape is changed from a spherical to an infinity symbol structure as the laser energy difference is higher [Figs.6-2-6-7]. Thus, the plasma structure leads to two high-intensity bowls [Fig.6-15]. The temperature in the kernel especially is high at the two high-intensity bowls since the reactants in the regions are heated by the plasma [Figs.6-2-6-7,8-4-8-9]. The energy transfer actively occurs between the two high-intensity bowls and the reactants of the surrounding [Figs.6-2-6-7,8-4-8-9]. Therefore, the kernel temperature increases from the edges nearby the two-high intensity bowls to the center as time elapses [Figs.6-2-6-7,8-4-8-9]. The distance between the two-high intensity bowls is farther away as the laser energy difference is higher [Figs.6-2-6-7,8-4-8-9]. This is

161

because plasma expansion toward a laser beam is stronger at a high laser energy difference than a low value due to a high laser irradiance of the laser beam [Figs.6-2-6-7][35,104]. Figure 8-10 at time = 4.3 ms after the ignition depicts an establish jet flame with four different ignition energies corresponding to the four advective velocities. Figure 8-10 shows that the MIE results in a stable jet flame for multiple jet velocities.
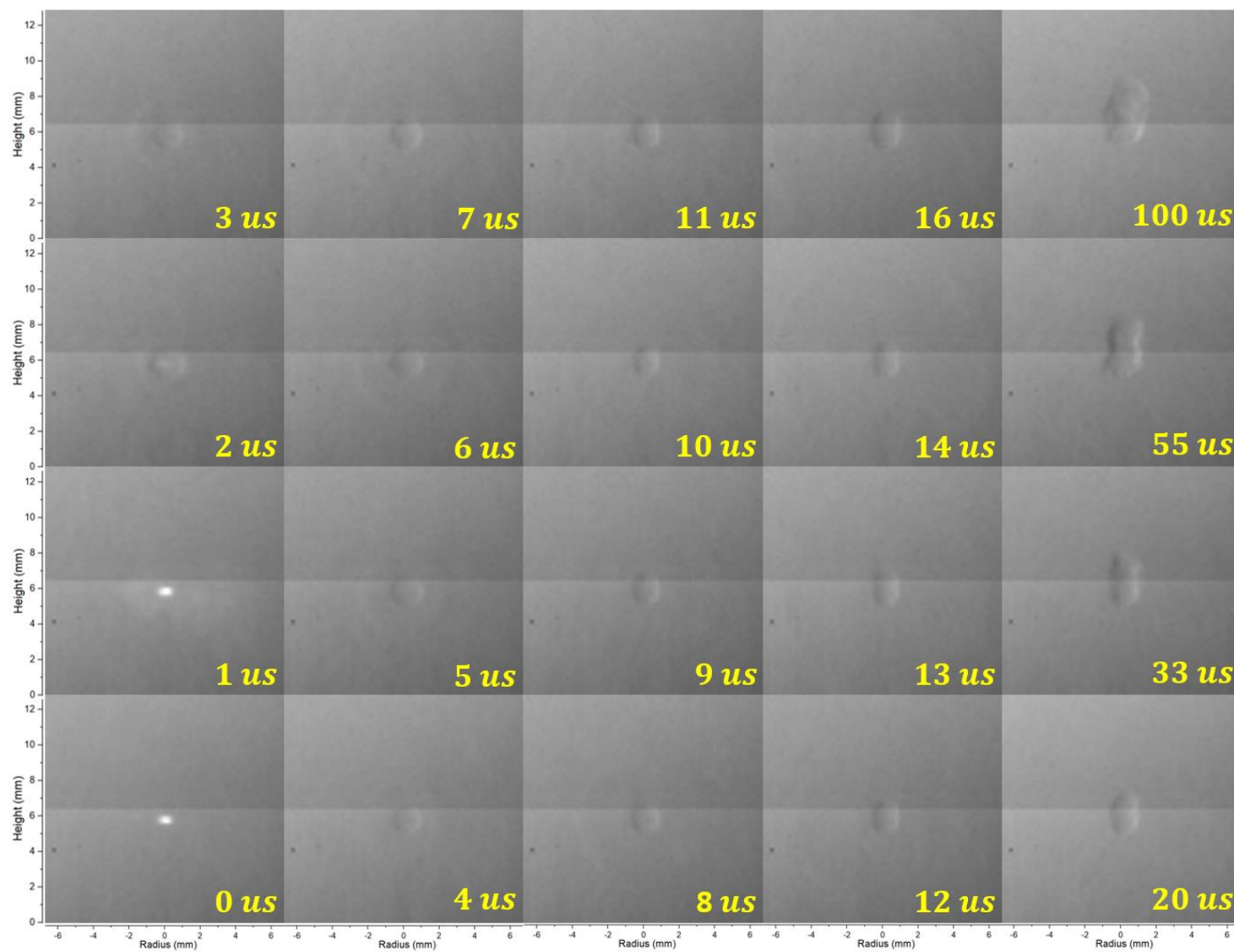
Fig.8-2. Schlieren images of kernel growth in the case 1.
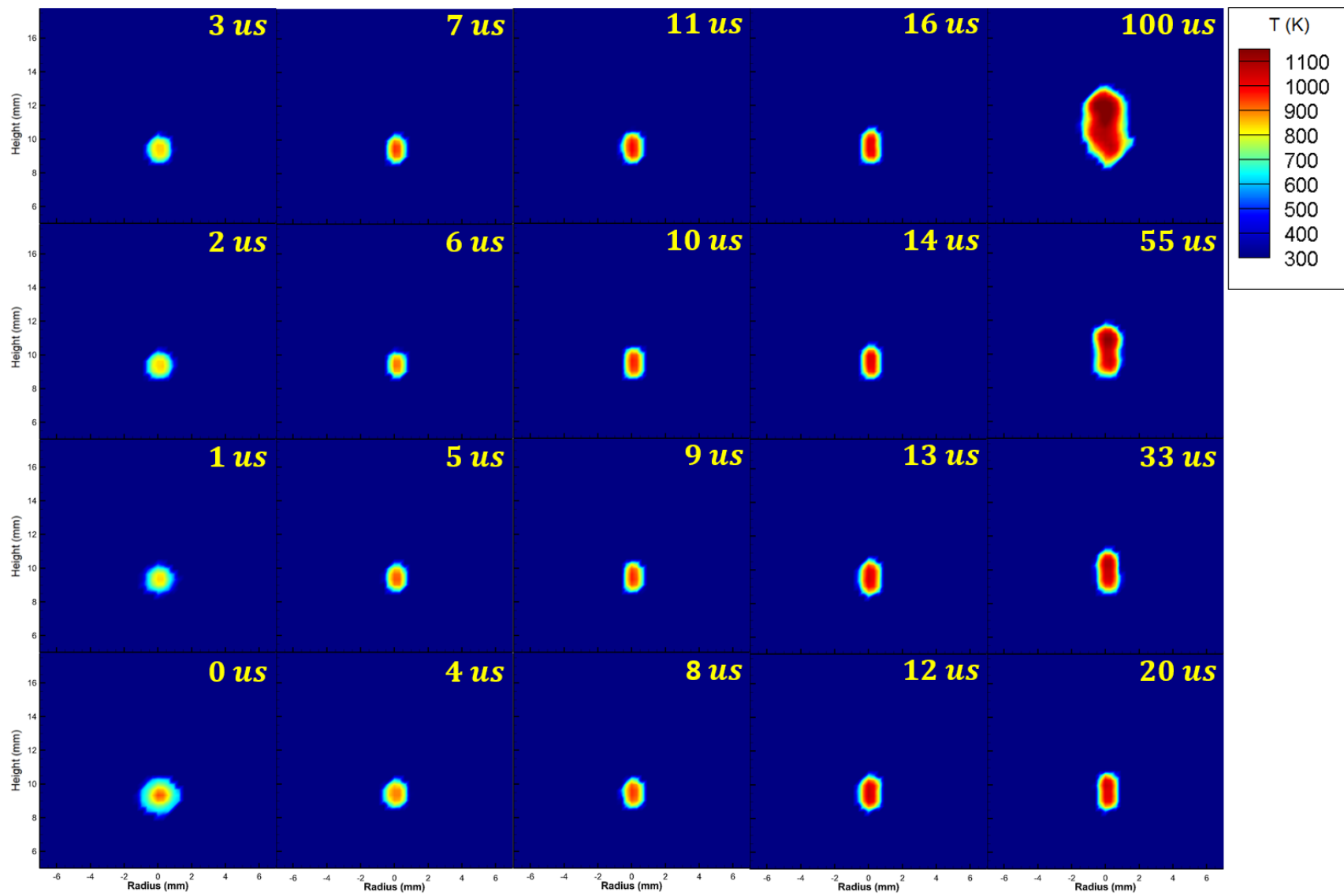
Fig.8-3. Temperature of kernel growth in the case 1.
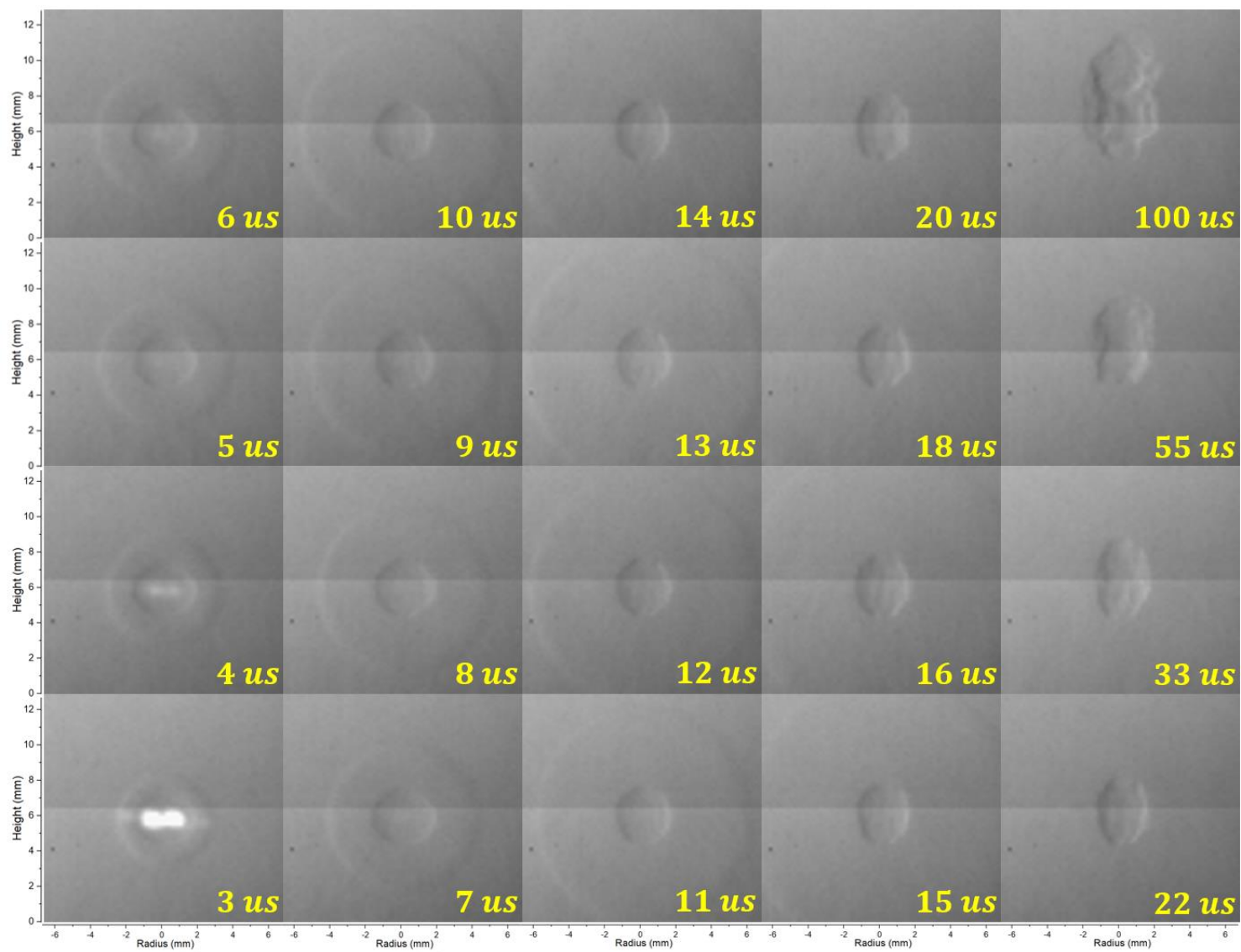
Fig.8-4. Schlieren images of kernel growth in the case 2.
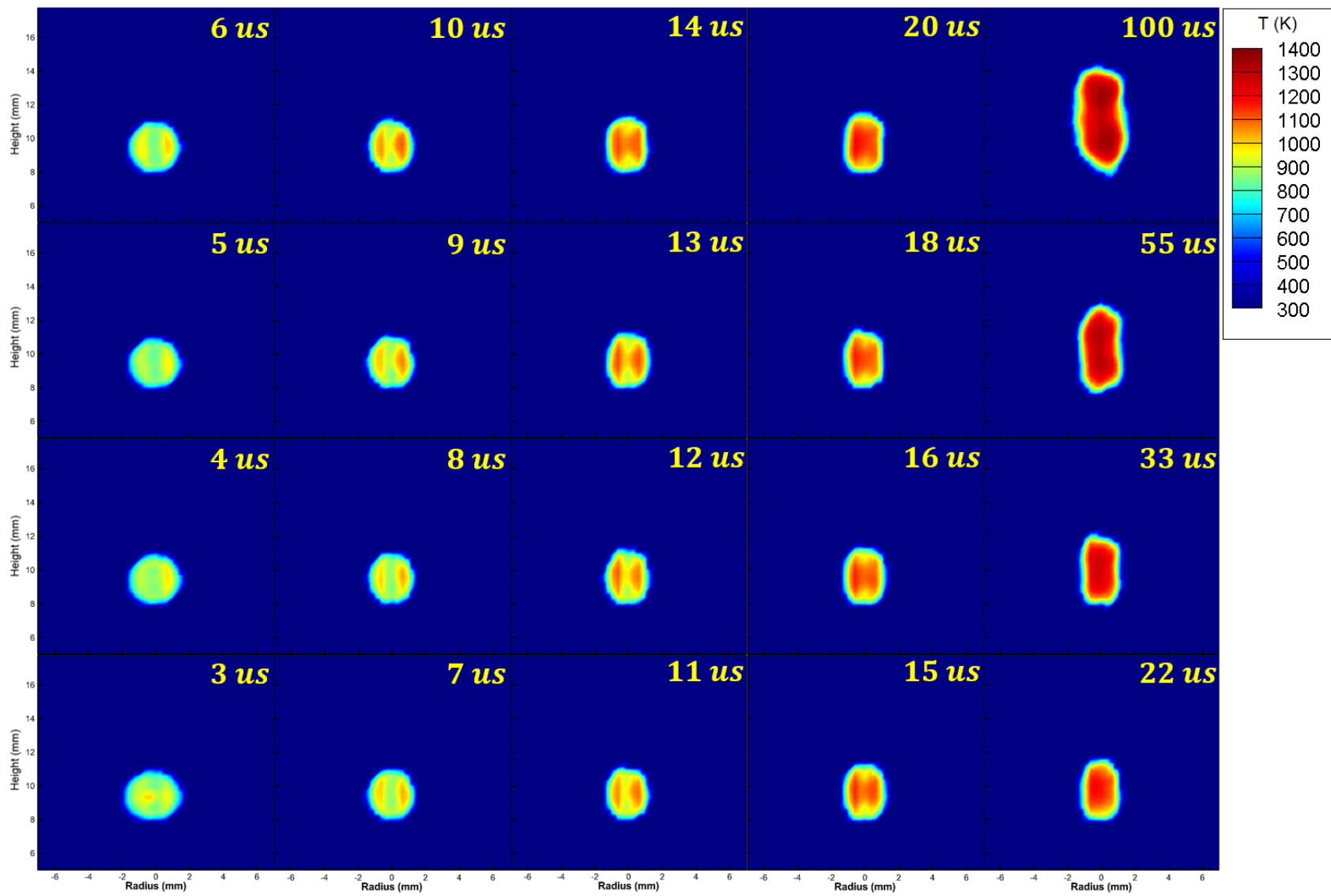
Fig.8-5. Temperature of kernel growth in the case 2.
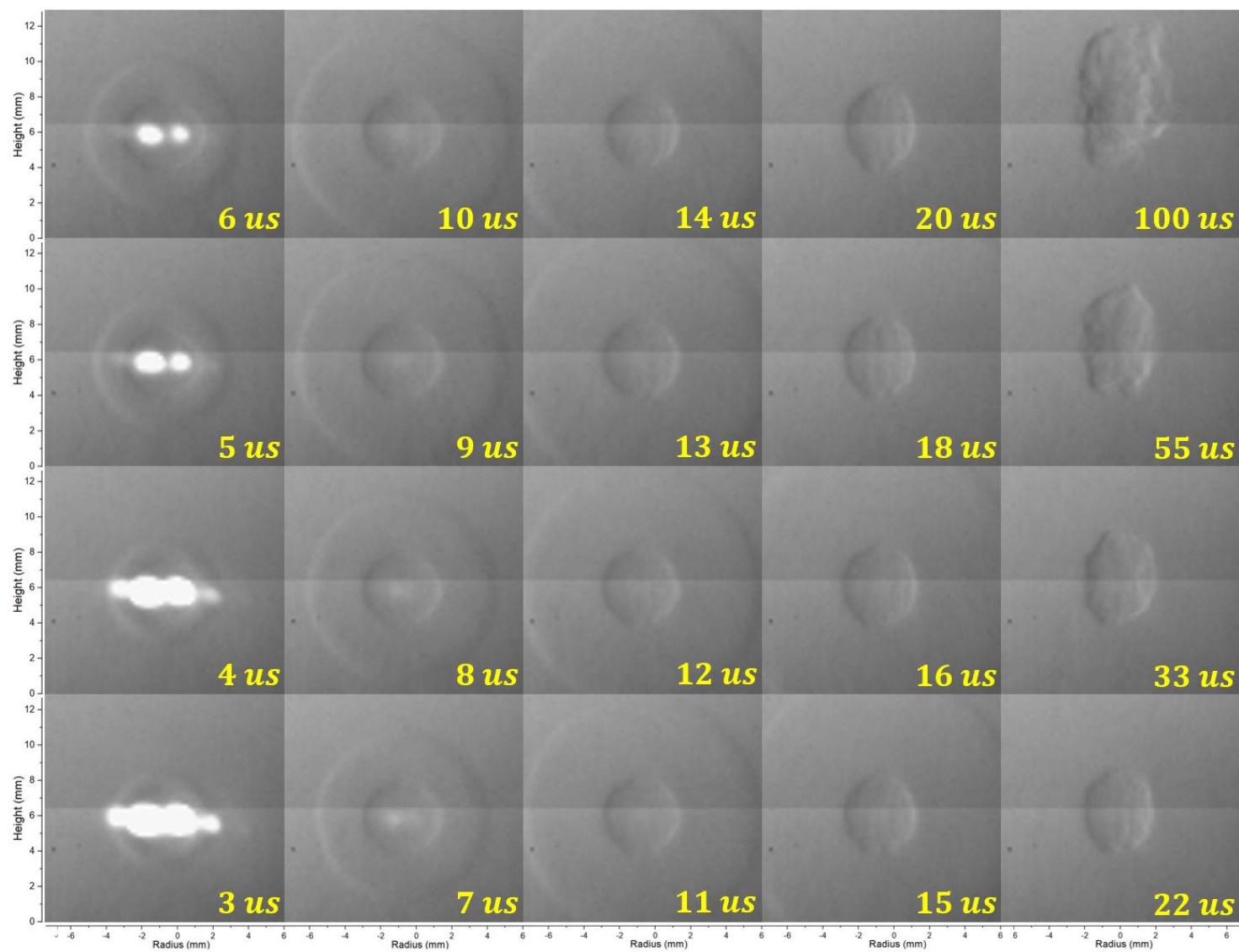
Fig.8-6. Schlieren images of kernel growth in the case 3.
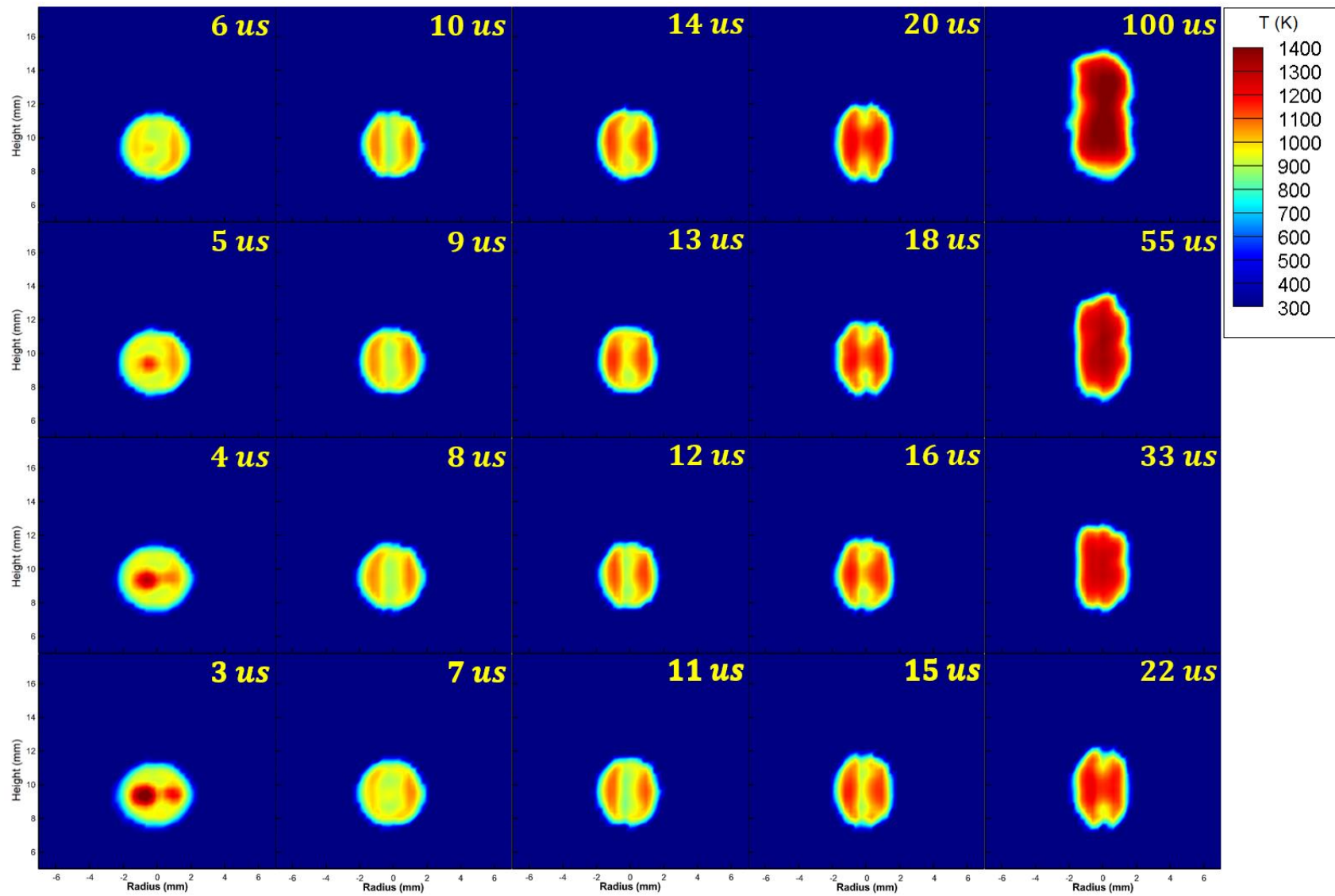
Fig.8-7. Temperature of kernel growth in the case 3..
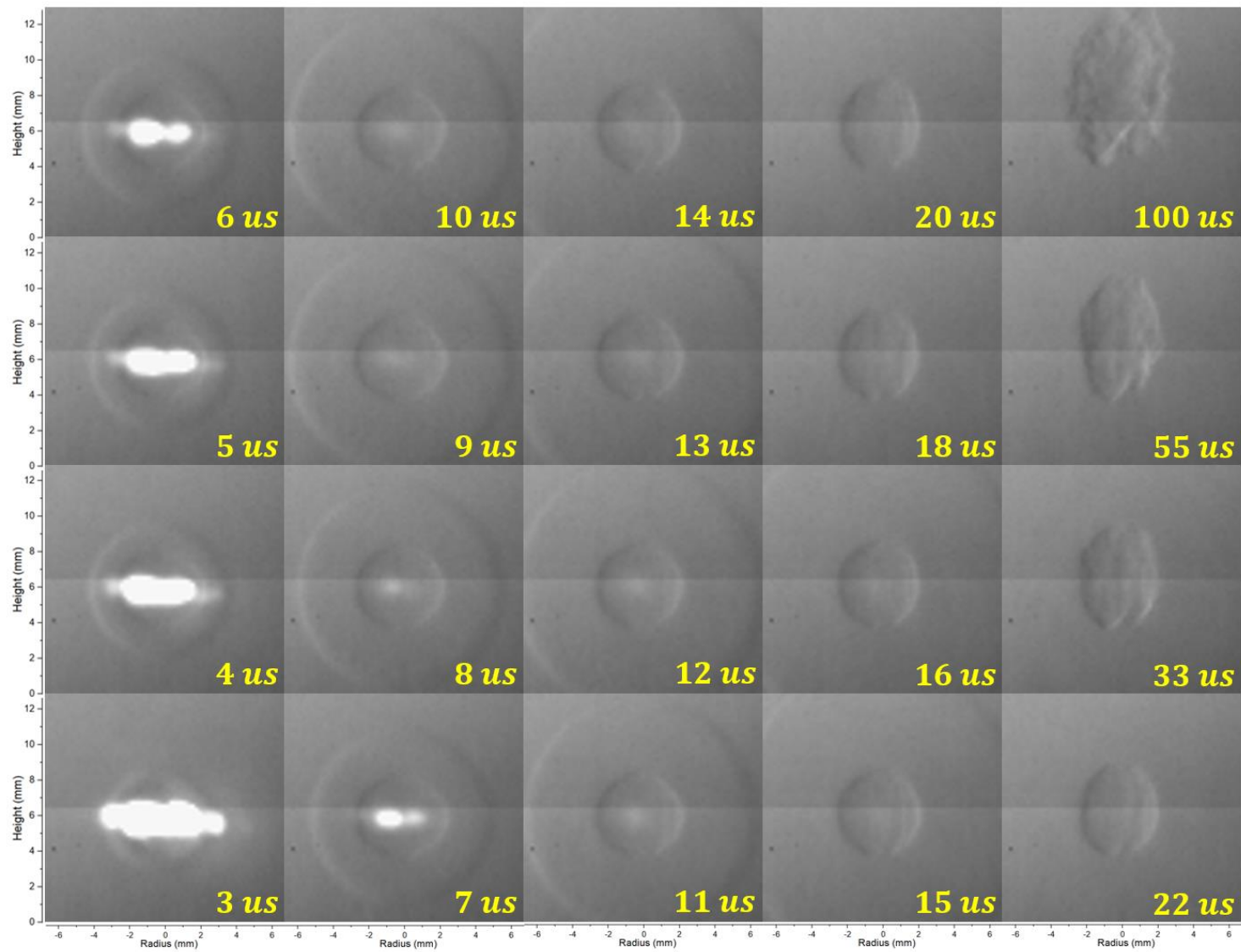
Fig.8-8. Schlieren images of kernel growth in the case 4.
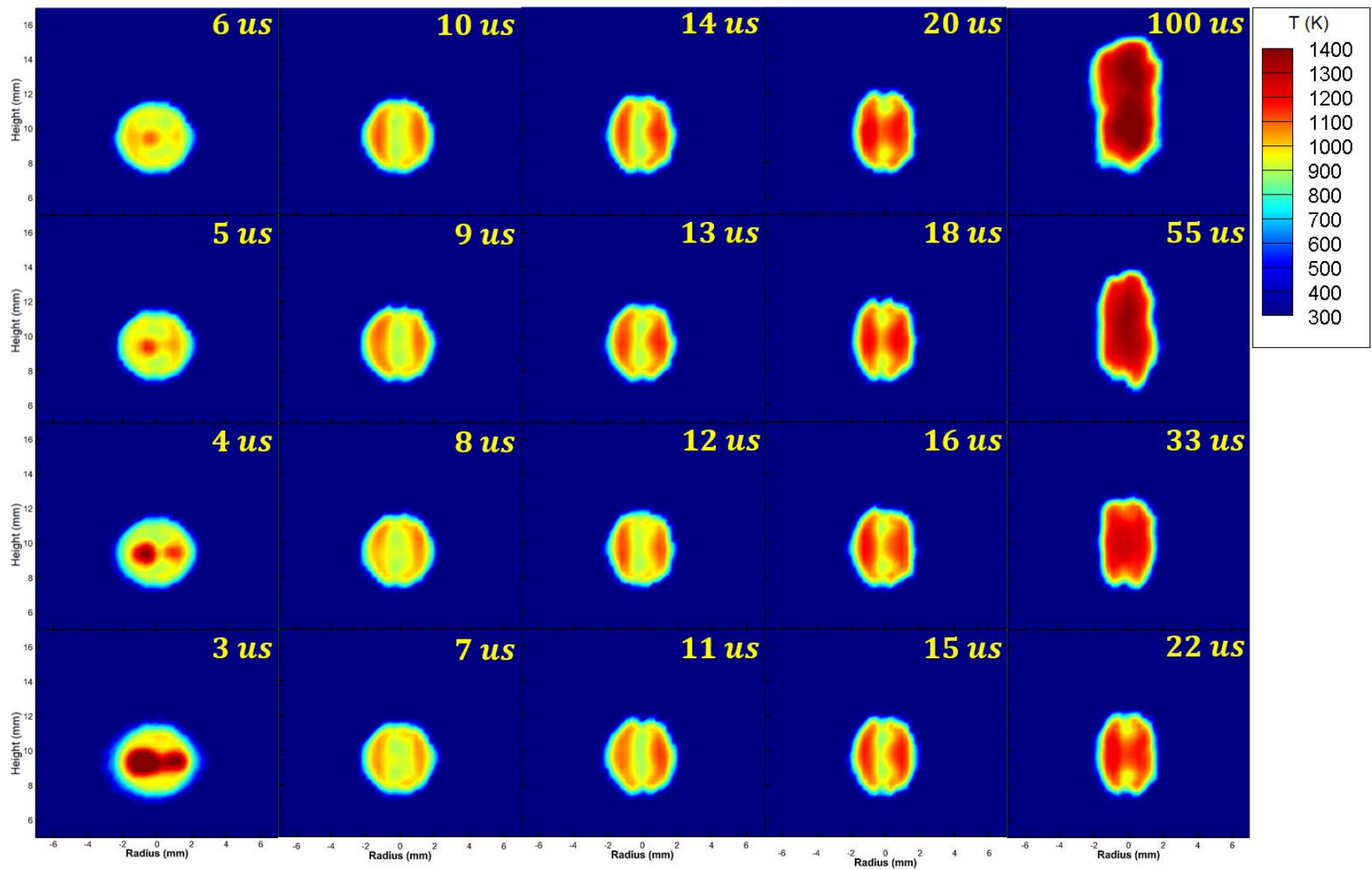
Fig.8-9. Temperature of kernel growth in the case 4.
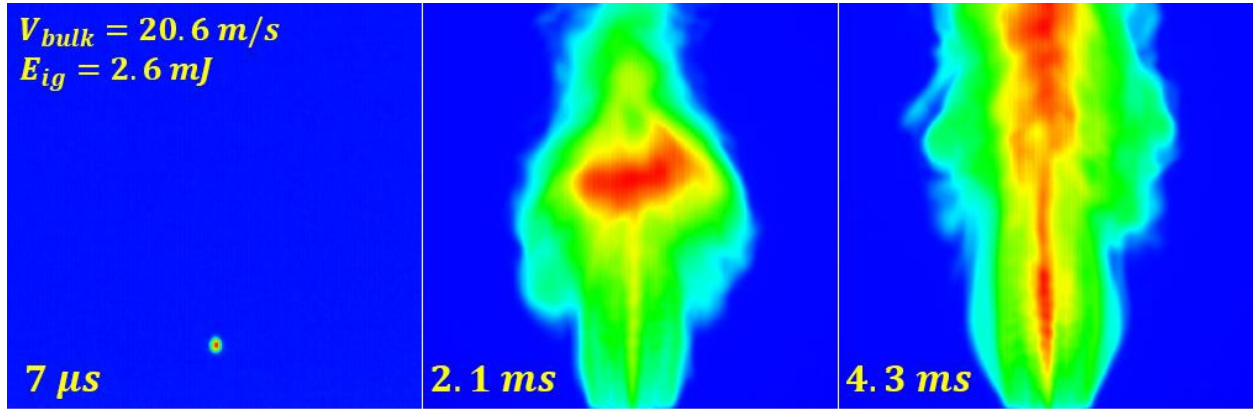
(a)
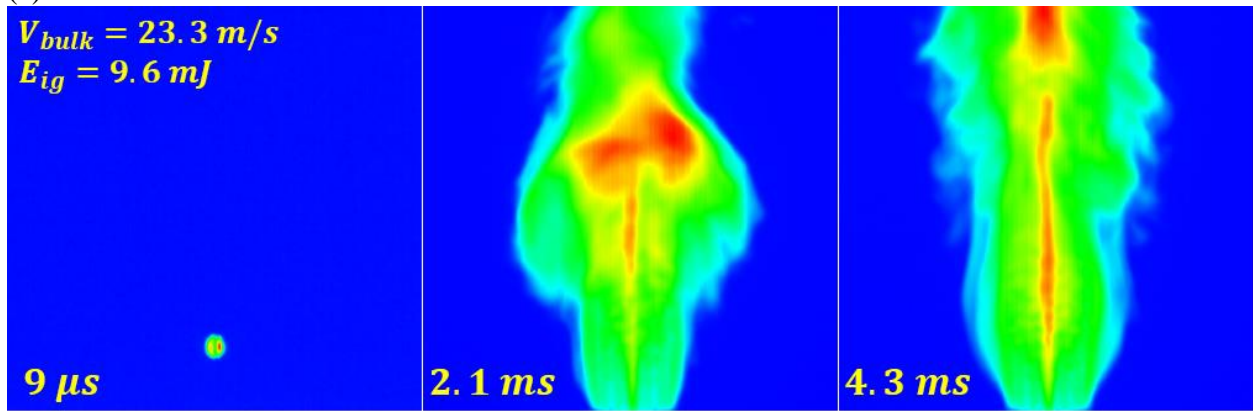
(b)
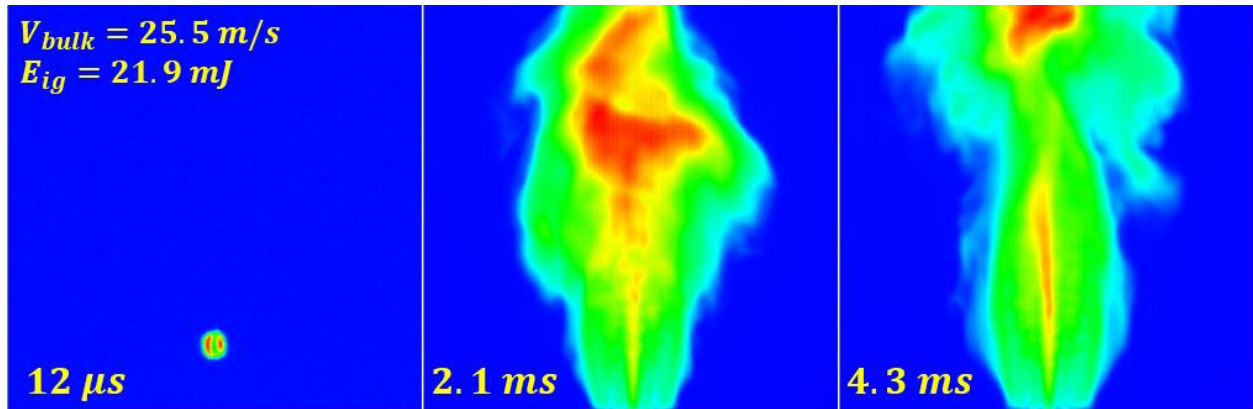
(c)

Fig. 8-10. Flame kernel development, infrared camera images, (a) $V_{bulk} = 20.6\ m/s$, $E_{ig} = 2.6\ mJ$, (b) $V_{bulk} = 23.3\ m/s$, $E_{ig} = 9.6\ mJ$, (c) $V_{bulk} = 25.5\ m/s$, $E_{ig} = 21.9\ mJ$, and (d) $V_{bulk} = 28.4\ m/s$.

Fig.8-10 continued
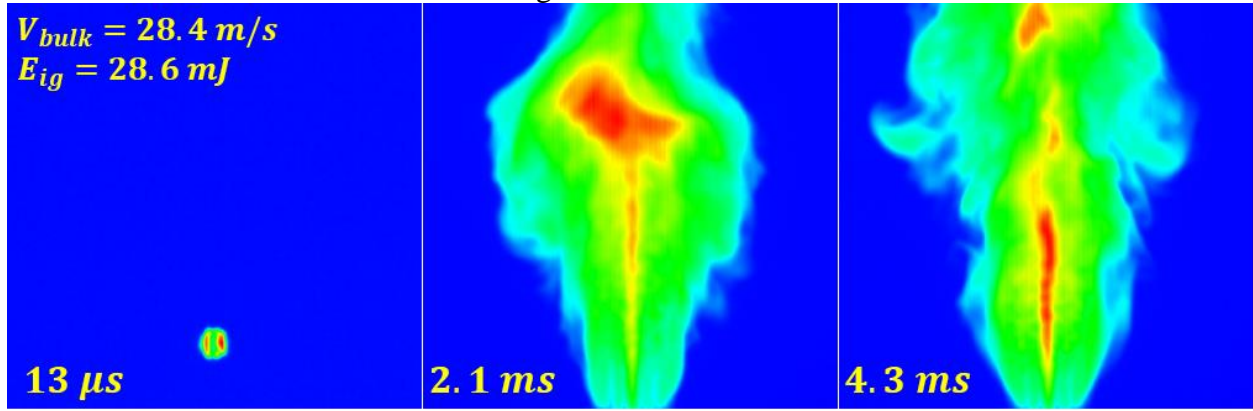
(d)

8.4 Effect of Velocity on Kernel Growth

8.4.1 Experimental Conditions

The Schlieren imaging was used to study the effect of velocity on the kernel development. An exposure time capturing the images was $2\,\mu s$. The frame speed was 100,000 per second. The array size of the high-speed camera was 128×64 pixel^2. A resolution of 0.214 mm/pixel resulted from the arrangement.

Table 8-3 Experimental conditions for the effect of velocity on kernel growth.

V_{bulk} (m/s)	ϕ	Blockage ratio (%)	Focal length of lens (mm)	Ignition height (mm)	Re	ΔE (mJ)
8	0.9	62	50	9.0	1140	9.0
14	0.9	62	50	9.0	2000	9.0
23.3	0.9	62	50	9.0	3330	9.0

The effect of velocity on the kernel growth was investigated during the early stage $(0 - 200\,\mu s)$ [Fig. 8-11]. Experiments were conducted at three bulk velocities: 8, 14, and 23.3 m/s, which change to the Reynolds number: Re = 1140, 2000, and 3330, respectively [Table 8-3]. The nozzle diameter of the burner and the bulk velocity at the burner exit were used to calculate the Reynolds number. Detailed experimental conditions are provided in Table 8-3. The Schlieren images were captured at the time delays after the laser pulse: 10, 20, 30, 70, 100, and 200 μs [Fig.

8-11]. The height of the laser-induced spark was 9 mm above the burner exit. The used laser energy difference, ΔE, was constant as 9.0 mJ.

8.4.2 Results
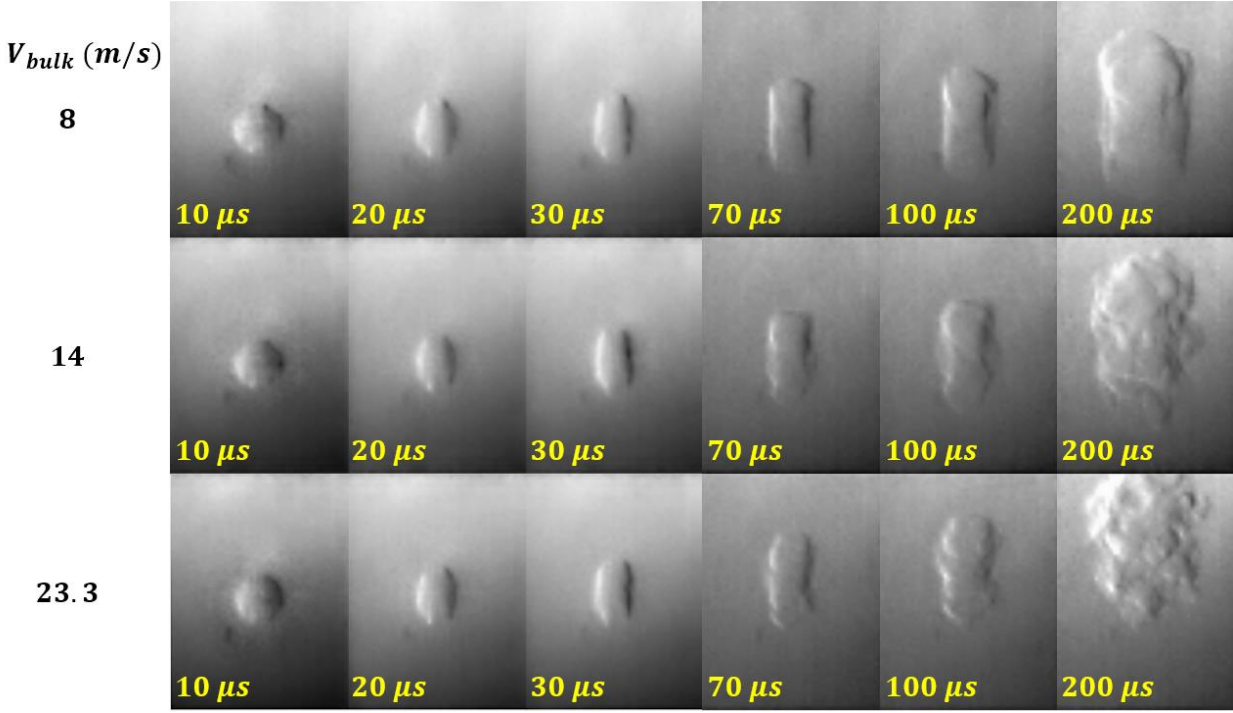
Fig. 8-11. Effect of velocity on Kernel development, the image size is $11.4\ mm \times 15.2\ mm$

Schlieren images of the flame kernels for three representative bulk jet velocities: 8, 14, and 23.3 m/s showing the density differences for the time interval $0 - 200\ \mu s$ following the laser energy deposition of $\Delta E = 9.0$ mJ are shown in [Fig. 8-11]. The jets with exit Re = 1140 and 2000 involve near-laminar flow at the burner exit and the jet with an exit Re = 3330 involves relatively low Reynolds number turbulent flow. The laser energy deposition of $\Delta E = 9.0$ mJ is significantly higher than the minimum ignition energy for the Re = 1140 and 2000 jets and close to the minimum ignition energy for the Re = 3330 jet. Consistent with the jet exit conditions, all three ignition kernels show minimal wrinkling of the schlieren surface for times less than 30 μs. For times within the 0-30 μs interval following the laser pulse, the kernel size does not change with the increases in the bulk exit velocity [Fig. 8-11]. Mulla et al. [71] also observed nearly constant kernel size for

a range of mixture velocities for the 0-100 μs time interval following the laser pulse. In laser-induced spark ignition, deposited laser energy governs the kernel growth during very early stages. Velocity, equivalence ratio, turbulence do not affect the kernel development since the kernel size is very small [71]. In other words, deposited laser energy influences the kernel during very early stages after laser pulse instead of velocity or turbulence. The Re = 3330 jet shows a wrinkled surface for times longer than 30 μs. The lower Reynolds number jets show wrinkling of the schlieren surfaces at much longer times of 70, 100, and 200 μs. As time elapses, the kernel grows and then velocity and turbulence intensity influence the kernel. The bulk velocity and fluctuation velocity both significantly affect kernel growth. The ignition kernel growth rate increases with bulk velocity at times longer than 30 μs most likely because of the effects of surface wrinkling [Fig. 8-11][71]. Axial advection of the heated material elongates the initial spherical kernels into ellipsoidal shapes for all three jets at times longer than 10 μs [Fig. 8-11].

8.5   Eenergy Balance

8.5.1   Experimental Conditions for Schlieren images, Infrared images, and Rayleigh Scattering

A minimum (critical) radius is a radius of a spherical volume in a kernel [180-184]. The kernel having the minimum (critical) radius can survive and propagate to a flame without aid [180-184]. When energy is minimum ignition energy (MIE) at a flow condition, a radius of a spherical volume is a minimum (critical) radius [184]. The Schlieren image was conducted with the measured MIE to find the minimum (critical) radius and the elapsed time after the laser pulse when the shape of the kernel was spherical [Fig.8-12] [Table 8-4]. A delay time of the high-speed camera was changed from 0 to 9 μs to collect images separated 1 μs. A frame speed was 100,000 per second. An array size of the high-speed camera was 256 × 64 Pixel^2. A resolution was 0.2 mm/pixel. Reynolds number was calculated using the minimum (critical) diameter, the bulk velocity, and unburnt mixture properties [Table 8-4].

The measured MIE at each case was utilized to study the kernel temperature. The Rayleigh scattering and the radiation intensity measurements were performed 50 times at each case to measure the kernel temperature. The kernel temperature was measured through the Rayleigh scattering and the IR camera at the elapsed time [Fig.8-13]. The characteristics of the ICCD camera

for the Rayleigh scattering were: gate time- 200 ns; resolution- 77 µm/pixel. The characteristics of the IR camera were: pixel count- 176×172 pixel^2; resolution- 0.33 mm/pixel; frame rate – 938 fps. The measured average temperature using the Rayleigh scattering and the IR camera agrees within 5 % [Fig.8-13][Table 8-4]. In the present work, the kernel temperature obtained from the Rayleigh scattering is used to calculate the energy loss in the flowing gases.

8.5.2 Results
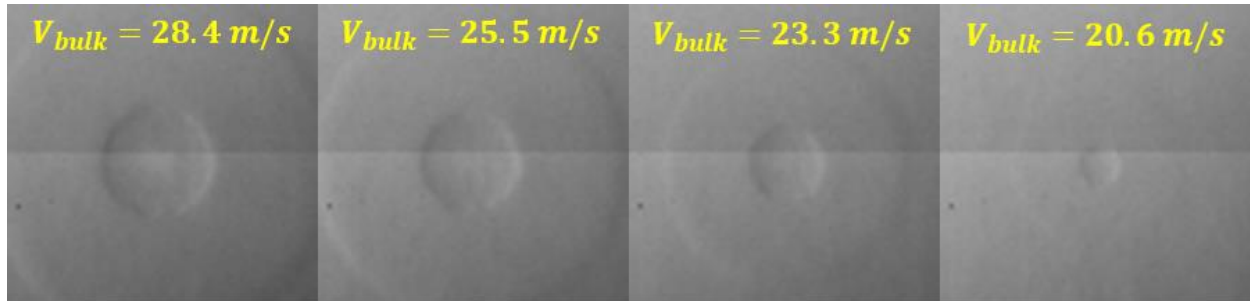
Fig.8-12. Minimum (critical) radius, the image size is $12.8\ mm \times 12.8\ mm$.

Figure 8-12 shows schlieren images of the incipient ignition kernel for the four bulk velocities for energy deposition corresponding to the MIE depicted in Fig. 8-1. The size of the kernels resulting from laser energy deposition values below those depicted in Fig. 8-12 do not lead to a sustainable flame. Therefore, the kernel radius of the spherical volume corresponding to the minimum ignition energy is defined as the minimum (critical) radius for ignition. With increasing bulk velocity, the critical radius increases significantly along with the increases in the minimum ignition energy. Table 8-4 shows the quantitative values of the minimum (critical) kernel radius for the four bulk velocities. The minimum (critical) kernel radius increases by approximately a factor of 2.5 with the increases in the advective velocity.

(a)

(b)
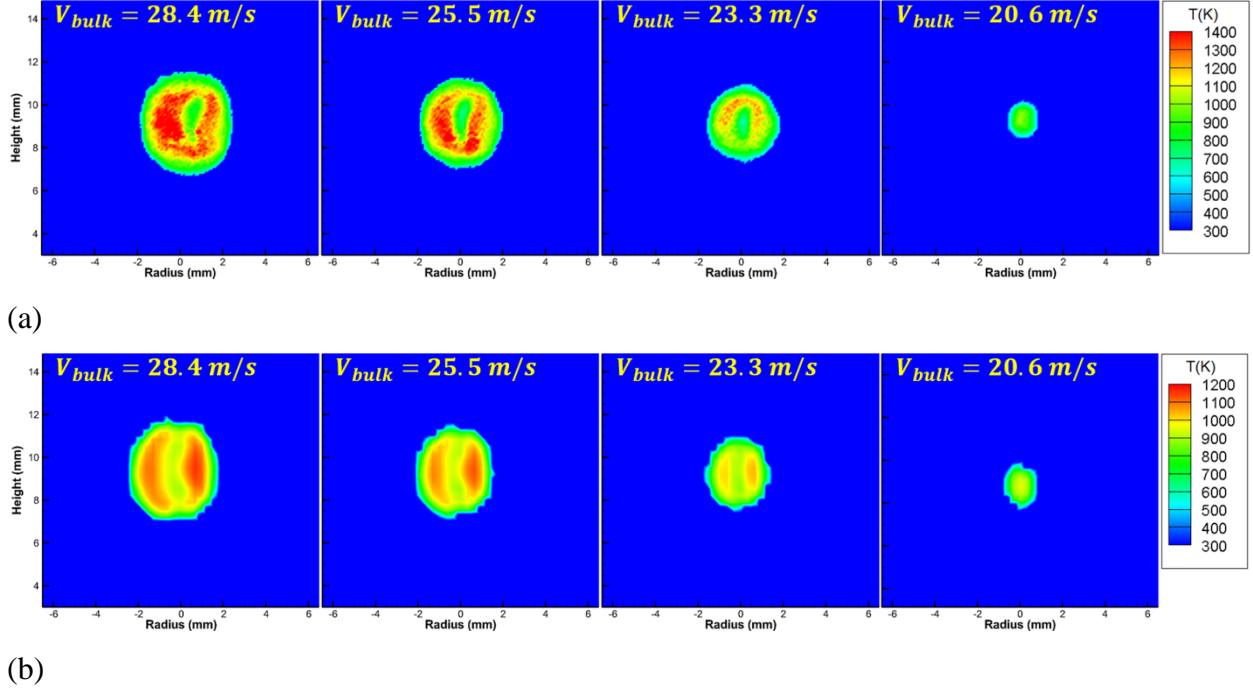
Fig.8-13. Kernel temperature (a) Rayleigh scattering, (b) IR camera.

Table 8-4. Experimental conditions and experimental results.

Jet	V_{bulk} (m/s)	E_{ig} (mJ)	R_{crit} (mm)	Time delay (μs)	$T_{k,R}$ (K)	$T_{k,IR}$ (K)	Re	$E_{loss,conv,S_L}$ (mJ)	$E_{loss,conv,S_t}$ (mJ)	$E_{loss,cond}$ (mJ)	$E_{loss,rad}$ (mJ)	$E_{loss,total,S_L}$ (mJ)
1	20.6	2.6	0.96	7	745	721	1950	1.63	0.4	0.14	5×10^{-4}	1.63
2	23.3	9.6	1.71	9	840	832	3930	8.77	1.9	0.54	0.01	8.78
3	25.5	21.9	2.22	12	924	892	5570	20.22	4.3	1.05	0.03	20.25
4	28.4	28.6	2.42	13	975	920	6770	28.55	5.3	1.35	0.04	28.59

Figure 8-13 depicts the measurements of incipient ignition kernel temperatures based on Rayleigh scattering ($T_{k,R}$) in the top panel and those based on the deconvolution of the measured infrared intensity ($T_{k,IR}$) in the bottom panel. The images depicted in Fig. 8-13 are ensemble averages of 50 laser pulses with constant ignition energy and advective velocity. Both the time elapsed after the laser pulse and the minimum size of the ignition kernel increase with increasing advective velocity.

The highest temperatures measured using Raleigh imaging reach 1400 K for all four advective velocities. The highest temperatures measured using the infrared imaging reach 1200 K. The quantitative differences between the measurements are because of the path integrated nature of infrared imaging and the differences in the spatial resolution of the two techniques. The

176

incipient ignition kernels depict an ellipsoidal ring like structure marking the regions of highest temperatures and decrease with steep gradients in all directions with a clearly defined outermost ring corresponding to a temperature of 500 K. The size of the ellipsoidal ignition kernels and of the highest temperature ellipsoidal rings within these kernels increase with increasing the deposited laser energy. The high temperature ellipsoidal rings are related to the plasma structure. Further, the ellipsoidal rings show variations in temperatures around their circumference with the higher temperatures aligning with the angles corresponding to the direction of laser propagation.
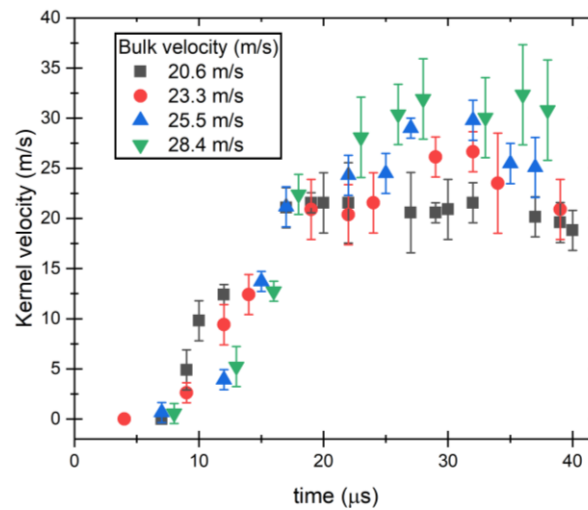
Fig. 8-14. Kernel velocity.

The kernel velocity is measured by tacking the kernel location versus time using the schlieren images. The time range examined for the kernel velocity is from 0 to 40 μs. Figure 8-14 shows the kernel velocity moving by the jet flow. The kernel is moved by the jet flow velocity coming from the burner exit. However, the kernel needs the response time to become a similar velocity with the jet velocity. The kernel size increases with the bulk velocity due to the increased ignition energy [Fig. 8-12] [Table 8-4]. Therefore, the response time is longer as the bulk velocity is faster due to the increased kernel size [Fig. 8-14]. Especially when the kernel is the critical radius, the kernel velocity is lower than the jet flow velocity [Fig. 8-14]. Therefore, the jet flow velocity around the kernel is not the same as the kernel velocity. Therefore, we can assume heat transfer occurs in the kernel by the turbulent flow around the kernel when the kernel is the critical radius.

The phenomenological model described in Chapter 7 is calibrated using approximate interpretations of the experimental data and then evaluated by comparing the computed MIE with the experimental results for a range of burner exit velocities. The model is evaluated further by extending it to the calculation of MIE for fuel rich hydrocarbon air mixtures.

Figure 8-15 and Table 8-4 illustrate a comparison of the ignition energy with the energy losses considering the laminar flame speed ($S_L = 1.79 \, m/s$) [156-160] and the turbulent flame speed [13]. The turbulent flame speed is calculated using a correlation based on experimental data by Koroll et al. [Eq. (4.1)] [13].

$$\frac{S_T}{S_L} = \left[1 + 16\left(\frac{u'}{S_L}\right)^2\right]^{0.5} + \left[1 - exp\left(-\frac{u'}{S_L}\right)\right] \cdot \frac{\frac{\rho_u}{\rho_b} - 1}{\sqrt{3}}. \qquad 4.1$$
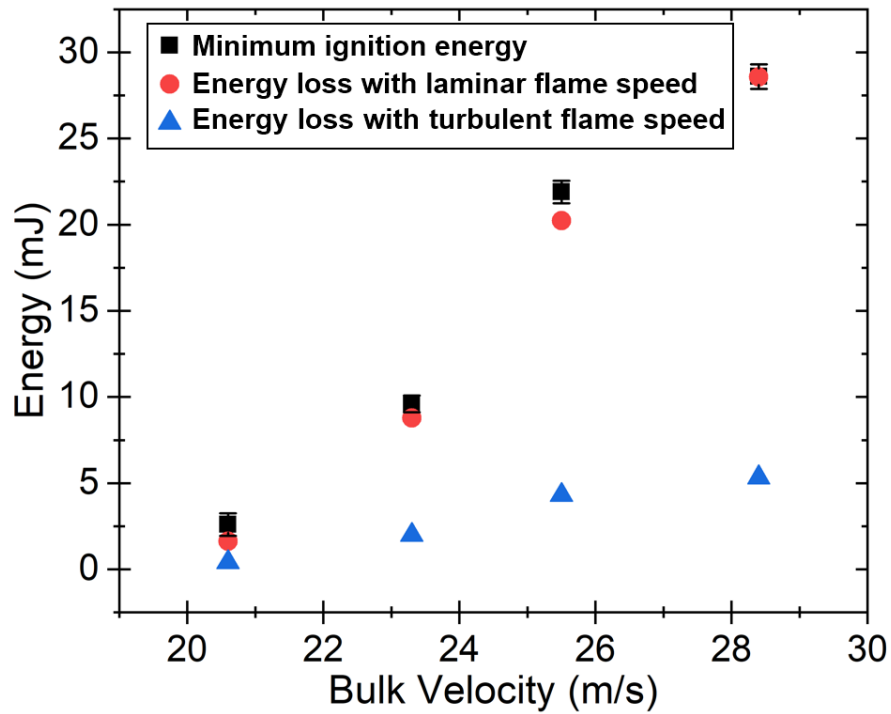
Fig. 8-15. Comparison between ignition energy and energy loss by forced convection heat transfer.

178
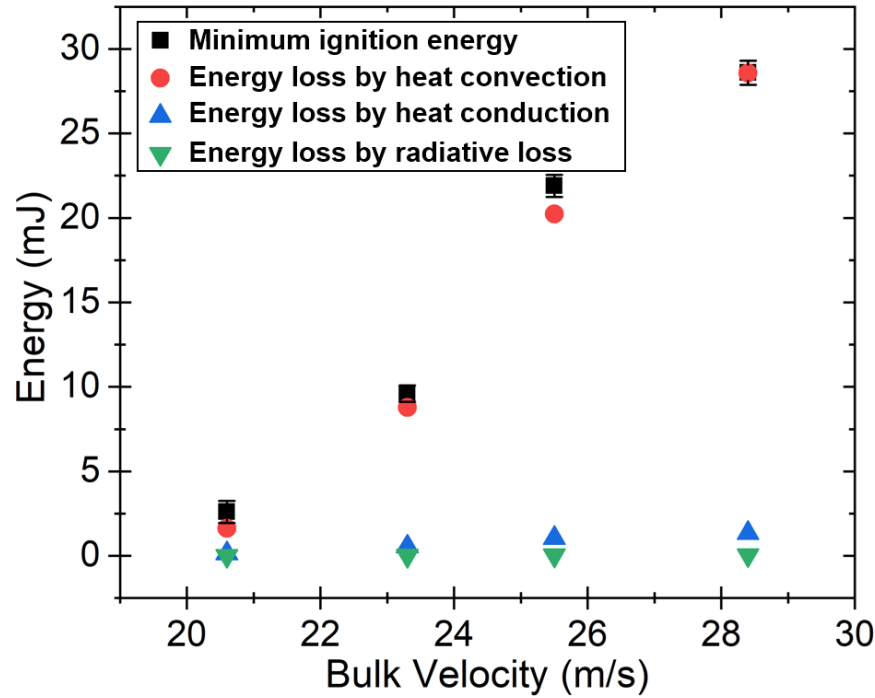
Fig. 8-16. Comparison between ignition energy, energy loss by forced convection heat transfer, energy loss by radiative heat loss and energy loss by heat conduction.

The calculated energy loss considering the convection and the laminar flame speed is a good agreement with the measured MIE [Eq. (7.4)] [Fig. 8-15]. It indicates that the approximate equation by the forced convection heat transfer can estimate the energy loss in the ignition process of flowing gases. The agreement with the results based on the laminar flame speeds supports our hypothesis that ignition occurs at scales relevant to laminar flow. Equation (7.4) is using the laminar flame speed instead of the turbulent flame speed. This is because the flame kernel size and the flame kernel development during the very early stage (till 30 μs) are dependent on the laser energy difference, ΔE, and independent on the velocity [Fig. 8-11][71]. The kernel propagates as the laminar flame speed during the very early stage. Using the laminar flame speed may be a valid method for the calculation of the energy loss by the convection [Eq. (7.4)][Fig. 8-15]. The heat convection energy losses by the turbulent flame speed have computed, but the values are very lower than the measured MIE because the flame kernel does not grow with the turbulent flame speed during the very early stage even the jets represent near turbulent flow [Figs. 8-11,8-15].

The energy loss using the heat conduction has calculated by Eq. (7.8). The energy loss equation using the heat conduction is too lower than the ignition energy [Fig. 8-16][Table 8-4].

179

Similarly, the radiative heat loss from the kernel has computed by Eq. (7.11). The calculated energy losses using the radiative heat loss are very lower than the measured MIE [Fig. 8-16][Table 8-4]. These losses increase with the bulk velocity [Fig. 8-16][Table 8-4]. However, the cause of the increased energy loss by the heat conduction or the radiative heat loss is an increase in the kernel temperature and the minimum (critical) radius, not the bulk. In other words, increasing the bulk velocity does not affect an increase in the energy loss by the radiative heat loss or the heat conduction. From the energy balance equation, the energy loss by the heat conduction or the radiative heat loss cannot explain the significant differences between the calculated energy loss and the measured MIE. It means the radiative heat loss or the heat conduction is not a dominant energy loss in the ignition of the flowing gases. Therefore, the dominant energy loss in the ignition of flowing gases is the molecular conduction heat transfer enhanced by the increase in temperature gradient caused by the flow.

The convection heat transfer has used as the dominant energy transfer in the ignition of the flowing gases instead of advection. Convection is energy transfer by bulk velocity (advection) and random motion of fluid molecules (conduction) [165]. Advection is energy transfer by bulk velocity [165]. When an ignition condition is flowing gases, energy loss in a kernel receives an effect not only from velocity of flowing gases but also from conduction by the random motion of fluid molecules. This is because a temperature difference between the kernel and a surrounding lead to a movement of the molecules, and the net transfer of energy by the movement of the molecules is conduction [165]. The calculated radiative heat losses are very low. Thus, we can neglect the radiative loss. Consequently, we consider the molecular conduction heat transfer enhanced by the increase in temperature gradient caused by the flow as the dominant heat transfer in the ignition of the flowing gases.

Laser-induced spark ignition in flowing gases generates a plasma with very high temperature. The laser-supported radiation wave rapidly increases the temperature and the pressure, heats the reactants to very high temperatures and produces a nearly isothermal kernel with a sharp temperature gradient defining the kernel surface. A shock wave is produced by the sudden change of properties and grows with the kernel. Flowing gases approaching the kernel do not instantly respond to the change in the kernel properties within a very short time interval. The sudden rise in the temperature difference between the kernel and the flowing gases leads to a

thermal boundary layer. Thus, processes resembling convective heat transfer are hypothesized to occur between the kernel and the gases flowing around it.

From the energy balance equation, MIE must be higher or equal to energy loss to develop a flame from a kernel [Eq. (7.1)]. Increasing bulk velocity increases the energy loss by the forced convection heat transfer [Eq. (7.4)]. Therefore, the MIE should be increased to overcome the energy loss by the forced convection heat transfer as the bulk velocity is faster. From the relationship between the MIE, the energy loss equation, and the energy balance equation, the MIE is written by

$$E_{ig} = h_{conv} \cdot 4\pi R_{crit}^2 (T_k - T_u) \frac{R_{crit}}{S_L}.$$

8.1

Encouraged by the agreement between the present measurements and results of the energy balance model for the lean hydrogen air jets, the model was examined for ignition of slightly rich near stoichiometric hydrocarbon/air mixture jets. Ballal and Lefebvre [1] examined ignition energy using an electrode spark for propane/air mixtures at an equivalence ratio of 1.04 [1,7]. Beduneau et al. [3] measured ignition energy using a laser-induced spark for methane/air mixtures at an equivalence ratio of 1.2. Ballal and Lefevre [1] and Lefebvre [7] experimentally measured quenching distances. These quenching distances were used as the minimum (critical) radius [Table 8-6]. For the experiments of Beduneau et al. [3], the minimum (critical) radius was obtained from schlieren images [Table 8-7]. A fixed value of the flame kernel temperature (870 K) was used for these calculations. Detailed chemical mechanisms for hydrocarbon air combustion include elementary steps involving H atoms and OH radicals that are also important for hydrogen air combustion. Therefore, it is our conjecture that the choice of the flame kernel temperature = 870 K is reasonable. However, future measurements of the ignition kernel temperature are essential. The results of these calculations are shown in Fig. 8-17(a) and Fig. 8-17(b) for both the propane-air and the methane-air mixtures. The results show that the MIE for both hydrocarbon air mixtures agree both qualitatively and quantitatively with the results of the present model. The reasonably good agreement may be because the velocity and the laminar flame speed are important in the ignition process of flowing gas mixtures. The results highlight

181

the importance of the laminar flame speed of the fuel air mixtures is highly relevant to the ignition process.

Table 8-5 Variables used in Eq. (7.4) [1,7].

V (m/s)	h_{conv} (W/m^2 · K)	R_{crit} (mm)	T_k (K)	S_L (m/s)
6.1	114	0.87	870	0.48
15.6	161	0.95	870	0.48
22.7	186	0.99	870	0.48
31.5	199	1.15	870	0.48
47.7	218	1.40	870	0.48

Table 8-6 Variables used in Eq. (7.4) [3].

V (m/s)	h_{conv} (W/m^2 · K)	R_{crit} (mm)	T_k (K)	S_L (m/s)
0.66	97	0.76	870	0.34
1.66	114	0.96	870	0.34
3.34	138	1.11	870	0.34
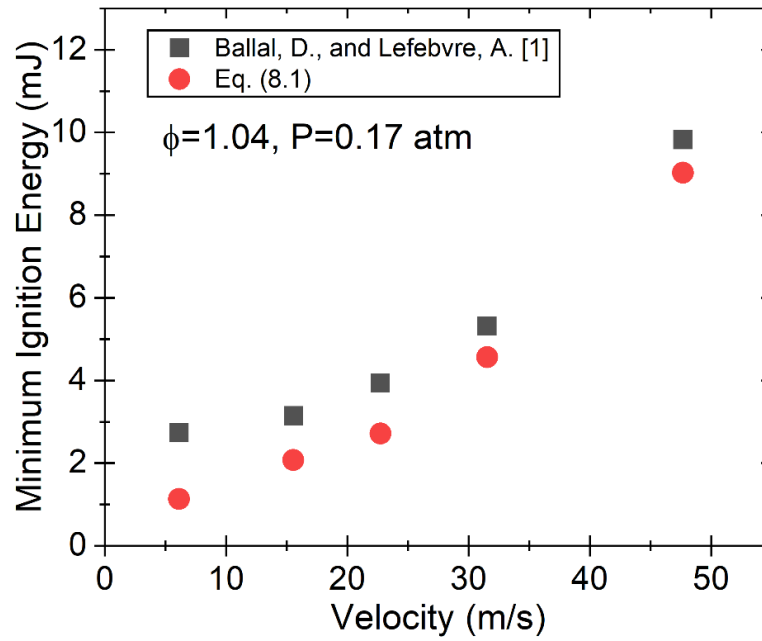
(a)
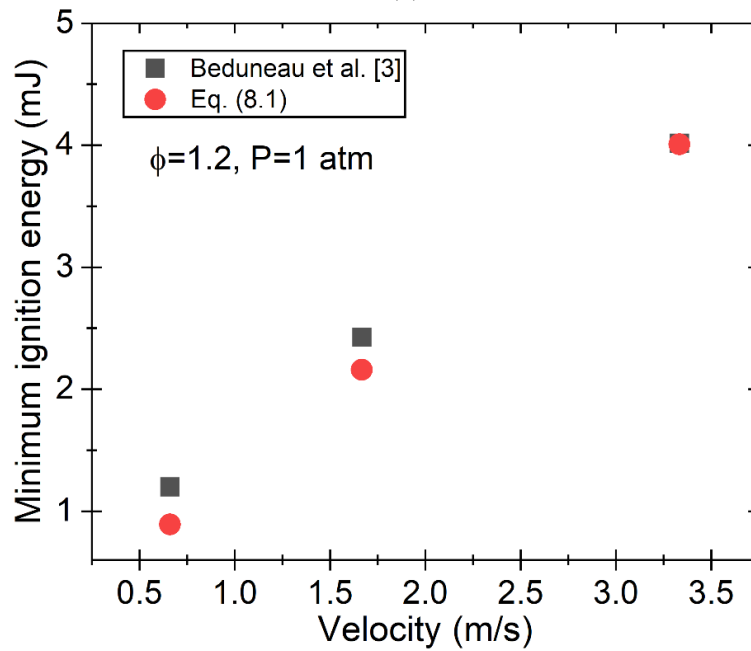
(b)

Fig. 8-17. (a) Comparison between the calculated MIE by Eq. (8.1) and the reference (propane and air) result [1], (b) comparison between the calculated MIE by Eq. (8.1) and the reference result [3] (methane and air).

9. ENERGY BALANCE BETWEEN MINIMUM IGNITION ENERGY AND ENERGY LOSS UNDER LAMINAR FLOW

9.1 Experimental Conditions

The jet burner of 12.6 mm (inner) diameter was used in the present ignition experiment [Fig. 2-2]. The diameter of the multiple nozzle holes in the perforated plate is 2.9 mm [Fig. 2-2]. The blockage ratio is 62 %. Premixed air and hydrogen flow out through the burner exit. The ignition experiment was conducted at atmospheric pressure and temperature. A representative bulk velocity was calculated using the flow rates and the opened area of the burner exit. The equivalence ratio (ϕ) was 0.4. Eight bulk velocities were used (6, 7, 8, 10, 11, 12, 13, and 14 m/s) [Table 9-1]. More detailed experimental conditions are presented in Table 9-1. Reynolds number in Table 9-1 is calculated using the bulk velocity, the nozzle diameter, and the mixture properties.

Table 9-1. Experimental conditions.

Jet	V_{bulk} (m/s)	ϕ	Ignition height (mm)	Reynolds number
5	6	0.4	17	980
6	7	0.4	17	1150
7	8	0.4	17	1310
8	10	0.4	5	1640
9	11	0.4	5	1800
10	12	0.4	5	1970
11	13	0.4	5	2130
12	14	0.4	5	2290

The laser-induced spark was applied as an ignition source [Fig. 2-2]. Chapter 2.2 explains more detailed information about the laser-induced spark. The ignition energy experiments for the MIE were performed 50 times for each experimental condition. The laser-induced spark was located at the burner axis. The ignition experiments used two ignition heights [Table 9-1]. The height of the laser-induced spark was 17 mm above the burner exit for Reynolds number below 1500 [Table 9-1] and the height of the laser-induced spark was 5 mm above the burner exit for Reynolds number above 1500 [Table 9-1]. The ignition probability used in the definition of the MIE was 100 %.

The infrared camera (FLIR sc6100) captured radiation intensity emitted from the kernel [Fig. 2-11]. The characteristics of the camera were: exposure time- 0.01056 ms; frame rate- 829 fps; pixel count- 112×248 pixel^2. A captured area of 38 mm $\times$ 85 mm and a resolution of 0.342 mm/pixel were archived.

The Rayleigh scattering was utilized to measure the kernel temperature [Fig. 2-16]. The laser sheet, generated by the 200 mm focal length cylindrical lens, was 13 mm of height and 350 μm of thickness [Fig. 2-16]. The Rayleigh scattering signal was captured through the intensified camera (PI-MAX 2, ICCD camera) [Fig. 2-16]. The gate time of the ICCD camera was 50 ns. The captured area was 51.2 mm $\times$ 51.2 mm and a resolution of 0.1 mm/pixel was used.

The Schlieren image visualized kernel development [Fig. 2-10]. The Schlieren system consisted of the 0.2-watt LED lamp, the concave mirror ($f = 250$ mm), the knife edge, and the high-speed camera (Vision Research Phantom v7.1) [Fig. 2-10]. An exposure time capturing the images was 2 μs. The time interval between images was 10 μs. The delay time of the high-speed camera was changed from 0 to 9 μs to collect images in every 1 μs. The frame speed was 100,000 per second. The array size of the high-speed camera is 128×64 pixel^2. A resolution of 0.419 mm/pixel resulted from the arrangement.

Equivalence ratio distributions in the flow field of the jet burner using the premixed hydrogen and air were investigated with commercial software ANSYS Fluent. 2D simulation was performed in the flow field. The species transport model was utilized with the mixtures modeled as a steady-state incompressible Newtonian fluid. The model assumed the premixed gases with the given equivalence ratio flow out to the flow field from the burner exit.

9.2   Results

9.2.1   Effect of Velocity on Minimum Ignition Energy

The present study ran ignition experiments under laminar flow to understand the effect of velocity on minimum ignition energy (MIE) in laminar flow. The bulk velocities were varied from 6 to 14 m/s [Table 9-1]. Therefore, these experimental conditions allow a focus on the influence of velocity on MIE under laminar flow. The MIE increases with increasing the bulk velocity [Fig. 9-1]. The relationship between the bulk velocity and the MIE is a general result from ignition

experiments with flowing jets and is similar to the MIE in the turbulent flow [Figs.8-1,9-1][1,3-6]. The reason for the increased MIE is an increase in energy loss by heat transfer.
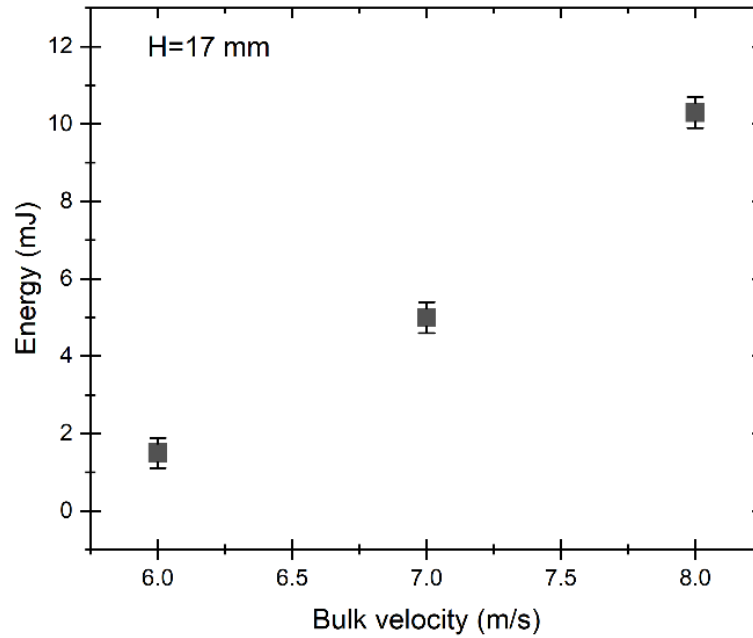
(a)
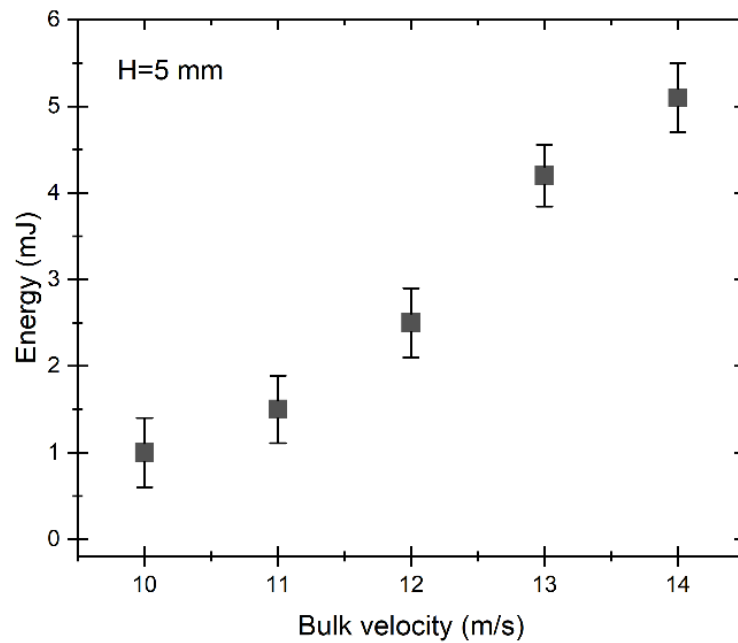
(b)

Fig. 9-1. Effect of bulk velocity on minimum ignition energy, (a) bulk velocities are from 6 to 8 m/s, (b) bulk velocities are from 10 to 14 m/s.

The MIE at Reynolds number of less than 1500 is higher than the MIE at Reynolds numbers greater than 1500 as indicated in [Fig. 9-1][Table 9-2]. This may also be related to the ignition height and the resulting mixing and fluctuations. A kernel is generally anchored to a burner and develops into an attached flame. A kernel generated at a high ignition height must be propagated for a longer distance before it can anchor to the burner lip. If a kernel does not attach to a burner, it will blow out because the jet flow continuously pushes the kernel upward into regions where the mixture composition and velocity may fluctuate and result in higher than the baseline laminar advection. If the ignition energy is higher, the kernel rapidly grows [11,103]. Thus, higher ignition energy may be required at a higher ignition height for transitioning to a fast kernel propagation over a longer distance. Past experiments have also shown different minimum ignition energies for different ignition heights [185,186]. Figures. 9-2 and 9-3 illustrate the change of the equivalence ratio in the flow fields studied using Fluent. The decay of the equivalence ratio along the axis for the present case is minimal [Figs. 9-2,9-3]. Thus, the equivalence ratios at the two ignition locations are nearly identical [Figs. 9-2,9-3]. However, the equivalence ratio is leaner at locations away from the axis of the injection holes because of radial diffusion towards the surrounding air [Figs. 9-2,9-3]. The equivalence ratio of the areas surrounding the 17 mm ignition height is slightly lower than that at the 5 mm ignition height [Figs. 9-2,9-3]. This may lead to increase in MIE since ignition is very sensitive to the mixture properties for the relatively lean mixture studied here. The effect of height on ignition energy becomes stronger at locations farther away from the exit particularly beyond the length of the potential core. Therefore, minimum ignition energy may increase with decreasing bulk velocity due to the effect of the ignition height.
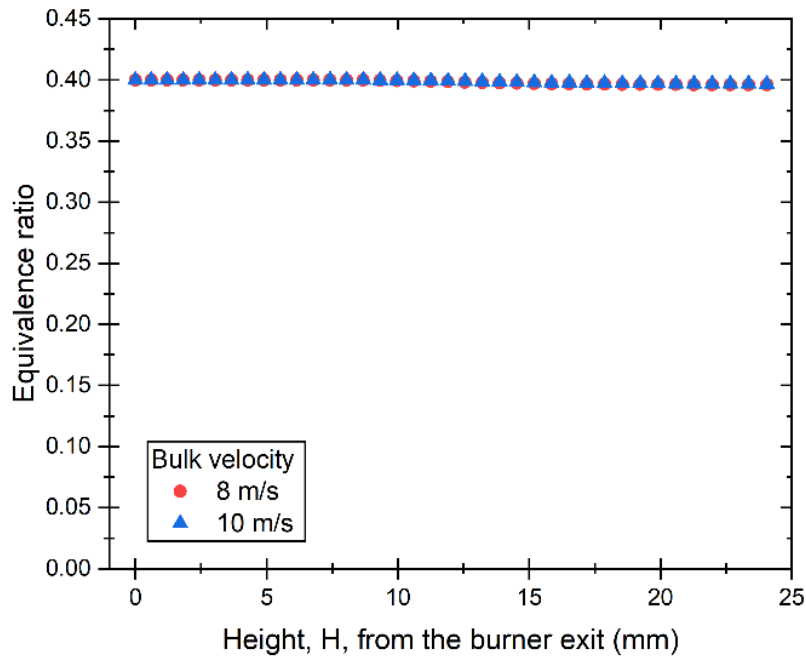
(a)
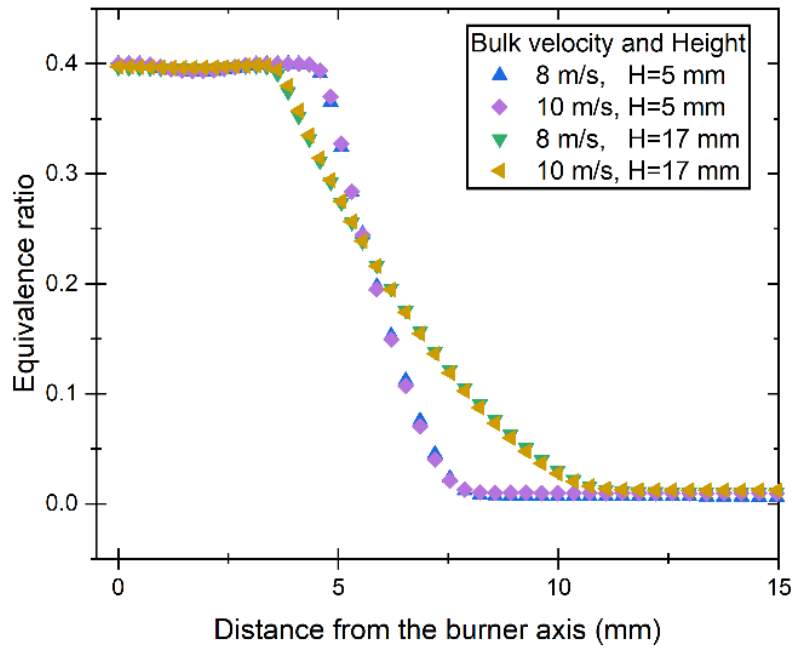
(b)

Fig. 9-2. (a) Equivalence ratio by the change of the height at the burner axis, (b) equivalence ratio by the change of the distance from the burner axis at the constant height.

ϕ | $V_{bulk} = 8\,m/s$
0.0
0.23
0.70
0.12
0.14
0.19
0.24
0.26
0.31
0.35
0.40

0   0.1 (m)

(a)

ϕ | $V_{bulk} = 10\,m/s$
0.0
0.23
0.70
0.12
0.14
0.19
0.24
0.26
0.31
0.35
0.40

0   0.1 (m)

(b)
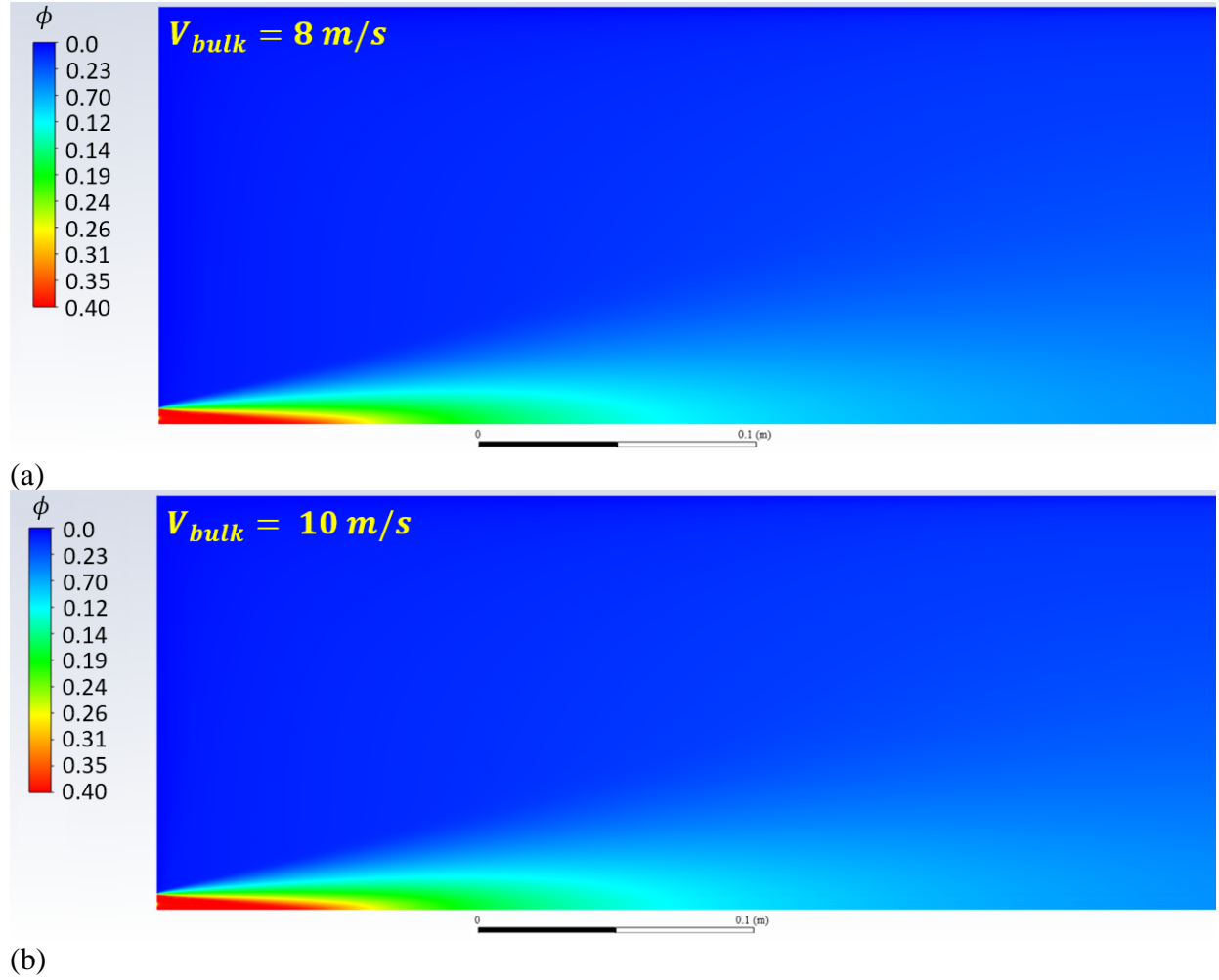
Fig. 9-3. Equivalence ratio distribution, (a) the bulk velocity is 8 m/s, and (b) the bulk velocity is 10 m/s.

9.2.2 Kernel Diameter

An important parameter in ignition studies is a minimum (critical) radius that is defined as a radius of a spherical volume in a kernel generated by MIE [180-184]. The present study uses the minimum (critical) radius to calculate the heat transfer in the ignition process.

The schlieren image was captured for estimating the size of the kernel under the present experimental conditions. The measured MIE was used to study the minimum (critical) radius for each of the bulk velocities [Table 9-2]. Reynolds number in Table 9-2 is calculated using the critical diameter ($2R_{crit}$), the bulk velocity, and the mixture properties. The minimum (critical)

189

radius increased with an increase in the MIE [Fig. 9-4][Table 9-2]. This result supports the observation by Beduneau. et al., Mulla et al. and the current work in Chapter 6.2.3 [3,71].

(a)

(b)
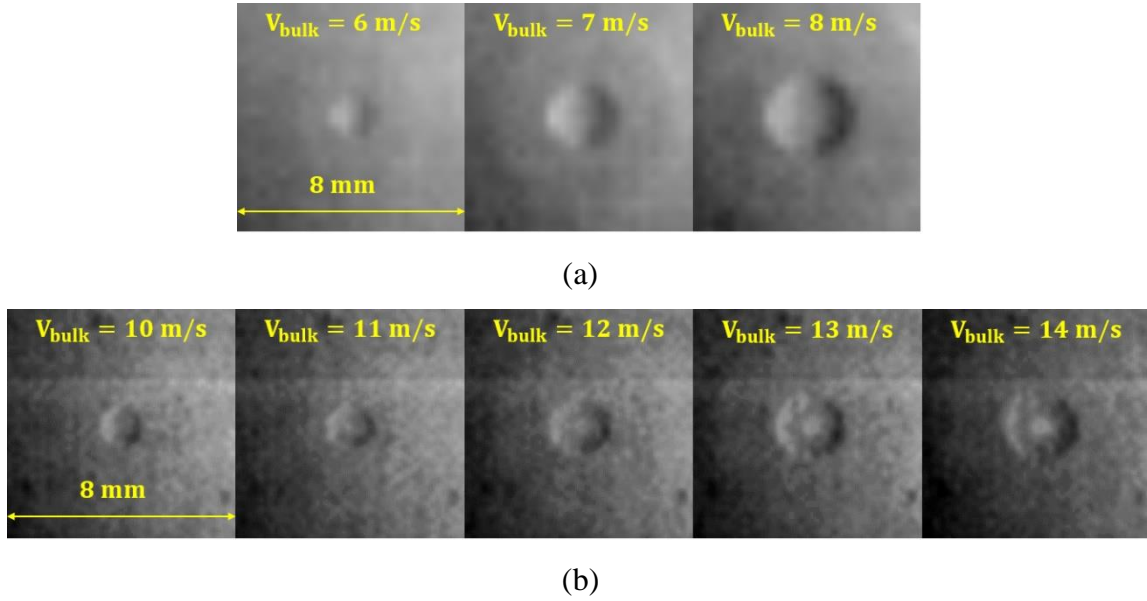
Fig. 9-4. Minimum (critical) radius, (a) bulk velocities are from 6 to 8 m/s and (b) bulk velocities are from 10 to 14 m/s.

9.2.3 Kernel Temperature

The kernel temperature was measured using the Rayleigh scattering and using the infrared camera (deconvolution technique). The elapsed time after laser pulse, used in the Rayleigh scattering and the infrared camera, were the same as the elapsed time for the schlieren image [Table 9-2]. The measured MIE was used to study the kernel temperature as a function of the bulk velocity [Table 9-2]. The kernel was captured 50 times at each experimental condition. The average value of the kernel temperature is defined as T_k [Table 9-2]. The measured kernel temperatures, $T_{k,IR}$, using the IR camera [Fig. 9-5(b)] are slightly lower than the measured kernel temperature, $T_{k,R}$, through the Rayleigh scattering [Fig. 9-5(a)] because the deconvolution equations, utilized in the IR camera, and the different image resolutions between the two measurements led to the differences. The kernel temperature increased with increasing MIE [Fig. 9-5] [Table 9-2].
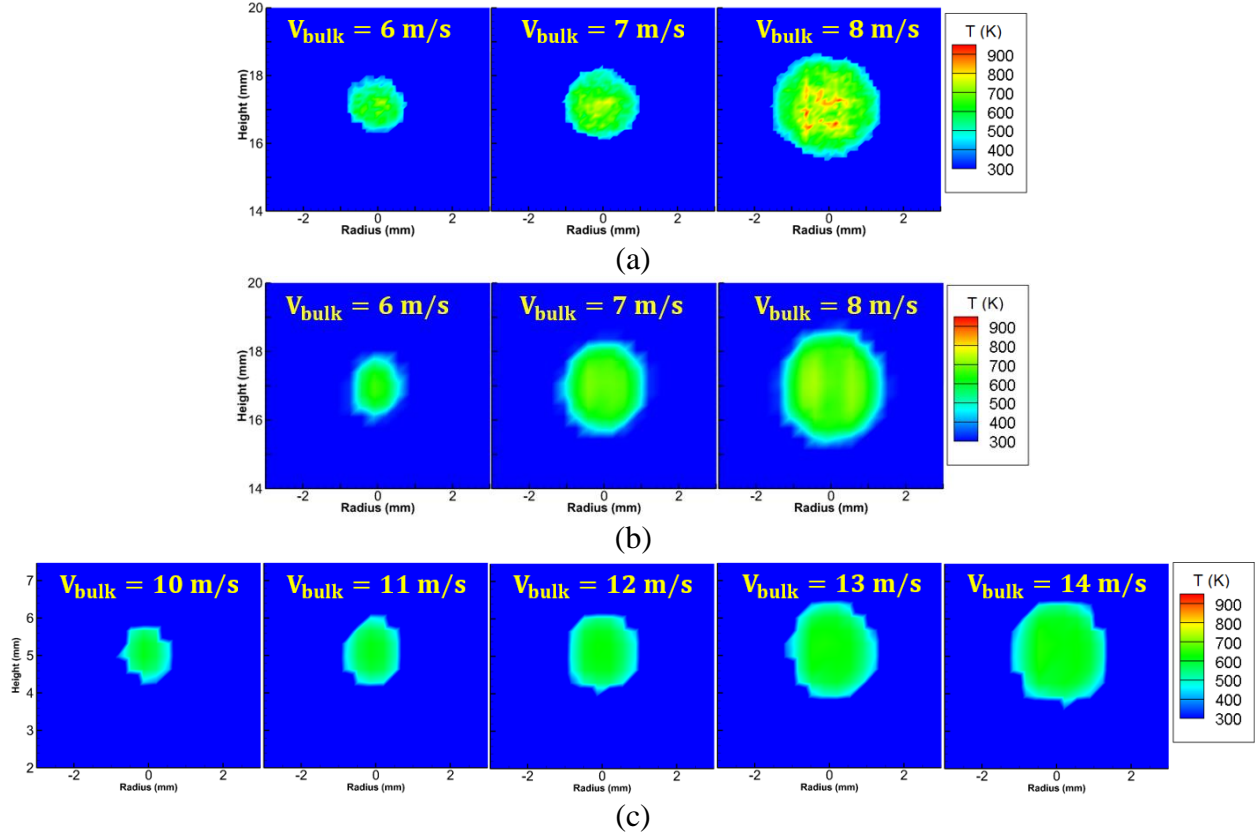
Fig. 9-5. Kernel temperature, (a) bulk velocities are from 6 to 8 m/s (Rayleigh scattering), (b) bulk velocities are from 6 to 8 m/s (Infrared camera), and (c) bulk velocities are from 10 to 14 m/s (Infrared camera).

Table 9-2. Experimental results.

Jet	V_{bulk} (m/s)	Ignition height (mm)	E_{ig} (mJ)	R_{crit} (mm)	Re	Elapsed time (μs)	$T_{k,IR}$ (K)	$T_{k,R}$ (K)
5	6	17	1.5	0.78	530	6	495	514
6	7	17	5.0	1.27	1000	8	550	563
7	8	17	10.6	1.77	1600	10	580	603
8	10	5	1.0	0.66	750	6	510	-
9	11	5	1.5	0.72	900	6	521	-
10	12	5	2.5	0.94	1280	7	528	-
11	13	5	4.2	1.13	1660	8	537	-
12	14	5	5.1	1.23	1940	8	551	-

9.2.4 Energy Balance

Figure 9-6 depicts different components of the energy balance including the minimum ignition energy (MIE) and the calculated energy losses by convection, conduction, and radiation [Table

191

9-3]. The calculated energy loss by heat convection is in good agreement with the measured minimum ignition energy [Fig. 9-6] [Table 9-3]. However, the computed energy losses by heat conduction and radiative are significantly lower than the MIE [Fig. 9-6] [Table 9-3]. The results indicate that the dominant energy loss during the ignition in the laminar flow is heat convection by the forced flow [Fig. 9-6] [Table 9-3]. In other words, if the heat conduction or the radiative loss is the dominant energy loss in the ignition of the jets, the energy losses cannot explain the increased MIE by the bulk velocity [Fig. 9-6] [Table 9-3]. The energy loss by heat conduction or radiative also increase with the bulk velocity, but the increase is relatively small and the cause of the increase is the change of the minimum (critical) radius and the kernel temperature, not the bulk velocity. To develop a flame from a kernel, MIE must be higher or equal to energy loss from the energy balance equation. Increasing the bulk velocity increases the energy loss by the forced convection heat transfer. Thus, as the bulk velocity is faster, the MIE should be increased to overcome the increased energy loss by the forced convection heat transfer. From the relationship between the MIE, the energy loss equation, and the energy balance equation, the MIE is written as:

$$E_{ig} = h_{conv} \cdot 4\pi R_{crit}^2 (T_k - T_u) \frac{R_{crit}}{S_L}.$$

9.1

Eq. (9.1) is the same with Eq. (8.1). It indicates that the dominant energy loss of the ignition process in flowing gases is the forced convection heat transfer.

Table 9-3. Energy comparison between the minimum ignition energy and the calculated energy loss.

Jet	V_{bulk} (m/s)	Ignition height (mm)	E_{ig} (mJ)	Heat convection (mJ)	Heat conduction (mJ)	Thermal radiation (mJ)
5	6	17	1.5	1.0	0.1	0.2×10^{-3}
6	7	17	5.0	4.4	0.5	2.1×10^{-3}
7	8	17	10.6	11.7	1.0	9.6×10^{-3}
8	10	5	1.0	0.8	0.1	0.1×10^{-3}
9	11	5	1.5	1.1	0.1	0.2×10^{-3}
10	12	5	2.5	2.3	0.2	0.5×10^{-3}
11	13	5	4.2	3.9	0.3	1.2×10^{-3}
12	14	5	5.1	5.1	0.4	1.8×10^{-3}
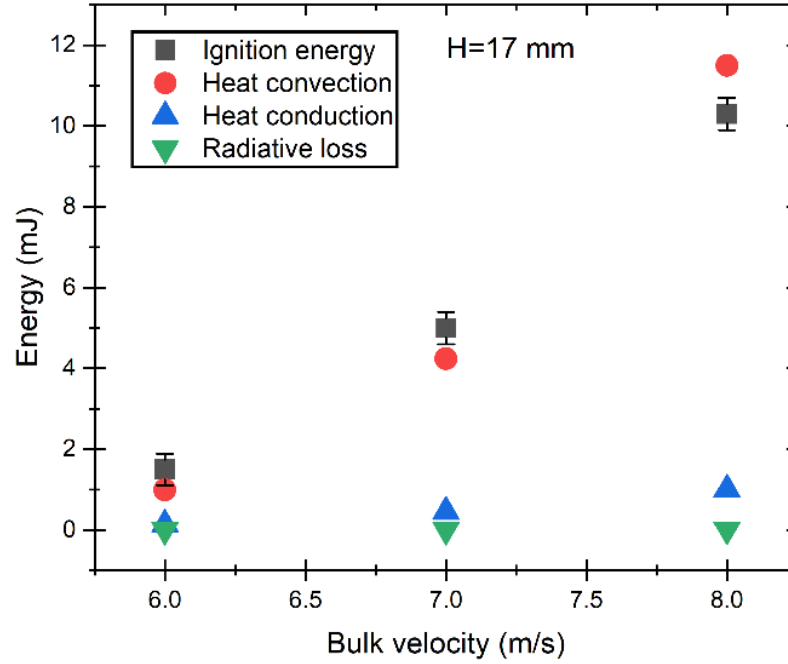
(a)
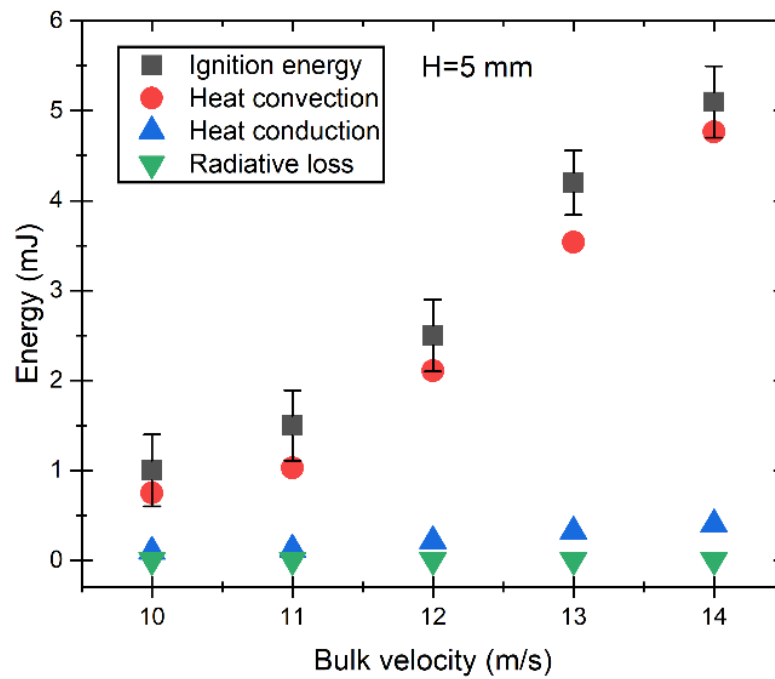
(b)

Fig. 9-6. Energy comparison between the minimum ignition energy and the calculated energy loss, (a) bulk velocities are from 6 to 8 m/s, (b) bulk velocities are from 10 to 14 m/s.

10. CONCLUSION

10.1 Summary

This research has been studied the laser-induced spark in flowing gases. The particle imaging velocimetry (PIV) was used to examine the flow field in the turbulent flow. The minimum ignition energy (MIE) was measured at the different turbulence intensities to study the the effect of the turbulence intensity on MIE. The kernel propagation speed was investigated to understand the relationship between the MIE, the turbulence intensity and the kernel propagation speed. The plasma generated by the laser-induced spark was studied in terms of the plasma shape, the plasma expansion wave speed, and the kernel generation. The phenomenological model was suggested for the energy loss by the heat transfer in the ignition of flowing gases. The MIE measured from the laminar flow to the turbulent flow. The energy balance equation in the ignition of the flowing gases was newly written considering the energy loss by the heat transfer.

The PIV experiment has investigated the flow fields at the different perforated plates and bulk velocities. The highest blockage ratio burner shows the deepest wake velocity deficits and the highest peak jet velocities. The peaks of jet velocities and the deepest wake velocity deficits decrease progressively with reductions in the blockage ratios. The fluctuation of the root-mean-square velocity (RMS velocity) relatively reduces as the nozzle diameter is larger. The velocity fluctuations increase significantly in the annular shear layers forming around the seven openings. The RMS velocities reach very high values in the annular wake region outside of the center nozzle. The turbulence intensity has the lowest values in the core of the seven nozzles in the turbulence generation plates and increases in regions corresponding to the wakes of the blocked areas between these nozzles. The turbulence intensity increases with an increase in the blocked annular area.

The ignition experiments were conducted to measure the MIE at the fixed height and the different turbulence intensity changed by the ignition locations and the perforated plates. The MIE decreases with increasing the turbulence intensity. Kernel growth, kernel expansion speed, and turbulent flame speed are fast as turbulence intensity is higher. An increase in turbulence intensity may provide a favorable condition in which a kernel, generated by even low ignition energy, can rapidly grow to a sustainable flame. We have compared the MIE results with the turbulence flame speed. Increasing the turbulent flame speed decreases the MIE. These results regarding the

194

turbulent flame speed show a similar tendency with the relationship between the MIE and the turbulence intensity. The fast turbulent flame speed may positively affect a decrease of the MIE. The effect of the Kolmogorov scale on the MIE is investigated. The Kolmogorov scale decreases as the turbulence intensity increases. The MIE decreases as the Kolmogorov scale reduces. A decrease in the size of the edges (the size of the length scale) improves mixing rates. An increase in the mixing rates due to the Kolmogorov scale contributes to a decrease in the MIE since the reaction between a kernel and unburned mixtures may be improved by the mixing rates. As a result, increasing the turbulence intensity facilitates ignition.

In order to understand the relationship between the MIE, the turbulence intensity, and the kernel propagation speed, the ignition experiments were performed at the constant laser energy difference, the various turbulence intensities changed by the ignition locations and the perforated plates. The kernel growth was visualized through the schileren imaging. The kernel propagaton speeds were calculated using the captured schileren images. The kernel propagation speeds in the y-direction, S_{F1}, and S_{F2}, increases with the turbulence intensity until $400 \, \mu s$. An increase in the turbulence intensity increases the wrinkles in the kernel area. Therefore, the increased kernel surface increases the contact between the kernel and the reactant in the surrounding. Thus, the turbulence positively affects the kernel propagation speeds, S_{F1}, and S_{F2}. The kernel center velocity in the y-direction and the kernel height decrease with an increase in the turbulence intensity. This is because the high turbulence suppresses the kernel movement and thus reduces the kernel movement in the y-direction. As time elapses, the kernel propagation speeds in the x-direction, S_{F3}, and S_{F4}, increase until the specific time and decrease after the specific time. The reason is the distribution of the reactant is leaner, as farther away from the center of the burner. The kernel propagation speeds in the x-direction, S_{F3}, and S_{F4}, rapidly reach on the maximum values with increasing the turbulence intensity since the high turbulence facilitates the kernel growth. The kernel propagation speeds in the y-direction, S_{F1}, and S_{F2}, rises as the bulk velocity increases. This is because the high bulk velocity increases the supply of the reactant into the kernel. An increase in the bulk velocity increases the kernel center velocity since the high momentum energy of the flow, generated by the increased bulk velocity, pushes the kernel from the burner exit. During the early time, at $50 \, \mu s$ after the laser pulse, an increase in the turbulence intensity increases the kernel propagation speeds in the y-direction, S_{F1}, and S_{F2}, since the high turbulence intensity increases the contact between the kernel and the reactant in the surrounding due to the

increased kernel surface. Thus, the minimum ignition energy (MIE) decreases with increasing the turbulent intensity because the kernel can rapidly anchor into the burner surface by the fast flame propagation speed at the high turbulent intensity. Increasing the turbulence intensity decreases the kernel center velocity as the turbulence intensity negatively affects the kernel movement. The MIE decreases as the kernel center velocity reduces. As the kernel center velocity is slower, the rear height of the kernel is lower. Thus the kernel can fastly anchor into the burner exit by the kernel growth. Therefore, the MIE decreases as the turbulence intensity increases when the ignition conditions, including the bulk velocity and ignition height, are constant since the high turbulence intensity increases the kernel propagation speed and decreases the kernel center velocity.

A focused laser beam produces electrons by multiphoton ionization. The electron density reaches a critical value, then the plasma is generated. The plasma expands toward the laser beam due to the laser absorption. As the laser energy is higher, the plasma expansion increases toward the laser beam by the strong laser absorption. The plasma shape is changed to the infinity symbol structure along the laser beam from the spherical due to the increased plasma expansion. In contrast, as the laser energy is lower, the laser absorption is weak. Hence the plasma movement approaching toward the laser beam is small. The change of the plasma shape occurs near the focal point.

The laser supported radiation (LSR) wave speed is measured at 3 ns using the captured images through the ICCD camera. The LSR wave speed increases with an increase in the irradiance due to the increased energy. The energy balance equation between the plasma radiation and the heated gas by the plasma radiation is newly written. The plasma temperature and the plasma emissivity are calculated with the energy balance equations. The plasma temperature and the emissivity increase as the irradiance is higher. The LSR wave speed is calculated using the energy balance equations at the estimated emissivity and compared with other experimental papers. The calculated LSR wave speed is a good agreement with the experiment results.

A plasma heats a mixture and produces a kernel. The plasma shape determines the kernel temperature distribution. At the low laser energy difference, 2.6 mJ, the kernel temperature heated by the plasma increases from the kernel center to the kernel edge over time since the plasma expansion and the change of plasma shape occur near the focal point. As the E_{in} and ΔE are higher, the plasma shape is changed, by the laser absorption, to the infinity symbol structure from the spherical. Therefore, the circles of the infinity symbol structure in the plasma heat the mixture. The kernel temperature increases from the two high-intensity bowls, heated by the plasma, to the

196

kernel center as time elapses. The distance between the two high-intensity bowls in the kernel increases with increasing the E_{in} and ΔE due to the plasma expansion approaching toward the laser beam. The bulk velocity does not affect the kernel temperature distribution during the early stage because the plasma expansion does not relate to the velocity. The plasma generates the kernel by heating the mixture. The kernel temperature during the early stage decreases with an increase in the bulk velocity. The reason is the energy loss by the convection between the kernel and the mixture of the surrounding increases with the velocity which leads to decreases the kernel temperature. As the E_{in} and ΔE are higher, the plasma keeps for a long time with the high intensity, and the plasma expansion toward the laser beam increases due to the laser absorption. At high E_{in} and ΔE, a plasma heats a mixture for a long time with a large plasma size. Therefore, kernel temperature and the kernel size increase which leads to a fast kernel propagation speed. Therefore, high ignition energy increases a chance that can ignite a mixture.

The phenomenoloical model involving an energy balance between the deposited laser energy and the energy loss by advection (convection), conduction, and radiation from the kernel has developed. The energy loss equation includes the minimum (critical) radius, the kernel temperature, the laminar flame speed, and mixture properties.

The MIE was measured at the various bulk velocities. The turbulence intensities were nearly constant in the turbulent flow. Thus, the experimental conditions are only dependent on the bulk velocity and independent of the turbulent intensity. The MIE increases with an increase in the bulk velocity under the laminar and turbulent flow. The bulk velocity affects the MIE.

The effect of the velocity on the kernel development was investigated. The kernel size and the kernel growth are almost identical at the constant laser energy difference and the various bulk velocities during the time scale of 0-30 μs. The velocity and turbulence do not significantly affect the kernel development and the kernel size until 30 μs. The kernel rapidly develops with increasing the bulk velocity due to the effect of turbulence after 30 μs.

The schlieren image visualized the minimum (critical) radius. The kernel temperature was measured at the elapsed time after the laser pulse, corresponding to the minimum (critical) radius, through the Rayleigh scattering and the radiation intensity (IR camera). The energy loss equation suggested by the phenomenological model is calculated using the critical radius, the kernel temperature, the laminar flame speed, and the mixture properties at the laminar flow and the

turbulent flow. The calculated energy loss considering the heat convection and the laminar flame speed is a good agreement with the measured MIE. It means that the energy loss in the ignition of the flowing gases can be estimated by the equation considering the forced convection heat transfer at the laminar flow and the turbulent flow. The energy loss considering heat conduction and radiative heat loss is respectively calculated to understand a dominant energy loss in the ignition of flowing gases. The computed energy losses utilizing the heat conduction and radiative heat loss are significantly lower than the measured MIE at the laminar and turbulent flow. The energy losses by the conduction and radiation also increase with the bulk velocity. However, the reason for the increase is the change in the kernel temperature and the minimum (critical) radius, not the velocity. The energy loss equation using heat conduction or radiative heat loss cannot explain an increase in the ignition energy by bulk velocity from the energy balance equation. Therefore, the dominant energy loss in the ignition of flowing gases under the laminar and turbulent flow is the molecular conduction heat transfer enhanced by the increase in temperature gradient caused by the free stream flow, not heat conduction or radiative heat loss. The energy balance equation in the ignition of flowing gases is newly written using the energy loss by the forced convection heat transfer at the laminar and turbulent flow.

REFERENCES

1. D. Ballal and A. Lefebvre, "The influence of spark discharge characteristics on minimum ignition energy in flowing gases," Combustion and Flame, vol. 24, pp. 99–108, 1975.

2. C. C. Swett Jr, "Spark ignition of flowing gases," NACA, Lewis Flight Propulsion Laboratory, Cleveland, United States, Tech. Rep., 1956.

3. J. L. Beduneau, B. Kim, L. Zimmer, and Y. Ikeda, "Measurements of minimum ignition energy in premixed laminar methane/air flow by using laser induced spark," Combustion and Flame, vol. 132, no. 4, pp. 653–665, 2003.

4. Y. Kobayashi, S. Nakaya, and M. Tsue, "Laser-induced spark ignition for DME–air mixtures with low velocity," Proceedings of the Combustion Institute, vol. 37, no. 3, pp. 4127–4135, 2019.

5. J. Griffiths, M. Riley, A. Borman, C. Dowding, A. Kirk, and R. Bickerton, "Effect of flow velocity and temperature on ignition characteristics in laser ignition of natural gas and air mixtures," Optics and Lasers in Engineering, vol. 66, pp. 132–137, 2015.

6. J. K. Lefkowitz, and O. Timothy, "An exploration of inter-pulse coupling in nanosecond pulsed high frequency discharge ignition," Combust and Flame, vol. 180, pp.136-147 2017.

7. D. Ballal and A. Lefebvre, "Ignition and flame quenching in flowing gaseous mixtures," Proceedings of the Royal Society of London. A. Mathematical and Physical Sciences, vol. 357, no. 1689, pp. 163–181, 1977.

8. C. Cardin, B. Renou, G. Cabot, and A. Boukhalfa, "Experimental analysis of laser-induced spark ignition of lean turbulent premixed flames," Comptes Rendus Mėcanique, vol. 341, no. 1-2, pp. 191–200, 2013.

9. D. R. Ballal and A. H. Lefebvre, "The influence of flow parameters on minimum ignition energy and quenching distance," Symposium (International) on Combustion, vol. 15, no. 1. Elsevier, 1975, pp. 1473–1481.

10. C. Cardin, B. Renou, G. Cabot, and A. M. Boukhalfa, "Experimental analysis of laser-induced spark ignition of lean turbulent premixed flames: New insight into ignition transition," Combustion and Flame, vol. 160, no. 8, pp. 1414–1427, 2013.

11. C. Ho and D. Santavicca, "Turbulence effects on early flame kernal growth," SAE Transactions, pp. 505–512, 1987.

12. D. A. Santavicca, "Spark ignited turbulent flame kernel growth," Pennsylvania State University, University Park, PA (US), Tech. Rep., 1995.

13. G. Koroll, R. Kumar, and E. Bowles, "Burning velocities of hydrogen-air mixtures," Combustion and Flame, vol. 94, no. 3, pp. 330–340, 1993.

14. S. Trautwein, A. Grudno, and G. Adomeit, "The influence of turbulence intensity and laminar flame speed on turbulent flame propagation under engine like conditions," Symposium (International) on Combustion, vol. 23, no. 1. Elsevier, 1991, pp. 723–728.

15. K. Smith and F. Gouldin, "Turbulence effects on flame speed and flame structure," AIAA Journal, vol. 17, no. 11, pp. 1243–1250, 1979.

16. T. Kitagawa, T. Nakahara, K. Maruyama, K. Kado, A. Hayakawa, and S. Kobayashi, "Turbulent burning velocity of hydrogen–air premixed propagating flames at elevated pressures," International Journal of Hydrogen Energy, vol. 33, no. 20, pp. 5842–5849, 2008.

17. R. Liu, D. S. Ting, and G. W. Rankin, "On the generation of turbulence with a perforated plate," Experimental Thermal and Fluid Science, vol. 28, no. 4, pp. 307–316, 2004.

18. F. Nicolleau, S. Salim, and A. Nowakowski, "Experimental study of a turbulent pipe flow through a fractal plate," Journal of Turbulence, vol. 12, p. N44, 2011.

19. S. Horender, "Turbulent flow downstream of a large solidity perforated plate: Near-field characteristics of interacting jets," Fluid Dynamics Research, vol. 45, no. 2, p. 025501, 2013.

20. G. Coppola and A. Gomez, "Experimental investigation on a turbulence generation system with high-blockage plates," Experimental Thermal and Fluid Science, vol. 33, no. 7, pp. 1037–1048, 2009.

21. J. Tan-Atichat, H. Nagib, and R. Loehrke, "Interaction of free-stream turbulence with screens and grids: a balance between turbulence scales," Journal of Fluid Mechanics, vol. 114, pp. 501–528, 1982.

22. C. Bindhu, S. Harilal, M. Tillack, F. Najmabadi, and A. Gaeris, "Laser propagation and energy absorption by an argon spark," Journal of Applied Physics, vol. 94, no. 12, pp. 7402–7407, 2003.

23. N. Glumac and G. Elliott, "The effect of ambient pressure on laser-induced plasmas in air," Optics and Lasers in Engineering, vol. 45, no. 1, pp. 27–35, 2007.

24. S. Harilal, P. Skrodzki, A. Miloshevsky, B. Brumfield, M. Phillips, and G. Miloshevsky, "On-and off-axis spectral emission features from laser-produced gas breakdown plasmas," Physics of Plasmas, vol. 24, no. 6, p. 063304, 2017.

25. J. L. Beduneau and Y. Ikeda, "Spatial characterization of laser-induced sparks in air," Journal of Quantitative Spectroscopy and Radiative Transfer, vol. 84, no. 2, pp. 123–139, 2004.

26. C. Bindhu, S. Harilal, M. Tillack, F. Najmabadi, and A. Gaeris, "Energy absorption and propagation in laser-created sparks," Applied Spectroscopy, vol. 58, no. 6, pp. 719–726, 2004.

27. Y. L. Chen, J. Lewis, and C. Parigger, "Spatial and temporal profiles of pulsed laser-induced air plasma emissions," Journal of Quantitative Spectroscopy and Radiative Transfer, vol. 67, no. 2, pp. 91–103, 2000.

28. N. Kawahara, J. Beduneau, T. Nakayama, E. Tomita, and Y. Ikeda, "Spatially, temporally, and spectrally resolved measurement of laser-induced plasma in air," Applied Physics B, vol. 86, no. 4, pp. 605–614, 2007.

29. M. Barwinkel, S. Lorenz, R. Sẗaglich, and D. Brüggemann, "Influence of focal point properties on energy transfer and plasma evolution during laser ignition process with a passively q-switched laser," Optics Express, vol. 24, no. 14, pp. 15189–15203, 2016.

30. D. K. Srivastava, M. Weinrotter, K. Iskra, A. K. Agarwal, and E. Wintner, "Characterisation of laser ignition in hydrogen–air mixtures in a combustion bomb," International Journal of Hydrogen Energy, vol. 34, no. 5, pp. 2475–2482, 2009.

31. T. X. Phuoc, "Laser-induced spark ignition fundamental and applications," Optics and Lasers in Engineering, vol. 44, no. 5, pp. 351–397, 2006.

32. D. C. Smith, "Laser radiation-induced air breakdown and plasma shielding," Optical Engineering, vol. 20, no. 6, 1981, pp. 206962.

33. E. Schwarz, S. Gross, B. Fischer, I. Muri, J. Tauer, H. Kofler, and E. Wintner. "Laser-induced optical breakdown applied for laser spark ignition," Laser and Particle Beams, vol 28, no. 1, p.109, 2010.

34. C.G. Morgan, "Laser-induced breakdown of gases," Reports on Progress in Physics, vol.38, p.621, 1975.

35. Y. P. Raizer, "Heating of a gas by a powerful light pulse, soviet physics," JETP, vol. 21, no. 5, 1965.

36. S. Ramsden and P. Savic, "A radiative detonation model for the development of a laser-induced spark in air," National Research Council of Canada Ottawa, Tech. Rep., 1964.

37. M. Gatti, V. Palleschi, A. Salvetti, D. Singh, and M. Vaselli, "Spherical shock waves in laser produced plasmas in gas," Optics Communications, vol. 69, no. 2, pp. 141–146, 1988.

38. S. Siano and R. Pini, "Analysis of blast waves induced by q-switched nd: Yag laser photodisruption of absorbing targets," Optics Communications, vol. 135, no. 4-6, pp. 279–284, 1997.

39. T. Shimano, J. A. Ofosu, K. Matsui, K. Komurasaki, and H. Koizumi, "Laser induced discharge propagation velocity in helium and argon gases," Transactions of the Japan Society for Aeronautical and Space Sciences, vol. 60, no. 6, pp. 378–381, 2017.

40. J. Hermann and T. Le Floch, "Generation of absorption waves by co 2 laser pulses at low power density," Journal of Applied Physics, vol. 96, no. 6, pp. 3084–3094, 2004.

41. C. Dumitrache, R. VanOsdol, C. M. Limbach, and A. P. Yalin, "Control of early flame kernel growth by multi-wavelength laser pulses for enhanced ignition," Scientific Reports, vol. 7, no. 1, pp. 1–8, 2017.

42. V. Bergelson, T. Loseva, I. Nemchinov, and T. Orlova, "Propagation of plane supersonic radiation waves," Fizika Plazmy, vol. 1, pp. 912–922, 1975.

43. S. Yal¸cin, D. Crosley, G. Smith, and G. W. Faris, "Influence of ambient conditions on the laser air spark," Applied Physics B Lasers and Optics, vol. 68, pp. 121–130, 1999.

44. I. Nemchinov, M. Popova, and L. Shubadeeva, "Supersonic radiation waves with motion of plasma," Journal of Engineering Physics, vol. 43, no. 4, pp. 1093–1097, 1982.

45. T. P. Hughes, Plasmas and laser light, New York, 1975.

46. C. Goldbach, G. Nollez, and R. Peyturaux, "Thermal arc plasmas as radiation sources," Astronomy and Astrophysics, vol. 21, p. 299, 1972.

47. D. Mandell and R. Cess, "Radiative transport quantities for a hydrogen plasma," Journal of Quantitative Spectroscopy and Radiative Transfer, vol. 9, no. 7, pp. 981–994, 1969.

48. T. X. Phuoc and F. P. White, "An optical and spectroscopic study of laserinduced sparks to determine available ignition energy," Proceedings of the Combustion Institute, vol. 29, no. 2, pp. 1621–1628, 2002.

49. M. Gilmore, "Engineering applications of plasma science," IEEE Potentials, vol. 17, no. 3, pp. 4–8, 1998.

50. G. Tartar, H. Ranner, F. Winter, and E. Wintner, "Simulation of optical breakdown in nitrogen by focused short laser pulses of 1064 nm wavelength," Laser and Particle Beams, vol. 26, no. 4, p. 567, 2008.

51. S. Mandel'Shtam, P. Pashinin, A. Prokhorov, Y. P. Raizer, and N. Sukhodrev, "Investigation of the spark discharge produced in air by focusing laser radiation II," Sov. Phys. JETP, vol. 22, pp. 91–96, 1966.

52. K. Matsui, T. Shimano, J. A. Ofosu, K. Komurasaki, T. Schoenherr, and H. Koizumi, "Accurate propagation velocity measurement of laser supported detonation waves," Vacuum, vol. 136, pp. 171–176, 2017.

53. H. Shiraishi and Y. Kumagai, "Numerical analysis of threshold between lasersupported detonation and combustion wave using thermal non-equilibrium and multi-charged ionization model," Transactions of the Japan Society for Aeronautical and Space Sciences, vol. 10, pp. Pb 59–Pb 63, 2012.

54. S. S. Harilal, B. E. Brumfield, and M. C. Phillips, "Lifecycle of laser-produced air sparks," Physics of Plasmas, vol. 22, p.063301, 2015.

55. Y. Qiu, J. Wu, Z. Zhang, T. Liu, F. Xue, Y. Hang, Y. Wu, H. Yu, and X. Li, "Comparisons of laser-produced plasma in atmosphere between fiberdelivery and direct-focusing laser pulse," Spectrochimica Acta Part B: Atomic Spectroscopy, vol. 155, pp. 12–23, 2019.

56. C. Dumitrache, C. M. Limbach, and A. P. Yalin, "Threshold characteristics of ultraviolet and near infrared nanosecond laser induced plasmas," Physics of Plasmas, vol. 23, no. 9, p. 093515, 2016.

57. J. F. Kielkopf, "Spectroscopic study of laser-produced plasmas in hydrogen," Physical Review E, vol. 52, no. 2, p. 2013, 1995.

58. J. Cowpe, J. Astin, R. Pilkington, and A. Hill, "Temporally resolved laser induced plasma diagnostics of single crystal silicon—effects of ambient pressure," Spectrochimica Acta Part B: Atomic Spectroscopy, vol. 63, no. 10, pp. 1066– 1071, 2008.

59. S. S. Harilal, "Spatial and temporal evolution of argon sparks," Applied Optics, vol. 43, no. 19, pp. 3931–3937, 2004.

60. L. Wermer, J. K. Lefkowitz, T. Ombrello, M. S. Bak, and S.-K. Im, "Spatiotemporal evolution of the plasma from dual-pulsed laser-induced breakdown in an atmospheric air," Plasma Sources Science and Technology, vol. 27, no. 1, p. 015012, 2018.

61. M. Capitelli, A. Casavola, G. Colonna, and A. De Giacomo, "Laser-induced plasma expansion: theoretical and experimental aspects," Spectrochimica Acta Part B: Atomic Spectroscopy, vol. 59, no. 3, pp. 271–289, 2004.

62. N. M. Shaikh, M. Kalhoro, A. Hussain, and M. Baig, "Spectroscopic study of a lead plasma produced by the 1064 nm, 532 nm and 355 nm of a nd: Yag laser," Spectrochimica Acta Part B: Atomic Spectroscopy, vol. 88, pp. 198–202, 2013.

63. D. Wiggins, C. Raynor, and J. Johnson III, "Evidence of inverse bremsstrahlung in laser enhanced laser-induced plasma," Physics of Plasmas, vol. 17, no. 10, p. 103303, 2010.

64. N. Glumac, G. Elliott, and M. Boguszko, "Temporal and spatial evolution of a laser spark in air," AIAA Journal, vol. 43, no. 9, pp. 1984–1994, 2005.

65. N. Kawahara, J. L. Beduneau, T. Nakayama, E. Tomita, and Y. Ikeda, "Spatially, temporally, and spectrally resolved measurement of laser-induced plasma in air," Applied Physics B, vol. 86, pp. 605-614, 2007.

66. J. X. Ma, D. R. Alexander, and D. E. Poulain, "Laser spark ignition and combustion characteristics of methane-air mixtures," Combustion and Flame, vol. 112, no. 4, pp. 492–506, 1998.

67. S. Joshi, H. El-Rabii, C. Dumitrescu, P. Puzinauskas, and A.P. Yalin, "Temperature and electron density measurements of laser-induced plasmas in air at elevated pressures," Spectroscopy Letters, vol. 44 no. 2, pp.103-112, 2011.

68. A. Alberti, A. Munaf`o, M. Koll, M. Nishihara, C. Pantano, J. B. Freund, G. S. Elliott, and M. Panesi, "Laser-induced non-equilibrium plasma kernel dynamics," Journal of Physics D: Applied Physics, vol. 53, no. 2, p. 025201, 2019.

69. P. D. Ronney, "Laser versus conventional ignition of flames," Optical Engineering, vol. 33, no. 2, pp. 510–522, 1994.

70. J. Tauer, H. Kofler, and E. Wintner, "Laser-initiated ignition," Laser & Photonics Reviews, Rev. 4, No. 1, pp. 99–122, 2010.

71. I. A. Mulla, S. R. Chakravarthy, N. Swaminathan, and R. Balachandran, "Evolution of flame-kernel in laser-induced spark ignited mixtures: A parametric study," Combustion and Flame, vol. 164, pp. 303–318, 2016.

72. D. K. Srivastava, M. Weinrotter, K. Iskra, A. K. Agarwal, and E. Wintner, "Characterisation of laser ignition in hydrogen–air mixtures in a combustion bomb," International Journal of Hydrogen Energy, vol. 34, no. 5, pp. 2475–2482, 2009.

73. J. Syage, E. Fournier, R. Rianda, and R. Cohen, "Dynamics of flame propagation using laser-induced spark initiation: Ignition energy measurements," Journal of Applied Physics, vol. 64, no. 3, pp. 1499–1507, 1988.

74. J. L. Beduneau and Y. Ikeda, "Application of laser ignition on laminar flame front investigation," Experiments in Fluids, vol. 36, no. 1, pp. 108–113, 2004.

75. M. Weinrotter, H. Kopecek, E. Wintner, M. Lackner, and F. Winter, "Application of laser ignition to hydrogen–air mixtures at high pressures," International Journal of Hydrogen energy, vol. 30, no. 3, pp. 319–326, 2005.

76. J. Beduneau, N. Kawahara, T. Nakayama, E. Tomita, and Y. Ikeda, "Laser-induced radical generation and evolution to a self-sustaining flame," Combustion and Flame, vol. 156, no. 3, pp. 642–656, 2009.

77. T. Spiglanin, A. McIlroy, E. Fournier, R. Cohen, and J. Syage, "Time-resolved imaging of flame kernels: laser spark ignition of h2/o2/ar mixtures," Combustion and Flame, vol. 102, no. 3, pp. 310–328, 1995.

78. H. Kojima, E. Takahashi, and H. Furutani, "Breakdown plasma and vortex flow control for laser ignition using a combination of nano-and femto-second lasers," Optics Express, vol. 22, no. 101, pp. A90–A98, 2014.

79. M. Lackner, S. Charareh, F. Winter, K. F. Iskra, D. Rüdisser, T. Neger, H. Kopecek, and E. Wintner, "Investigation of the early stages in laser-induced ignition by schlieren photography and laser-induced fluorescence spectroscopy," Optics Express, vol. 12, no. 19, pp. 4546–4557, 2004.

80. M. Mansour, N. Peters, and L.-U. Schrader, "Experimental study of turbulent flame kernel propagation," Experimental Thermal and Fluid Science, vol. 32, no. 7, pp. 1396–1404, 2008.

81. Y.L. Chen and J. Lewis, "Visualization of laser-induced breakdown and ignition," Optics Express, vol. 9, no. 7, pp. 360–372, 2001.

82. B. Lewis and G. Von Elbe, Combustion, flames and explosions of gases, Elsevier, 2012.

83. S. P. M. Bane, "Spark ignition: experimental and numerical investigation with application to aviation safety," Ph.D. dissertation, California Institute of Technology, 2010.

84. F. A. Williams, Combustion theory, CRC Press, 2018.

85. S. R. Turns et al., Introduction to combustion, McGraw-Hill Companies, 1996.

86. O. Akindele, D. Bradley, P. Mak, and M. McMahon, "Spark ignition of turbulent gases," Combustion and Flame, vol. 47, pp. 129–155, 1982.

87. R. Herweg and G. Ziegler, "Flame kernel formation in a spark-ignition engine," International symposium COMODIA, vol. 90, 1990, pp. 173–178.

88. G. Wang, M. Boileau, D. Veynante, and K. Truffin, "Large eddy simulation of a growing turbulent premixed flame kernel using a dynamic flame surface density model," Combustion and Flame, vol. 159, no. 8, pp. 2742–2754, 2012.

89. F. Creta and M. Matalon, "Propagation of wrinkled turbulent flames in the context of hydrodynamic theory," Journal of Fluid Mechanics, vol. 680, p. 225, 2011.

90. F. Meier, J. Köhler, W. Stolz, W. Bloss, and M. Al-Garni, "Cycle-resolved hydrogen flame speed measurements with high speed schlieren technique in a hydrogen direct injection si engine," SAE Transactions, pp. 1754–1765, 1994.

91. C.W. Chiu, Y.C. Dong, and S. S. Shy, "High-pressure hydrogen/carbon monoxide syngas turbulent burning velocities measured at constant turbulent reynolds numbers," International Journal of Hydrogen energy, vol. 37, no. 14, pp. 10935–10946, 2012.

92. Y. Cho, D. Santavicca, and R. Sonntag, "The effect of spark power on sparkignited flame kernel growth," SAE Technical Paper, Tech. Rep., 1992.

93. H. M. Li, G. X. Li, Y. H. Jiang, L. Li, and F. S. Li, "Flame stability and propagation characteristics for combustion in air for an equimolar mixture of hydrogen and carbon monoxide in turbulent conditions," Energy, vol. 157, pp. 76–86, 2018.

94. A. Elbaz, M. Mansour, and D. Mohamed, "Experimental investigation of flame kernel in turbulent partial premixed flames," International Journal of Applied, vol. 3, no. 2, p. 21, 2012.

95. M. S. Mansour, A. M. Elbaz, and M. Zayed, "Flame kernel generation and propagation in turbulent partially premixed hydrocarbon jet," Combustion Science and Technology, vol. 186, no. 4-5, pp. 698–711, 2014.

96. T. Badawy and M. S. Mansour, "Assessment of flame kernel propagation in partially premixed turbulent jet under different turbulence levels," Fuel, vol. 191, pp. 350–362, 2017.

97. F. Wu, A. Saha, S. Chaudhuri, C. K. Law, Facilitated ignition in turbulence through differential diffusion, Phys. Rev. Lett. 113 (2014) 024503.

98. A. Saha, Y. Sheng and C. K. Law, On the competing roles of turbulence and differential diffusion in facilitated ignition, Proc. Combust. Inst. 37 (2019) 2383-2390.

99. S. S. Shy, M. T. Nguyen, S.Y. Huang, and C. C. Liu, Is turbulent facilitated ignition through differential diffusion independent of spark gap?, Combust. Flame 185 (2017) 1-3.

100. L. J. Jiang, S. S. Shy, M. T. Nguyen, and S. Y. Huang, Spark ignition probability and minimum ignition energy transition of the lean iso-octane/air mixture in premixed turbulent combustion, Combust. Flame 187 (2018) 87-95.

101. S. S. Shy, M. T. Nguyen, and S. Y. Huang, Effects of electrode spark gap, differential diffusion, and turbulent dissipation on two distinct phenomena: Turbulent facilitated ignition versus minimum ignition energy transition, Combust. Flame 205 (2019) 371-377.

102. M. T. Nguyen, S. S. Shy, Y. R. Chen, B. L. Lin, S. Y. Huang, and C. C. Liu, Conventional spark versus nanosecond repetitively pulsed discharge for a turbulence facilitated ignition phenomenon, Proc. Combust. Inst. (2020).

103. S. Essmann, D. Markus, H. Grosshans, and U. Maas, "Experimental investigation of the stochastic early flame propagation after ignition by a low-energy electrical discharge," Combustion and Flame, vol. 211, pp. 44–53, 2020.

104. R. G. Root, "Modeling of post-breakdown phenomena," Laser-Induced Plasmas and Applications, 1989.

105. S. Jo, and J. P. Gore, "Laser Induced Spark Ignition for Laminar Premixed Hydrogen Air Jets," AIAA Scitech 2021 Forum, 0681, 2021.

106. B. A. Ochs, R. Ranjan, D. Ranjan, and S. Menon, S. Topology and flame speeds of turbulent premixed flame kernels in supersonic flows, Combust. Flame 210 (2019) 83-99.

107. D. Fries, B. A. Ochs, A. Saha, D. Ranjan, and S. Menon, Flame speed characteristics of turbulent expanding flames in a rectangular channel, Combust. Flame, 199 (2019) 1-13.

108. B. A. Ochs, and S. Menon, Laser ignition in supersonic channel flow, Combust. Flame 214 (2020) 90-102.

109. B. Sforzo, A. Lambert, J. Kim, J. Jagoda, S. Menon, and J. Seitzman, Post discharge evolution of a spark igniter kernel. Combust. Flame 162 (2015) 181-190.

110. Y. Tang, M. Hassanaly, V. Raman, B. Sforzo, and J. Seitzman, Probabilistic modeling of forced ignition of alternative jet fuels. Proc Combust Inst. (2020).

111. D. Veynante, J. M. Duclos, and J. Piana, "Experimental analysis of flamelet models for premixed turbulent combustion," Symposium (International) on Combustion, vol. 25, no. 1. Elsevier, 1994, pp. 1249–1256.

112. G. S. Settles, Schlieren and shadowgraph techniques: visualizing phenomena in transparent media, Springer Science & Business Media, 2012.

113. M. Raffel, C. E. Willert, F. Scarano, C. J. Kähler, S. T. Wereley, and J. Kompenhans, Particle image velocimetry: a practical guide, Springer, 2018.

114. M. F. Modest, Radiative heat transfer, Academic press, 2013.

115. F. Q. Zhao and H. Hiroyasu, "The applications of laser rayleigh scattering to combustion diagnostics," Progress in Energy and Combustion Science, vol. 19, no. 6, pp. 447–485, 1993.

116. R. B. Miles, W. R. Lempert, and J. N. Forkey, "Laser rayleigh scattering," Measurement Science and Technology, vol. 12, no. 5, p. R33, 2001.

117. R. Seasholtz, J. Panda, and K. Elam, "Rayleigh scattering diagnostic for measurement of velocity and density fluctuation spectra," 40th AIAA Aerospace Sciences Meeting & Exhibit, 2002, p. 827.

118. W. Adams and E. Hecht, "Technical report: Rayleigh scattering combustion diagnostic," Sandia National Lab, Albuquerque, United States, Tech. Rep., 2015.

119. A. C. Eckbreth, Laser diagnostics for combustion temperature and species, CRC press, 1996, vol. 3.

120. R. Dibble and R. Hollenbach, "Laser rayleigh thermometry in turbulent flames," NASA STI/Recon Technical Report, N 81, p.27515, 1981.

121. A. Soika, F. Dinkelacker, and A. Leipertz, "Measurement of the resolved flame structure of turbulent premixed flames with constant reynolds number and varied stoichiometry," Symposium (International) on Combustion, vol. 27, no. 1. Elsevier, 1998, pp. 785–792.

122. F. T. Yuen and O. L. Gülder, "Investigation of dynamics of lean turbulent premixed flames by rayleigh scattering," AIAA Journal, vol. 47, no. 12, pp. 2964– 2973, 2009.

123. P. Tamadonfar and O. L. Gülder, "Effect of burner diameter on the burning ¨ velocity of premixed turbulent flames stabilized on bunsen-type burners," Experimental Thermal and Fluid Science, vol. 73, pp. 42–48, 2016.

124. F. T. Yuen and O. L. Gülder, "Premixed turbulent flame front structure inves- ¨ tigation by rayleigh scattering in the thin reaction zone regime," Proceedings of the Combustion Institute, vol. 32, no. 2, pp. 1747–1754, 2009.

125. J. Smith, "Rayleigh temperature profiles in a hydrogen diffusion flame," Laser Spectroscopy: Applications and Techniques, pp. 84–90, 1978.

126. T. Takagi, Z. Xu, and M. Komiyama, "Preferential diffusion effects on the temperature in usual and inverse diffusion flames," Combustion and Flame, vol. 106, no. 3, pp. 252–260, 1996.

127. R. W. Schefer, W. G. Houf, and T. Williams, "Investigation of small-scale unintended releases of hydrogen: buoyancy effects," International Journal of Hydrogen Energy, vol. 33, no. 17, pp. 4702–4712, 2008.

128. R. Schefer, W. G. Houf, and T. Williams, "Investigation of small-scale unintended releases of hydrogen: momentum-dominated regime," International Journal of Hydrogen Energy, vol. 33, no. 21, pp. 6373–6384, 2008.

129. R. Schefer, G. Evans, J. Zhang, A. Ruggles, and R. Greif, "Ignitability limits for combustion of unintended hydrogen releases: Experimental and theoretical results," International Journal of Hydrogen Energy, vol. 36, no. 3, pp. 2426–2435, 2011.

130. M. Komiyama, T. Fujimura, T. Takagi, and S. Kinoshita, "Dynamic behavior of diffusion flame interacting with a large-scale vortex by laser imaging techniques," Proceedings of the Combustion Institute, vol. 30, no. 1, pp. 465–473, 2005.

131. M. Komiyama, R. Kawabe, and T. Takagi, "Extinction and interruption of diffusion flame interacting with a large scale vortex," Proceedings of the Combustion Institute, vol. 32, no. 1, pp. 1099–1106, 2009.

132. N. S. Okhovat, J. M. Hauth, and D. L. Blunck, "Temperatures of spark kernels discharging into quiescent or crossflow conditions," Journal of Thermophysics and Heat Transfer, vol. 31, no. 1, pp. 120–129, 2017.

133. D. L. Blunck, B. V. Kiel, L. Goss, and A. Lynch, "Spatial development and temperature of spark kernels exiting into quiescent air," Journal of Propulsion and Power, vol. 28, no. 3, pp. 458–465, 2012.

134. B. Rankin, J. Gore, J. Hoke, and F. Schauer, "Radiation measurements and temperature estimates of unsteady exhaust plumes exiting from a turbine driven by pulsed detonation combustion," 51st AIAA Aerospace Sciences Meeting including the New Horizons Forum and Aerospace Exposition, 2013, p. 886.

135. J. R. Howell, M. P. Menguc, and R. Siegel, Thermal radiation heat transfer, CRC press, 2015.

136. C. C. Ferriso, C. B. Ludwig, and A. L. Thomson, "Empirically determined infrared absorption coefficients of H2O from 300 to 3000 K," Journal of Quantitative Spectroscopy and Radiative Transfer, vol 6, no. 3, pp. 241-275, 1966.

137. A. L. Brundage, A. Burl Donaldson, W. Gill, S. P. Kearney, V. F. Nicolette, and N. Yilmaz, "Thermocouple response in fires, part 1: considerations in flame temperature measurements by a thermocouple," Journal of Fire Sciences, vol. 29, no. 3, pp. 195–211, 2011.

138. V. Hindasageri, R. Vedula, and S. Prabhu, "Thermocouple error correction for measuring the flame temperature with determination of emissivity and heat transfer coefficient," Review of Scientific Instruments, vol. 84, no. 2, p. 024902, 2013.

139. M. Summerfield, S. H. Reiter, V. Kebely, and R. W. Mascolo, "The structure and propagation mechanism of turbulent flames in high speed flow," Journal of Jet Propulsion, vol. 25, no. 8, pp. 377–384, 1955.

140. M. M. Hossain, G. Lu, D. Sun, and Y. Yan, "Three-dimensional reconstruction of flame temperature and emissivity distribution using optical tomographic and two-colour pyrometric techniques," Measurement Science and Technology, vol. 24, no. 7, p. 074010, 2013.

141. D. Bradley and K. Matthews, "Measurement of high gas temperatures with fine wire thermocouples," Journal of Mechanical Engineering Science, vol. 10, no. 4, pp. 299–305, 1968.

142. R. Shurtz, "Total hemispherical emissivity of metals applicable to radiant heat testing." Sandia National Lab.(SNL-NM), Albuquerque, NM (United States), Tech. Rep., 2018.

143. J. A. Sutton and J. F. Driscoll, "Rayleigh scattering cross sections of combustion species at 266, 355, and 532 nm for thermometry applications," Optics Letters, vol. 29, no. 22, pp. 2620–2622, 2004.

144. J. Fielding, J. H. Frank, S. A. Kaiser, M. D. Smooke, and M. B. Long, "Polarized/depolarized rayleigh scattering for determining fuel concentrations in flames," Proceedings of the Combustion Institute, vol. 29, no. 2, pp. 2703–2709, 2002.

145. I. Namer and R. Schefer, "Error estimates for rayleigh scattering density and temperature measurements in premixed flames," Experiments in Fluids, vol. 3, no. 1, pp. 1–9, 1985.

146. S. Gordon and B. J. McBride, "Computer program for calculation of complex chemical equilibrium compositions and applications. part 1: Analysis," NASA, United States, Tech. Rep., 1994.

147. M. J. Papageorge, T. A. McManus, F. Fuest, and J. A. Sutton, "Recent advances in high-speed planar rayleigh scattering in turbulent jets and flames: increased record lengths, acquisition rates, and image quality," Applied Physics B, vol. 115, no. 2, pp. 197–213, 2014.

148. R. Patton, K. Gabet, N. Jiang, W. Lempert, and J. Sutton, "Multi-khz temperature imaging in turbulent non-premixed flames using planar rayleigh scattering," Applied Physics B, vol. 108, no. 2, pp. 377–392, 2012.

149. B. Bork, B. B¨ohm, C. Heeger, S. Chakravarthy, and A. Dreizler, "1d high-speed rayleigh measurements in turbulent flames," Applied Physics B, vol. 101, no. 3, pp. 487–491, 2010.

150. H. H. Reising, T. W. Haller, N. T. Clemens, P. L. Varghese, R. Fiévet, and V. Raman, "Spontaneous raman scattering temperature measurements and large eddy simulations of

vibrational non-equilibrium in high-speed jet flames," 32nd AIAA Aerodynamic Measurement Technology and Ground Testing Conference, 2016, p. 3550.

151. J. George, T. P. Jenkins, and R. B. Miles, "Diagnosis of high speed flows using filtered rayleigh scattering," 30th AIAA Aerodynamic Measurement Technology and Ground Testing Conference, 2014, p. 2231.

152. J. George, T. P. Jenkins, and Miles, "Measurement of density in high speed shear layers and oblique shocks using filtered rayleigh scattering," 55th AIAA Aerospace Sciences Meeting, 2017, p. 1407.

153. D. Feng, B. M. Goldberg, M. Naphade, M. N. Shneider, and R. B. Miles, "A model study of filtered rayleigh scattering sensitivity to pressure and temperature," 2018 AIAA Aerospace Sciences Meeting, 2018, p. 2042.

154. R. A. Patton and J. A. Sutton, "Seed laser power effects on the spectral purity of q-switched nd: Yag lasers and the implications for filtered rayleigh scattering measurements," Applied Physics B, vol. 111, no. 3, pp. 457–468, 2013.

155. P. L. O'Neill, D. Nicolaides, D. Honnery, J. Soria et al., "Autocorrelation functions and the determination of integral length with reference to experimental and numerical data," 15th Australasian Fluid Mechanics Conference, vol. 1. Univ. of Sydney Sydney, NSW, Australia, 2004, pp. 1–4.

156. C. K. Law, Combustion physics. Cambridge university press, 2010.

157. M. Kuznetsov, S. Kobelt, J. Grune, and T. Jordan, "Flammability limits and laminar flame speed of hydrogen–air mixtures at sub-atmospheric pressures," International Journal of Hydrogen Energy, vol. 37, no. 22, pp. 17580–17588, 2012.

158. D. R. Dowdy, D. B. Smith, S. C. Taylor, and A. Williams, "The use of expanding spherical flames to determine burning velocities and stretch effects in hydrogen/air mixtures," Symposium (International) on Combustion, vol. 23, no. 1. Elsevier, 1991, pp. 325–332.

159. K. Aung, M. Hassan, and G. Faeth, "Flame stretch interactions of laminar premixed hydrogen/air flames at normal temperature and pressure," Combustion and Flame, vol. 109, no. 1-2, pp. 1–24, 1997.

160. O. Kwon and G. Faeth, "Flame/stretch interactions of premixed hydrogen-fueled flames: measurements and predictions," Combustion and Flame, vol. 124, no. 4, pp. 590–610, 2001.

161. S. B. Pope, Turbulent flows, Cambridge University Press, 2001

162. F. L. Pedrotti, L. M. Pedrotti, and L. S. Pedrotti, Introduction to optics, Cambridge University Press, 2017.

163. Y. P. Raizer, "Breakdown and heating of gases under the influence of a laser beam," Soviet Physics Uspekhi, Vol. 8, p.650, 1966.

164. L. J. Radziemski, "Laser-induced plasmas and applications, CRC Press," pp.69-103,1989. 69-103.

165. T. L. Bergman, F. P. Incropera, D. P. DeWitt, and A. S. Lavine, Fundamentals of heat and mass transfer, John Wiley & Sons, 2011.

166. O. Hofer, "Study of laser heated propulsion devices. part 1: Evaluation of laser devices, fuels and energy coupling mechanisms," Lockheed Missiles and Space Co., Huntsville, AL, United States, Tech. Rep., 1982.

167. B. Lei, J. Wang, J. Li, J. Tang, Y. Wang, W. Zhao, and Y. Duan, "Influence of humidity on the characteristics of laser-induced air plasma," Japanese Journal of Applied Physics, vol. 57, no. 10, p. 106001, 2018.

168. V. Zvorykin, "Analysis of gasdynamic regimes of interaction of co 2 laser radiation with targets in air at normal and reduced density," Journal of Soviet Laser Research, vol. 14, no. 1, pp. 42–61, 1993.

169. B. Lei, J. Wang, J. Li, J. Tang, Y. Wang, W. Zhao, and Y. Duan, "Signal enhancement of laser-induced breakdown spectroscopy on non-flat samples by single beam splitting," Optics Express, vol. 27, no. 15, pp. 20541–20557, 2019.

170. V. Danilychev and V. Zvorykin, "Experimental investigation of radiationgasdynamic processes that develop under the action of high-power λ= 10.6 μm laser pulses on a solid in a gas," Journal of Soviet Laser Research, vol. 5, no. 6, pp. 667–715, 1984.

171. B. Lei, B. Xu, J. Wang, J. Li, Y. Wang, J. Tang, W. Zhao, and Y. Duan, "Timeresolved characteristics of laser induced breakdown spectroscopy on non-flat samples by single beam splitting," RSC Advances, vol. 10, no. 65, pp. 39 553– 39 561, 2020.

172. X. Li, R. Fan, H. Zhu, X. Yu, and D. Chen, "Characterization of laser induced plasmas in nitrogen using an ungated spectrometer," Journal of Quantitative Spectroscopy and Radiative Transfer, vol. 118, pp. 1–7, 2013.

173. F. Rongwei, Z. Hai, L. Xiaohui, P. Jiangbo, Y. Xin, and C. Deying, "Characterization of laser-induced plasma in nitrogen," Journal of Russian Laser Research, vol. 34, no. 4, pp. 369–374, 2013.

174. L. D. Landau and E. M. Lifshits, Fluid mechanics, Pergamon Press Oxford, UK, 1959.

175. J. B. Will, N. P. Kruyt, and C. H. Venner, An experimental study of forced convective heat transfer from smooth, solid sphere, International Journal of Heat and Mass Transfer 109 (2017) 1059-1067.

176. M. Yovanovich , General expression for forced convection heat and mass transfer from isopotential spheroids, 26th Aerospace Sciences Meeting (1988) 743.

177. G. Refai Ahmed and M. Yovanovich, Approximate analytical solution of forced convection heat transfer from isothermal spheres for all Prandtl numbers, J. Heat Transfer. 116 (1994) 838-843.

178. S. W. Churchill, A comprehensive correlating equation for laminar, assisting, forced and free convection, AIChE Journal 23 (1977) 10-16.

179. R. Barlow, A. Karpetis, J. Frank, and J. Y. Chen, "Scalar profiles and no formation in laminar opposed-flow partially premixed methane/air flames," Combustion and Flame, vol. 127, no. 3, pp. 2102–2118, 2001.

180. A. P. Kelley, G. Jomaas, and C. K. Law, "Critical radius for sustained propagation of spark-ignited spherical flames," Combustion and Flame, vol. 156, no. 5, pp. 1006–1013, 2009.

181. M. Baum and T. Poinsot, "Effects of mean flow on premixed flame ignition," Combustion Science and Technology, vol. 106, no. 1-3, pp. 19–39, 1995.

182. C. T. d'Auzay, V. Papapostolou, S. F. Ahmed, and N. Chakraborty, "On the minimum ignition energy and its transition in the localised forced ignition of turbulent homogeneous mixtures," Combustion and Flame, vol. 201, pp. 104– 117, 2019.

183. Y. Ko, R. Anderson, and V. S. Arpaci, "Spark ignition of propane-air mixtures near the minimum ignition energy: Part i. an experimental study," Combustion and Flame, vol. 83, no. 1-2, pp. 75–87, 1991.

184. D. R. Ballal and A. Lefebvre, "A general model of spark ignition for gaseous and liquid fuel-air mixtures," Symposium (international) on Combustion, vol. 18, no. 1. Elsevier, 1981, pp. 1737–1746.

185. C. Manfletti, "Laser ignition of an experimental cryogenic reaction and control thruster: ignition energies," Journal of Propulsion and Power, vol. 30, no. 4, pp. 952–961, 2014.

186. B. An, Z. Wang, L. Yang, X. Li, and J. Zhu, "Experimental investigation on the impacts of ignition energy and position on ignition processes in supersonic flows by laser induced plasma," Acta Astronautica, vol. 137, pp. 444–449, 2017.

187. T. X. Phuoc, F. P. White, "Laser-induced spark ignition of CH4/air mixtures," Combustion and Flame, vol. 119, pp. 203-216, 1999.

APPENDIX A. IGNITION ENERGY MEASUREMENT

This present research has used the ignition probability of 100 % in the ignition energy measurements for the reliability of ignition in combustion devices. Ignition energy increases with increasing ignition probability. Ignition tests were conducted to measure ignition energies considering ignition probabilities. The trials of the ignition tests for each ignition energy to find the ignition probability was 50 times. Figure A.1 shows the ignition probability as a function of the ignition energy. This is a common result in ignition energy measurements [10, 83].
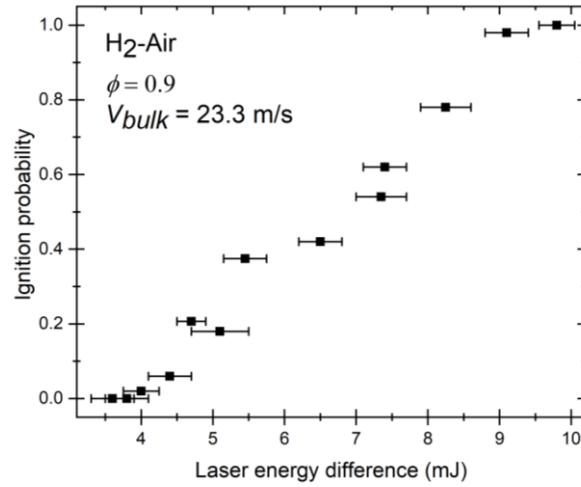

Fig.A.1. Ignition probability versus ignition energy.

Minimum ignition energy (MIE) values in methane-air were measured at various equivalence ratios to verify the present experiment method. This is because Beduneau et al. [3] who measured MIE in a Bunsen burner utilized methane-air for their experiments. The bulk velocity of 3.33 m/s, and the ignition height of 20 mm were utilized. This condition is the same as the measurement reported by Beduneau et al. [3]. The ignition probability of 50 % was used for this ignition experiment. The reason is the ignition probability of 50 % is commonly used [10]. Lewis and Von Elbe [82] measured ignition energy in a chamber using an electrode spark. Phuoc et al. [187] studied ignition energy in a chamber with a laser-induced spark. Beduneau et al. [3] conducted ignition experiments with a laser focused height of 20 mm, a velocity of 3.33 m/s and

a laser-induced spark. The MIE results obtained from the present work are slightly different from the values studied by Beduneau et al. [3] [Fig.A.2]. Optic components, including flash lamps, the lenses, mirrors, and the blockage ratio of the burner might have contributed to the small difference. The MIE data measured by Phuoc et al. [187] was higher than our results due to the focal length (75 mm) [Fig.A.2]. Generally, as a focal length is longer, ignition energy increases due to low laser irradiance [3]. The ignition energy examined in the present work is similar to the data available in the literature [3,82,187] [Fig.A.2]. Therefore, the MIE measurements using in the present study are accurate.
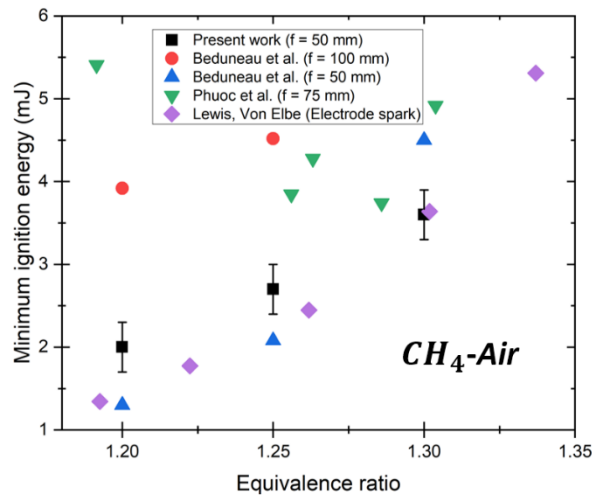

Fig.A.2. Minimum ignition energy in methane air mixture. Comparison with results reported by Beduneau et al. [3], Lewis and Von Elbe [82], and Phuoc et al. [187].